University of Tehran
ISSN: 2322-2093
Volume 58, Number 1, June 2025

Civil Engineering Infrastructures Journal

CEIJ

Available online at
www.ceijournal.com

Civil Engineering Infrastructures Journal (CEIJ)
Volume 58, Number 1, June 2025

Civil Engineering Infrastructures Journal (CEIJ)
Semiannual Publication

Published by:

University of Tehran
College of Engineering

Indexed by:

Web of Science (ESCI)

Scopus

Civil Engineering Infrastructures Journal (CEIJ)
College of Engineering
University of Tehran
P.O. Box: 11155-4563
Tehran, Iran.
Tel/ Fax: +98-21-88956097
Email: ceij@ut.ac.ir
Web Site: www.ceij.ir

Editorial Board

Advisory Board

CONTENTS
Volume 58, Number 1, June 2025

Civil Engineering Infrastructures Journal 2025, 58(1): 1-13
DOI: 10.22059/ceij.2024.361854.1947

REVIEW PAPER

Effects of Inclusion of SAP as an Internal Curing Agent in Concrete, A Review

Jindal, A.[1*] and Mehra, D.[2]

[1] Assistant Professor, Department of Civil Engineering, School of Engineering and Technology, Central University of Haryana, India.
[2] Research Scholar, Department of Civil Engineering, School of Engineering and Technology, Central University of Haryana, India.

Received: 27 Jul. 2023; Revised: 14 Dec. 2023; Accepted: 27 Jan. 2024

ABSTRACT: Concrete in today's world has a major role in construction industry and is the most frequently used material in construction having high compressive strength and durability. Concrete needs proper curing to achieve desirable properties and insufficient curing affects the strength of concrete badly. Nowadays, Internal Curing (IC) has come into research which has many positive advantages in terms of enhancement of properties of concrete. By utilizing the water that is already in the concrete and adding certain amounts of self-curing agents, this method of curing is used that helps in the curing of the concrete internally. It is done 'from the inside to outside' using internal reservoirs. Also, shrinkage reducing agents like Polyethylene-glycol and Light-Weight Aggregates (LWA) are used to achieve effective curing results. In cement-based materials, Superabsorbent Polymer (SAP) is generating a lot of debate. This study offers a review for cement-based materials containing SAP for different w/c values, the conclusions on the properties including workability, mechanical characteristics, and durability of SAP-modified concrete and SAP cement-based materials. In most of the studies found on high-performance concrete, w/c is restricted to 0.3 - 0.35. Hence, properties are described on the basis of different w/c ratios as mentioned in this paper. Total 60 articles are reviewed (including 59 research paper and 1 review report) in this study.

Keywords: Internal Curing, Concrete, Superabsorbent Polymer, Mechanical Properties, Hydration Process.

1. Introduction

There might be an urgent need to look into water conservation in concrete and building construction that water resources become more scarce. The curing effect is crucial to getting the desired qualities out of concrete. Efficient concrete curing preserves the moisture content of the concrete, which aids in the preservation of an efficient hydration process in early age. The process of curing involves keeping the concrete at the right temperature and moisture level for a certain period of time before it hardens. Promoting cement hydration and reducing shrinkage are two main objectives of curing, in order to enhance concrete properties at later stage.

There are various curing techniques,

* Corresponding author E-mail: ajindal@cuh.ac.in

including internal, exterior, and sealed curing. According to Wang et al. (2019), Internal Curing (IC) can stop UHPC from desiccating on its own, while external curing methods like water curing cannot.

The effect of temperature altered thermal curing was also discussed by Shen et al. (2019). They concluded that the development of UHPC strength is significantly influenced by thermal curing. The process used to produce C-S-H gels results in a dense microstructure, which greatly boosts the material's strength. The formation of quartz and the formation of hydrates and microstructures as a result of different curing regimes are important factors in the erratic behavior of the strength ratio and the enhancement of mechanical properties.

IC is a potential approach to remove cracks in cement concrete, which have become a major problem. It is the process of adding porous substances into cement-based products to create "reservoirs" that quickly provide water when hydration is required or to compensate moisture loss. The water which is already present in cementitious materials may release during the hydration process due to the effect of capillary tension and humidity gradient. The advantages of internal curing include higher internal moisture content results in better hydration and higher relative humidity. Thus the concrete does not require external water curing (Amin et al., 2021). Super-Absorbent Polymers (SAP) and Lightweight Aggregates (LWA) like zeolite or natural pumice are frequently used as internal curing materials (Liu et al., 2019). Concrete experiences autogenous shrinkage during cement hydration, which is characterized by lack of moisture exchange with the surrounding environment. Although, autogenous shrinkage is minimal, it can be significant in concrete that has a very low water/cement ratio (Neville, 1995).

Hamzah et al. (2022) demonstrated that SAP aggregates can decrease the autogenous shrink ability of UHPC without changing its new behavior, mechanical properties, or density. Wang et al. (2022) demonstrated that SAP has a high moisture-carrying ability and may have enhanced self-healing properties. The qualities of concrete will be also improved by the size and quantity of SAP. When SAP is added, regulated water-filled microscopic inclusions are created.

These inclusions lessen autogenous shrinkage, encourage the hydration of anhydrate cement, and stop internal moisture evaporation from compensating for water loss during the curing process. The autogenous shrinkage and chemical shrinkage are roughly equal in the initial stages of hydrations, before hardness occurs (Ghanem et al., 2024). SAP has the following advantages over light-weight aggregates. IC may only require a small amount of SAP, and neither the workability nor the mechanical qualities will be significantly affected (Jensen and Hansen, 2001). To increase the resistance of material to the effects of freeze-thaw, SAP might be used as an air-entraining substance (Jensen and Hansen, 2001). During the preparation of the specimen, the water absorption rate of SAP can be determined.

1.1. SAP (Superabsorbent Polymer)

Superabsorbent Polymer (SAP), a cross-linked hydrophilic polymer, also termed as slush powder, mostly white in colour and in powdered form. Several studies have been made on the SAP regarding its cross-linked densities such as: Zhong et al. (2019) discovered that SAP exhibiting a high density of anionic groups or both ionic groups demonstrated an enhanced self-curing effect in minimizing autogenous shrinkage. Additionally, much less released water was seen in the case of SAP exhibiting a low density of anionic groups. Furthermore, a minor effect was observed for non-ionic SAP with increased crosslinking density, but lower equilibrium absorptivity was the result for ionic and zwitterionic SAP.

When SAP comes in contact with water,

it instantly increases in size after absorption of water and transforms into a hydrogel structure with a certain viscosity. SAP particles can absorb large amounts of water during the mixing process and then swell to produce a hydrogel, due to the creation of water incorporation which prevents self-desiccation during cement hydration (Yang et al., 2019) Superabsorbent polymers (SAPs) can be added to a concrete mixture to provide IC and reduce the risk for early-age shrinkage cracking. Jensen and Hansen (2002) used SAP as IC in high performance concrete. Dejian et al. (2020) utilized SAP in order to decrease the high-strength resistance to cracking of concrete.

The autogenous shrinkage was enhanced with SAP. There was a greater increase in the w/c ratio, which improved the mechanical properties, shrinkage, and creep. SAP has good water absorption and retention abilities. SAP readily absorbs water while making cement-based products. the development of a water wrapper vicinity of the SAP particles is facilitated by the absorption capabilities of SAP and the ionic concentration of cement paste. As the material's internal humidity lowers during the curing process, the osmotic pressure rises, causing the water inside SAP to slowly release.

Cement-based products may develop cracks during the course of their service lifespan as a result of loading and environmental influences. It has been demonstrated that materials made with SAP cement have self-healing qualities (Snoeck et al., 2014). Water can react with anhydrate cement in ordinary concrete with no SAP penetrates its tiny cracks, providing the hydration support and enabling the filling of the small cracks. The said self-healing crack width limit is 0.05 mm or smaller (Snoeck et al., 2014). However, the average crack width produced by external forces is more than 0.05 mm.

When SAP is used in cement-based products as a self-healing additive, it can slowly let go the water to interact with the surrounding anhydrate cement. The hydration products created may help in the healing and subsequent filling of the micro cracks. Additionally, when water enters SAP, the SAP gel expands and fills macro cracks, restricting the flow of water. It was previously noted that as water flows through cracks, the SAP molecules nearest to the upstream side expand into a gel-like substance that covers the voids and cracks in the SAP, while those towards the downstream face remain dry (Snoeck et al., 2014). Larger SAP particles may leave larger pore volume in cement-based products after they release water. Yet it was claimed that the cement's continued hydration was a result of a water loss, which led to decrease the porosity at hardened state (Igarashi, 2006). The high-water absorption capacity of SAP has an impact on the mechanical properties and fresh state of cement-based composites.

According to reports, SAP had a negative impact on mechanical properties, especially at early stage (Wehbe and Ghahremaninezhad, 2017). According to Klemm and Sikora (2013), the mechanical properties of SAP cement-based materials are significantly influenced by the SAP type and the water absorption and desorption kinetics. Faxiang et al. (2021) investigated the structural behavior of SAP concrete under constant load. Also, examined the shear and compression properties of concrete. They demonstrated that although the cohesive stresses and the friction coefficient of the compression-shear strength dropped as the SAP content increased, the resulting residual strength and the compression-shear strength of SAP improved linearly with the axial pressure.

Lokeshwari et al. (2021) assessed several strength analyses using a superabsorbent polymer to add SAP agent Polyethylene glycol 400 to M30 grade concrete mixture to produce high compression strength. As a result, concrete will have greater strength than regular concrete when PEG-400 is applied properly. In dealing with the issue of water scarcity, Khushpreet Singh (2020) explored

a variety of techniques to address this issue. In addition to resulting in poor curing, self-desiccation can adversely affect the energy and durability of the concrete. According to Jensen (2008), the dried SAP particulate may alter the plastic viscosity of fresh concrete, which would affect the rheological behavior of the concrete.

The SAP content and additional water that should be included in a mix design for cement-based products must thus be carefully considered. Additionally, there is not any specific process for designing SAP cement-based material yet. Hence, there are variations between the diverse behavior of SAP materials based on cement. Critical issues include how to accurately calculate the SAP cement-based mix proportions products and comprehend how differing SAP contents affect the fundamental mechanical properties.

2. Rheological Properties of Sap-Based Cement Concrete (CC)

The rheological properties of CC with inclusion of SAP; are influenced by its tendency to absorb water and the gel formation. Although there are many characteristics that affect how workable CC is (including fluidity, viscosity, mobility, compaction ability, etc.). The concept of workability is a little bit complex. The Bingham's model by Bingham (1922) shows concrete as a non-Newtonian fluid and can be represented by the Eq. (1).

$$\tau = \tau\_0 + \mu\gamma \quad (1)$$

where τ: is shear stress; τ_o: is yield stress; μ: is plastic viscosity and γ: is rate of shear strain. The rheological characteristics of CC are influenced by the plastic viscosity (μ) and yield stress (τ_o). For illustrate, these previous two factors have an inverse relationship with the workability of the CC.

The extra water (IC water) provided has an impact on how SAP behaves to the matrix's rheological characteristics. For illustration, the workability of SAP incorporated CC will decrease if no additional water is supplied and the contrary will happen if IC water is provided (Jensen and Hansen, 2002). However, Shen et al. (2021) have shown that the workability of the cementitious composite is greatly reduced when SAP is used. The temperature, as well as the size of the SAP used, affect how well CC works as explained by Figure 1.

The solid lines indicate the absence of SAPs, while the dashed lines indicate the presence of SAPs (Secrieru et al., 2016). Figure 1 illustrates how cement pastes with and without SAP's plastic viscosity and yield stress change with temperature. It is clear that plastic viscosity and yield stress steadily rises at temperatures that are higher (20 °C and 30 °C) whereas at lower temperatures, the same parameter reduces rapidly.

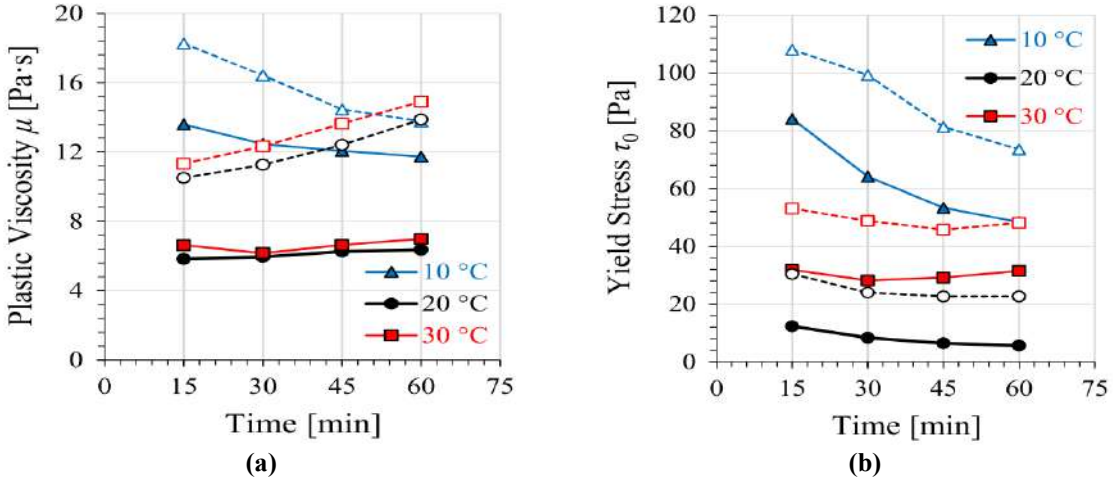

(a) **(b)**

Fig. 1. Effects of temperature on plastic viscosity and yield stress

Table 1. Statistical parameters values for testing and training by M5P model

Type of composite	Compressive strength of reference mix (MPa)	w/c ratio	Size of SAP particles (µm)	Dosage of SAP	Slump (mm)		References
					Reference mix	Modified with SAP	
HPC (High performance concrete)	97.6	0.32	-	1.11 (kg/m^3)	45	75	Craeye et al. (2011)
				1.56 (kg/m^3)		40	
				2 (kg/m^3)		60	
UHPC (Ultra-high performance concrete)	-	0.15	< 63	0.206%	1060	770	Justs et al. (2015)
				0.313%		710	
HPC	93.2	0.25	441	0.18%	70	85	Savva and Petrou (2018)
			384	0.20%		80	
Normal concrete	45-50	0.38	25-425	0.2%	212	200	Dang et al. (2017)
			150-180			190	

It may also be observed that the SAP inclusion in cement pastes enhances yield stress and plastic viscosity, which reduces workability (Secrieru et al., 2016). However, SAP particle size has also an impact on the rheological characteristics of CC, as per a study that investigated the impact of particle size (fine versus coarse) and ways of addition of SAP (i.e. dry or pre-soaked). According to Ma et al. (2019) the workability with large particle size reduces due to increment of yield stress and plastic viscosity.

The findings displayed how fine SAP enhances workability significantly than coarse SAP and adding pre-soaked SAP is more effective in enhancing workability than using dry SAP, which can be related to dry SAP's ability to absorb more mixing water (required for hydration). In conclusion, the direct incorporation of SAP to the matrix causes an increase in CC's plastic viscosity (or its workability to decrease). To improve the matrix's utility, more IC water as well as pre-soaked SAP is required. But according to the literature analysis, because the method of water release for SAP during complicated hydration processes (of cement and water) is unforeseen, SAP's impact on rheological characteristics of CC can be unpredictable. Thus, additional research is essential for fully comprehending how SAP affects the characteristics of CC's rheology.

3. Mechanical Properties and SAP

According to the majority of research studies on CC with SAP, the development of pores and voids in the hardened CC matrix causes mechanical properties including compressive, flexural, and tensile strength decline with time, mainly in the first phases (Jensen and Hansen, 2002; Craeye et al., 2011; Wong, 2018). While other research has also demonstrated that mechanical strength makes up for age at maturity (Qin et al., 2011). Table 2 shows the effect of SAP on different mechanical properties; mentioned in different research studies which shows the variation in mechanical properties like compressive strength, flexural strength, split tensile strength, etc. at matured age. In conclusion of Table 2 it is clear that the mechanical properties at matured age has slight variations (i.e. slightly increased or decreased). Here, Table 3 shows the effect of SAP modified cc under different curing conditions.

In conclusion, the majority of the above findings show that CC's mechanical properties are decreased by SAP inclusion. However, by using different fibres or additives, the strength loss can be countered (or increased). Moreover, the mixture composition and curing circumstances influence how SAP inclusion will respond to CC's mechanical properties.

Table 2. Effect of SAP on different mechanical properties

Type of composite	w/c ratio	Mechanical property	Strength (MPa) (28-days) (without SAP)	Strength (MPa) (28-days) (with SAP)	References
Mortar	0.48	Compressive strength	42.02	63.92	Tan et al. (2019)
UHPC	0.15	Compressive Strength	183	184	Justs et al. (2015)
		Flexural strength	24	26	
Mortar	0.30	Compressive Strength	89.6	92	Sensale and Goncalves (2014)
Cement paste	0.45	Compressive strength	43.35	41.8888	Pourjavadi et al. (2012)
		Flexural strength	6.5	6	
HPC	0.38	Compressive strength	52 55.5	53 56	Dang et al. (2017)
Normal concrete	0.45	Compressive strength	36.9	39.11	Karthikeyan et al. (2018)
		Flexural strength	4.25	43	
		Split tensile strength	3.75	3.70	
Normal concrete	0.5 0.4 0.35	Compressive strength	51 69 73	43 58 67.5	Hasholt et al. (2010)
HPC	0.25	Compressive strength	93.2	80.4 81.6	Savva and Petrou (2018)

Table 3. Effect of SAP modified CC under different curing conditions

Composite types	Mechanical property	Various curing condition			Remarks	References
		Sealed	Dry	Moist		
HPC	Compressive strength	16-31	-	-	Decrease	Craeye and Schutter (2008)
Normal concrete	Compressive strength	28-35	26-28	-	Decrease	Lam (2005)
HPC	Compressive strength	-	-	3-22	Decrease	Igarashi and Watanabe (2006)
	Tensile strength	-	-	11-33	Decrease	
HPC	Compressive strength	12-14	-	-	Fluctuations at water curing i.e. almost same	Savva and Petrou (2018)
HPC	Compressive strength	30	20	-	decrease	Mechtcherine et al., (2006)
UHPC	Compressive strength Flexural strength	-	-	Same	No change	Dudziak and Mechtcherine (2008)

4. Impact of SAP on Durability

The ability of CC to withstand a number of damaging elements, the cost of long-term maintenance and repair of mechanical and aesthetic components and properties, to be designed as per requirement enhances its employability as a construction material. Many methods (including the integration of SAP in CC**)** are employed to make concrete constructions more durable because of the high expense of maintenance and reconstructions.

Here, literature pertaining to permeability and freezing behavior of concrete is discussed, on the behalf of which durability can be comprehend.

4.1. Permeability

The permeability of a concrete specimen under examination can be estimated by determining its pore structure, which includes pore size, pore distribution, and cumulative surface area. This information then helps to evaluate the specimen's durability (Jindal and Ransinchung, 2022). The property of CC that regulates the flow rate of fluids such as water, CO_2 etc.; into the porous solid is termed to as permeability. This characteristic is influenced by the size, connectivity of voids/pores, and viscosity of the fluid (Liu

et al., 2018, 2019). This could be considered to explain why SAP incorporation in CC makes it more impermeable. SAP swells after absorbing water, which resists further water or gas entry. When SAP releases absorbed water, hydration takes place, and form hydration products which further leads to filling of voids and reduce ingress of water.

There is very less literature available regarding the effect on permeability of CC due to inclusion of SAP. However, the studies available are discussed to evaluate the effect of SAP on permeability of concrete. Snoeck et al. (2012) performed permeability test on samples having SAP and not having SAP. The results showed that the samples having SAP had diminished permeability because of swelling of SAP which cease the voids and lowered the ingress of water. On the other hand; the samples without SAP were susceptible to water penetration (even in less than 40 s).

The impact of SAP on concrete's chloride migration coefficient was investigated by Hasholt et al. (2015) using neutron tomography. In comparison to samples without SAP, the results showed that adding SAP (without IC water) improved chloride migration. This increase in chloride migration was attributed to the decline in the w/c ratio carried by SAP's water absorption. It was claimed that SAP could only enhance chloride migration and boost hydration in the presence of IC water.

Dang et al. (2017) conducted research on the chloride migration coefficient of concrete containing SAP. Compared to the SAP-free specimen, it was claimed that SAP dramatically lowers the concrete's chloride migration coefficient. They attributed this to the development of a pore structure with smaller pores following the addition of SAP, which prevents the capillary pores from connecting. Ma et al. (2017) investigated into the impact of the size of the SAP particle on the chloride migration coefficient in a cement mortar.

The results show that bigger SAP performs better than smaller SAP in preventing chloride ion migration. They provided an explanation for this by pointing out that between the hardened cement matrix and the SAP void, larger SAPs produced better ITZ than smaller ones. Graf et al. (1986) tested mixes at various temperatures to see how temperature affected the concrete and mortar's permeability including gas and fluid in different regions. They found that increasing moisture contents result in lower permeability. Furthermore, it was highlighted that SAP-incorporated specimens displayed lower permeability than reference specimens under standard climatic circumstances (temperature: 20 °C and RH: 65%), which might be related the delay in self-desiccation of specimens with SAP. In conclusion, adding SAP to CC may decrease permeability of ions, gases and liquids. But the size, curing conditions, w/c ratio, and inclusion of IC water all have an impact on how well SAP reduces permeability.

4.2. Frost Resistance

The phenomena of crack occurrence known as freeze-thaw only happens in cold climates when water that seeps into CC cracks and freezes to form ice which results in expansion due to volume enlargement of ice formed which results in further cracking known as freeze-thaw cracking. Many preventive measures, such as an efficient design of cement concrete, should be implemented because freeze-thaw cycles have a negative effect on CC. To produce CC for better frost resistance, air entrainment is generally used. Some of the technical difficulties expected to be noticed during the air entrainment process include the air void distribution and void reduction caused by pumping or other factors, and voids not being compatible with other admixtures such as superplasticizers.

Air entrainment is a void system that is problematic because of the issues mentioned that cannot successfully withstand freeze-thaw cycles. Although

SAP properties (such as size, volume distribution) may be customized to satisfy required criteria, SAP has been found to be a great substitute to increase CC's resistance to freezing as shown in Figure 2a (Wong, 2018; Mignon et al., 2017). As previously explained, the swollen SAP particles shrink after SAP desorption, causes uniform distribution of air-filled voids in the matrix as shown in Figure 2b. The voids produced by SAP can be used to generate space for pore water expansion during freezing, boosting CC's resistance to frost.

According to several research such as Mignon et al. (2017) on the effectiveness SAP's ability to provide frost protection, CC modified with SAP (with or without IC water) is more resistant to frost than CC that has not been modified with SAP. The improvement in frost resistance of concrete/mortar with SAP-incorporated (without extra water) can be explained by the decrease in the water cement ratio and the allocation of SAP-created voids to accommodate ice formation. Additionally, the creation of SAP voids and the further hydration of unreacted binder granules are responsible for the performance of SAP (with additional water) modified CC against protection from frost. Due to their greater stability during mixing and transportation, SAPs exceed air-entrained admixtures in terms of frost resistance. Moreover, voids produced by SAP are permanent and can be built in the optimal and as desirable.

In addition to the benefits of SAP against resistance to frost that have previously been mentioned, there are a few other areas that need to be investigated to establish SAP's incorporation. For instance, due to frequent freeze-thaw cycles or the hydration of SAP gaps, SAP incorporated CC cannot offer long-term frost resistance. A summary of a several research on how well SAP performs regards frost resistance is discussed as below.

According to Hasholt et al. (2015), smaller SAP voids are more effective in resisting frost than larger ones. But according to other research, freeze-thaw cycles are more likely to affect small SAP voids (Mignon et al., 2017). Jones et al. (2014) used concrete that had been pre-soaked SAP of size 1 mm and exposing it to three hundred thawing-freezing cycles. The results showed that concrete cannot be protected from cycles of freezing and thawing by large-size SAPs.

To analyze the SAP's interface form with a distinct particle sizes but identical quantity, Assmann et al. (2013) employed image analysis. As a result, it can be seen that amount of void space produced by SAP is not affected by the particle size. Additionally, it was shown that SAP's ability to absorb moisture is unrelated to how well it resists frost. According to Reinhardt et al. (2012), scaling in SAP-incorporated concrete with particle sizes lower than 63 m was twice as large following twenty-eight cycles of freezing and thawing as scaling in SAP with particulate having sizes between 63 and 125 μm. In conclusion, SAP provides better protection from frost when compared to air-entrained admixtures. Their output is influenced by the size, spacing, and number of SAP voids that are produced, among other factors.

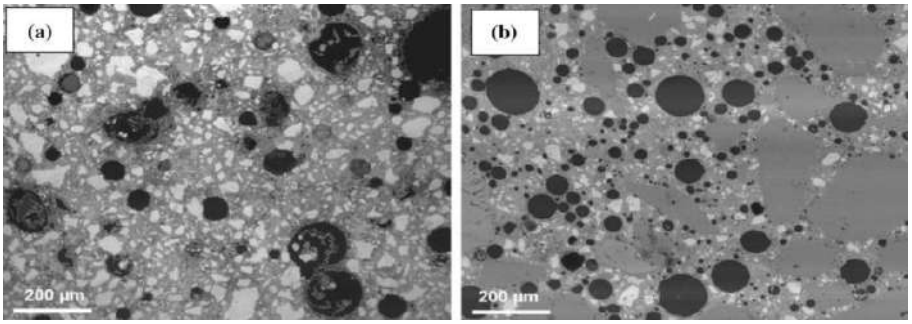

Fig. 2. For resistance to frost, CC with: a) SAP and; b) SAP-created air gaps (Wong, 2018)

Further, research should be carried out to extend SAP's resistance to the cracking brought on by freeze-thaw cycles. To get a unified conclusion, it is also important to thoroughly investigate the contradictory opinions of researchers regarding the variables (particularly the size of voids produced by SAP) that affect SAP's performance in terms of resistance to frost.

Although SAP properties (such as size, volume distribution) may be customized to satisfy required criteria, SAP has been found to be a great substitute to increase CC's resistance to freezing as shown in Figure 2a (Wong, 2018; Mignon et al., 2017). As previously explained, the swollen SAP particles shrink after SAP desorption, causes uniform distribution of air-filled voids in the matrix as shown in Figure 2b.

The voids produced by SAP can be used to generate space for pore water expansion during freezing, boosting CC's resistance to frost. According to several research such as Mignon et al. (2017) on the effectiveness SAP's ability to provide frost protection, CC modified with SAP (with or without IC water) is more resistant to frost than CC that has not been modified with SAP. The improvement in frost resistance of concrete/mortar with SAP-incorporated (without extra water) can be explained by the decrease in the water cement ratio and the allocation of SAP-created voids to accommodate ice formation. Additionally, the creation of SAP voids and the further hydration of unreacted binder granules are responsible for the performance of SAP (with additional water) modified CC against protection from frost. Due to their greater stability during mixing and transportation, SAPs exceed air-entrained admixtures in terms of frost resistance. Moreover, voids produced by SAP are permanent and can be built in the optimal and as desirable.

In addition to the benefits of SAP against resistance to frost that have previously been mentioned, there are a few other areas that need to be investigated to establish SAP's incorporation. For instance, due to frequent freeze-thaw cycles or the hydration of SAP gaps, SAP incorporated CC cannot offer long-term frost resistance. A summary of a several research on how well SAP performs regards frost resistance is discussed as follows.

According to Hasholt et al. (2015), smaller SAP voids are more effective in resisting frost than larger ones. However, according to other research, freeze-thaw cycles are more likely to affect small SAP voids (Mignon et al., 2017). Jones et al. (2014) used concrete that had been pre-soaked SAP of size 1 mm and exposing it to three hundred thawing-freezing cycles. The results showed that concrete cannot be protected from cycles of freezing and thawing by large-size SAPs. To analyses the SAP's interface form with a distinct particle sizes but identical quantity, Assmann et al. (2013) employed image analysis. As a result, it can be seen that amount of void space produced by SAP is not affected by the particle size.

Additionally, it was shown that SAP's ability to absorb moisture is unrelated to how well it resists frost. According to Reinhardt et al. (2012), scaling in SAP-incorporated concrete with particle sizes lower than 63 m was twice as large following twenty-eight cycles of freezing and thawing as scaling in SAP with particulate having sizes between 63 and 125 µm. In conclusion, SAP provides better protection from frost when compared to air-entrained admixtures. Their output is influenced by the size, spacing, and number of SAP voids that are produced, among other factors. Further, research should be carried out to extend SAP's resistance to the cracking brought on by freeze-thaw cycles. To get a unified conclusion, it is also important to thoroughly investigate the contradictory opinions of researchers regarding the variables (particularly the size of voids produced by SAP) that affect SAP's performance in terms of resistance to frost.

5. Challenges and Discussions

The challenges are found as per the study

are described below:

- Optimum dosage: One of the most challenging thing is to decide the optimum dosage/ amount of SAP to be added in the cement concrete
- Sorption kinetics: The testing methods to check the sorption kinetics such as absorption and desorption behavior.
- Design mix: It is also difficult to determine how much extra water needs to be added to the design mix in order to decrease issues like segregation, bleeding and to evaluate the workability, slump, handling of cement concrete etc.
- Durability criteria: The assessment of the resistance to cracking, shrinkage, chemical attack, and other durability concerns of SAP-modified concrete, over the life span of the structure is also not easy.
- Economic consideration: Considering the economic viability of SAP-modified concrete, including the additional cost of incorporating SAP compared to traditional concrete.
- Environmental impact: Evaluation of the environmental implications of SAP-modified concrete, such as the sourcing and disposal of SAP materials and their impact on the environment and sustainability is not being discussed yet.

6. Conclusion

From the investigation of the use of SAP as an IC agent in concrete in past studies, the following findings are made.

- Inclusion of SAP may lead to reduction in compressive strength at early ages. However, the compressive strength at 28 days (with matured age) could equally or slightly increased. Hence, the type of SAP has an influence on cement's mechanical properties and absorption/desorption kinetics of different SAP available.
- According to published research, adding SAP to concrete increases its tensile strength at mature age. Tensile strength is related to cracking; hence, self-desiccation and shrinkage reduction will increase cracking resistance.
- Tensile strength is sensitive to cracking; so there will be an improvement of cracking resistance by means of self-desiccation / shrinkage mitigation.
- Higher SAP dosage cause strength reduction, so SAP should be used in optimum amount (i.e. the behavior of concrete regarding its mechanical properties are influenced by the optimum amount and particle size of SAP used. The optimum dosage of SAP was found 0.3-0.4% of weight of cement).
- Although it has been discovered from earlier studies that additional water must be supplied for the IC in order to prevent SAP from absorbing the water provided for hydration, there will be a workability improvement. This will also result in a reduction of the w/c ratio, strength, and workability (slump).
- There will be reduction of permeability of water due to inclusion of SAP and improve chlorine migration as discussed above. SAP addition decreases permeability as per the curing conditions, the water-to-cement ratio, and the addition of IC water
- According to the literature cited above a bout the impact of freeze and thaw, SAP in clusion can lessen or resist the frost action.

7. References

Amin, M., Zeyad, A.M., Tayeh, B.A. and Agwa, I.S. (2021). “Engineering properties of self-cured normal and high strength concrete produced using polyethylene glycol and porous ceramic waste as coarse aggregate“, *Construction and Building Materials*, 299, 124243, https://doi.org/10.1016/j.conbuildmat.2021.124243.

Assmann, A. (2013). “Physical properties of concrete modified with superabsorbent polymers“, Ph.D. Thesis, Stuttgart University, Stuttgart, Germany, https://elib.uni-stuttgart.de/handle/11682/510.

Bingham, E.C. (1922). *Fluidity and plasticity*, McGraw-Hill, New York, https://openlibrary.org/books/OL7204671M/Fluidityandplasticity.

Craeye, B. and De Schutter, G. (2008). “Experimental evaluation of mitigation of autogenous shrinkage by means of a vertical dilatometer for concrete”, In: *8th International Conference on Creep, Shrinkage and Durability*

Mechanics of Concrete and Concrete Structures, CRC Press, Balkema, 909-914, https://biblio.ugent.be/publication/670680.

Craeye, B., Geirnaert, M. and De Schutter, G. (2011). "Super absorbing polymers as an icagent for mitigation of early-age cracking of high-performance concrete bridge decks", *Construction and Building Materials*, 25(1), 1-13, http://doi.org/10.1016/j.conbuildmat.2010.06.063.

Dang, J., Zhao, J. and Du, Z. (2017). "Effect of superabsorbent polymer on the properties of concrete", *Polymers*, 9(12), 672, https://doi.org/10.3390/polym9120672.

de Sensale, G.R. and Goncalves, A.F. (2014). "Effects of fine LWA and SAP as internal water curing agents", *International Journal of Concrete Structures and Materials*, 8(3), 229-238, https://doi.org/10.1007/s40069-014-0076-1.

Dudziak, L. and Mechtcherine, V. (2008), "Mitigation of volume changes of ultra-high performance concrete (UHPC) by using super absorbent polymers", In: *Proceedings of the 2nd International Symposium on Ultra-High Performance Concrete*, Kassel University Press, Kassel, 8, 425-432, https://www.researchgate.net/publication/303077153_Mitigation_of_volume_changes_of_ultra-highperformanceconcreteUHPCbyusingsuperabsorbentpolymers.

Faxiang, X., Dingpeng, C., Lin, J., Chuanlong, Z., Jing, R. and Xiao, L. (2021). "Combined compression-shear performance and failure criteria of internally cured concrete with super absorbent polymer", *Construction and Building Materials*, 266, 120888, https://doi.org/10.1016/j.conbuildmat.2020.120888.

Ghanem, H., Ramadan, R., Khatib, J. and Elkordi, A. (2024). "A review on chemical and autogenous shrinkage of cementitious systems", *Materials*, 17(2), 283, https://doi.org/10.3390/ma17020283.

Graf, H. and Grube, H. (1986). "Verfahren zur prühung der durchläsirgkeit von mörtel und beton gegenüber gasen und wasser", Beton, 5, 184-187, https://mitglieder.vdz-online.de/fileadmin/gruppen/vdz/3LiteraturRecherche/Fachaufsaetze/1981_1990/Betontechnischer_Bericht_86-88_Verfahren_zur_Pruefung_der_Durchlaessigkeit_von_Moertel_und_Beton_gegenueber_Gasen_und_Wasser.pdf.

Hamzah, N., Mohd Saman, H., Baghban, M.H., Mohd Sam, A.R., Faridmehr, I., Muhd Sidek, M.N., Benjeddou, O. and Huseien, G.F. (2022), "A review on the use of self-curing agents and its mechanism in high-performance cementitious materials", *Buildings*, 12(2), 152, https://doi.org/10.3390/buildings12020152.

Hasholt, M.T. and Jensen, O.M. (2015). "Chloride migration in concrete with superabsorbent polymers", *Cement and Concrete Composites,* 55, 290-297, https://doi.org/10.1016/j.cemconcomp.2014.09.023.

Hasholt, M.T., Jensen, O.M. and Laustsen, S. (2015). "Superabsorbent polymers as a means of improving frost resistance of concrete", *Advances in Civil Engineering Materials*, 4(1), 237-256, https://doi.org/10.1520/ACEM20150012.

Hasholt, M.T., Jespersen, M.H.S. and Jensen, O.M. (2010). "Mechanical properties of concrete with sap, Part I: Development of compressive strength", In: *International RILEM Conference on Use of Superabsorbent Polymers and Other New Additives in Concrete*, Rilem Publications SARL, https://researchgate.net/publication/284604715_Mechanical_properties_of_concrete_with_SAP_Part_IDevelopmentofcompressivestrength.

Igarashi, S.I., Watanabe, A. (2006). "Experimental study on prevention of autogenous deformation by internal curing using super-absorbent polymer particles", In: *International RILEM Conference on Volume Changes of Hardening Concrete: Testing and Mitigation*, RILEM Publication SARL, 77-86, https://doi.org/10.1617/2351580052.009.

Jensen, O.M. and Hansen, P.F. (2002). "Water-entrained cement-based materials-II, Experimental observations", *Cement and Concrete Research*, 32(4), 973-978, https://doi.org/10.1016/S0008-8846(02)00737-8.

Jensen, O.M. (2008), "Use of superabsorbent polymers in construction materials", In: *1st International Conference on Microstructure Related Durability of Cementitious Composites*, (pp. 757-764), Rilem Publications, https://orbit.dtu.dk/en/publications/use-of-superabsorbent-polymers-in-construction-materials.

Jensen, O.M. and Hansen, P.F. (2001). "Water-entrained cement-based materials: I, Principles and theoretical background", *Cement and Concrete Research*, 31(4), 647-654, https://doi.org/10.1016/S0008-8846(01)00463-X.

Jindal, A. and Ransinchung, G.D.R.N. (2022). "Behavioral study of incorporation of recycled concrete aggregates and mineral admixtures in pavement quality concrete", *Civil Engineering Infrastructures Journal*, 55(2), 351-372, https://doi.org/10.22059/ceij.2022.326564.1766.

Jones, W.A. and Weiss, W.J. (2014). "Freeze thaw durability of internally cured concrete made

using superabsorbent polymers", *International Conference on Durability of Concrete Structures*, https://doi.org/10.5703/1288284315376.

Justs, J., Wyrzykowski, M., Bajare, D. and Lura, P. (2015). "Internal curing by superabsorbent polymers in ultra-high performance concrete", *Cement and Concrete Research*, 76, 82-90, https://doi.org/10.1016/j.cemconres.2015.05.005.

Karthikeyan, V., Sabari, K., Sasikumar, S., Seyatharasan, S. and Thirumoorthi, S. (2018). "Self-curing concrete by using super absorbent polymer", 6(7), *International Journal of Engineering Research and Technology*, https://ijert.org/self-curing-concrete-by-using-super-absorbent-polymer.

Klemm, A.J. and Sikora, K.S. (2013). "The effect of superabsorbent polymers (sap) on microstructure and mechanical properties of fly ash cementitious mortars", *Construction and Building materials*, 49, 134-143, https://doi.org/10.1016/j.conbuildmat.2013.07.039.

Lam, H. (2005). "Effects of internal curing methods on restrained shrinkage and permeability", http://hdl.handle.net/1807/119896.

Liu, R., Xiao, H., Liu, J., Guo, S. and Pei, Y. (2019). "Improving the microstructure of ITZ and reducing the permeability of concrete with various water/cement ratios using nano-silica", *Journal of Materials Science*, 54(1), 444-456, https://doi.org/10.1007/s10853- 018-2872-5.

Liu, K., Yu, R., Shui, Z., Li, X., Ling, X., He, W., Yi, S. and Wu, S. (2018). "Effects of pumice-based porous material on hydration characteristics and persistent shrinkage of ultra-high performance concrete (UHPC)", *Materials*, 12(1), 11, https://doi.org/10.3390/ma12010011.

Lokeshwari, M., Bandakli, B.P., Tarun, S.R., Sachin, P. and Kumar, V. (2021). "A review on self-curing concrete", *Materials Today: Proceedings*, 43, 2259-2264, https://doi.org/10.1016/j.matpr.2020.12.859.

Ma, X., Liu, J., Wu, Z. and Shi, C. (2017). "Effects of SAP on the properties and pore structure of high performance cement based materials", *Construction and Building Materials*, 131, 476-484, http://doi.org/10.1016/j.conbuildmat.2016.11.090.

Ma, X., Yuan, Q., Liu, J. and Shi, C. (2019). "Effect of water absorption of SAP on the rheological properties of cement based materials with ultra-low w/b ratio", *Construction and Building Materials*, 195, 66-74, https://doi.org/10.1016/j.conbuildmat.2018.11.050.

Mechtcherine, V., Dudziak, L., Schulze, J. and Staehr, H. (2006). "Internal curing by super absorbent polymers, Effects on material properties of self-compacting fibre-reinforced high performance concrete", In: *International RILEM Conference on Volume Changes of Hardening Concrete: Testing and Mitigation*, Lyngby, Denmark, 87-96, https://researchgate.net/publication/288961188_Internal_curing_by_super_absorbent_polymers_SAP_-Effectsonmaterialpropertiesofself-compactingfibre-reinforcedhighperformanceconcrete.

Mignon, A., Snoeck, D., Dubruel, P., Van Vlierberghe, S. and De Belie, N. (2017). "Crack mitigation in concrete: superabsorbent polymers as key to success?", *Materials*, 10(3), 237, https://doi.org/10.3390/ma10030237.

Pourjavadi, A., Fakoorpoor, S.M., Khaloo, A. and Hosseini, P. (2012). "Improving the performance of cement-based composites containing superabsorbent polymers by utilization of nano-SiO2 particles", *Materials and Design*, 42, 94-101, https://doi.org/10.1016/j.matdes.2012.05.030.

Qin, H., Gao, M., Pang, C.M. and Sun, W. (2011), "Research on performance improvement of expansive concrete with internal curing agent SAP and its action mechanism", *Journal of Building Materials and Structures*, 14(3), 394-399, http://doi.org/10.3969/j.issn.1007-9629.2011.03.021.

Reinhardt, H.W. and Assmann, A. (2012). "Effect of superabsorbent polymers on durability of concrete", In: Mechtcherine, V. and Reinhardt, H.W. (eds.), *Application of Super Absorbent Polymers in Concrete Construction*, Springer, New York, 115-135, http://doi.org/10.1007/978-94-007-2733-59.

Savva, P. and Petrou, M.F. (2018). "Highly absorptive normal weight aggregates for Internal curing of concrete", *Construction and Building Materials*, 179, 80-88, https://doi.org/10.1016/j.conbuildmat.2018.05.205.

Secrieru, E., Mechtcherine, V., Schröfl, C. and Borin, D. (2016). "Rheological characterization and prediction of pump ability of strain-hardening cement-based-composites (SHCC) with and without addition of superabsorbent polymers (SAP) at various temperatures", *Construction and Building Materials*, 112, 581-594, https://doi.org/10.1016/j.conbuildmat.2016.02.161.

Shen, D., Liu, C., Jiang, J., Kang, J. and Li, M. (2020). "Influence of super absorbent polymers on early-age behavior and tensile creep of internal curing high strength concrete", *Construction and Building Materials*, 258, 120068, https://doi.org/10.1016/j.conbuildmat.2020.120

068.

Shen, P., Lu, J., X., Lu, L., He, Y., Wang, F. and Hu, S. (2021). "An alternative method for performance improvement of ultra-high performance concrete by internal curing: Role of physicochemical properties of saturated lightweight fine aggregate", *Construction and Building Materials*, 312, 125373, https://doi.org/10.1016/j.conbuildmat.2021.125373.

Shen, P., Lu, L., He, Y., Wang, F. and Hu, S. (2019). "The effect of curing regimes on the mechanical properties, nano-mechanical properties and microstructure of ultra-high performance concrete", *Cement and Concrete Research*, 118, 1-13, https://doi.org/10.1016/J.CEMCONRES.2019.01.004.

Singh, K. (2021). "Mechanical properties of self-curing concrete studied using polyethylene glycol-400: A review", *Materials Today: Proceedings*, 37, 2864-2871, https://doi.org/10.1016/j.matpr.2020.08.662.

Snoeck, D., Steuperaert, S., Van Tittelboom, K., Dubruel, P. and De Belie, N. (2012). "Visualization of water penetration in cementitious materials with superabsorbent polymers by means of neutron radiography", *Cement and Concrete Research*, 42(8), 1113-1121, https://doi.org/10.1016/j.cemconres.2012.05.005.

Snoeck, D., Van Tittelboom, K., Steuperaert, S., Dubruel, P. and De Belie, N. (2014). "Self-healing cementitious materials by the combination of microfibres and superabsorbent polymers", *Journal of Intelligent Material Systems and Structures*, 25(1), 13-24, https://doi.org/10.1177/1045389X12438623.

Tan, Y., Chen, H., Wang, Z., Xue, C. and He, R. (2019). "Performances of cement mortar incorporating super absorbent polymer (SAP) using different dosing methods", *Materials*, 12(10), 1619, https://doi.org/10.3390/ma12101619.

Wang, X., Chen, S., Ren, J., Huang, R., Yang, Z., Wang, W. and Liu, J. (2022). "Effect of super absorbent polymer and mineral additives on mechanical, shrinkage and healing properties of self-healing lightweight aggregate concrete under different curing regimes", *Construction and Building Materials*, 357, 129377, https://doi.org/10.1016/j.conbuildmat.2022.129377.

Wang, X., Yu, R., Shui, Z., Song, Q., Liu, Z., Liu, Z. and Wu, S. (2019). "Optimized treatment of recycled construction and demolition waste in developing sustainable ultra-high performance concrete", *Journal of Cleaner Production*, 221, 805-816, https://www.researchgate.net/publication/331856644_Optimized_treatment_of_recycled_construction_and_demolitionwasteindevelopingsustainableultra-highperformanceconcrete.

Wehbe, Y. and Ghahremaninezhad, A. (2017). "Combined effect of shrinkage reducing admixtures (SRA) and superabsorbent polymers (SAP) on the autogenous shrinkage, hydration and properties of cementitious materials", *Construction and Building Materials*, 138, 151-162, http://doi.org/10.1016/j.conbuildmat.2016.12.206.

Wong, H.S. (2018). "Concrete with superabsorbent polymer", In: Pacheco-Torgal, F., Melchers, R.E., Shi, X., De Belie, N., Van Tittelboom, K., Sáez, A. (eds), *Eco-Efficient Repair and Rehabilitation of Concrete Infrastructures*, Elsevier, Amsterdam, 467-499, https://doi.org/10.1016/B978-0-08-102181-1.00017-4.

Yang, L., Shi, C. and Wu, Z. (2019). "Mitigation techniques for autogenous shrinkage of ultra-high-performance concrete, A review", *Composites Part B: Engineering*, 178, 107456, https://doi.org/10.1016/j.compositesb.2019.107456.

Zhong, P., Wyrzykowski, M., Toropovs, N., Li, L., Liu, J. and Lura, P. (2019). "Internal curing with superabsorbent polymers of different chemical structures", *Cement and Concrete Research*, 123, 105789, http://doi.org/10.1016/j.cemconres.2019.105789.

Civil Engineering Infrastructures Journal 2025, 58(1): 15-34
DOI: 10.22059/ceij.2024.362561.1943

RESEARCH PAPER

Assessment of Polypropylene Fiber for Effect on Fresh and Physical Performance with Durability of Self-Compacted Recycled Aggregate Concrete

Tiwari, P.[1*] and Singh, V.[2]

[1] P.G. Scholar, Department of Civil Engineering Madan Mohan Malaviya University of Technology Gorakhpur, Uttar Pradesh, India.
[2] Assistant Professor, Department of Civil Engineering Madan Mohan Malaviya University of Technology Gorakhpur, Uttar Pradesh, India.

Received: 19 Jul. 2023; Revised: 26 Oct. 2023; Accepted: 02 Dec. 2023

ABSTRACT: Manuscript targets to develop Self-Compacted High-Performance Concrete (SCHPC) by substituting 50% of Natural Aggregate (NA) with Recycled Coarse Aggregate (RCA), along with incorporation of Polypropylene Fiber (PP) reinforcement at varying volume fractions. Manuscript focuses on the effects of different proportions of polypropylene fibers (0.2%, 0.4% and 0.6%) when replacing 50% of NA with RCA. The impact of PP reinforcement on various mechanical properties of concrete, like compressive strength, flexural strength and split tensile strength are examined thoroughly. For durability of SCHPC, carbonation resistance, water absorption and acid resistance are also explored in the presented paper. Compressive strength of both Natural Aggregate Concrete (NAC) and Recycled Aggregate Concrete (RAC) initially increases up to a fiber concentration of 0.4% before declining with increased fiber contents. Identical patterns appear for split tensile strength, where 0.4% fiber content is found to be ideal to optimize strength. At 0.4% PP fiber, minimum carbonation depth for NAC was reported as 2.94, 4.91 and 7.12 percent for 7, 14 and 28 days, respectively. Comparable results are obtained for RAC, for fiber volume proportion of 0.4%. So, the reduction of approximately 16.67% for NAC (28 days) and 17.54% for RAC (28 days) at control mix.

Keywords: Polypropylene Fiber, Recycled Coarse Aggregate, Self-Compacted High-Performance Concrete, Carbonation depth, Split Tensile Strength.

1. Introduction

Concrete is a widely used building material in construction industry due to its ease of mold ability, workability and durability properties. Currently, concrete constitutes around 80% of construction materials used worldwide, surpassing other building materials. This growing demand for concrete is driven by modernization of society and advancements in people's daily lives. As the rate of demolition of existing structures increases, consequently rises the generation of Construction and Demolition (C and D) waste. Unfortunately, primary method of disposing of this waste is through landfilling, which leads to a decrease in efficiency of land utilization.

Simultaneously, demand for High-Performance Concrete continues to rise

* Corresponding author E-mail: pawankumartiwari712@gmail.com

over time. As a result of inadequate recycling methods and insufficient environmental regulations regarding disposal, most of these waste materials end up in landfills.

Currently, nearly all nations are grappling with a severe shortage of landfills to accommodate substantial volume of solid waste produced as a result of demolishing aged concrete structures. Estimations suggest that nearly 70% of potential built-up area is yet to be developed, and it is anticipated that total built-up area will increase fivefold by 2030. According to reports from Central Pollution Control Board (CPCB) (2017) in India, country generates approximately 10-12 million tons of C and D waste each year. Utilization of recycled aggregates, whether in partial or full replacement of natural aggregates, in concrete presents a potential solution to various challenges confronted by society?

These include environmental pollution, scarcity of natural resources and need for waste disposal lands. By incorporating recycled aggregates into concrete, these issues can be addressed effectively. In last few years, there has been a growing interest in exploring structural applications of RCAs.

Extensive investigations and research efforts have been dedicated to understanding potential of RCAs in various construction projects. This surge in interest reflects the recognition of RCAs as a viable and sustainable alternative in construction industry. In their research work, Yoda and Shintani (2014) implemented mid-quality RAC for super structure of a building in japan. They closely monitored durability properties of RAC over course of one year and obtained promising results. This study highlights potential of using recycled aggregates in concrete construction and suggests that RAC can exhibit satisfactory durability characteristics.

Importance of recycling and reusing concrete waste has been emphasized in the report of Maio (2016). This report highlights significance of adopting advanced technologies to promote sustainable practices in construction industry.

Additionally, in India, revised regulations of Ministry of Environment (2016) have been implemented, focusing on engaging various stakeholders in recovery, recycling, reuse, and proper management of C and D wastes. These regulations aim to enhance sustainable management of C and D wastes and encourage responsible practices among all involved parties.

Multiple researches in existing studies have confirmed that recycled aggregates tend to exhibit higher water absorption rates in comparison to natural aggregates. Consequently, it is often suggested that when incorporating recycled aggregates into concrete, there may be a need to increase water content to achieve desired workability Güneyisi et al. (2014) and Mefteh et al. (1963). These findings emphasize importance of carefully managing water-to-cement ratio when utilizing recycled aggregates to maintain desired workability and ensure overall performance of concrete mixture.

Fiber-reinforced concretes have constantly stood out for their exceptional deformational properties, including high flexural strength, reduced shrinkage, and excellent resistance to abrasion. Through comprehensive analysis of existing literature and a thorough review of latest research by renowned concrete scientists in field of SCCs, coupled with advancements has concluded that current state offers an opportunity to develop SCCs with exceptional physical and technical properties (Utepov et al., 2020). This indicates potential for creating self-consolidating concretes that exhibit superior performance and meet demand requirements in various applications.

Conventional concrete is inherently brittle, characterized by low tensile strength and limited resistance to crack opening and propagation (Brandt et al., 2008; Poon et al., 2004). Concept of fiber reinforcement in concrete was initially introduced by

Romualdi and Mandel (1964). They pioneered use of randomly distributed steel fibers in concrete, marking beginning of incorporating fibers to enhance mechanical properties and durability of concrete structures. Addition of fibers provides improved tensile strength and crack resistance, thereby mitigating inherent brittleness of concrete and enhancing its overall performance. Previously published papers have primarily focused on potential of reinforcing traditional dense concrete with fibers, addressing specific challenges. For instance, one study by Smirnova et al. (2018) investigated enhancement of flexural strength through the utilization of polyolene microfibers.

Another study by Mukhatar et al. (2023) aimed to overcome issue of brittle fracture in high-strength concrete. Additionally, a research has been conducted by Faraj et al. (2019), on mechanical, fracture and durability properties of SCHSC containing Recycled Polypropylene Plastic Particles (RPPP), both with and without presence of silica fume. These studies contribute to understanding of incorporating fibers and recycled materials in concrete, targeting specific improvements in strength, fracture resistance, and overall performance.

Boulekbache et al. (2010) determined that flexural strength of fiber-reinforced concrete is significantly influenced by distribution and orientation of fibers. Lawler et al. (2002) also observed that inclusion of fibers in concrete aids in reducing shrinkage. However, several studies have reported a decrease in workability as a result of fiber addition.

Therefore, it is generally recommended to limit fiber content to below 3% (lie et al., 2017; Li et al., 2018; Hsie et al., 2008; Kamal et al., 2014) to maintain an acceptable level of workability while still benefiting from enhanced mechanical properties and reduced shrinkage provided by fibers. Kang et al. (2019) found that addition of 0.15% steel fibers can result in flexural performance comparable to that of NAC beams in beams composed entirely of RCAs. However, Gao and Zhang (2018) reported that improvement in flexural performance is only observed when steel fiber content exceeds 0.5%, with no noticeable effect below that threshold.

Carneiro et al. (2014) investigated indicating an increase in toughness of RAC with inclusion of steel fibers. Furthermore, behavior of RAC with steel fibers exhibited similarities to that of fiber-reinforced NAC under compression. These studies shed light on potential benefits of incorporating steel fibers into RAC to enhance it is flexural performance and toughness properties.

After considering issues surrounding C and D waste generation and it is disposal, as well as impact of high demand for natural aggregates on environment, it becomes crucial to prioritize sustainable construction practices to safeguard the environment and preserve natural resources for future generations. Based on literature survey, it is observed that different researchers conducted the experiments for variation of RCA from 0% to 100% of replacement, which is a wide range. So, for validation of those experiments it is wise to perform experiments for variation of RCA with 0%, 25%, 50% and 75% replacement. Among these variations replacement of RCA up to 50% is closer to the obtained results which is convincing.

For the step towards sustainable construction, the objective of research is to prioritize the substitute 50% of Natural Aggregate with RCA to produce SCHPC with incorporation of Polypropylene Fiber Reinforcement at various volume fractions of 0.2%, 0.4% and 0.6%. For High-Performance Concrete production with superior mechanical properties and excellent workability which could also provide the high resistance for aggressive chemical attacks, a concrete mix has been designed.

2. Methodology and Experimental Program

In this study, investigation for performance

of fresh properties of concrete when using Recycled Aggregate compared to traditional aggregate, both with and without incorporation of polypropylene fiber. Efforts are also done to examine mechanical and durability performance of SCHPC. Based on previous studies, it has been observed that addition of fibers to concrete mixture enhances it is tensile and flexural performance, reinforces behavior of concrete, and improves it is durability. Therefore, main focus of this study is to assess mechanical properties of SCHPC reinforced with polypropylene fiber.

Primary goal is to quantify and analyze impact of different volume fractions of polypropylene fiber on enhancing mechanical properties of SCHPC. Additionally, this research aims to explore optimum content of polypropylene fiber that significantly enhances mechanical properties of SCHPC.

3. Material Requirement

SCHPC was prepared using the following ingredients:

3.1. Cement and Additives

Grade 43 (ultra tech) Ordinary Portland Cement (OPC 43) was utilized in concrete mix. OPC 43 is a common type of cement widely used in construction due to its reliable performance and availability. It conforms to Indian Standard Specifications for cement (IS: 8112-2013) and possesses adequate strength characteristics for various construction applications. OPC 43 is typically composed of a blend of clinker, gypsum, and other additives to achieve desired chemical and physical properties required for concrete production. Chemical and physical properties of cement are tabulated in Table 1. A high-performance additive, superplasticizer (FOSROC Aura mix 450) was used as a water-reducing agent in production of concrete mix. The purpose of using this superplasticizer was to improve workability of concrete by reducing amount of water required while maintaining desired consistency and flow ability.

The used Superplasticizer (FOSROC Aura mix 450) is known for its effectiveness in dispersing cement particles, which helps in achieving better particle suspension and improved flow properties of concrete mixture. It allows for better cohesion and reduces viscosity of mixture, enabling easier placement and compaction of concrete. Specific dosage of superplasticizer used in concrete mix may vary depending on factors such as the desired workability, ambient conditions and other admixtures present in mix. Superplasticizer is typically added to concrete mix during mixing process to ensure proper dispersion and effectiveness. Physical properties of superplasticizer are mentioned in Table 2.

3.2. Aggregates

In concrete mixture, both Natural Aggregate and RCA were used as coarse aggregates. Natural Aggregate consists of crushed granite stones, which are locally available in market of Gorakhpur, Uttar Pradesh, India. These granite stones are commonly used as a construction material and provide necessary strength and stability to concrete. Grading chart of coarse aggregate on basis of size distribution test as per IS: 383-1970 code is mentioned in Figure 1. RCA was obtained from demolition waste of central library of Madan Mohan Malaviya University of Technology, Gorakhpur and Uttar Pradesh. After obtaining the RCA from the source proper procedure is adopted for preparing the samples to use it in concrete mix. The process to obtain the good quality RCA is depicted in Figure 2.

Table 1. Chemical and physical composition of ordinary Portland cement (Grade 43)

Mineral/Chemical composition (%)						Physical properties				
C_3S	C_2S	C_3A	C_3AF	f-Cao	f-Mgo	Density(g/cm^3)	$f_{cs\cdot f3}$ /MPa	$f_{cs\cdot f7}$ /MPa	$f_{cs\cdot f28}$ /MPa	Fineness (m^3/kg)
61	18	7.5	8.87	0.89	1.5	3.18	32.6	43.1	54	289

Table 2. Physical properties of superplasticizer

Type	Colour	Specific gravity	Relative density	Chloride content	Physical state	PH value
Poly carboxylic ether polymer (for Types F and G)	Light yellowish	1.09 - 1.11	1.5 – 25 ^{0}C	Nil to IS:456	liquid	Minimum 6.0

This RCA is a sustainable alternative to use fresh natural aggregates, as it involves recycling and reusing waste material from demolition process. By incorporating RCA into concrete mixture, it helps reduce demand for new natural aggregates and promotes environmental sustainability. Physical and mechanical properties of natural and recycled aggregate are listed in Table 3. River sand sourced from local market in Gorakhpur, Uttar Pradesh, was used as fine aggregate in concrete mix. Sand is classified as Zone-II, which indicates that it meets specified requirements for use in concrete construction. Use of appropriate sand with desired grading helps improve workability, strength, and durability of concrete. Size distribution grading curve of fine aggregate (sand) as per IS: 383-1970 code listed below in Figure 3. It is noted that specific characteristics and properties of NA, RCA and river sand may vary based on actual materials used and their respective sources. It is recommended to conduct proper testing and evaluation to determine suitability and quality of these aggregates for concrete mix in specific projects.

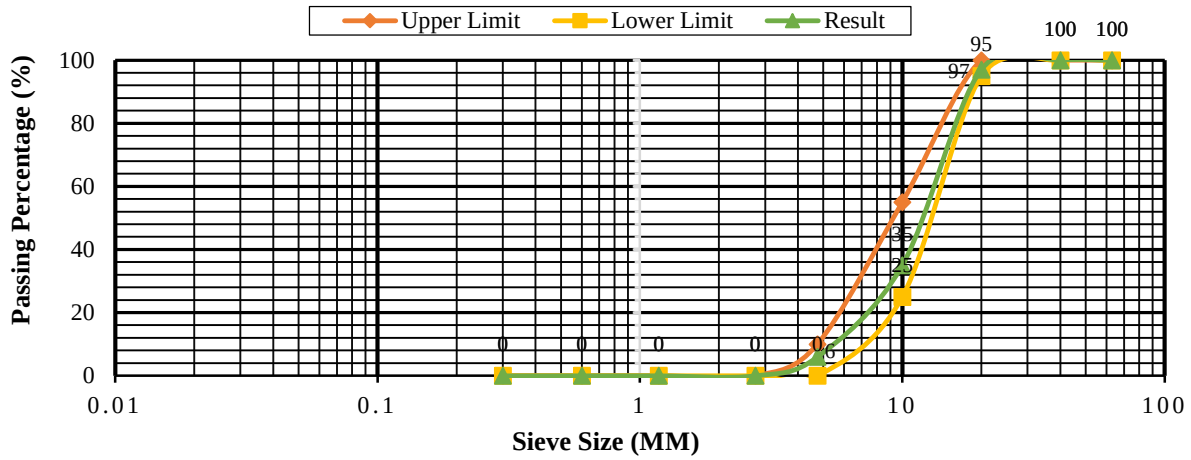

Fig. 1. Grading curve of coarse aggregate test as per IS: 383-1970

Table 3. Physical and mechanical properties of aggregates

Properties		Virgin crushed granite aggregate Max. size of aggregate 10 mm	Virgin crushed granite aggregate Max. size of aggregate 20 mm	Recycled concrete aggregate Max. size of aggregate 10 mm	Recycled concrete aggregate Max. size of aggregate 20 mm
Physical properties					
Specific gravity		2.78	2.81	2.25	2.33
Water absorption		0.28	0.23	2.9	2.85
Bulk density kg/m^3	Loose	1410	1480	1320	1380
	Rodded	1556	1610	1464	1570
Percentage of voids	Loose	51	48	45	42
	Rodded	45	42	41	39
Mechanical properties					
Crushing value (%)		29.3	28.65	36.87	36.18
Impact value (%)		20.91	20.24	30.80	29.64
Abrasion value (%)		30.23	27.18	47.23	38.64

Fig. 2. Process for production of recycled concrete aggregate

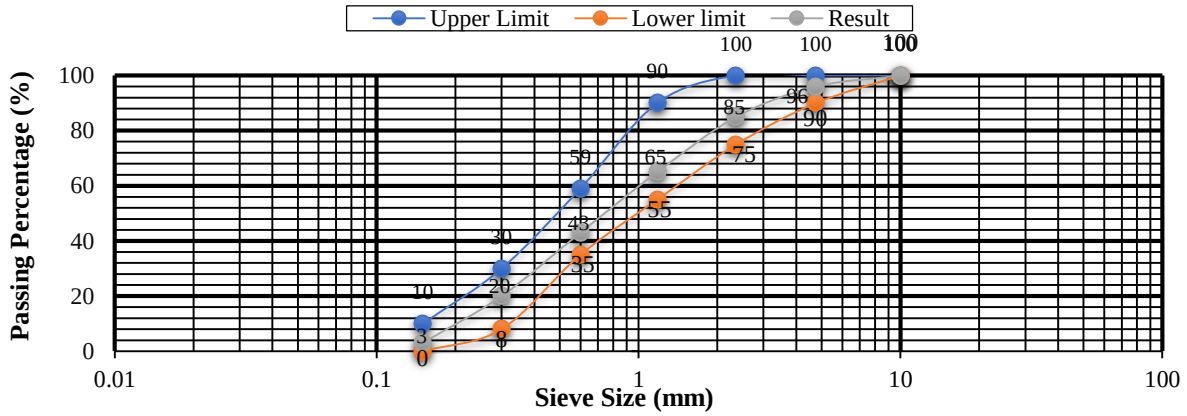

Fig. 3. Grading curve of fine aggregate according IS: 383-1970 for Zone II

3.3. Polypropylene (PP) Fiber Reinforcement

Reliance recorn 3 s fiber is a kind of polypropylene fiber that is used in production of SCHPC. Polypropylene fibers are commonly added to concrete to enhance it is mechanical properties, such as Tensile Strength (TS), Flexural Strength (FS), and impact resistance. Reliance recorn 3 s fiber is specifically designed to provide reinforcement and improve overall performance of concrete.

These fibers are typically in form of short, discrete strands or fibrillated microfibers. When added to concrete mix, they help control cracking and enhance post-crack behavior of concrete. Exact specifications and characteristics of reliance recorn 3 s fiber, such as fiber length, aspect ratio, and dosage, may vary based on the specific requirements of the SCHPC mix design and project specifications. Properties of Reliance recorn 3 s fiber is mentioned in Table 4.

3.4. Water

Drinking tap water which available in campus laboratory is used in concrete mix with all permissible criterion which was mentioned in Indian Standard (IS) code 456, 2000. IS code 456, 2000 provides guidelines for design and construction of reinforced concrete structures. It also specifies permissible limits for various constituents, including water, in concrete mix. Specific requirements for water quality may vary depending on project location and local regulations.

3.5. Method of Addition of Fibber

Method of introducing fibers into concrete plays a crucial role in achieving a uniform distribution of fibers throughout concrete matrix and reducing fiber agglomeration. Several investigations, such as AKç et al. (2015) and Matar et al. (2019) have investigated different techniques for incorporating polypropylene fibers into concrete. Observations from these studies indicate that order in which water and fibers are added can influence mechanical properties of fiber-reinforced concrete.

When fibers are added to concrete before water, it facilitates formation of a three-dimensional fiber skeleton within matrix and reduces occurrence of fiber aggregation and voids. This method promotes better dispersion of fibers throughout concrete. On other hand, when casting method is used, where mixing water is added before fibers, dispersion of fibers in concrete is not as effective. This is due to water acts as a binding agent, strengthening already tangled fibers and creating more significant voids. Consequently, mechanical properties of fibers may be compromised. Therefore, it is important to carefully consider method of introducing fibers into concrete mix to ensure optimal dispersion and achieve desired mechanical performance. By incorporating fibers before adding water, it is possible to enhance uniform distribution of fibers and improve overall performance of fiber-reinforced concrete.

Table 4. Characteristics properties of polypropylene fiber

Fiber type	Shape	Length (mm)	Effective diameter (μm)	Specific gravity	Tensile strength (GPa)	Elongation (%)	Young's modulus (MPa)	Melting point (^{0}C)	Alakline stability
Polypro pylene	Tri-angular	12	25-40	0.90-0.91	4.6	60-90	> 4000	160-165	Very good

Fig. 4. Materials requirement for SCHPC

4. Concrete Mix Design

In this study, several concrete mixes were prepared with different proportions of NA and RCA, as well as varying volume fractions of polypropylene fibers. Mix designs were prepared for target mean strength of concrete as per the IS 10262, 2019. Following concrete mixes were used:

1. NSCC-100, 0: NASCC with 100% NA and no polypropylene fibers.
2. FNSCC-100, 0.2: fiber-reinforced NASCC with 100% NA and 0.2% proportion of PP fibers.
3. FNSCC-100, 0.4: fiber-reinforced NASCC with 100% NA and 0.4% proportion of PP fibers.
4. FNSCC-100, 0.6: fiber-reinforced NASCC with 100% NA and 0.6% proportion of PP fibers.
5. RSCC-50, 0: recycled aggregate RSCC with 50% RCA and no PP fibers.
6. FRSCC-50, 0.2: fiber-reinforced RSCC with 50% RCA and 0.2% proportion of PP fibers.
7. FRSCC-50, 0.4: fiber-reinforced RSCC with 50% RCA and 0.4% proportion of PP fibers.
8. FRSCC-50, 0.6: fiber-reinforced RSCC with 50% RCA and 0.6% proportion of PP fibers.

Proportions of each mix are provided in Table 5.

Table 5. Mix proportion of self-compacted concrete with use of polypropylene fiber (Kg/m^3)

Concrete reference	Cement	River sand	Natural aggregate	Recycled aggregate	Water	Super plasticizer	Polypro-pylene fiber
NSCC - 100, 0	445	975	737	0	180	3.56	0.00
FNSCC- 100, 0.2	445	975	737	0	180	3.56	4.68
FNSCC - 100, 0.4	445	975	737	0	180	3.56	9.36
FNSCC - 100, 0.6	445	975	737	0	180	3.56	14.04
RSCC - 50, 0	445	975	368.5	368.5	180	3.56	0.00
FRSCC - 50, 0.2	445	975	368.5	368.5	180	3.56	4.68
FRSCC - 50, 0.4	445	975	368.5	368.5	180	3.56	9.36
FRSCC - 50, 0.6	445	975	368.5	368.5	180	3.56	14.04

Additionally, FOSROC Aura mix 450 superplasticizers is used in all mixes to maintain consistent fresh properties of SCC. Superplasticizer should be added at a weight of 1% of the cementitious material to achieve a slump flow between 650 and 730 mm. Superplasticizer is available in a light brownish-colored liquid form. Concrete mixtures were proportioned with a water-cement ratio of 0.40, following guidelines of BIS (IS: 10262-2019). Proportions were selected to achieve a characteristic strength of 30 MPa. Three different volume proportions of PP fibers (0.2%, 0.4% and 0.6%) were added to both NAC and RAC.

It is important to note that both recycled and natural aggregates were utilized in a condition of saturated surface dryness during mixing process, as recommended by Brand et al. (2015) to obtain best outcomes. Tap water from a regular faucet, suitable for drinking, was used in concrete mixing process. Prior to mixing process, the water adsorption capacity of the RCA must be determined. This could be done by using the water adsorption experiment for RCA.

The RCAs are initially dried in this test, after 24 hours of immersion in water, the amount of water absorbed is measured. The aggregates must be dried at 105 ^{o}C. This leads to the adding of additional water needed for the mix of concrete. Since, RCAs have the more porosity than the natural aggregate for which this addition water is required, and this additional water also affects the workability and durability of concrete.

5. Casting and Curing

In laboratory, a manual concrete mixer is used to mix concrete. Process involves the following steps:

1. Water is first combined with superplasticizer to create a homogeneous dispersion. Dosage of superplasticizer is 1% by weight of water to achieve desired slump value of SF3 flow (660 mm - 750 mm).
2. Recycled coarse aggregate is sprinkled with water a day before use to control production of concrete. It is then covered with a plastic sheet to maintain a high humidity level. Aggregate used is wetted to reduce it is water absorption capacity, aiming for a moisture content of 80% of total absorption capacity.
3. Both NAC and RAC contain superplasticizer to consider it is effect on hardened properties.
4. Mixing process involves adding aggregate, sand, and cement with PP fibers and mixing for two minutes. Then, water is added and mixed again to achieve desired workability.
5. To ensure workability, each type of specimen is subjected to Slump flow, V-funnel, and J-ring tests following the specifications of BIS (IS: 10262-2019).
6. After 24 hours, all prepared concrete samples are taken out of mold and placed in a curing tank for specified number of days.

Process of making mix of concrete is given in Figure 3. For both NAC and RAC, six cube samples (size 150 mm × 150 mm × 150 mm) are prepared with various volume fractions of PP fibers to determine CS for

each sample of mix. Tests are conducted after 7 days and 28 days of the curing period. Similarly, three flexural strength samples (aspect 500 mm × 100 mm × 100 mm) are prepared for each NAC and RAC with different volume fractions of PP fibers. FS test is performed after 28 days of curing. For Split Tensile Strength (STS), three cylindrical samples were prepared for each NAC and RAC using different volume fractions of polypropylene fibers. Specimen detail of each test were mentioned in the following Table 6.

Concrete cubes with dimensions of 150 mm are tested after 7 days and 28 days of curing period. Average CS values of at least three samples for each type of concrete are calculated and reported. For STS test, cylindrical specimens with dimensions of 150 mm in diameter and 300 mm in length were prepared. Test was conducted after a 28-day curing period, following specifications of BIS (IS: 5816 - 1999). STS values are determined using a 3000 KN compressive testing apparatus.

FS test, as per BIS (IS: 516 - 1959), is performed after a 28-day curing period on prism samples measuring 500 mm × 100 mm × 100 mm. Flexural strength, represented as modulus of rupture, was calculated using expression described in code 516-1959. Average FS values of three samples for each type of concrete are reported in Section 7.2.4.

6. Standards Followed for Experimental Setup

CS of concrete cubes is assessed according to guidelines of BIS (IS: 516 - 1959).

7. Results and Discussion

7.1. Fresh Properties

A reported in previous studies of Das et al. (2018), when PP fiber is added to NAC or RAC, fresh properties of concrete are affected. Presence of PP fibers forms a matrix that restricts flow of concrete.

Fiber particles also adsorb water and bridge gaps between them and concrete mix. It has been observed that concrete with PP fiber has a slump value up to 40% lower.

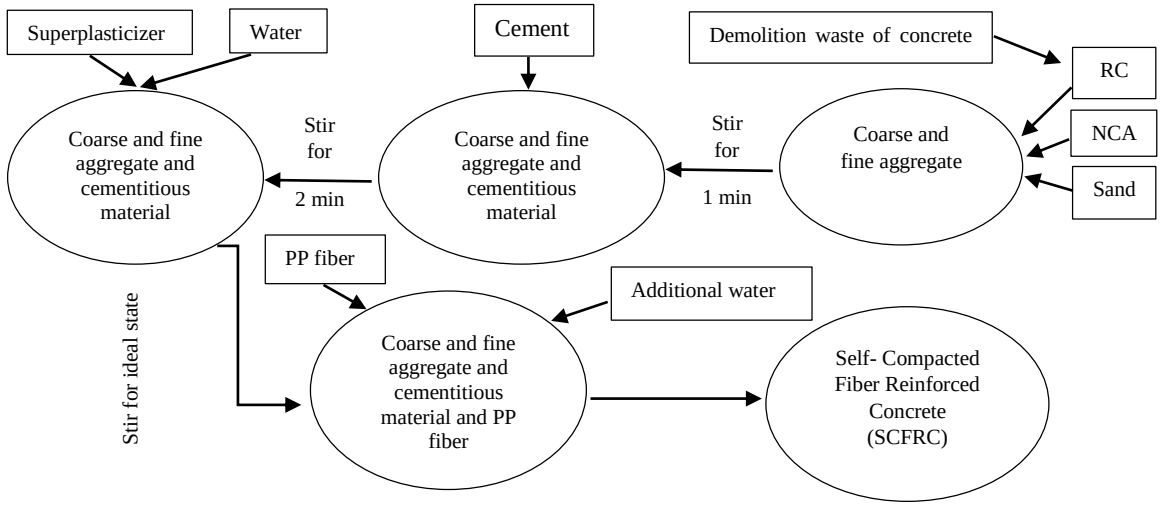

Fig. 5. Flowchart of SCFRC preparation

Table 6. Specimen detail of casting

Experiment name	Number of sample	Size of test samples for concrete mix with max. size of aggregate of 10 and 20 mm
Compressive strength	48	Cube – 150 × 150 × 150 mm
Split tensile strength	24	Cylinder – 150 mm diameter and 300 mm height
Flexural strength	24	Beam – 100 × 100 × 500 mm
Modulus of elasticity	24	Cylinder – 150 mm diameter and 300 mm height

Increased friction between aggregates and fiber particles in mix requires more potential energy for SCC to flow. This study found that SCC containing up to 0.2% volume fraction of PP fiber met requirements for SCC (like flow ability, filling ability, passing ability, finish ability and pump ability etc.), but higher dosages did not meet requirements. Table 7 provides a summary of studies of fresh properties.

Based on the study data presented in Table 6, here are key findings regarding fresh properties of SCRAC containing PP fibers:

1. Slump: slump values decrease as percentage of PP fiber increases. Mixes with lower PP fiber content, such as NSCC-100, 0 and RSCC-50, 0, have higher slump values, indicating better workability. However, as PP fiber content increases, slump values decrease. Mixes FNSCC-100, 0.6 and FRSCC-50, 0.6 have lowest slump values, indicating a decrease in workability.
2. L-Box Test Ratio: L-Box test ratio (H_2/H_1) is a measure of passing ability of SCC. Mixes NSCC-100, 0, FNSCC-100, 0.2, RSCC-50, 0 and FRSCC-50, 0.2 have L-Box test ratios between 0.80 and 0.92, indicating good filling and passing ability. However, mixes FNSCC-100, 0.4, FNSCC-100, 0.6, FRSCC-50, 0.4, and FRSCC-50, 0.6 have L-Box test ratios below 0.8, indicating poor passing ability.
3. V-Funnel Test: V-Funnel test measures flow ability of SCC. Mixes NSCC-100, 0, FNSCC-100, 0.2, RSCC-50, 0 and FRSCC-50, 0.2 have flow times between 5 and 12 seconds, which are within acceptable limits for SCC. However, as PP fiber content increases, flow time also increases. Mixes FNSCC-100, 0.4, FNSCC-100, 0.6, FRSCC-50, 0.4 and FRSCC-50, 0.6 have flow times greater than 12 seconds, indicating reduced flow ability.
4. Bleeding: inclusion of PP fibers significantly reduces bleeding in SCC. Mixes NSCC-100, 0 and RSCC-50, 0 exhibit small bleeding, indicating improved homogeneity. Large surface area of PP fibers requires more cement paste to cover them, reducing escape of free water onto surface of SCC and improving mixture is homogeneity. Based on the above observations, it could be said that better SCC mixes which meets all requirement of SCC are FNSCC-100, 0.2 and FRSCC-50, 0.2, contain 0.2% PP fibers by weight in concrete mix.

However, mixes with a fraction of PP fiber exceeding 0.2%, such as FNSCC-100,0.4, FNSCC-100, 0.6, FRSCC-50,0.4, and FRSCC-50, 0.6, do not meet all requirements of SCC (like flow ability, filling ability, passing ability, finish ability and pump ability etc.). Subsequently, it is suggested to use PP fibers up to 0.2% by weight of concrete mix to achieve good fresh properties in SCRAC.

7.2. Mechanical Behavior of FRRASCC

7.2.1. Density

Figure 7 demonstrates variation in density for both RAC and NAC as volume fraction of fibers increases. In RAC, the density is lower compared to NAC due to increased porosity resulting from presence of attached mortar on surface of RCA.

Table 7. Fresh properties of self-compacted recycled aggregate concrete with incorporation of PP fiber

Concrete reference	Slump (mm)	L-box test (H_2/H_1)	V-funnel test (s)	T 50 – slump flow	remarks
NSCC - 100, 0	722	0.92	05	2.7	Small bleeding
FNSCC- 100, 0.2	641	0.84	07	4.5	Good scc
FNSCC - 100, 0.4	596	0.79	13	5.9	Small stiff
FNSCC - 100, 0.6	553	0.68	16	08	Too stiff
RSCC - 50, 0	698	0.86	06	2.9	Small bleeding
FRSCC - 50, 0.2	626	0.82	12	05	Small stiff
FRSCC - 50, 0.4	573	0.76	15	07	Too stiff
FRSCC - 50, 0.6	540	0.67	17	8.1	Too stiff

Mortar adhered to RCA creates voids and reduces overall density of RAC. The graphs also illustrate that as volume fraction of fibers increases, density of concrete decreases. This drop-in density is attributed the difference in specific gravity between PP fibers and concrete mixture. Specific gravity of PP fibers is significantly lower (~ 0.90) than that of concrete mixture. Therefore, inclusion of PP fibers in concrete mix lowers overall density of mixture.

7.2.2 Compressive Strength (CS)

Figure 6 illustrates variation in CS values for both RAC and NAC as volume percentage of PP fibers varies. Experimental results indicate that both NAC and RAC exhibit a decrease in CS with addition of PP fibers, reaching a minimum value at a 0.6% fiber addition. On other hand, an increase in CS values is observed with addition of PP fibers up to 0.4%. Maximum CS values for both NAC and RAC are achieved at a 0.4% PP fiber content. However, it should be noted that modifications in CS due to incorporation of PP fibers are relatively small. Highest increase in CS at a 0.4% PP fiber content is 3.1% for RAC and 4.75% for NAC. Thus, it can be founded that PP fibers have a limited impact on CS measurements, aligning with previous studies Yap et al. (2013) and Bayashi et al. (1993) that also found minimal effects on CS. Fineness and variable length of primary PP fibres, which create a network serving as a bridge and inhibiting the propagation of micro cracks, are responsible for the behavior of FRC.

Fig. 6. Slump flow test on self-compacted recycled aggregate concrete

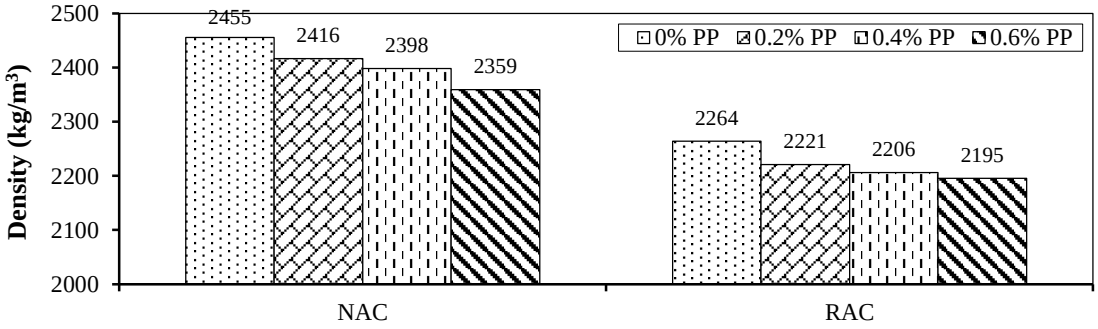

Fig. 7. SCC density varies with pp fibre at various volume fractions

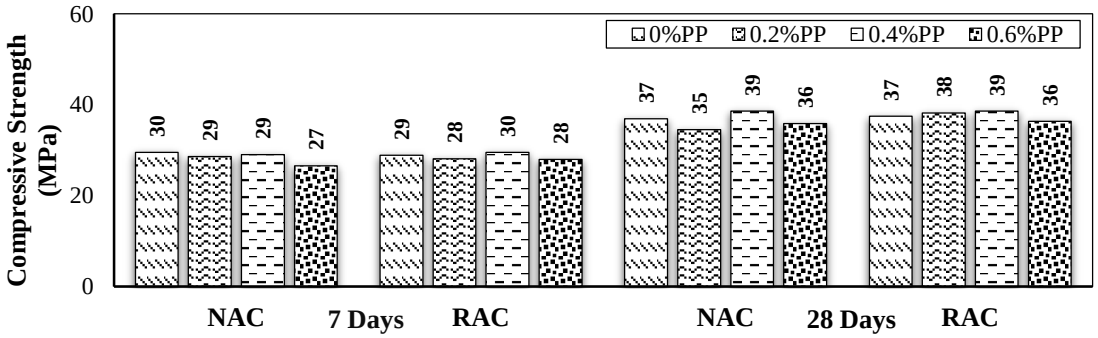

Fig. 8. Impact of pp fibre volume fraction on SCC is CS

However, when PP fibers are not evenly distributed in concrete due to poor mixing and decreased workability, fiber clusters can create relatively weaker spots that act as voids and are more prone to cracking, resulting in a decrease in CS. Compressive Testing Machine (CTM) with capacity of 2000 KN was used for compressive strength test. Comparatively, reductions in CS at a 0.6% PP fiber content are 2.9% for NAC and 3.46% for RAC, respectively, in comparison to controlled unreinforced concrete.

It is also noteworthy that RAC and NAC exhibit comparable CS. This can be justified by higher water absorption capacity of RCA compared to NCA due to adhered mortar increasing porosity of RCA. As a result, effective W/C ratio for RAC is lower than that for NAC, leading to improved CS. The grading curve for RCA shows (Figure 1) that it lies in the same range, which is applicable for NCA and guided by the IS, 383, 1970. The qualities of aggregates for both NCA and RCA are considerably influenced by physical properties such as crushing value, impact value, and Los Angeles abrasion value of aggregates. Additionally, the crushing strength, size and quality of recycled aggregate contributed to designed strength of RAC compared to NAC depends on the origin of parent concrete of recycled aggregated, as indicated by Akbarnezhad et al. (2013); Singh and Shukla (2021) and Kapoor et al. (2020). As in Akbarnezhad et al. (2013), the above results suggested that addition of PP fibers to concrete enhances its resistance to crack propagation.

Disparity in crack propagation between concretes is clear in Figures 9 and 10. Volume fraction of PP fibers plays a role in reducing pace of crack propagation by acting as a bridge between mortar, aggregate, and fibers. Fibers also form a matrix with concrete, trapping fiber particles between aggregates and mortar and providing reinforcement. Actual mean value of workability and compressive strength of specimen is defined in the Table 8.

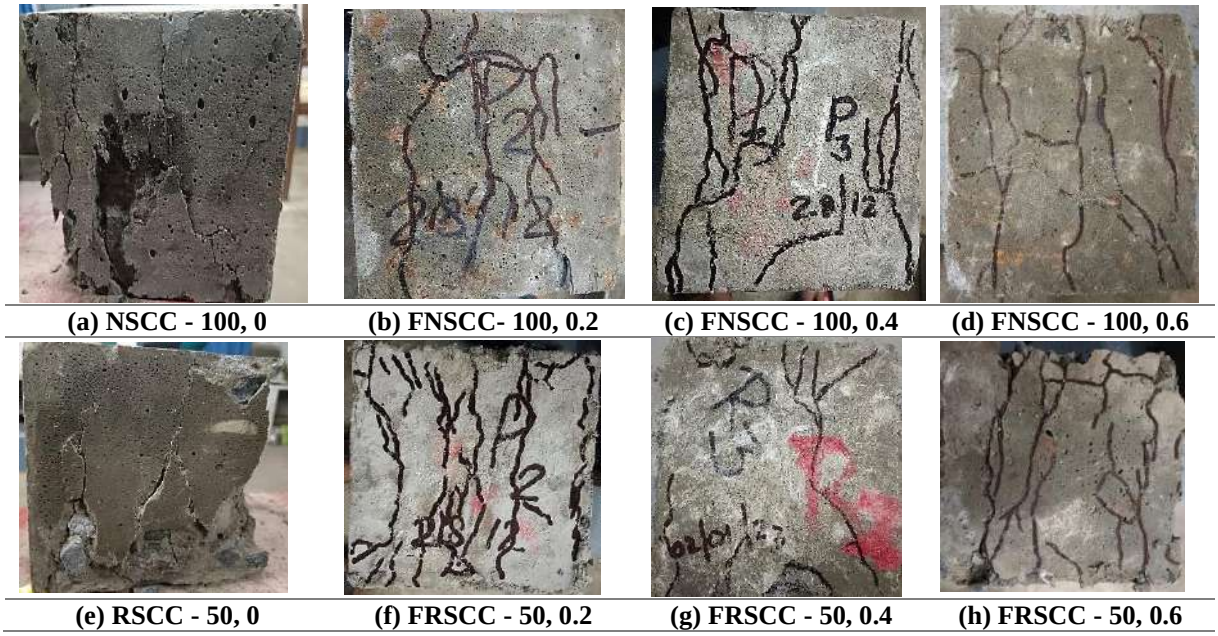

(a) NSCC - 100, 0 **(b) FNSCC- 100, 0.2** **(c) FNSCC - 100, 0.4** **(d) FNSCC - 100, 0.6**

(e) RSCC - 50, 0 **(f) FRSCC - 50, 0.2** **(g) FRSCC - 50, 0.4** **(h) FRSCC - 50, 0.6**

Fig. 9. Crack propagation in NAC and RAC without and with use of PP fiber

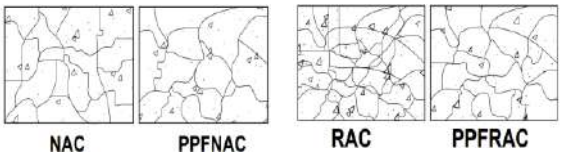

Fig. 10. Crack propagation in NAC and RAC without and with use of PP Fiber

Table 8. Actual mean value of workability and CS of the specimen

Proportion of polypropylene fiber (%)	Actual workability and mean compressive strength of recycled aggregate concrete for different proportion of polypropylene fiber reinforcement					
	Natural aggregate concrete (NAC)			Recycled aggregate concrete (RAC)		
	Actual slump flow (mm)	V – funnel flow (s)	Comp. strength (N/mm^2)	Actual slump flow (mm)	V – funnel flow (s)	Comp. strength (N/mm^2)
00	722	05	36.89	698	06	37.46
0.2	641	07	37.54	626	12	38.2
0.4	596	13	38.6	573	15	38.62
0.6	553	16	35.82	540	17	36.32

7.2.3 Split Tensile Strength (STS)

According to Bureau of Indian Standards (BIS) guidelines IS, 5816-1999, TS tests were conducted on both NAC and RAC Figure 10, demonstrates how STS values vary with different fiber volume proportions. Results indicate that addition of PP fibers significantly increases values for STS. Adding fibers up to a 0.4% proportion fraction in both NAC and RAC enhances STS values before they start to decline again. Maximum value for NAC is 2.805 MPa at a 0.4% fiber volume proportion, which represents a 29.57% improvement over unreinforced control concrete. Correspondingly, highest improvement for RAC at a 0.4% fiber volume fraction is 23.79%, with an STS of 2.845 MPa. After splitting process is complete, fibers act as bridging elements, effectively transferring load from the matrix to fibers and taking additional load from matrix to fibers. This results in higher ST values compared to unreinforced concrete.

Improvement in split elasticity of cement also depends on size and shape of PP fibers. Additionally, STS values of RAC are generally higher than those of NAC for same fiber content due to lower effective water-to-cement ratio in a dispersed fiber concrete matrix, stress concentrations are same throughout entire length of fiber.

STS benefits more from addition of PP fibers compared to CS. They exhibit similar behavior, with STS showing positive impacts when PP fibers are added to concrete to promote flexibility by delaying development of tension cracks or preventing their generation. According to Lim and Ozbakkaloglu (2014), fibres act as crack reducers rather than crack preventers. Fibers are well recognized for their post-cracking behavior that increases TS. Reinforced concrete demonstrates better performance compared to unreinforced controlled concrete. Fibers are recognized for their post-cracking behavior that increases tensile strength Figure 11.

Depicts cracking behavior of controlled concrete with and without PP fiber reinforcement.

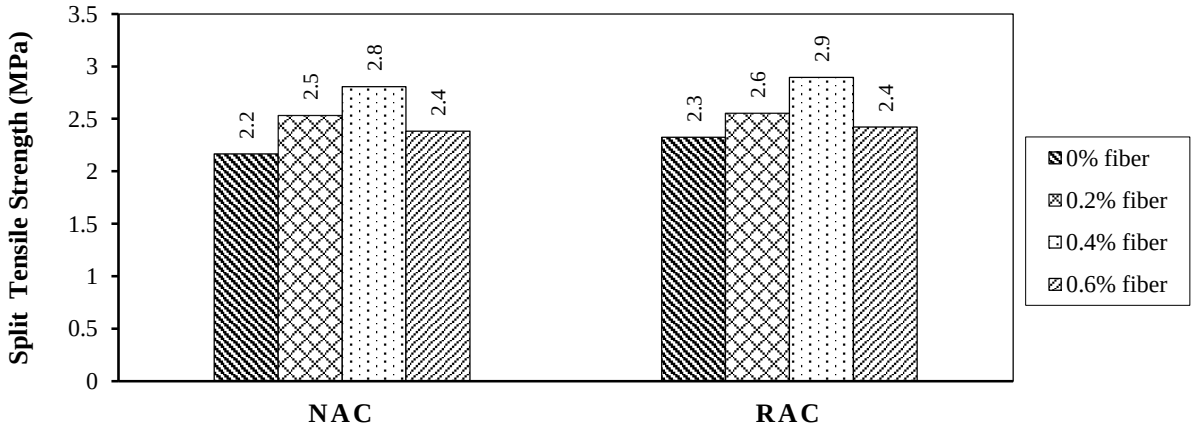

Fig. 11. Impact of different volume proportions of pp fibre on STS

7.2.4 Flexural Strength (FS)

Figure 12 illustrates relationship between volume percentage of PP fiber and FS of both NAC and RAC. FS tests were conducted following guidelines of Bureau of Indian Standards IS: 516 - 1959. Results show that FS initially increases for both NAC and RAC up to a fiber volume proportion of 0.4%. However, beyond this point, as percentage of PP fiber volume content increases, FS starts to decrease. This contrasts with behavior observed in CS, where addition of fibers resulted in an increase in strength. In comparison to unreinforced concrete, which has a maximum FS value of 3.5 MPa, NAC achieves a maximum value of 3.8 MPa, representing a 10.8% improvement.

Similarly, RAC reaches a maximum FS of 4.1 MPa compared to 3.7 MPa for unreinforced concrete, resulting in a 12.7% increase. FS values for RAC are slightly higher than those for NAC, consistent with findings for CS and STS values. Overall, addition of PP fibers has a positive impact on FS of both NAC and RAC, up to a certain fiber volume proportion. However, beyond this point, FS starts to decrease. It is important to consider optimal fiber content to achieve desired flexural performance in concrete.

7.2.5. Modulus of Elasticity

Figure 13 presents relationship between volume fraction of pp fiber and MOE for both NAC and RAC. It is observed that both NAC and RAC follow a similar trend as volume percentage of PP fibers changes.

Results indicate that as fiber volume percentage increases, MOE decreases. This is attributed to presence of a greater number of micro cracks along length of cracks and increased fiber content. Both NAC and RAC exhibit similar MOE values for control mix, indicating comparable stiffness.

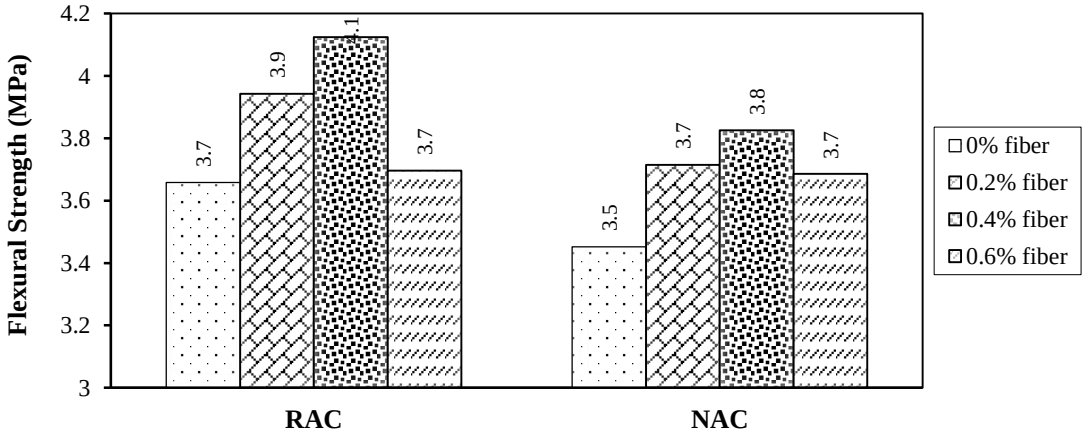

Fig. 12. Variations in PP fiber volume proportion influence both NAC and RAC FS

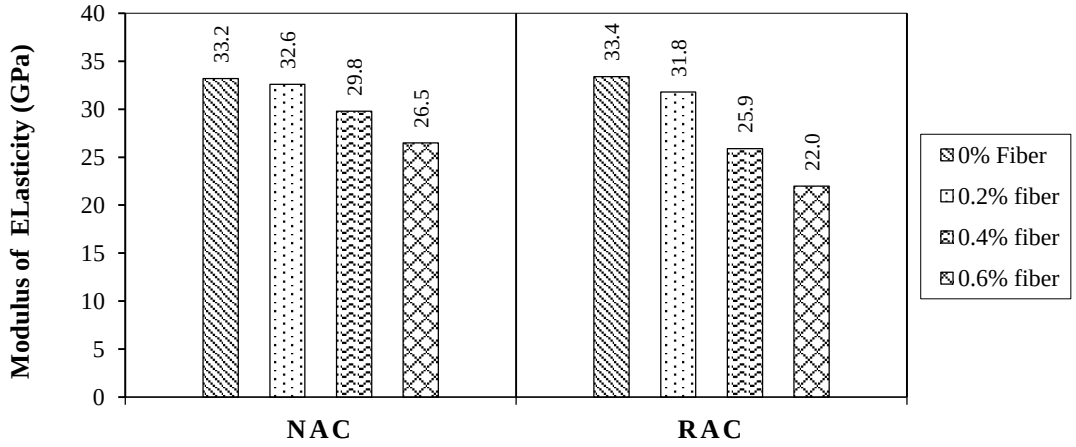

Fig. 13. Impact of Different volume proportions of PP Fiber on MOE

However, when maximum fiber volume percentage of 0.6% is reached, there is a reduction in MOE value. Specifically, for NAC, there is a 20.18% decrease in MOE, while for RAC, decrease is 34.13%. This reduction in MOE can be attributed to weakest link for cracking, which is interface between old adhering mortar and the aggregates. Most of cracks tend to follow this ITZ. It is important to note that addition of PP fibers can lead to a decrease in MOE of both NAC and RAC. However, specific decrease in MOE varies between two types of concrete.

7.3. Durability of Concrete

7.3.1. Water Absorption (WA)

Concrete durability is an important aspect that can be indirectly measured by water absorption. Water contains chemicals that can adversely affect properties of concrete when they interact with its constituents. One of durability concerns is freeze-thaw effect caused by presence of additional water in concretes pores during temperature changes. This effect leads to expansion and contraction of concrete, resulting in cracks and reduced durability.

In order to evaluate water absorption characteristics, PP Fibers were subjected to a water absorption test for different durations (seven days, fourteen days and 28 days) with varying volume proportions. Water absorption test for concrete is conducted as per IS 1199-1959. This code provides guidelines for determining water absorption characteristics of concrete specimens. Figure 14 illustrates outcomes of water absorption test.

Generally, it is observed that ability of fiber-reinforced concrete to adsorb water decreases as volume fraction of PP fibers increases up to 0.4% in both NAC and RAC. Addition of PP fibers enhances tensile characteristics of concrete, thereby preventing initiation and propagation of early cracks. However, it is evident that adding more than 0.4% proportion of PP fibers to concrete leads to fiber clustering. This clustering phenomenon can cause formation of numerous micro cracks in both NAC and RAC, consequently increasing water absorption of concrete, particularly in SCC. Therefore, it is crucial to carefully consider volume proportion of PP fibers in order to achieve desired improvement in concrete properties without compromising its durability and water absorption characteristics.

7.3.2. Acid Resistance

Indian Standard codes do not specifically provide guidelines for acid resistance tests for concrete. However, there are internationally recognized standards that can be followed to assess the acid resistance of concrete.

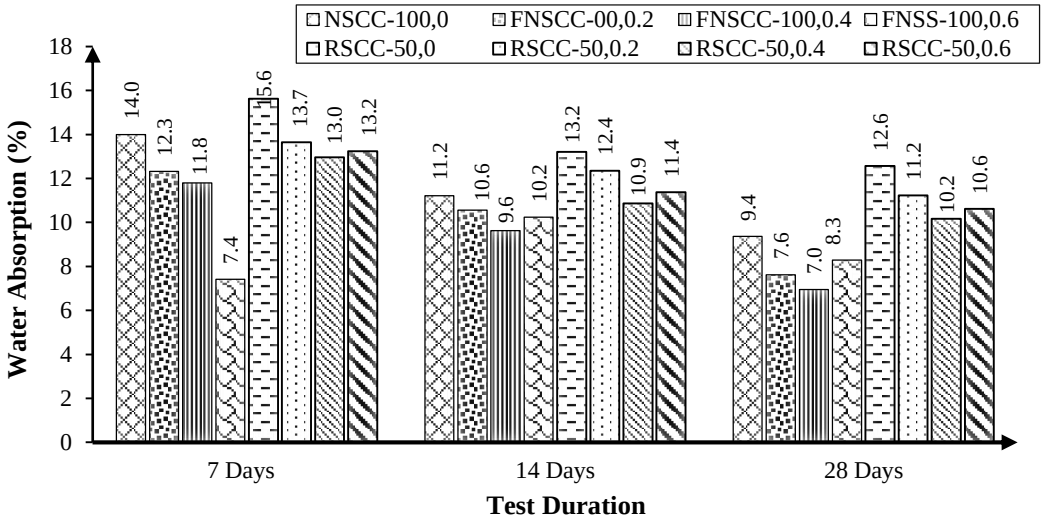

Fig. 14. Impact of Different volume proportions of PP Fiber on MOE

One such commonly used standard is ASTM C267. In study on acid resistance, Hydrochloric Acid (HC l) was utilized as an acid to assess resistance of concrete samples with varying volume proportions of PP fibers. Acid resistance test involved measuring loss in concrete mass caused by acidic attack of HC l on specimens for different durations (7 days, 14 days, and 28 days) for each mix proportion of both NAC and RAC. Results of acid resistance test are presented in Figure 15. Findings clearly indicate addition of PP fibers at volume proportion up to 0.4% for both NAC and RAC significantly reduce weight loss caused by HC l acid. This can be attributed to use of PP fibers, which effectively slow down development and propagation of early fractures and decrease porosity of concrete.

Consequently, penetration of HC l acid into concrete is hindered, preventing rapid deterioration. In acidic environments, HC l acid reacts with calcium aluminate and calcium hydroxide, leading to erosion of concrete. Rate at which HC l acid penetrates concrete and reaches these components determines speed of erosion. By incorporating PP fibers, concretes resistance to acid attack is improved.

However, it is important to note that at higher PP fiber dosages (0.6%), density of SCC significantly decreases due to reduced workability. This decrease in density can result in increased weight loss from HC l acid attack. Therefore, it is crucial to carefully consider dosage of PP fibers in order to achieve optimal acid resistance while maintaining the desired workability and density of concrete.

7.3.3. Carbonation Resistance Test

The carbonation depth test, as per the ASTM standard, specifically ASTM D7705, provides a method for determining the depth of carbonation in hardened concrete. This test helps assess the carbonation resistance of concrete and evaluate its durability in carbonation-prone environments as discussed by Singh and Singh (2018). Carbonation depth of concrete is influenced by percentage of PP fibers in both NAC and RAC. As proportion of PP fibers increases from 0% to 0.4%, carbonation depth of concrete decreases.

Furthermore, carbonation depth continues to decrease as percentage of PP fibers increases up to 0.6%. It is observed that concrete containing PP fibers exhibits less carbonation compared to control mix without fibers.

In specimen, at a volume percentage of 0.4% PP fiber, minimum carbonation depth for NAC was reported as 2.94%, 4.91% and 7.12% at 7 days, 14 days, and 28 days, respectively. Similar results were obtained for RAC, where minimum carbonation depth was 3.21%, 5.87% and 8.1% at 7 days, 14 days, and 28 days, respectively, when fiber volume proportion was 0.4%. This represents a reduction of approximately 16.67% for NAC (28 days) and 17.54% for RAC (28 days) compared to control mix. Inclusion of PP fibers in concrete obstructs diffusion channel for CO_2, increasing resistance to CO_2 diffusion and slowing down carbonation process. This is illustrated in Figure 16, which shows correlation between volume percentage of PP fiber and carbonation depth. However, at higher dosages of PP fiber (0.6%), fibers can prevent cement paste from filling voids in microstructure, increasing internal porosity and potentially creating a new pathway for CO_2 to enter concrete structure. This can accelerate carbonation process. It is important to consider dosage of PP fibers to achieve desired balance between carbonation resistance and other concrete properties.

The addition of these fibers outcomes with novel improvement in splitting tensile capacity, flexural capacity, toughness, and ductile failure of concrete owing to their small microstructural size which retards the origination and expansion of early micro-cracks inside the concrete matrix. Novelty has been noted in comparison to NAC, as these fibers in RAC are more valuable in several aspects. Firstly, RAC matrix is weak and the bonding between cement and

aggregate phase is poor therefore the tensile strength and durability of RAC is more pronounced than NAC, as these properties are enhanced by PP fibers, which further results in preventing the formation and propagation of micro-cracks. These impacts of fibers in RAC were also ratified in another research works (Gao et al., 2020). Secondly, owing to the glued mortar, RCA develops higher shrinkage cracks in RAC. The deployment of these PP fibers benefits RAC by restricting the expansion of shrinkage cracks, which results in a durable concrete.

8. Conclusions

In the presented manuscript investigation for impact of PP fibers on properties of NAC and RAC through experimental assessment using fiber integration at 0.2%, 0.4% and 0.6% in both types of concrete have been done. The key findings of this study can be summarized as follows:

1. PP fibers significantly reduce workability of concrete by increasing friction between particles. RAC is less workable than NAC due to larger water absorption capacity of recycled coarse aggregate caused by old mortar adhering to it is surface.
2. Presence of PP fibers obstructs bleeding and segregation in concrete mix, as fibers flocculate with aggregates and mortar, restricting their movement and adsorbing some water.

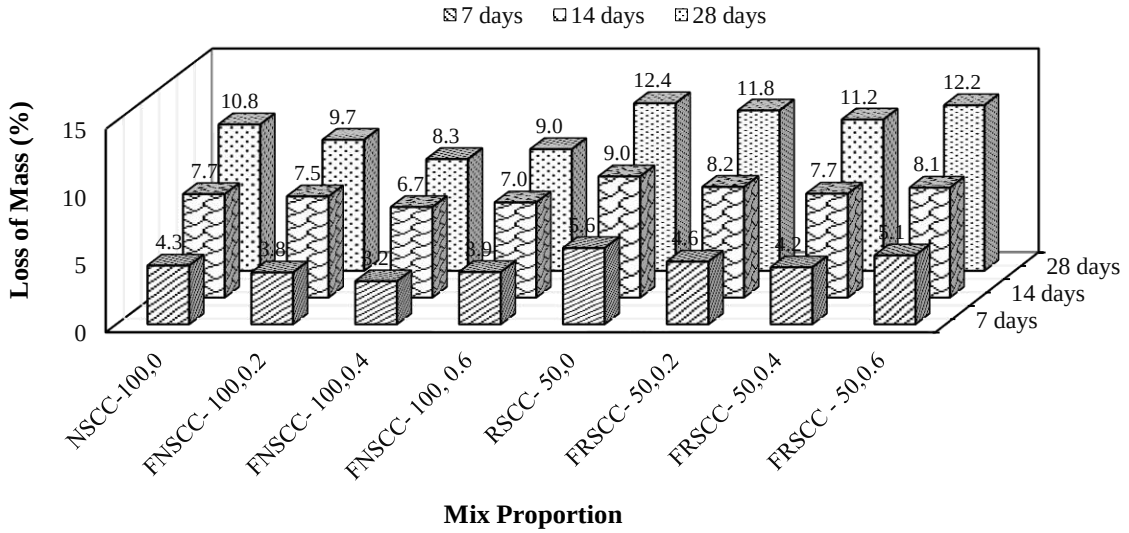

Fig. 15. Influence of various PP fibre volume fractions on acid resistance

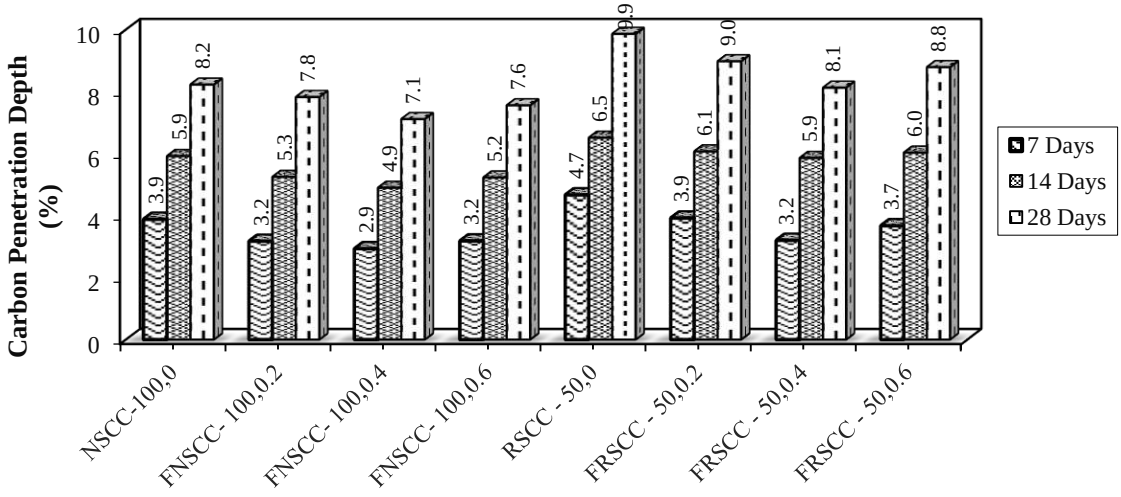

Fig. 16. Influence of different volume proportion of PP fiber on carbonation resistance

3. RAC has a lower density compared to NAC, and addition of PP fibers further reduces density of RAC due to lower specific gravity of fibers.
4. CS of both NAC and RAC initially increases up to a fiber content of 0.4% but starts to decline with higher fiber contents. This is attributed to higher stresses present at ends of fibers in a dispersed fiber concrete matrix.
5. Similar trends are observed for STS, where optimal fiber content for enhancing strength is found to be 0.4%.
6. Addition of PP fibers greatly improves aspects of durability such as water absorption, acid resistance, and carbonation depth.
7. Overall, PP fibers have a positive impact on mechanical performance of SCC, regardless of whether its NAC or RAC.

This study concludes that use of RCA in construction projects is increasing, and successful incorporation of PP fibers into concrete enables creation of Polypropylene Fibre Reinforced Recycled Aggregate Self Compacted Concrete (PFRRASCC). Use of RCA is expected to be a significant development in construction, benefiting both environment and ecosystem in a sustainable manner.

9. Acknowledgements

The authors delightedly acknowledge the Department of Civil Engineering, Madan Mohan Malaviya University of Technology, Gorakhpur and Uttar Pradesh, India to facilitate for conducting the experimental work of this study.

10. Abbreviations

C and D: Construction and Demolition
CS: Compressive Strength
FNSCC: Fiber-Reinforced Natural Aggregate Self-Compacting Concrete
FRSCC: Fiber-Reinforced Recycled Aggregate Self-Compacting Concrete
FS: Flexure Strength
HPC: High Performance Concrete
NA: Natural Aggregate
NAC: Natural Aggregate Concrete
NASCC: Natural Aggregate Self-Compacting Concrete
NSCC: Natural Aggregate Self-Compacting Concrete
PFRRASCC: PP Fiber Reinforced Self-Compacted Concrete
PP Fiber: Polypropylene Fiber
PPFNAC: Polypropylene Fiber Natural Aggregate Concrete
PPF RAC: Polypropylene Fiber Recycled Aggregate Concrete
RAC: Recycled Aggregate Concrete
RSCC: Recycled Aggregate Self-Compacting Concrete
STS: Split Tensile Strength
SCC: Self-Compacted Concrete
SCHPC: Self-Compacted High Performance Concrete

11. References

Akç, K.R., Çakir, Ö. and İpek, M. (2015). "Properties of polypropylene fiber reinforced concrete using recycled aggregates", *Construction of Building Materials*, 98(1), 620-630, https://doi.org/10.1016/j.conbuildmat.2015.08.133.

Akbarnezhad, A., Ong, K.C.G., Tam, C.T. and Zhang, M.H. (2013). "Effect of the parent concrete properties and crushing procedure on the properties of coarse recycled aggregates", *Journal of Materials in Civil Engineering*, 25(1), 17951802, http://doi.org/10.1061/(ASCE)MT.193-5533.0000789.

Bayashi, Z. and Zeng, J. (1993). "Properties of polypropylene fiber reinforced concrete", *ACI Materials Journals*, 90(6), https://doi.org/605-610.10.14359/4439.

Brand, A.S., Roesler, J.R. and Salas, A. (2015). "Initial moisture and mixing effects on higher quality recycled coarse aggregate concrete", *Construction and Building Materials*, 79(1), 83-89, http://doi.org/10.1016/j.conbuildmat.2015.01.047.

Brandt, A.M. (2008). "Fiber reinforced cement-based composites after over 40 years of development in building and civil engineering", *Composite Structures*, 86(1), 39, https://doi.org/10.1016/j.compstruct.2008.03.006.

Boulekbache, B., Hamrat, M., Chemrouk, and Amziane, S. (2010). "Followability of fibre-reinforced concrete and its effect on the mechanical properties of the material", *Construction and Building Materials*, 24(1), 16641671,

https://doi.org/10.1016/j.conbuildmat.2010.02.025.

Carneiro, J.A., Lima, P.R.L., Leiti, M.B. and Filho, R.D.T.F. (2014). "Compressive stress–strain behavior of steel fiber reinforced-recycled aggregate concrete", *Cement and Concrete Composites*, 46(1), 65-72, https://doi.org/10.1016/j.cemconcomp.2013.11.006.

Central Pollution Control Board (CPCB). (2017). *Guidelines on environmental management of c and d wastes*, Ministry of Environment, Forests and Climate Change, India, guidelines-final-c and d-march 2017, pdf (https://py.gov.in).

Das, C.S., Dey, T., Mukherjee, B.B. and Kumar, J. (2018). "Performance evaluation of polypropylene fiber reinforced recycled aggregate concrete", *Construction and Building Materials*, 189(1), 649-659, https://doi.org/10.1016/j.conbuildmat.2018.09.036.

Faraj, R.H., Sherwani, A. and Daraei, A. (2019), "Mechanical, fracture and durability properties of self-compacting high strength concrete containing recycled polypropylene plastic particles", *Journal of Building Engineering*, 25(1), 100808, https://doi.org/10.1016/j.jobe.2019.100808.

Gao, D. and Zhang, L. (2018). "Flexural performance and evaluation method of steel fiber reinforced recycled coarse aggregate concrete", *Construction and Building Materials*, 159(1), 126-136, https://doi.org/10.1016/j.conbuildmat.2017.10.073.

Güneyisi, E., Gesoğlu, M. and Yazici, H. (2014). "Effect of surface treatment methods on the properties of self-compacting concrete with recycled aggregates", *Construction and Building Materials*, 64(1), 172-183, https://doi.org/10.1016/j.conbuildmat.2014.04.090.

Hsie, M., Tu, C. and Song, P.S. (2008). "Mechanical properties of polypropylene hybrid fiber-reinforced concrete", *Materials Science and Engineering*, A, 494(1), 153-157, http://doi.org/10.1016/j.msea.2008.05.037.

I.S. 2386-Part-IV (reaffirmed in 2021). *Indian standard method of test for aggregate for concrete*, New Delhi, Bureau of Indian Standards, https://law.resource.org/pub/in/bis/S03/is.2386.4.1963.pdf.

I.S. 383-2016. (2016). *Indian standard specification of coarse and fine aggregate from natural sources*, New Delhi, Bureau of Indian Standards, https://law.resource.org/pub/in/bis/S03/is.383.1970.pdf.

I.S. 456-2000 (reaffirmed in 2021). (2000). *Indian standard plain and reinforced concrete code of practice*", New Delhi, Bureau of Indian Standards, https://law.resource.org/pub/in/bis/S03/is.456.2000.pdf.

I.S. 516-1959 (reaffirmed in 2018). (1959). *Indian standard method of tests for strength of concrete*, New Delhi, Bureau of Indian Standards, https://law.resource.org/pub/in/bis/S03/is.516.1959.pdf.

I.S. 5816-1999 (reaffirmed in 2004). (1999). *Indian standard splitting tensile strength of Concrete - method of test*, New Delhi, Bureau of Indian Standards, https://law.resource.org/pub/in/bis/S03/is.5816.1999.pdf.

I.S. 8112-2013. (2013). *Indian standard specification 43 grade ordinary portland cement specification*", New Delhi, Bureau of Indian Standards, https://law.resource.org/pub/in/bis/S03/is.8112.1989.pdf.

I.S. 10262-2019. (2019). *Indian standard recommended guideline for concrete mix design*, New Delhi, Bureau of Indian Standards, https://law.resource.org/pub/in/bis/S03/is.10262.2009.pdf.

I.S. 1199-1959 (reaffirmed in 2018). (1959). *Methods of sampling and analysis of concrete*, new-delhi, Bureau of Indian Standards, https://ia903000.us.archive.org/21/items/gov.in.is.1199.1959/is.1199.1959.pdf.

India, M.O. (2016). "The gazette of India, Part II, Section-3, Sub-section (ii): *Forest and climate change*", Retrieved from https://www.moef.gov.in/sites/default/files/C%20&D%202016.Pdf.

Jindal, A. and Ransinchung, G.D. (2022), "Behavioral study of incorporation of recycled concrete aggregates and minerals admixtures in pavement quality concrete", *Civil Engineering Infrastructures Journal*, 55(2), 351-372, https://doi.org/10.22059/ceij.2022.326564.1766.

Kamal, M.M., Safan, M.A., Etman, Z.A. and Kasem, B.M. (2014). "Mechanical properties of self-compacted fiber concrete mixes", *Housing and Building National Research Center HBRC Journal*, 10(1), 25-34, https://doi.org/10.1016/j.hbrcj.2013.05.012.

Kang, W.H., Ramesh, R.B., Mirza, O., Senaratne, S., Tam, V. and Wigg, D. (2017). "Reliability based design of RC beams with recycled aggregate and steel fibres", *Journal of Structures*, 11(1), 135-145, https://doi.org/10.1016/j.istruc.2017.05.002.

Kapoor, K., Singh, S.P. and Singh, B. (2020). "Permeability of self-compacting concrete made with recycled concrete aggregates and Portland cement-fly ash-silica fume binder", *Journal of Sustainable Cement - Based Materials*, 10(1), 1-27,

http://doi.org/10.1080/21650373.2020.1809029.
Lawler, J.S., Zampini, D.P.S. (2002). "Permeability of cracked hybrid fiber reinforced mortar under load", *Journal of American Concrete Institute Materials Journal*, 99(4), 379-385, https://doi.org/10.14359/12220.
Li, L.G., Chu, S.H., Zeng, K.L., Zhu, J. and Hawan, A.K.H. (2018). "Roles of water film thickness and fibre factor in workability of polypropylene fibre reinforced mortar", *Cement and Concrete Composites*, 93(1), 196-204, https://doi.org/10.1016/j.cemconcomp.2018.07.014.
Li, J., Niu, J., Wan, C., Liu, X. and Jin, Z. (2017). "Comparison of flexural property between high performance polypropylene fiber reinforced lightweight aggregate concrete and steel fiber reinforced lightweight aggregate concrete", *Construction and Building Materials*, 157(1), 729-736. http://doi.org/10.1016/j.conbuildmat.2017.09.149.
Maio, F.D., Rem, P., Lofti, S. and Serranti, S. (2016). "Advanced technologies for the production of cement and clean aggregates from construction and demolition waste", R 2016, https://www.researchgate.net/publication/309309338_Cement_and_clean_aggregates_from_cdw_The_c2ca_project.
Matar, P. and Zéhil, G.P. (2019). "Effects of polypropylene fibers on the physical and mechanical properties of recycled aggregate concrete", *Journal of Wuhan University of Technology-Material*, Sci, Ed, 34(1), 1327-1344, http://doi.org/10.1007/s11595-019-2196-6.
Mefteh, H., Kebaïli, O., Berredjem, L. and Arabi, N. (2013). "Influence of moisture conditioning of recycled aggregates on the properties of fresh and hardened", concrete, *Journal of Cleaner Production*, 54(1), 282-288, https://doi.org/10.1016/j.jclepro.2013.05.009.
Mukhatar, F. and El-Tohfa, A. (2023). "A review on fracture propagation in concrete, models, methods, and benchmark tests", *Engineering Fracture Mechanics*, 281(1), 109100, https://doi.org/10.1016/j.engfracmech.2023.109100.
Ozbakkaloglu, T. and Lim, J.C. (2014). "Confinement model for frp confined high - strength concrete", *Journal of Composites for Construction*, 18(4), 04013058, http://doi.org/10.1061/(ASCE)CC.1943-5614.0000376.
Poon, C.S., Shui, Z.H. and Lam, L. (2004). "Effect of microstructure of itz on compressive strength of concrete prepared with recycled aggregate", *Construction and Building Materials*, 18(6), 461-468, https://doi.org/10.1016/j.conbuildmat.2004.03.005.
Romualdi, J.P. and Mandel, J.A. (1964). "Tensile strength of concrete affected by uniformly distributed and closely spaced short lengths of wire reinforcement", *Journal of American Concrete Institute*, 61(6), 657-672, https://doi.org/10.14359/7801.
Singh, N. and Singh, S.P. (2018). "Validation of carbonation behavior of self-compacting concrete made with recycled aggregates using", *European Journal of Environmental and Civil Engineering*, 24(1), 2187-2210, https://doi.org/10.1080/19648189.2018.1500312.
Singh, V.K. and Shukla, A. (2021). "Structural application of concrete made of recycled aggregate sourced from construction and demolition waste", *Proceedings of SECON 21*, Springer International Publishing, 171(1), https://doi.org/10.1007/978-3-030-80312-474.
Smirnova, O.M. and Kharitonovs, A. (2018). "Strength and strain-stress properties of fiber concrete with macro-fiber on the basis of polyolefin", *Stroitel nye Materially*, 766(12), 44-48, http://doi.org/10.31659/0585-430X-2018-766-12-44-48.
Tiwari, P.K. and Singh, V.K. (2023), "The ompact of fiber reinforcement on fresh and physical properties with durability of recycled coarse aggregate concrete, A review", *Journal of Engineering Science and Technology Review*, 16(4), 85-93, http://doi.org/10.25103/jestr.164.11.
Utepov, Y., Akhmetov, D. and Ilnur, A. (2020). "Effect of fine fillers from industrial waste and various chemical additives on the placeability of self-compacting concrete", *Computers and Concrete*, 25(1), 59-65. https://doi.org/10.12989/cac. 2020.25.1.059.
Yap, S.P., Alengaram, U.J. and Jumaat, M.Z. (2013). "Enhancement of mechanical properties in polypropylene and nylon fiber reinforced oil palm shell concrete", *Materials and Design*, 49(1), 1034-1041, http://doi.org/10.1016/j.matdes.2013.02.070.
Yoda, K. and Shintani, A. (2014). "Building application of recycled aggregate concrete for upper-ground structural elements", *Construction and Building Materials*, 67(1), 379-385, https://doi.org/10.1016/j.conbuildmat.2013.12.096.

Civil Engineering Infrastructures Journal 2025, 58(1): 35-47
DOI: 10.22059/ceij.2024.366034.1968

RESEARCH PAPER

Experimental and Numerical Investigations on a Stone Column in Sandy Ground Contains Clayey Lens

Bazazzadegan, N.[1], Ganjian, N.[2*] and Nazariafshar, J.[2]

[1] Ph.D. Candidate, Department of Civil Engineering, Science and Research Branch, Islamic Azad University, Tehran, Iran.
[2] Assistant Professor, Department of Civil Engineering, Shahr-e-Qods Branch, Islamic Azad University, Tehran, Iran.

Received: 02 Oct. 2023; Revised: 29 Nov. 2023; Accepted: 02 Jan. 2024

ABSTRACT: Utilizing stone columns proves highly effective in altering the behavior of challenging ground conditions. The combined application of stone columns with surrounding reinforcement enhances the methods efficiency for layered ground formations. The current study investigates the effectiveness and behavior of unreinforced and geotextile-reinforced stone columns integrated into sandy ground containing a soft clayey lens. This problem was investigated employing a Frustum Confined Vessel (FCV) in physical models and using ABAQUS software in numerical analyses. The results of experimental tests, demonstrated that reducing soft lens thickness significantly augmented the bearing capacity of both unreinforced and geotextile-encased stone columns. As soft lens depth increased, both unreinforced and reinforced stone columns exhibited approximately 40% and 10% increases in bearing capacity, respectively. The results of numerical analysis showed that in the presence of soft lens, the change in the length of a stone column had no effect on the occurrence of bulging failure and decreasing placement level of the soft lens, increased the bulging failure occurrence proportional. On the other hand, increasing the thickness of the soft lens reduced the bearing capacity of the ordinary and reinforced stone column. The phenomenon of bulging can occur at the level of the lens placement and up to a depth of about 4 times the diameter of the ordinary column because of existence of a soft lens in a relatively loose sandy bed, while mechanism of failure is not bulging anymore if using encasement.

Keywords: Frustum Confined Vessel (FCV), Stone Column, Bearing Capacity, Clayey Lens, ABAQUS, Reinforcement.

1. Introduction

In the realm of constructing engineered structures like buildings and road embankments, grappling with soft or loose soil beds that display inadequate bearing capacity and susceptibility to settlement exceeding permissible limits remains an unrelenting challenge. By embedding stone columns within such soil beds, the bearing capacity is augmented, and settlement is curtailed. These columns are effective for reinforcing soft and loose soils to depths of up to 20 meters. The method involves substituting a fraction, ranging from 15% to 35%, of the loose bed volume with gravel

* Corresponding author E-mail: N.Ganjian@srbiau.ac.ir

or crushed stone. This material is meticulously placed within wells of predetermined dimensions, thereby enhancing soil bearing capacity and minimizing settlement. However, the presence of soft lenses within the soil bed introduces complexity. These soft lenses encompass zones of diminished shear strength within the soil matrix, thereby increasing the probability of bulging failure. In many instances, this failure is observed at depths spanning 2 to 3 times the diameter of a stone column. Notably, this failure mode is accentuated in cases where the column length greatly exceeds 4 to 6 times its diameter, particularly within a uniform soil matrix. In regions characterized by the existence of soft lenses, it becomes crucial to bolster soil bearing capacity and mitigate compressibility through the reinforcement of stone columns. This reinforcement strategy is pivotal in evaluating the soft lens is impact on these key parameters.

Moreover, the presence of heterogeneous layers, such as fine-grained strata within sandy beds, contributes to the intricacy of decision-making when assessing the behavior of geotechnical structures. Engineering guidelines (Schaefer et al., 2017), based on valid principles further reveal that the failure mechanism of a stone column in a sandy bed housing an extremely soft lens hinges on the thickness and depth of the lens. Lone et al. (2015) performed experimental studies of the behavior of stone columns by changing the column diameter and length as well as the length and stiffness of the geosynthetic encasement material. They concluded that the bearing capacity of the column increased after encasement with an appropriate geosynthetic in the rigid-base, semi-encased and floating states.

Most studies have reported that bulging failure occurs at a depth of D to 2.5 D (D = stone column diameter) from the top of the stone column (Ghazavi and Afshar, 2013; Afshar and Ghazavi, 2014; Mehrannia et al., 2018). Studies on the behavior of stone columns having different diameters with and without geotextile encasement in layered soil have shown that soil improved by such columns had a greater bearing capacity than did unimproved soil (Prasad et al., 2017). Mohanty and Samantha (2015) conducted experimental and numerical tests on the response of stone columns in layered sand and concluded that the behavior differed in layered and homogeneous soils.

Shamsi et al. (2019) performed experimental and numerical studies of the behavior of sand columns reinforced by vertical geotextile encasement and horizontal geotextile layers. Gu et al. (2020) conducted numerical tests on the bearing capacity of footing supported by geogrid encased stone columns on soft soil.

Nazariafshar et al. (2022) performed experimental studies of the effect of construction method on the performance of ordinary and geotextile-encased stone columns. Danish et al. (2021) by numerical modeling the behavior of stone column in soft clay soil, found that increasing the diameter of the column and the internal friction angle of gravel materials increase the bearing capacity of the stone column.

Also, Pereira et al. (2021) by numerical analyzing a soft embankment that has got improved with a stone column using plaxis and slide software, concluded that the mohr-coulomb behavior model predicts vertical displacements better than the cam-clay behavior model. Saxena and Roy (2022) analyzed the effect of using two different types of gravel materials in the construction of stone columns on the behavior of the column with plaxis software and compared the length and diameter of the stone column in both cases. Hajiazizi and Nasiri (2019) conducted experimental and numerical tests on the stabilizing of reinforced sand slope using geogrid encased stone column. Also, Shahraki et al. (2018) performed studies on the behavior of stone columns in saturated soft grounds using Finite Element (FE) numerical method. Gu et al. (2022) performed model test on the behavior of floating stone columns

reinforced with geogrid encasement. This study, uniquely, investigates the impact of soft lenses on the failure mode and defects in stone columns situated within sandy beds containing such lenses. This examination is driven by excavation logs from northern Iran indicating the presence of layered conditions beneath the surface in specific areas. Here, the results of experimental models in FCV are used to validate the software, and along with, the effect of different parameters on the behavior of a stone column in sandy ground contains clayey lens will be investigated numerically.

2. Experimental Modelling

2.1. Material

The sand used to form the bed was the relatively medium sand from Bandar-e-Anzali in Iran that has a relative density of 60% and a moisture content of about 8%, with other specifications given in Table 1.

To prepare the soft clayey lens, the dry unit weight was set at 80% of the maximum dry density resulting from the standard compaction test (ASTM D 698). Uniaxial compressive strength testing (ASTM D 2166) was conducted on a sample with a 20% moisture content to find out unconfined compressive strength (q_u) of lense. The specifications of the clayey materials are given in Table 2. The materials used for the stone column were crushed stone with a particle size of 2-10 mm, as suggested by Nayak (1983) and Fattah et al. (2011) as presented in Table 3.

Calculating the minimum and maximum dry densities (14.1 and 16.5 kn/m^3, respectively), the dry unit weight of stone column material was set at 15.7 kn/m^3, which was equal to a relative density of 70% (Mehran Nia et al., 2018).

Table 1. Properties of bandar-e-anzali sand

Parameters	Unit	Value
Specific gravity (Gs)	-	2.7
Maximum dry unit weight	kn/m^3	15.4
Minimum dry unit weight	kn/m^3	13.3
Internal friction angle (φ) at 60% relative density	°	32
Dry unit weight for test at 60% relative density	kn/m^3	14.4
Moisture content	%	8
Uniformity coefficient (C_U)	-	1.65
Curvature coefficient (C_c)	-	1.01
Unified soil classification system	-	sp

Table 2. Properties of clay

Parameters	Unit	Value
Specific gravity (Gs)	-	2.67
Maximum dry unit weight	kn/m^3	18.1
Optimum moisture content	%	14.6
Bulk unit weight at 20% water content	kn/m^3	17.4
Plasticity index	%	12
Liquid limit	%	29
Unified soil classification system	-	cld

Table 3. Properties of stone column material

Parameters	Unit	Value
Specific gravity (Gs)	-	2.7
Maximum dry unit weight	kn/m^3	16.5
Minimum dry unit weight	kn/m^3	14.1
Internal friction angle (φ) at 70% relative density	°	45
Bulk unit weight for test at 70% relative density	kn/m^3	15.7
Uniformity coefficient (C_U)	-	2
Curvature coefficient (C_c)	-	1.23
Unified soil classification system	-	gp

The sand, stone and clay particle size distribution curves resulting from the soil gradation tests (ASTMD 422) are depicted in Figure 1. The reinforcing material specifications were determined based on the scale effect. Considering the similar strain conditions:

$$\varepsilon = \frac{T}{J} = \frac{\sigma_v . k . l}{J} \quad (1)$$

$$\frac{J_{(p)}}{J_{(m)}} = \lambda \quad (2)$$

where ε: is the encasement strain, T: is the tension force per length unit of encasement, J: is the encasement stiffness, σ_v: is the vertical stress, k: is the lateral pressure coefficient, l: is the length of encasement and $1/\lambda$: is the model-to-real-condition scale. The geotextile material stiffness under real conditions is usually less than about 2000 kN/m. In the current study, a scale factor of 1:10 was used based on the scale effect for selection of the reinforcing material stiffness. Specifications of the geotextile reinforcing material are given in Table 4.

2.2. Experimental Investigation (Frustum Confined Vessel)

Testing of a full-scale model that is conducted on-site produces the best results. However, the heavy cost of full-scale testing and the inability to repeat tests under exactly equal conditions have led to the popularity of small-scale physical model tests. A physical model is, in fact, a smaller version of an actual geotechnical structure.

For small-scale physical modeling of geotechnical structures such as stone columns, the scale selected is usually 1:10 so that the model is not unduly large to complicate working with it and not unduly small to cause a considerable difference in the behavior of the model and the prototype. In conventional small-scale physical models (1 g), limitations concerning stress conditions exist because the stress level is much lower than the actual stress.

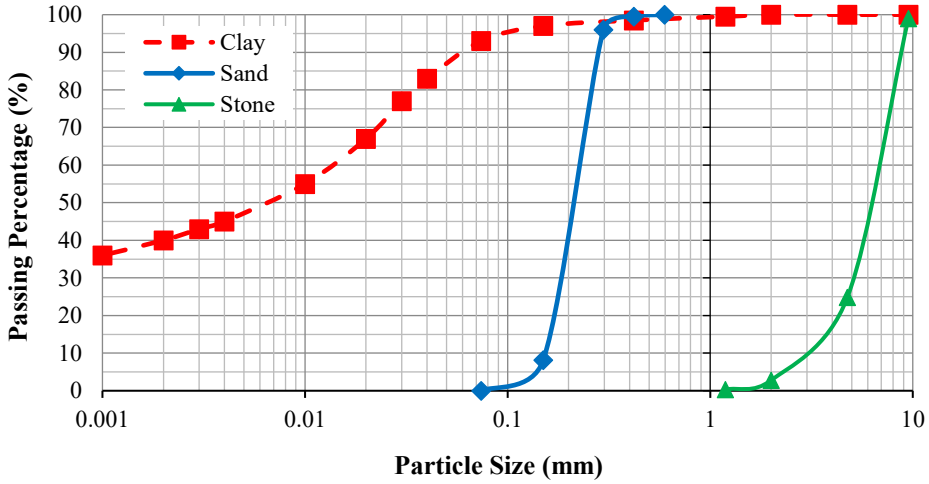

Fig. 1. Particle size distribution of Bandar-e-Anzali sand, clay and stone

Table 4. Properties of geotextile (manufacturer information)

Parameters	Unit	Value
Mass	g/m^2	500
Thickness	mm	3.6
Tensile strength (md)	kn/m	37
Tensile strength (cd)	kn/m	37
Tensile elongation (md)	%	55
Tensile elongation (cd)	%	50
Tensile modulus (md) at 55% tensile elongation	kn/m	67.3
Tensile modulus (cd) at 50% tensile elongation	kn/m	74

In conventional small-scale physical models (1 g), limitations concerning stress conditions exist because the stress level is much lower than the actual stress. Moreover, the small dimensions of a centrifuge model can complicate the installation of measurement tools having fixed volumes and weights, which would, thus, change the soil behavior (Mitchell, 1991). When using an FCV as a part of regular physical modeling (1 g), actual stresses can be applied. The FCV is a container in the shape of a frustum in which the sandy soil layer (bed soil materials) and fine-grained lens are prepared by layer by layer soil compaction.

In the current research, the FCV developed by Jassim et al. (2022) was used for geotechnical modeling. The FCV physical model used as the main container had an upper base diameter of 50 cm, lower base diameter of 170 cm and height of 100 cm. Seling and Mckee (1961) and Chummer (1972) showed that wedge failure occurring under a foundation will extend from the center to the sides up to a distance of 2 - 2.5 times that of the foundation width. In the current study, the distance of container walls to the foundation center was more than 3 times the loading plate width. The stone column had a constant diameter of 80 mm and length of 600 mm (constant length to diameter ratio of 7.5). To prevent deformation of the walls of the FCV boundaries of the physical model, the cylindrical container wall was composed of a rigid, thick steel sheet. The hydraulic pressure was transferred to the soil from the bottom of the test device through a flexible rubber membrane.

To this end, a compressor transferred compressed air to the air-water tank, thereby forcing the water into the flexible rubber membrane between the bottom of the device and the soil. This transferred the water pressure from the bottom of the device to the soil. Figure 2 is a 3D schematic view of the FCV device showing the dimensions of its parts and physical modeling.

Due to the specific geometrical shape of the container, along with the application of upward vertical pressure proportionate to the actual conditions from the bottom of the frustum, the horizontal stress increased as the depth increased along the device axis. Thus, the stress above the soil surface (in contact with the air) was 0 and increased proportionally as the depth increased. As stated, due to the geometrical shape of the device, the lateral pressure of the soil as a coefficient of the vertical stress and a function of the soil geotechnical properties also increased as the soil depth increased.

This means that the FCV device conditions were similar to the site conditions, which is a considerable advantage over other physical modelling devices. The distribution of vertical stress in the test device was evaluated experimentally (Mitchell, 1991).

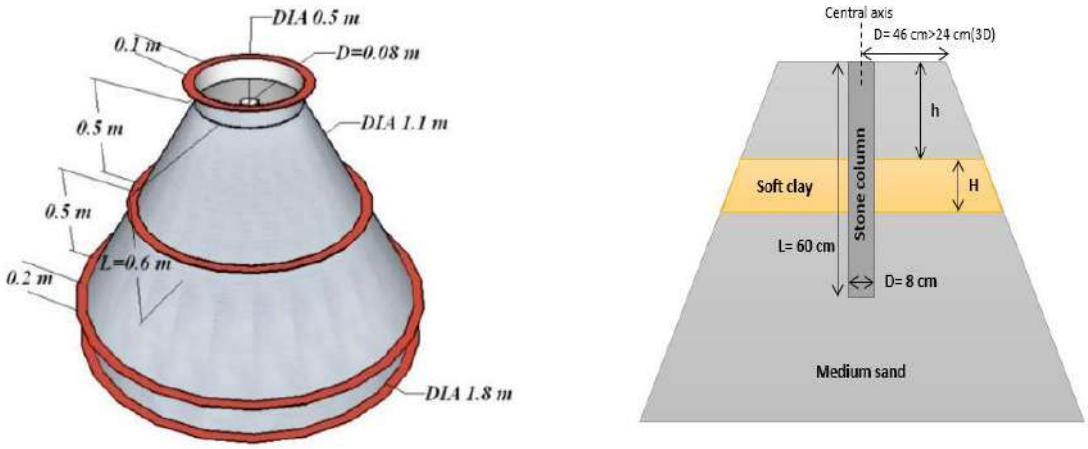

Fig. 2. Schematic profile of FCV and physical modeling

The loading setup comprised the loading device frame, a 5 ton (500 kN) hydraulic load application device and a circular loading plate (foundation) with a diameter of 180 mm. The data measurement system included a regular load cell, miniature load cell and two LVDTs. The data collection and recording system comprised an eight-channel data logger and a laptop (Figure 3). Two LVDTs are placed on the loading plate to record displacement.

A load cell with a capacity of 5000 kg revealed the total force applied to the loading plate. A miniature load cell with a capacity of 500 kg was placed on the stone column to determine the stone column bearing force and the stress distribution on the stone column to determine the stress concentration ratio. Loading was based on the force control with a velocity of 10 kg/min.

The loading plate (diameter of 18 cm and thickness of 3 cm) was made of rigid steel with its center positioned over the center of the stone column. All tests continued until the loading plate had settled for 45 mm. The capacity and combined error of load cell are 10 tf and 0.03%, although for the miniature load cell these are 500 kgf and 0.15% respectively. LVDT measurement stroke and linearity is also 100 mm and +/- 0.2%, respectively, based on the factory catalogs.

2.3. Experimental Plan

Ten small-scale tests were conducted. Control tests were also carried out to ensure the repeatability and consistency of the results and showed good compatibility between the findings. Table 5 presents a summary of the test plans. The models comprised a stone column with a constant length of 60 cm (L/D = 7.5) placed in a sandy bed containing a soft lens. The encased (ESC) and unreinforced (OSC) forms had different thickness to column diameter ratios (H/D) and lens depth to column-diameter ratios (h/D). Figure 2 shows the parameters of physical modeling.

Fig. 3. Overview of FCV apparatus and FCV accessories: a) FCV; b) Load cell; c) Mini-load cell, loading plate; and d) Data logger and laptop

Table 5. Outline of load tests on stone column

Test description	Reinforcement	Lens level (mm)	Lens thickness (mm)
O-200-80	-	200	80
O-200-160	-	200	160
E-200-80	geotextile	200	80
E-200-160	geotextile	200	160
O-280-80	-	280	80
O-280-160	-	280	160
E-280-80	geotextile	280	80
E-280-160	geotextile	280	160
unreinforced	-	-	-
reinforced	geotextile	-	-

3. Experimental Test Results

The load-settlement curves for unreinforced and reinforced stone columns were examined according to the lens placement level (-20 and -28 cm) for soft lenses with thicknesses of 8 and 16 cm and also in the absence of a soft lens. Figures 4 and 5 depict the behavior of unreinforced and reinforced stone columns placed in the sand bed with and without a lens at a level of -20 cm.

Figures 6 and 7 depict this behavior at a level of -28 cm. Comparison of Figures 4 and 5 shows that, when the 8 cm lens was positioned at -20 cm, the ultimate load on the unreinforced column was 42% greater than that for a lens thickness of 16 cm. The load bearing capacity of the reinforced column with an 8 cm soft lens was about 28% greater than of a 16 cm lens.

For the unreinforced column, the absence of a soft lens compared to the existence of an 8 cm lens at -20 cm in depth increased the bearing of the unreinforced column 2.1 fold and that of the reinforced column by 63%. Furthermore, the absence of a soft lens for the unreinforced column compared to the existence of a 16 cm soft lens at 20 cm in depth increased the bearing of the unreinforced column by 2.9 fold and that of the reinforced column by 2.1 fold.

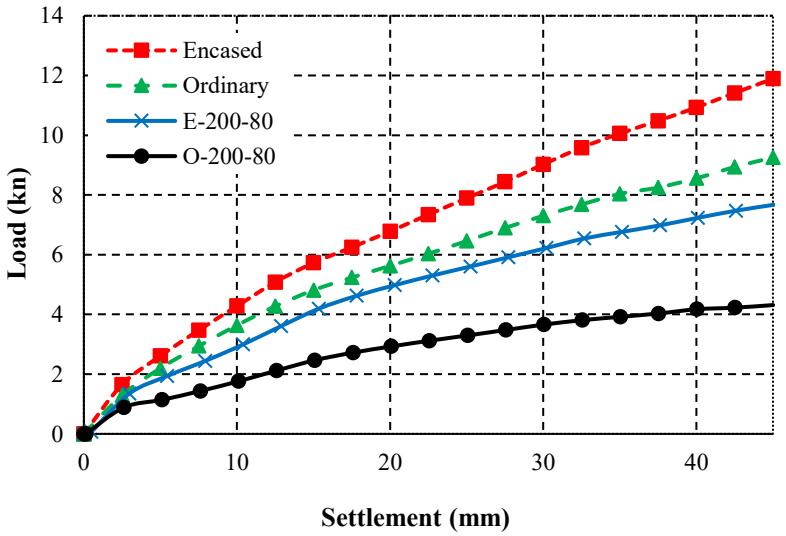

Fig. 4. Load-settlement of reinforced and unreinforced stone column with and without lens with a thickness of 8 cm embedded at -20 cm

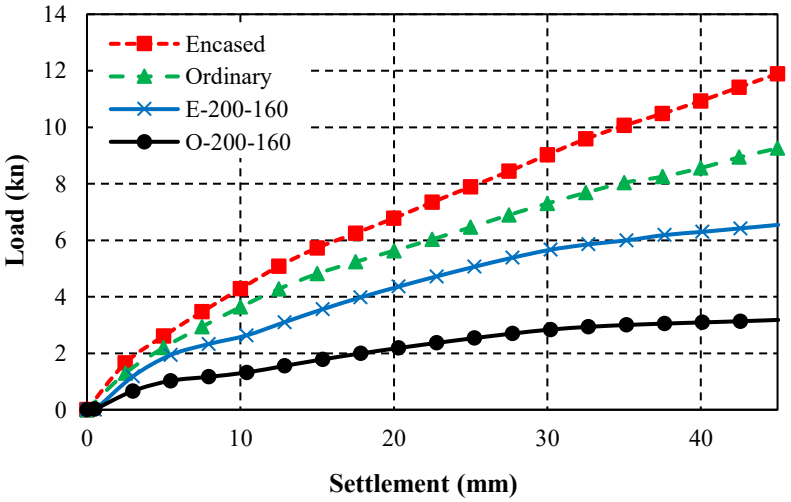

Fig. 5. Load-settlement of reinforced and unreinforced stone column with and without lens with a thickness of 16 cm embedded at -20 cm

Figures 6 and 7 reveal that, when the 8 cm soft lens is located at a depth of -28 cm, the ultimate loading capacity of the unreinforced column was 23% greater than for a 16-cm soft lens at a depth of -28 cm. The load bearing capacity of the reinforced column with an 8 cm soft lens at a depth of -28 cm increased by 11% compared to a 16 cm soft lens at a depth of -28 cm. In soil with no soft lens compared to soil with an 8 cm soft lens at -28 cm in depth, the load bearing capacity of the unreinforced column by increased by 62% and that of the reinforced stone column by 51%. For the unreinforced column, the absence of a soft lens compared to the existence of a 16 cm soft lens at -28 cm in depth increased the bearing capacity of the unreinforced column 2 fold and that of the reinforced column by 68%.

Compared to the soft lens located at -28 cm in depth, which is outside the possible bulging failure depth, the unreinforced column in soil with a soft lens at -20 cm in depth (the critical bulging failure depth of 2-3 times the diameter of the column) showed 36% lower load bearing capacities for both the 8 cm and 16 cm soft lenses. The reinforced column under similar conditions showed a 16% lower load bearing capacity, on average.

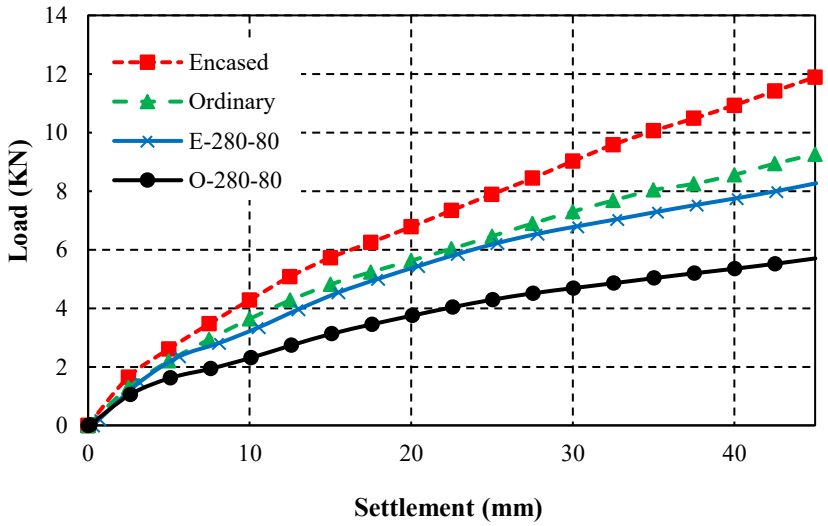

Fig. 6. Load-settlement of reinforced and unreinforced stone column with and without an 8 cm soft lens embedded at -28 cm

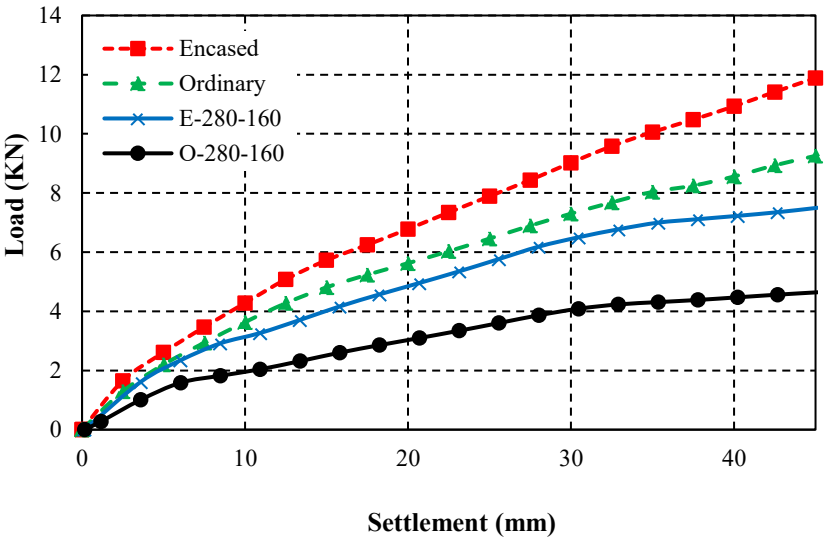

Fig. 7. Load-settlement of reinforced and unreinforced stone column with and without a 16 cm soft lens embedded at -28 cm

4. Numerical Modeling

4.1. Numerical Model Specifications

The current study examined the effect of a soft lens on the failure mode and defects in ordinary and geotextile-encased stone columns located in a saturated sandy bed containing a soft lens using a ABAQUS finite element software. The dimensions of the model are based on the site dimensions of the stone column which are being used in the bed containing the soft lens. The sand used to model the bed is the relatively loose poor graded sand.

Based on the model geometric conditions, axisymmetric modeling has been used. The behavior of sand, clay and stone column materials were also determined based on the Mohr-Coulomb elastic-perfectly plastic failure mode which is widely used for geotechnical analysis and flow law is also assumed to be independent.

The water table is at the same level as the natural ground level and linear elastic behavior is considered for geotextile materials (Ghazavi and Afshar, 2013, Afshar and Ghazavi, 2014, Mehrannia et al., 2018).

4.2. Model Geometry and Boundary Conditions

Figure 8 is a 2D schematic view of the properties of the axisymmetric model showing the dimensions and materials used for numerical model. The vertical displacement is applied to the rigid plate uniformly and the stone column failure criterion is assumed as 45 cm settlement (vertical displacement) rate in all the analyzed models.

This value is equal to 0.25 of the diameter of the loading plate, which is considered as the ultimate failure limit in some references (Ghazavi and Afshar, 2013). According to the behavior and related failure mechanism, in the stone columns analysis the soil interaction or interface with the stone column and/or geotextile is not considered (Afshar and Ghazavi, 2014).

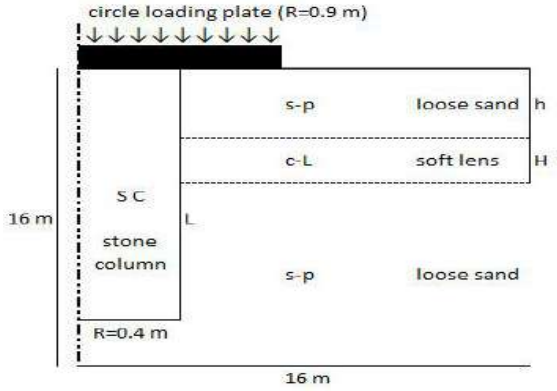

Fig. 8. 2D schematic of model properties

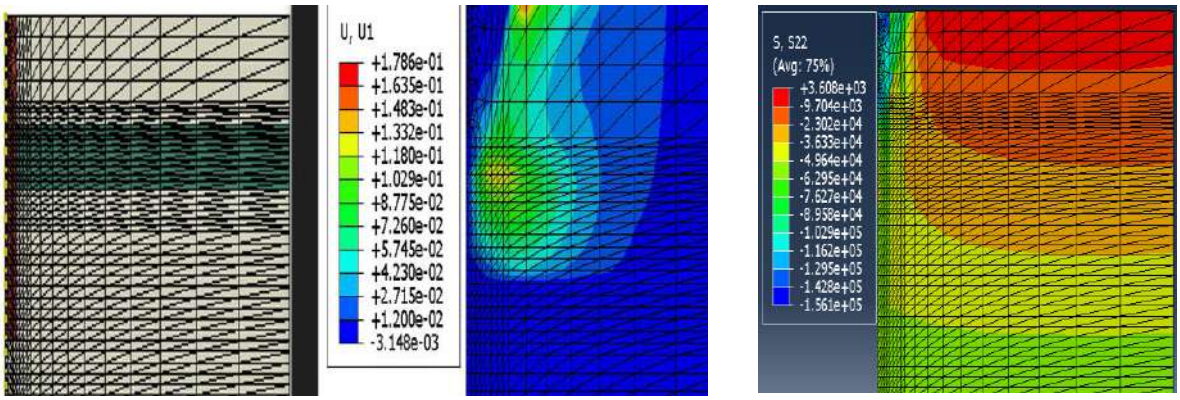

Fig. 9. Meshing of the model in the software, obtained horizontal displacement and vertical stress contours

Figure 9 shows an example of the meshing of the model in the software as well as the horizontal displacement and vertical stress counters in the area of the stone column.

4.3. Numerical Model Investigated and Validation

6 numerical models were analyzed on the whole, which 3 models were ordinary and 3 models were reinforced. In these models, a stone column with three lengths of 600, 800 and 1000 cm also a soft clay lens in level of -200 cm with thicknesses of 120 cm are considered. The analyzed models have been investigated on failure mode (bulging) and bearing capacity of the stone column. Conform to the conditions of the numerical models two physical models were also built with a scale of 1:10 in the FCV (Sedran, 1999) and the results were used to validate and calibrate the results of the numerical models. Considering the scale effect, the results of two physical models have been used to validate the results of numerical modeling. The materials specifications defined in the validation models are not similar to the same materials defined in the numerical models. Figures 10 and 11 show the load-settlement curves obtained from physical and numerical models with similar conditions, respectively.

5. Numerical Results

To illustrate the effect of stone columns length on the behavior of them, three different lengths of 600, 800 and 1000 cm have been assumed for the stone column and the behavior of the unreinforced and reinforced column with geotextile in variable states of alignment and thickness of the soft lens has been investigated.

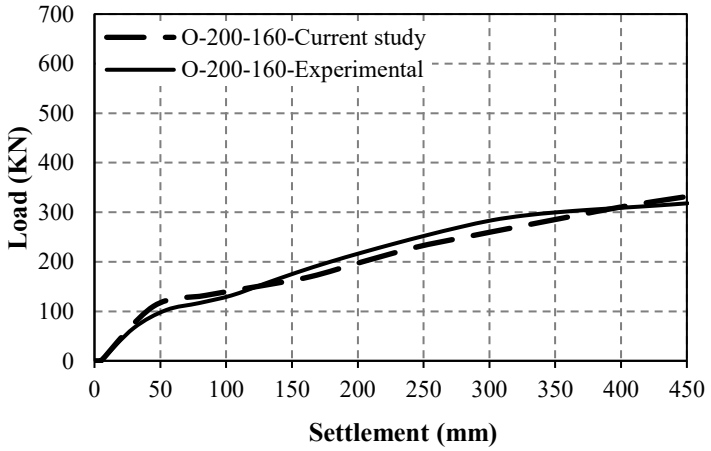

Fig. 10. Load-settlement of ordinary stone column in lens with a thickness of 160 cm embedded at -200 cm

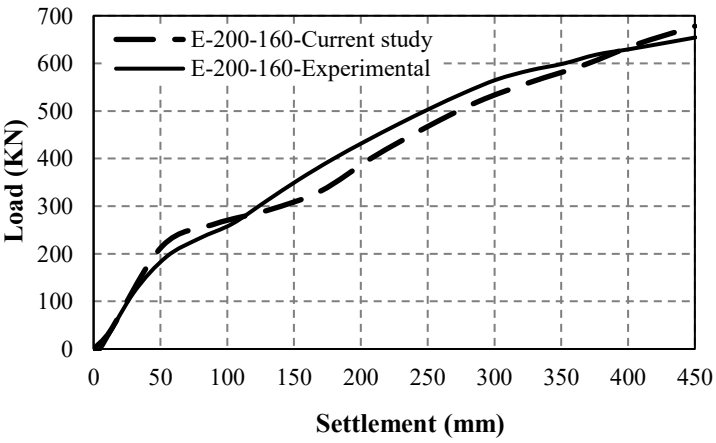

Fig. 11. Load-settlement of reinforced stone column in lens with a thickness of 160 cm embedded at -200 cm

It can be seen in Figures 12 and 13 that changing the length of the column has no effect on the maximum lateral displacement (bulging) and the failure of the stone column, and the stone column with different lengths suffers bulging failure in the range of soft lens placement. Moreover, reinforcing stone column with geotextile has reduced the maximum bulging by 60%.

Furthermore, based on Figures 14 and 15, it can be seen that, due to the occurrence of bulging, changing the length of the column did not affect its bearing capacity, and increasing the length of the stone column did not increase its bearing capacity. It is clear that, reinforcing stone column with geotextile increases the bearing capacity of the stone column by 32%.

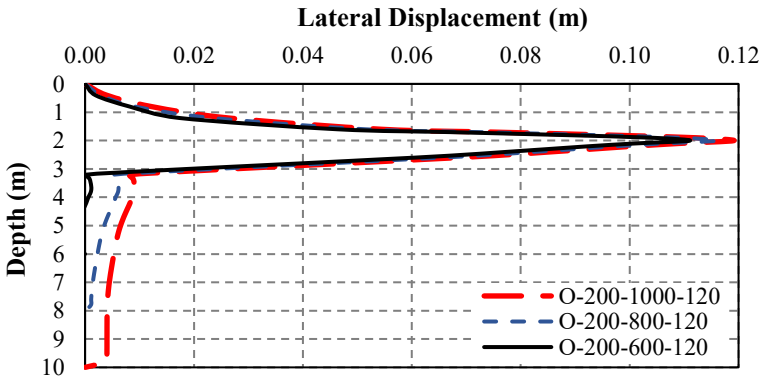

Fig. 12. Lateral displacement along ordinary stone column with a thickness of 120 cm embedded lens at -200 cm level

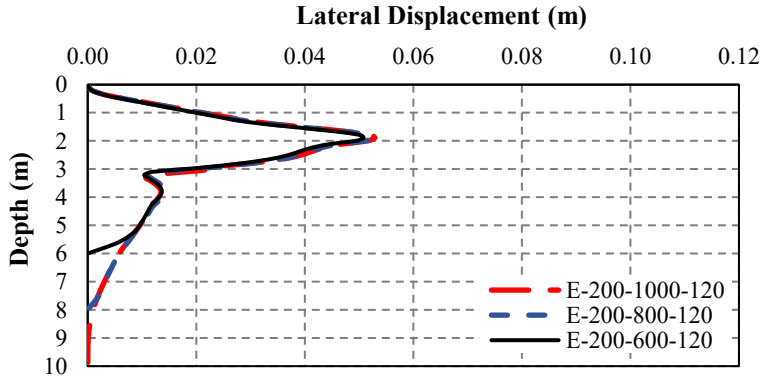

Fig. 13. Lateral displacement along reinforced stone column with a thickness of 120 cm embedded lens at -200 cm level

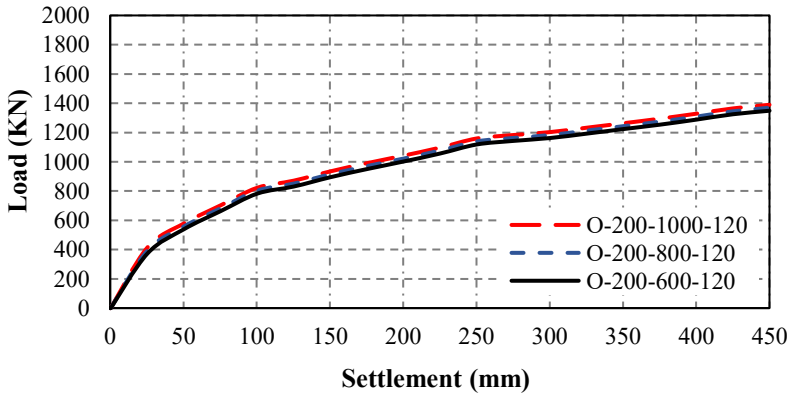

Fig. 14. Load-settlement of ordinary stone column with a thickness of 120 cm embedded lens at -200 cm

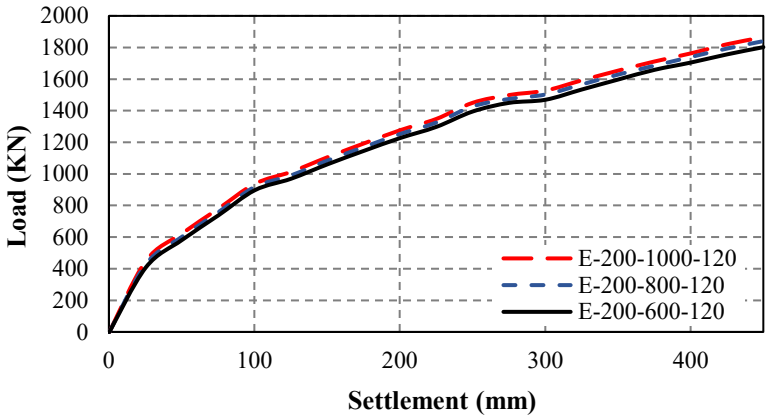

Fig. 15. Load-settlement of reinforced stone column with a thickness of 120 cm embedded lens at -200 cm

6. Conclusions

The experimental investigation represents the inaugural effort to analyze the behavior of stone columns, both with and without reinforcement, situated in sandy ground containing a soft weak lens. This investigation was conducted experimentally utilizing a FCV and also numerically using ABAQUS software. The outcomes gleaned from the load-settlement graphs have yielded the ensuing findings:

- The presence of a soft lens at depths ranging from 1 to 4 times the diameter of the column substantially reduced the bearing capacity of the columns. Notably, a 16 cm thickness of the soft lens accentuated this adverse effect more prominently compared to a 8 cm thickness. The augmentation in bearing capacity for the unreinforced stone columns exhibited an almost twofold increase with diminishing soft lens thickness, surpassing the enhancement observed in the reinforced stone columns.
- A 8 cm clayey lens positioned at a depth of -20 cm led to a twofold decrease in the bearing capacity of both unreinforced and reinforced stone columns. Conversely, when a soft lens was located at -28 cm in depth, the bearing capacity of the stone columns witnessed a 16% increment.
- Elevating the thickness of the soft lens from 8 to 16 cm at a depth of -20 cm precipitated a decline in bearing capacity, affecting unreinforced and reinforced stone columns by approximately 42% and 27%, respectively. Nevertheless, at a depth of -28 cm, augmenting the soft lens thickness translated to a 23% and 11% rise in bearing capacity for unreinforced and reinforced stone columns, respectively.
- With the existence of soft lens increasing the length of the stone column has no effect on reducing the maximum radial displacement and its failure mode. Also, the stone column with different lengths, with the existence of soft lens has bulging failure.
- With the existence of soft lens, increasing the length of the stone column has no effect on increasing of bearing capacity, and increasing the length of the stone column does not increase its bearing capacity. Only reinforcing stone column with geotextile increases the bearing capacity. According to the results of this research, if stone columns are used to improve ground where there is a possibility of very weak lenses in a depth of less than 5 meters from the surface of the earth, special considerations should be taken into account in the design of stone columns. In these cases, it is recommended to use an encasement stone column to prevent bulging failure.

7. References

Afshar, J.N. and Ghazavi, M. (2014). "Experimental studies on bearing capacity of geosynthetic reinforced stone columns", *Arabian Journal for Science and Engineering*, 39, 1559-1571, https://doi.org/10.1007/s13369-013-0709-8.

Chummar, A. (1972). "Bearing capacity theory from

experimental results", *Journal of the Soil Mechanics and Foundations Division*, 98(12), 131-1324-1, https://doi.org/10.1061/JSFEAQ.0001816.

Danish, A., Taib, S.N.L., Ayadat, T. and Hasan, A. (2021). "Numerical investigation on the performance of stone columns under raft foundation in soft clayey soils", *IOP Conference Series*, *Materials Science and Engineering*, IOP Publishing, 1101, 012015, https://10.1088/1757-899X/1101/1/012015.

Fattah, M.Y., Shlash, K.T. and Al-Waily, M.J.M. (2011). "Stress concentration ratio of model stone columns in soft clays", *Geotechnical Testing Journal*, 34(1), http://doi.org/10.1520/GTJ103060.

Ghazavi, M. and Afshar, J.N. (2013). "Bearing capacity of geosynthetic encased stone columns", *Geotextiles and Geomembranes*, 38, 26-36, https://doi.org/10.1016/j.geotexmem.2013.04.003.

Gu, M., Han, J. and Zhao, M. (2020). "Three-dimensional DEM analysis of axially loaded geogrid-encased stone column in clay bed", *International Journal of Geomechanics*, 20(3), 04019180, https://doi.org/10.1061/(ASCE)GM.1943-5622.0001595.

Gu, M., Mo, H., Qiu, J., Yuan, J. and Xia, Q. (2022). "Behavior of floating stone columns reinforced with geogrid encasement in model tests", *Front Mater*, 9, 980851, https://doi.org/10.3389/fmats.2022.980851.

Hajiazizi, M. and Nasiri, M. (2019). "Experimental and numerical investigation of reinforced sand slope using geogird encased stone column", *Civil Engineering Infrastructures Journal*, 52(1), 85-100, https://doi:10.22059/ceij.2019.253069.1468.

Jassim, A., Ganjian, N. and Eslami, A. (2022). "Design and fabrication of frustum confining vessel apparatus for model pile testing in saturated soils", *Innovative Infrastructure Solutions*, 7(5), 1-11, http://doi.org/10.1007/s41062-022-00877-x.

Lone, U.R., Dar, M.H. and Ahanger, M.Y. (2015). "Effect of l/b ratio of stone column on bearing capacity and relative settlement of sandy soil (an experimental study)" , *International Journal of Civil Engineering and Technology*, 6(1), 55-61, https://iaeme.com/masteradmin/journal_uploads/ijciet/volume6issue1/ijciet0601007.pdf.

Mehrannia, N., Kalantari, F. and Ganjian, N. (2018). "Experimental study on soil improvement with stone columns and granular blankets", *Journal of Central South University*, 25, 866-878, https://doi.org/10.1007/s11771-018-3790-z.

Mitchell, R. (1991). "Centrifuge modelling as a consulting tool", *Canadian Geotechnical Journal*, 28(1), 162-167, https://doi.org/10.1139/t91-018.

Mohanty, P. and Samantha, M. (2015). "Experimental and numerical studies on response of the stone column in layered soil", *International Journal of Geosynthetics and Ground Engineering*, 1(27), 1-14, https://doi.org/10.1007/s40891-015-0029-z.

Nayak, N. (1983). "Recent advances in ground improvements by stone column", *Proceedings of Indian Geotechnical Conference,* Madras, IGC 83, https://www.issmge.org/uploads/publications/1/33/1989020155.pdf.

Nazariafshar, J., Shafiee, A. and Mehrannia, N. (2022). "Effect of construction method on the performance of ordinary and geotextile-encased stone columns", *Iranian Journal of Science and Technology*, *Transactions of Civil Engineering*, 46, 4751-4761, https://doi.org/10.1007/s40996-022-00888-9.

Pereira, P.G.D.S., Pachenco, M.P. and Lima, B.T. (2021). "Numerical analysis of soft soil improved with stone column technique", *REM-International Engineering Journal*, 74, 319-327, https://doi.org/10.1590/0370-44672020740062.

Prasad, S.S.G., Vasavi, C. and Sai, K.P. (2017). "Behavior of stone column in layered soils using geotextile reinforcement", *International Journal of Civil Engineering*, 8(8), 453-462, https://www.academia.edu/34738935/behaviour_of_stone_column_in_layered_soils_using_geotextile_reinforcement.

Saxena, S. and Roy, L.B. (2022). "Suitability analysis of stone column materials with plaxis", *Engineering*, *Technology and Applied Science Research*, 12(2), 8421-8425, https://doi.org/10.48084/etasr.4761.

Schaefer, V., Berg, R., Collin, J., Christopher, B., DiMaggio, J., Filz, G., Bruce, D. and Ayala, D. (2017). *Ground modification methods-reference manual-volume ii*, US Department of Transportation Federal Highway Administration, Washington, DC, USA, https://geotechnical-library.geotill.com/ground-modification-methods-reference-manual-volume-ii-fhwa-nhi-16-028.pdf.

Sedran, G. (1999). "Experimental and analytical study of a frustum confining vessel", http://hdl.handle.net/11375/6498.

Selig, E. and Mckee, K. (1961). "Static and dynamic behavior of small footings", *Journal of the Soil Mechanics and Foundations Division*, 87(6), 29-45, https://doi.org/10.1061/JSFEAQ.0000378.

Shahraki, M., Rafiee-Dehkharghani, R. and Behnia, K. (2018). "Three-dimensional finite element modeling of stone column-improved soft saturated ground", *Civil Engineering Infrastructures Journal*, 51(2), 389-403, https://doi.org/10.7508/ceij.2018.02.009.

Shamsi, M., Ghanbari, A. and Nazariafshar, J. (2019). "Behavior of sand columns reinforced by vertical geotextile encasement and horizontal geotextile layers", *Geomechanics and Engineering*, 19(4), 329-342, https://doi:10.12989/gae.2019.19.4.329.

Civil Engineering Infrastructures Journal 2025, 58(1): 49-70
DOI: 10.22059/ceij.2024.364758.1955

RESEARCH PAPER

Parametric Analysis of Axially Loaded Partially Concrete-Filled Cold-Formed Elliptical Columns Subjected to Lateral Impact Load

Ghandi, E.[1*], Mohammadi Rana, N.[2] and Esmaeili Niari, SH.[1]

[1] Associate Professor, Faculty of Technical and Engineering, University of Mohaghegh Ardabili, Ardabil, Iran.
[2] M.Sc., Faculty of Technical and Engineering, University of Mohaghegh Ardabili, Ardabil, Iran.

Received: 04 Sep. 2023; Revised: 28 Nov. 2023; Accepted: 11 Dec. 2023

ABSTRACT: This research investigates the dynamic behavior of hollow and Partially Concrete-Filled Cold-Formed Steel Tubular (PCFCFST) columns that have elliptical cross-sections under simultaneous loading of dynamic lateral impact load and static compressive axial load. Utilizing Finite Element Analysis (FEA) by the ABAQUS is studied. In order to confirm the numerical modeling's precision, the study outcomes are compared to the outcomes of former experimental and numerical investigations. The effect of various factors namely aspect ratio, axial load ratio, impact angle, steel tube wall thickness, and concrete filling ratio on the performance of PCFCFST columns has been examined. The numerical analysis results indicate that specimens with higher concrete filling ratios show greater performance than hollow specimens. The columns' failure modes are significantly influenced by the impact angle and axial load ratio, particularly when the column aspect ratio is low. Surging the steel tube wall thickness from 2.25 mm to 4 mm decreases the maximum displacement by approximately 70%.

Keywords: Elliptical Section, Cold-Formed Steel, Lateral Impact, Partially Concrete-Filled Column.

1. Introduction

Recently, Concrete-Filled Steel Tubular (CFST) columns have become broadly utilized because of their ability to reduce the structures' weight, especially in docks, bridge piers, subway stations, and high-rise buildings. Fire resistance is an additional benefit of concrete-filled steel sections.

Steel sections have low fire resistance due to their definite heat capacity and high conductivity. The infilled concrete is like a sink, preventing temperature surges, and also the concrete has poor conductivity that makes a high fire resistance (Rahnavard et al., 2022a; Craveiro et al., 2022; Moradi et al., 2021). Furthermore, building cost-effective and economical structures is one of the aims of structural design, while completely filling the column with concrete is an inefficient activity. Accordingly, in certain structures, concrete fills just the portions that are to be expected to be hit by impact, unless additional strength and ductility, particularly concerning earthquakes, are taken into account (Rondal, 2000; Yu, 2000). Today, the use of Cold-Formed Steel (CFS) cross-sections

* Corresponding author E-mail: ghandi@uma.ac.ir

because of their exceptional benefits, namely their high strength to weight ratio, ductility, fast fabrication, and installation, have been more considered in CFST columns. When the steel component is utilized as a part of the composite column, it indicates more compression strength compared to when it is utilized alone. This enhancement is because of the protection provided by the concrete filling, which prevents the cold-formed steel component from experiencing buckling deformation (Rahnavard et al., 2022b; Rahnavard et al., 2023). By elliptical hollow sections as fairly novel sections, both structural engineers and architectural designers are given further selections for having improved structural and aesthetics of the structure, respectively.

The bending capacity in these sections is more than the Circular Hollow Section (CHS) with a similar weight and size. These types of sections are also considered economical (Yang et al., 2017). Some investigations have been accomplished on CFT columns against impact loads. Yousuf et al. (2014) carried out numerical and experimental research on stainless steel columns and concrete-filled steel mild exposed to impact loading and transverse static with a pre-compressive axial load. The results indicated that the stainless steel specimens illustrate enhanced energy-dissipating features and higher strength in comparison with the mild steel columns.

Wang et al. (2015) presented a collective experimental, theoretical, and numerical research on the transverse for impact performance steel pipes filled with ultra-lightweight cement composite. Aghdamy et al. (2015) presented an investigation of the outcome of axially loaded concrete-filled cold-formed steel tube columns under lateral impact load with explicit nonlinear Finite Element (FE) methods. In general, they concluded that the CFST columns impact response is a significant factor that is heavily influenced by the slenderness ratio and tube thickness to diameter ratio (t/D).

Yang et al. (2015) studied a numerical and experimental investigation of steel structures filled with Recycled Aggregate Concrete (RAC) under lateral impact loading behavior. The findings indicated that square RAC-filled steel tubular specimens have nearly equivalent lateral impact resistance as normal CFST counterparts. Shakir et al. (2015) investigated recycled and normal aggregate concrete-filled steel tube columns dynamic behavior exposed to lateral projectile impact and the influence of the Carbon Fiber-Reinforced Polymer (CFRP) jacketing on the structural performance of those columns.

Alam et al. (2016) performed numerical simulations to assess the influence of CFRP on concrete-filled steel tubular columns under vehicle impact loading. The dynamic impact analysis outcomes showed that adhesively attached CFRP sheets offer strengthened columns' enhanced impact resistance capacity by lessening lateral displacement by approximately 40% compared to normal CFST columns. Also, Han et al. (2019) examined the performance of stainless steel tubular columns and joints filled with concrete. They specifically focused on how these structures behaved when subjected to lateral and axial impact loads at both normal and elevated temperatures.

Zhu et al. (2018) examined the effect of lateral impact loads on cold-formed rectangular hollow steel columns filled with self-compacting concrete under lateral impact loads in both the front and corner directions. The results presented that the partially concrete-filled steel tubular specimens had much-improved behavior than the rectangular hollow steel tubular specimens. The concrete filling height influenced the failure mode remarkably, particularly when the specimens were verified under high-impact energy.

The impact direction and energy remarkably influenced the specimen is impact resistance. Xu et al. (2018) numerically investigated the anti-impact behavior of partially concrete-filled steel

tubular columns under lateral impact loading. The outcomes of parameter analysis indicated that the PCFST columns anti-impact performances remarkably surged when either the yield strength of steel or the concrete filling height rose significantly.

Zhang et al. (2019) examined the circular CFT columns' performance under compressive axial load and lateral impact loading. They concluded that lateral impact has adverse influences on the circular CFST columns' residual ultimate axial capacity. Residual ultimate axial capacity declines as impact energy surges and impact location approaches the end of the specimen. Furthermore, research has shown that the compressive strength of concrete might mitigate the negative effects of the impact site on the remaining maximum axial capacity. Wan et al. (2017) examined the lateral impact loading's effect on the residual axial strength of CHS columns. The outcomes designated that lateral impact significantly influences the axial compression behavior of CHS columns. When the impact energy increases, the residual axial strength is reduced, and the lateral plastic deformation increases. Additionally, the outcomes indicate that CHS columns axial bearing capacity is significantly influenced by the impact location.

Du et al. (2018) investigated the remaining axial bearing capacity of Concrete-Filled Circular Steel Tubular Columns (CFCSTCs) following transverse impact stress. In some studies, CFT columns with elliptical cross-sections have been studied. The outcomes indicated that the impact height and the outer diameter to thickness of the outer steel tube ratio have obvious impacts on the CFCSTCs axial compression behavior. The samples failure mode is usually local buckling. Furthermore, the maximum lessening of the columns axial bearing capacity attains approximately 35% in comparison with that of untreated columns.

The numerical and experimental investigations carried out by Liu et al. (2017) refer to the investigation of the behavior of concrete-filled cold-formed elliptical sections with different aspect ratios under axial compression load. The findings demonstrated that the design approach advocated in the Chinese Standard (GB50936-2014), as well as the design strategy for circular CFST columns in EC4, yielded precise forecasts. Wang et al. (2018) considered the behavior of elliptical concrete-filled thin-walled steel tube columns (ECFT) under compressive axial load by FE modeling with ABAQUS software. The analysis outcomes indicated that the confinement factor influences the axial force-axial displacement curves of the elliptical concrete-filled thin-walled steel tube stub columns. Finally, two simplified design approaches were proposed to predict the axial compressive capacities of elliptical concrete-filled thin-walled steel tube columns, on the basis of the unified theory approach and simple superposition approach.

Numerous numerical and experimental researches have been executed on CFT columns regarding different sections and loads. Nevertheless, as can be perceived from the above-mentioned investigations, the performance of elliptical hollow and PCFCFST columns under simultaneous loading of lateral impact load and axial static compressive load is not studied. Consequently, the lateral impact response of elliptical hollow and PCFCFST axially loaded columns by considering the effect of different factors, namely impact shape, impact velocity, impact block mass, impact block size, impact angle, and height were investigated by Mohammadi Rana et al. (2021).

In this paper, the previous work of Mohammadi Rana et al. (2021) is extended by studying the effect of aspect ratio, axial load ratio, concrete filling ratio, and steel tube wall thickness on the response of elliptical PCFCFST columns under simultaneous loading of lateral impact load and axial static compressive load.

ABAQUS, as the FE software (ABAQUS/CAE 6.13) is used for numerical modeling and investigating the effect of various parameters.

2. Numerical Modeling

Figure 1 depicts the characteristics of the studied PCFCFST columns with elliptical cross-sections under simultaneous loading of lateral impact load and axial static compressive load. The column consists of a steel tube with an elliptical cross-section and a concrete core with height h_c. The column is first subjected to a compressive axial load *N*, and then a lateral impact load is employed at the height of h_0 from the lower support of the column. The lateral impact is applied by an impact block. The performance of the columns is investigated by two types of analysis (Static/General and Dynamic/Explicit).

Static/General analysis is utilized to specify the columns under axial compressive loading's ultimate axial load capacity. The lateral impact loading is determined by Dynamic /Explicit analysis. Both types of analysis are performed by considering geometric and material nonlinearities. The features of concrete material in ABAQUS software are defined by 2 types of behavior: plastic and elastic.

The elastic properties of concrete were characterized using Young's modulus and Poisson's ratio. The present investigation employed self-compacting concrete, as described by Liu et al. (2017, for the purpose of filling cold-formed steel tubes. For replicating the nonlinear performance of concrete in ABAQUS, the Concrete Damage Plasticity (CDP) model was also assumed. Specifications of concrete and cold-formed steel materials and details of their modeling has been given in Mohammadi Rana et al. (2021). The eight-node hexagonal solid element (C3D8R) is utilized to model core concrete, stiffeners, and end plates involved in columns. In order to model the steel tube, the 4-node shell element (S4R) with 6 degrees of translational and rotational freedom in every node and reduced integration has been used.

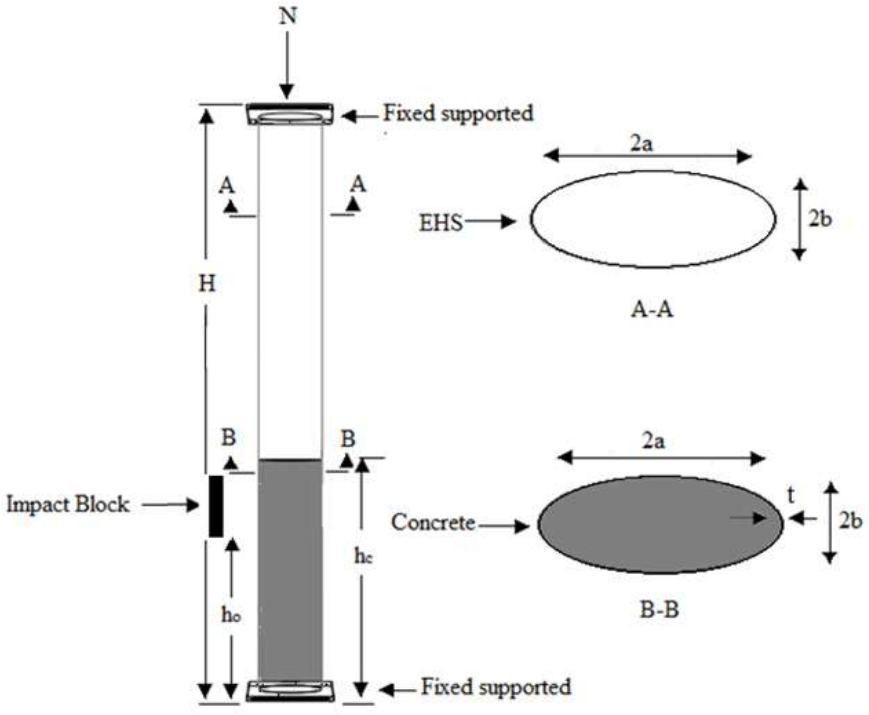

Fig. 1. Characteristics of the studied columns: a) The general view of the column at height (*H*: is the total length of the steel tube, h_c: is the concrete filling height, and h_0: location of lateral impact load); and b) Cross-section of the studied columns

The R3D4 solid stiff element is utilized to simulate the impact block. In a FEA, the contact conditions allow the force to be transferred from one part of the model to another. In composite columns, the force is transmitted between concrete and steel through contact between these two materials. The surface-to-surface contact element is used to model the contact between the concrete part and the steel tube and between the column and the impact block. This element defines the contact between a deformable surface and a rigid surface or between 2 deformable surfaces.

The parameters utilized to apply the contact features between steel and concrete are as follows:

(Normal behavior): Considering the hard contact between the concrete and the steel surface, the penetration of the concrete surface into the steel surface is allowed to a minimum and does not allow the transfer of tensile stress during the interaction, and only the pressure on the two surfaces transfer by contact, and when it separates, there is no pressure between the two surfaces.

(Tangential Behavior): The Columbus friction model was utilized to model the tangential and sliding behavior of the two surfaces. The penalty option is defined to determine the friction factor between steel surfaces and concrete. The friction factor between steel surfaces and concrete is considered as 0.47 (Baltay and Gjelvik, 1990). The initial geometrical imperfection was considered for steel hollow sections as the lowest buckling mode shape with an amplitude of t_s/100, in which t_s: is defined as the tube wall thickness. In the FE model, residual stresses were not calculated and were not regarded.

The effect of local imperfections and residual stress for CFST stub columns are insignificant because of the inner concrete, and consequently, these factors were not considered in the Finite Element (FE) model (Liu et al., 2017). In order to simulate boundary conditions, total degrees of freedom at the lower end plate were limited, and the load transfer in the axial direction was carried out by rigid plates. Rectangular end plates with a uniform thickness of 20 mm have been utilized in entire specimens.

In this paper, the columns are exposed to axial loading without eccentricity. The compressive axial load is applied as a displacement control method in Static/General analysis. A rectangular stiff body with dimensions of 150 mm × 400 mm and 3750 J impact energy, which is located at a lateral distance of 300 mm from the columns, was used for impact block modeling. The position of lateral impact is $\frac{1}{3}$ of column height. For applying the impact load on the column, the impact block is modeled with an initial mass and velocity.

The velocity option in the Predefined field is used to define the initial velocity of the impact. For this purpose, a constant mass impact block weighing 300 kg is utilized to apply a consistent impact load at a velocity of 5 m/s.

3. Validation of the FE model

To ensure the precision of numerical modeling, first, a PCFCFST column with a rectangular cross-section under lateral impact loading (first model: Zhu et al. (2018)) and then a PCFCFST column with elliptical cross-section under axial compression loading (second model: Liu et al. (2017)) are modeled in ABAQUS, and the results of numerical modeling are compared with the outcomes of the former studies in mentioned references. The first model has a rectangular cross-section with rounded corners, which has been impacted once by a lateral impact load from the front and again from the corner. The total height of the column is 1500. The impact block has an average velocity of 6.5 m/s, which hits the column at a height of 320 mm.

Details of the verification of the first model are given in the authors' former work (Mohammadi Rana et al., 2021). As an example of the verification results of this model, displacement - time curves of PCFCFST specimen with the concrete

filling height of 400 mm under front impact load and PCFCFST specimen with the concrete filling height of 700 mm under corner impact load in numerical modeling and experimental tests are compared in Figure 2 and Table 1. Figure 2 and Table 1 indicate a strong concurrence between the numerical results of the present study and the experimental and numerical findings of Zhu et al. (2018), affirming the precision of the numerical modeling employed in this study.

The observed difference between the experimental and numerical findings can be related to the friction between the devices and the interference of environmental factors in the laboratory conditions, which are not considered in the numerical modeling. The second model is a concrete-filled cold-formed steel elliptical column under a compressive axial load. The aspect ratios (a/b) of cold-formed elliptical steel sections vary from 1 to 2.5. The ratio between the cross-sectional area of the steel tube and the cross-sectional area of the concrete core ($\alpha_s = A_s/A_c$) is defined between 5 and 12%. Cold-formed steel sheets with a thickness of 2.75 mm have been used for the column tubes. Figure 3 depicts the geometric model of the column that is created in ABAQUS. In this model, the axial load is applied as a displacement control at the center of the upper rigid plate, in the direction of the column axis.

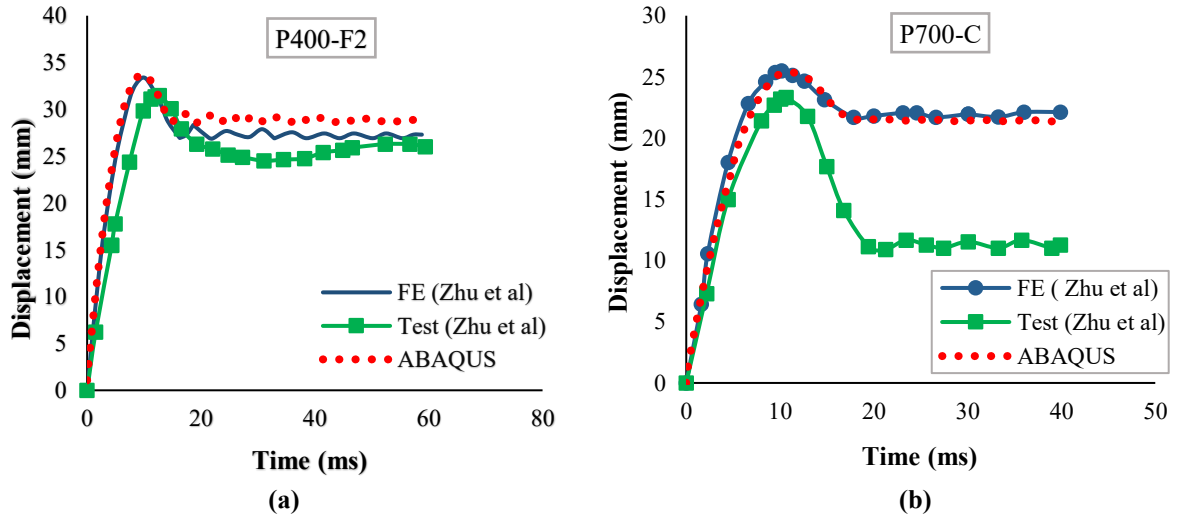

Fig. 2. Displacement - time curves of PCFCFST specimens: a) Concrete filling height of 400 mm under front impact load; and b) Concrete filling height of 700 mm under corner impact load

Table 1. Quantitative comparison between Zhu et al. (2018) results and ABAQUS results of this research

Specimen	Peak displacement (mm)					t_d (ms) (duration from initial impact to the Δ_{max})				
	Test[a] Zhu et al. (2018)	FE[b] Zhu et al. (2018)	ABAQUS[c]	Error (%) (c-a)/a	Error (%) (c-b)/b	Test[d] Zhu et al. (2018)	FE[e] Zhu et al. (2018)	ABAQUS[f]	Error (%) (f-d)/d	Error (%) (f-e)/e
P400-F2	31.49	33.59	33.75	7.20	-0.48	12.68	10.89	11.00	-13.9	1.07
P700-C	32.60	33.40	31.28	-3.41	-5.73	10.62	10.17	11.00	3.49	8.14

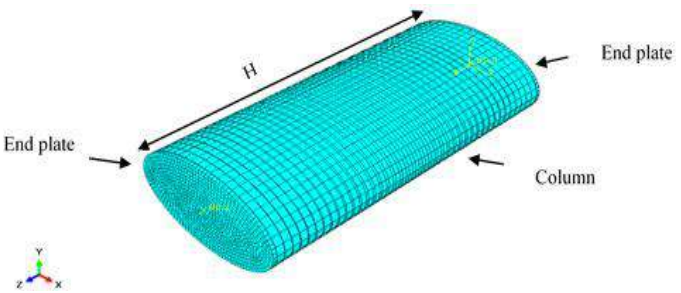

Fig. 3. CFT column meshes modeled in ABAQUS

The dimensions of every mesh size in the model range from 5 to 10 mm. The steel tube and concrete were modeled, in turn, with four-nodded shell element S4R and eight-nodded solid element C3D8R. The dimensions of the cold-formed hollow steel column are 2a = 203.3 mm, 2b = 101.6 mm (CH20-a) and H = 407 mm. Also, the concrete-filled column with the same dimensions as the hollow column (C20-8-a) and with α_s ratio equal to 8% is considered. The distinction between the experimental and numerical outcomes of Liu et al. (2017) with the numerical results of this paper in the form of axial displacement - load curves in Figure 4 and the difference ratio in Table 2 shows a qualified agreement between the outcomes.

4. Parametric Studies

The behavior of PCFCFST columns under simultaneous compressive lateral impact and axial load depends on many parameters.

In this paper, the influence of aspect ratio (R = a/b), compressive axial load ratio (N = n/$N_{u,F}$) (n: is the compressive axial load on the column, $N_{u,F}$: is the ultimate axial compressive capacity of the partially concrete-filled steel column), the impact angle (A), the concrete filling ratio (P) and steel tube thickness (T) are investigated on the behavior of the mentioned columns.

In this study, the columns will first be exposed to compressive axial load to obtain the ultimate axial bearing capacity of the columns with diverse filling ratios. The columns will then be exposed to lateral impact loads simultaneously with the axial compressive load.

Figure 5 depicts the impact angles. For investigating the effect of different factors on the behavior of PCFCFST columns, an entire 51 specimens have been investigated, the naming pattern of which is given in Figure 6. The general features of the specimens are illustrated in Table 3. In the current paper, the column has an entire height of 3600 mm.

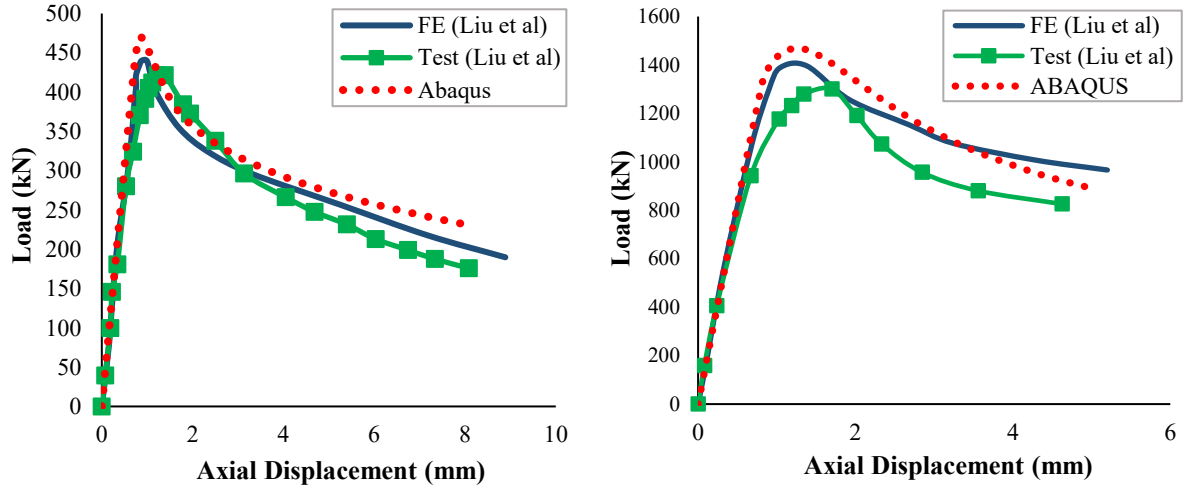

Fig. 4. Axial displacement - load curves of elliptical hollow column: a) (CH20-a); and b) (C20-8-a)

Table 2. Quantitative comparison between Liu et al. (2017) results and ABAQUS results of this paper

Specimen	Peak load (kN)			Error (%)		Δu (mm) (displacement at peak load)			Error (%)	
	Test[a] Liu et al. (2017)	FE[b] Liu et al. (2017)	ABAQUS[c]	(c-a)/ a	(c-b)/b	Test[d] Liu et al. (2017)	FE[e] Liu et al. (2017)	ABAQUS[f]	(f-d)/d	(f-e)/e
CH20-a	439.81	421.29	470.48	11.58%	6.89%	1.23	0.87	0.83	-32.50	-4.78
C20-8-a	1300.46	1396.4	1466.52	12.76%	5.01%	1.78	1.38	1.34	-24.71	-3.33

4.1. Static Analysis of the Columns to Specify the Ultimate Bearing Capacity

This section's goal is to specify the PCFCFST columns' ultimate compressive bearing capacity. First, the analysis of entirely concrete-filled elliptical steel columns under compressive axial load is performed, and the columns axial bearing capacity has been obtained. Then, to ensure the precision of the analysis, the calculated axial bearing capacity is compared with Eq. (1) result that computes the columns' axial bearing capacity based on the EC4 (Zhang et al., 2019):

$$N_{u.EC4} = f_y A_s + \acute{f}_c A_c \quad (1)$$

where f_y and $\acute{f}_c$: are the yield strength of steel and the compressive strength of concrete, respectively. Also, A_s and A_c: are the steel and concrete's cross-sectional area, respectively.

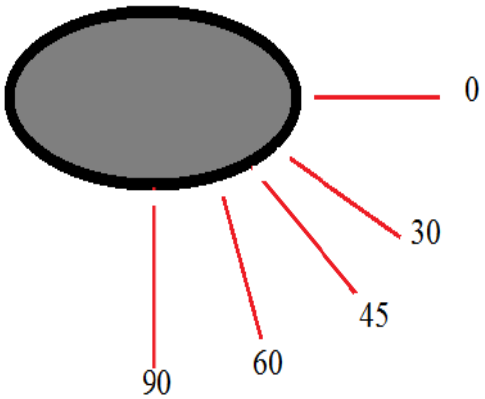

Fig. 5. Impact angles (degree)

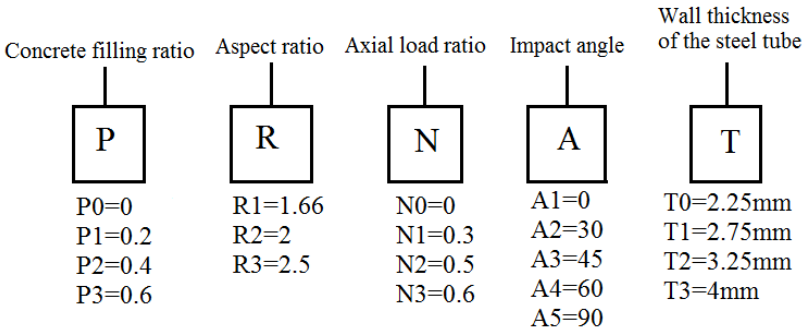

Fig. 6. The naming pattern of the studied specimens

Table 3. Detailed information on each specimen

Specimen Name	P	R	N	A(Degree)	T(mm)	Specimen Name	P	R	N	A(Degree)	T(mm)
P0R1N2A2T1	0	1.66	0.5	0	2.75	P2R3N2A5T1	0.4	2.5	0.5	90	2.75
P1R1N2A2T1	0.2	1.66	0.5	0	2.75	P2R1N0A2T1	0.4	1.66	0	30	2.75
P2R1N2A2T1	0.4	1.66	0.5	0	2.75	P2R1N1A2T1	0.4	1.66	0.3	30	2.75
P3R1N2A2T1	0.6	1.66	0.5	45	2.75	P2R1N2A2T1	0.4	1.66	0.5	30	2.75
P0R2N2A2T1	0	2	0.5	45	2.75	P2R1N3A2T1	0.4	1.66	0.6	30	2.75
P1R2N2A2T1	0.2	2	0.5	45	2.75	P2R2N0A2T1	0.4	2	0	30	2.75
P2R2N2A2T1	0.4	2	0.5	0	2.75	P2R2N1A2T1	0.4	2	0.3	30	2.75
P3R2N2A2T1	0.6	2	0.5	0	2.75	P2R2N2A2T1	0.4	2	0.5	30	2.75
P0R3N2A2T1	0	2.5	0.5	0	2.75	P2R2N3A2T1	0.4	2	0.6	30	2.75
P1R3N2A2T1	0.2	2.5	0.5	45	2.75	P2R3N0A2T1	0.4	2.5	0	30	2.75
P2R3N2A2T1	0.4	2.5	0.5	45	2.75	P2R3N1A2T1	0.4	2.5	0.3	30	2.75
P3R3N2A2T1	0.6	2.5	0.5	45	2.75	P2R3N2A2T1	0.4	2.5	0.5	30	2.75
P2R1N2A1T1	0.4	1.66	0.5	0	2.75	P2R3N3A2T1	0.4	2.5	0.6	30	2.75
P2R1N2A2T1	0.4	1.66	0.5	30	2.75	P2R1N2A2T0	0.4	1.66	0.5	30	2.25
P2R1N2A3T1	0.4	1.66	0.5	45	2.75	P2R1N2A2T1	0.4	1.66	0.5	30	2.75
P2R1N2A4T1	0.4	1.66	0.5	60	2.75	P2R1N2A2T2	0.4	1.66	0.5	30	3.25
P2R1N2A5T1	0.4	1.66	0.5	90	2.75	P2R1N2A2T3	0.4	1.66	0.5	30	4
P2R2N2A1T1	0.4	2	0.5	0	2.75	P2R2N2A2T0	0.4	2	0.5	30	2.25
P2R2N2A2T1	0.4	2	0.5	30	2.75	P2R2N2A2T1	0.4	2	0.5	30	2.75
P2R2N2A3T1	0.4	2	0.5	45	2.75	P2R2N2A2T2	0.4	2	0.5	30	3.25
P2R2N2A4T1	0.4	2	0.5	60	2.75	P2R2N2A2T3	0.4	2	0.5	30	4
P2R2N2A5T1	0.4	2	0.5	90	2.75	P2R3N2A2T0	0.4	2.5	0.5	30	2.25
P2R3N2A1T1	0.4	2.5	0.5	0	2.75	P2R3N2A2T1	0.4	2.5	0.5	30	2.75
P2R3N2A2T1	0.4	2.5	0.5	30	2.75	P2R3N2A2T2	0.4	2.5	0.5	30	3.25
P2R3N2A3T1	0.4	2.5	0.5	45	2.75	P2R3N2A2T3	0.4	2.5	0.5	30	4
P2R3N2A4T1	0.4	2.5	0.5	60	2.75						

Figure 7 depicts an overview of the investigated specimens created in ABAQUS software. In this section, for each aspect ratio (R), four filling heights have been considered, and in each case, a Static/General analysis has been performed. An initial geometric imperfection has been regarded in the static analysis, which is according to the columns first buckling mode under compressive axial load.

Table 4 indicates the columns axial compressive capacity (N_u) and is compared with the axial capacity calculated with Eq. (1) ($N_{u,EC4}$) for filling ratio P =1. As can be seen from this table, the consistency of the results is well. Also, partially concrete-filled columns have a lower capacity than completely concrete-filled columns. Figure 8 demonstrates the axial load-axial displacement curves of the columns with different aspect ratios R and filling ratios P.

It can be seen that for each aspect ratio, the ultimate axial capacity of columns with different filling ratios are close to each other approximately and the rate of increase of the column stiffness with rising the column filling ratio is different in each case. It is also observed that for the same filling ratio, the columns ultimate axial capacity surges with a rising aspect ratio.

According to the performed studies (Mohammadi Rana et al., 2021) and observing the significant effect of compressive axial load on the lateral deflection of partially concrete-filled columns under lateral impact loading, in the present study, 50% of column's the ultimate axial capacity in Table 4 (N_u) is considered as the compressive axial load.

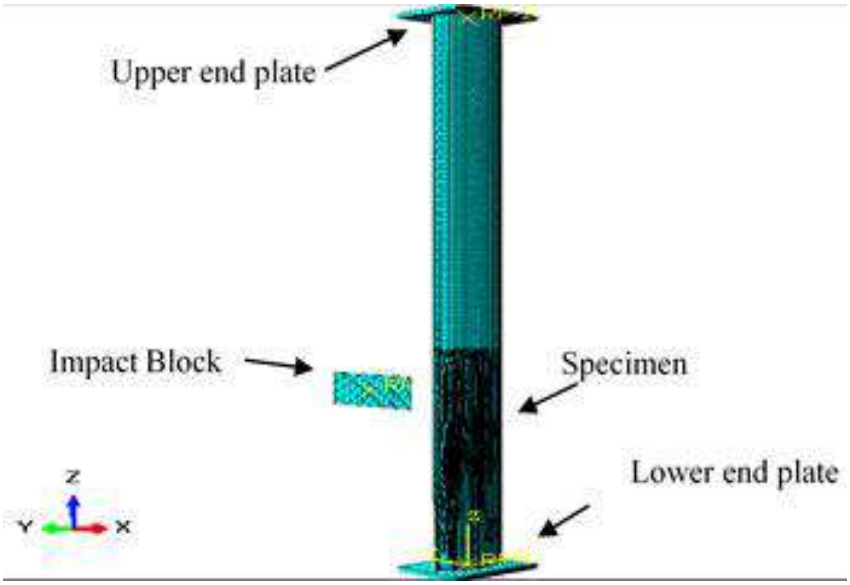

Fig. 7. An overview of the studied specimens created in ABAQUS

Table 4. The ultimate capacity of the columns with different aspect ratios and filling ratios

a × b	A_s (mm^2)	A_c (mm^2)	R	P	$N_{u.EC4}$(N) Eq.(1)	N_u(N) (ABAQUS)
100×60	1358.4	17491	1.66	0.2	-	383981
				0.4	-	389559
				0.6	-	397594
				1	1103781	1067300
150×75	1920.3	33423	2	0.2	-	528847
				0.4	-	536722
				0.6	-	539978
				1	1864845	1850830
250×100	3000.3	75539	2.5	0.2	-	541631
				0.4	-	568498
				0.6	-	587518
				1	3729865	3713870

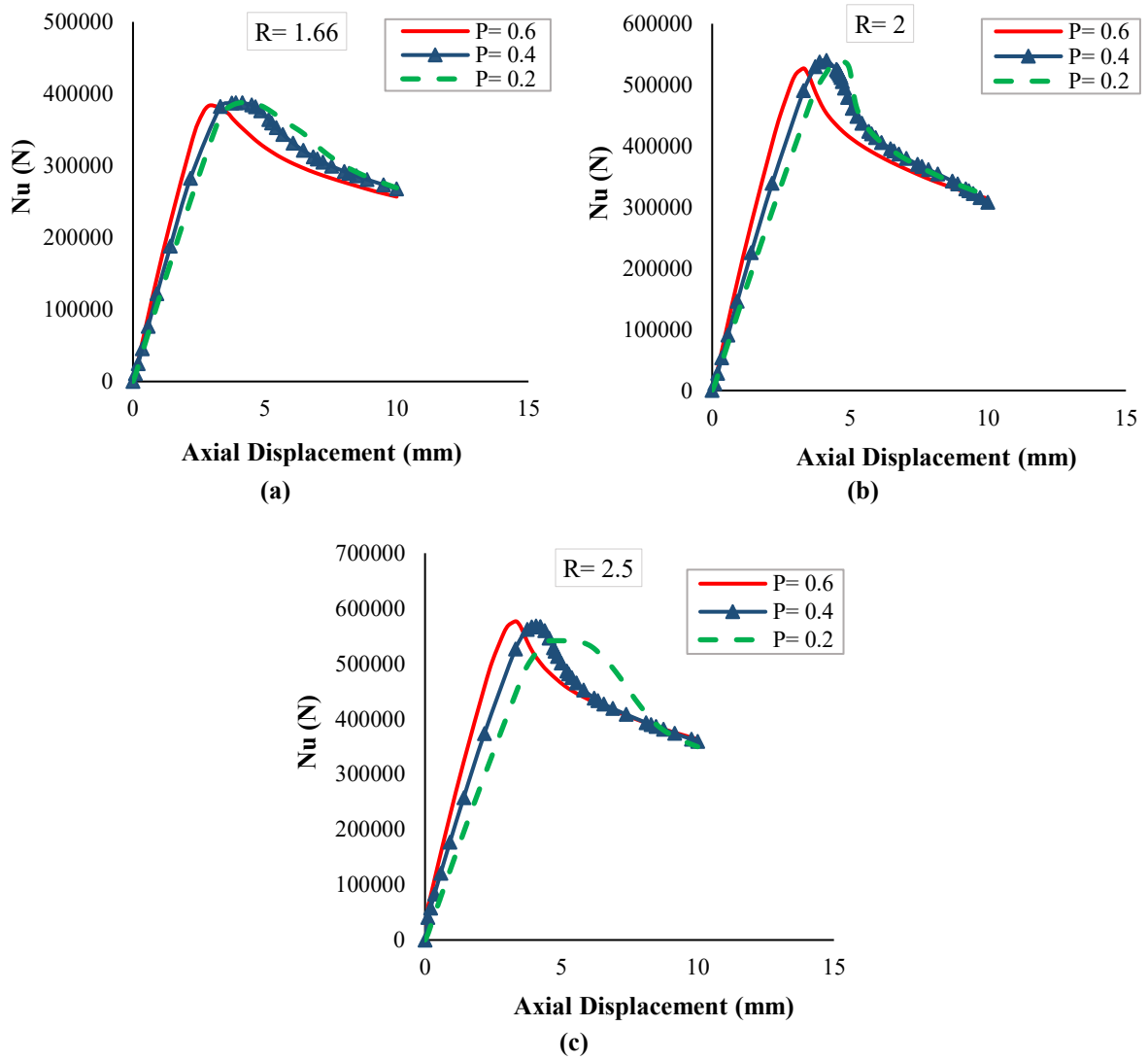

Fig. 8. Axial load - axial displacement curves of specimens with different aspect ratios R and different filling ratios P

4.2. Concrete Filling Ratio Effect

The aim of this section is to scrutinize the influence of the concrete filling ratio on the behavior of PCFCFST columns under lateral impact loading. In the present study, three ratios of filling 0.2, 0.4, and 0.6 have been selected to study the influence of filling ratio (P). Also, cold-formed steel hollow sections have been analyzed for comparison. In the analysis of this section, the impact angle has been considered A2 (30°). Considering the aspect ratios R1, R2, and R3, it can be said that for each aspect ratio, four specimens have been analyzed.

The specifications of the 12 specimens considered in this section are obtained from Table 3. The specimens were subjected to simultaneous loading of compressive axial load and lateral impact load and were analyzed by dynamic/explicit analysis. Figures 9-11 display the analysis results in the form of displacement-time curves, impact force-time curves, and failure modes, respectively. The output of the analysis is extracted at the opposite point of the impacted region in the direction of the impact. Based on Figure 9, it is clear that with increasing filling ratio, the displacements decrease. It also reduces the time to reach the maximum displacement (Δ_{max}). The displacement increases linearly up to t_d (duration from initial impact to the Δ_{max}) and after the Δ_{max} point, vibrates a little, attaining a relatively stable amount.

Maximum values of t_d and Δ_{max} are 36.176 (MS) and 96.1686 mm, respectively.

Both of which are related to the P0R1N2A2T1 specimen. By Comparing the bar charts in Figure 9d, it is evident that hollow columns have the highest Δ_{max} for the different aspect ratios, and columns with the highest filling ratio (0.6) have the lowest Δ_{max}. Figure 10 demonstrates the increase in impact force with increasing filling ratio and aspect ratio.

The maximum impact force is 408.43 kN, connected to the P3R3N2A2T1 specimen. Based on the diagrams in Figure 10, it can be noticed that the force-time curves consist of three stages. First, the impact force at the moment of impact quickly reaches its maximum value, and this procedure is explained as the peak stage. After that, the impact force decreases to an oscillation level, and after fluctuations that occur after the peak, the amount of force remains almost constant (especially in the filling ratios P0 and P1).

By the impact energy dissipation, the impact force slowly reaches 0, called the final stage. Furthermore, the results show that the lower the filling ratio, the duration of contact between the column and impact block is longer and the lower the impact load. Figure 10d indicates that with rising the filling ratio, the maximum impact force also increases, and at larger filling ratios, the effect of the aspect ratio on increasing the maximum impact force is more noticeable. Of all the specimens studied in this section, specimens with R1 aspect ratio have the highest deformation under impact load. Therefore, the failure modes of specimens with R1 impact ratio for different filling ratios are revealed in Figure 11.

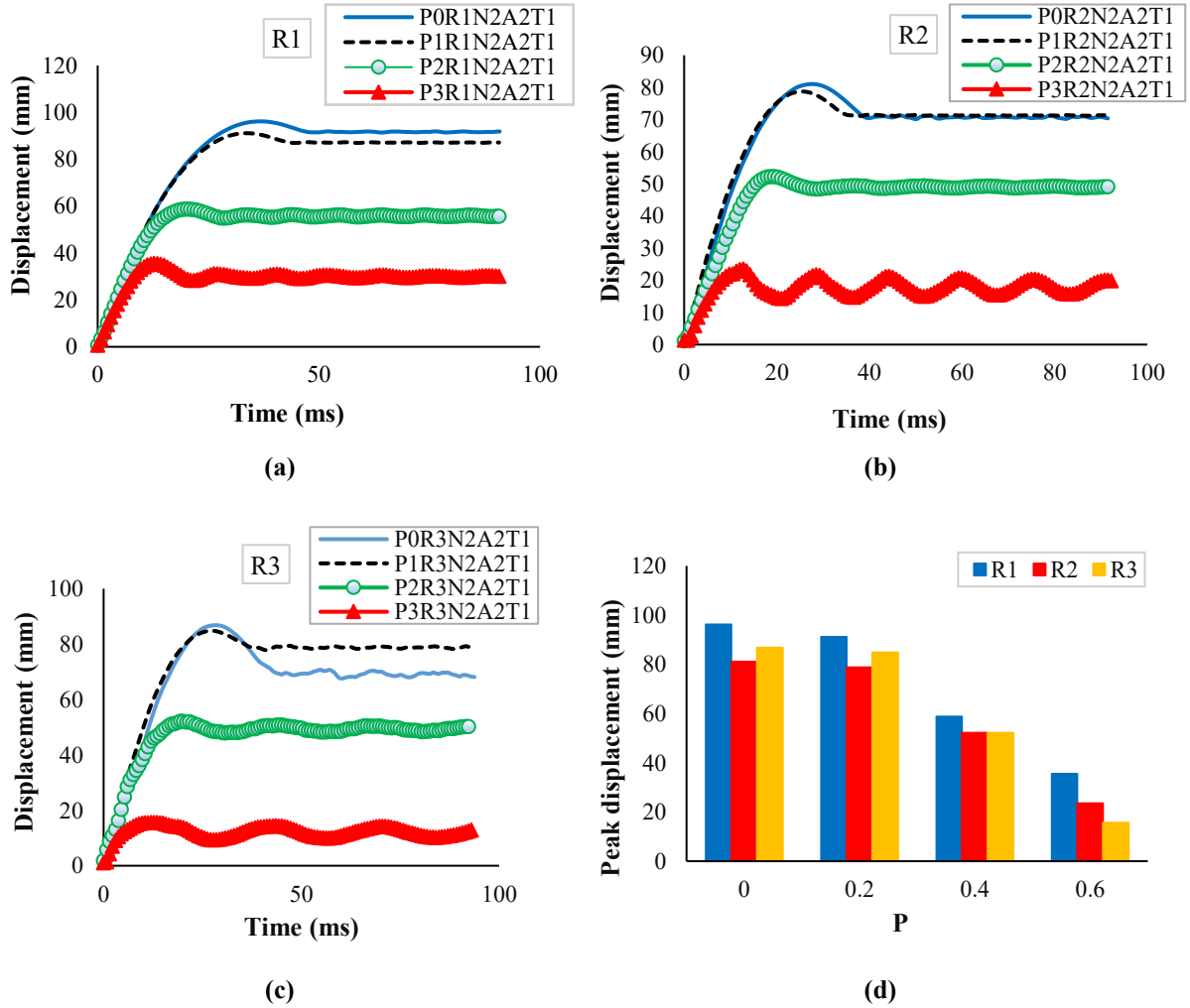

Fig. 9. The displacement - time curves of the columns with different filling ratios: a) Aspect ratio R1; b) Aspect ratio R2; c) Aspect ratio R3 ;and d) Comparison of peak displacements

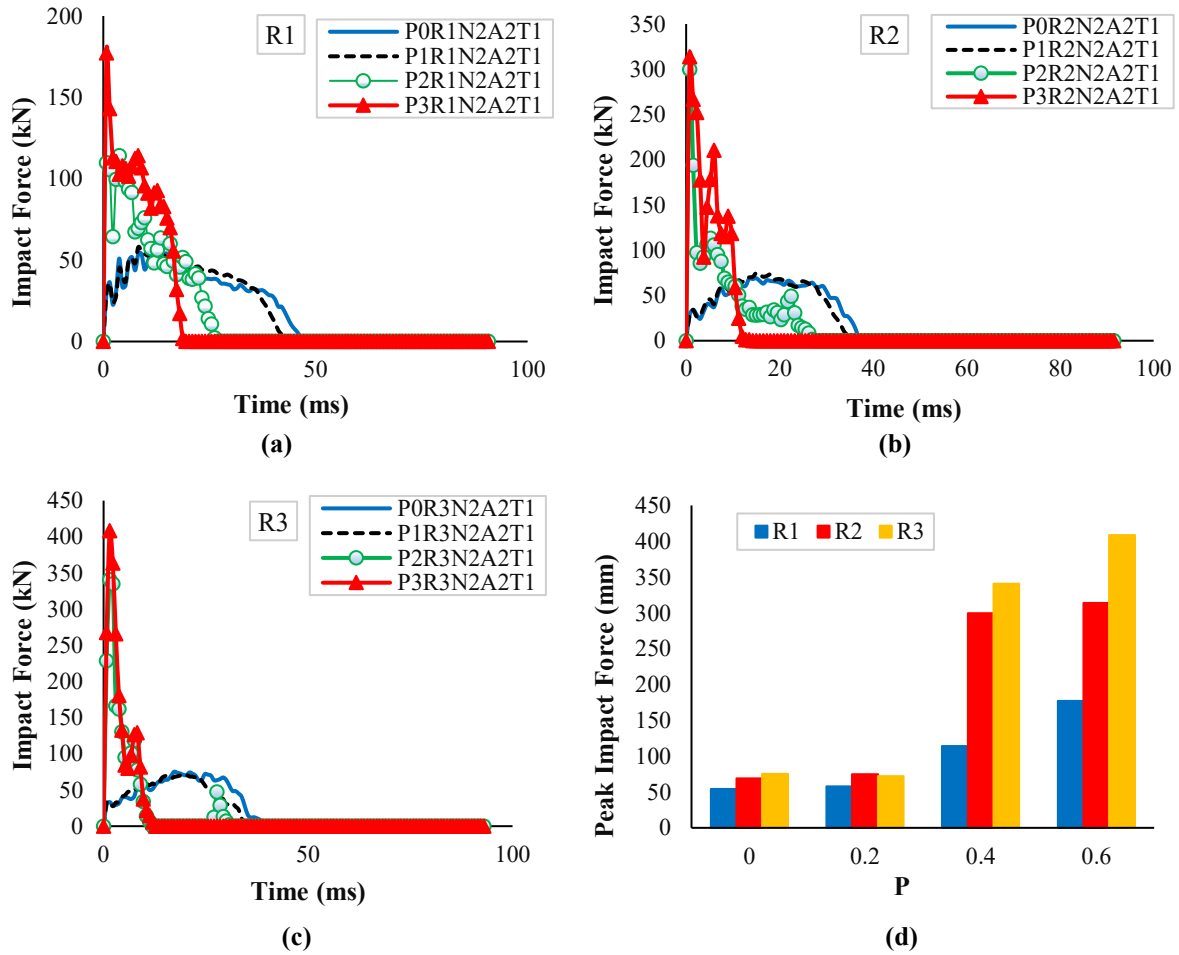

Fig. 10. The impact force-time curves of columns with different filling ratios: a) Aspect ratio R1; b) Aspect ratio R2; c) Aspect ratio R3; and d) Comparison of peak impact forces

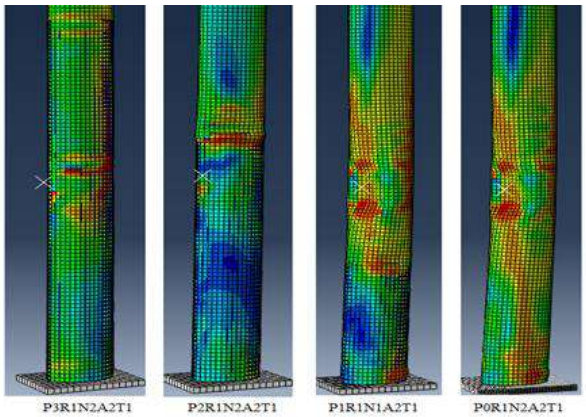

Fig. 11. The failure modes of the columns with the R1 aspect ratio with different filling ratios

It is clear that the specimen with a filling ratio of P0 has the maximum deformation, and the specimen with the highest filling ratio (P3 = 0.6) has the minimum deformation.

4.3. The Effect of Impact Angle

The primary aim of this section is to examine the effect of impact angle on the performance of elliptical PCFCFST columns. In this research, the influence of impact angle (A) is investigated by considering five angles of 0, 30, 45, 60, and 90 degrees, as demonstrated in Figure 5. In the analysis of this part, the filling ratio is considered P2, and the aspect ratios are R1, R2 and R3. The specifications of the 15 specimens considered in this section are

gained from Table 3. Having applied the lateral impact load, the analyses' results which include displacement-time curves in Figure 12, impact force-time curves in Figure 13, and failure modes in Figure 14, are illustrated. Based on Figure 12, it is clear that at the impact angle of A1 (0°), where the impact is applied along the large diameter of the ellipse section, the displacements created at the impact block is opposite point are far less than the displacements at other impact angles, so that the maximum amount of displacements occurs at the impact angle A5 (90°) along the ellipse section's small diameter. The P2R1N2A5T1 type is associated with a maximum displacement of 89.85 mm. In the R1 and R2 aspect ratios for all impact angles, first, the displacements surge linearly up to the peak point, and after that, displacements become relatively stable.

However, in the R3 aspect ratio, displacements increase linearly up to the peak point, but after that, it is accompanied by an oscillating state. The increasing trend of maximum displacement by increasing the impact angle can be seen in the bar chart of Figure 12d.

It is also observed that by altering the impact angle from A1 (0°) to A5 (90°), the increase in displacement in the R3 aspect ratio is much less than the R1 and R2 aspect ratios. According to Figure 13, it is clear that for all impact angles, the impact force increases with surging aspect ratio, and for a fixed aspect ratio, the impact force also rises with increasing impact angle from A1 (0°) to A5 (90°). The greatest impact force of 701.639 kN is associated with the P2R3N2A5T1 specimen. Also, as the impact angle increases, the duration of contact between the impact block and column is extended following the collision.

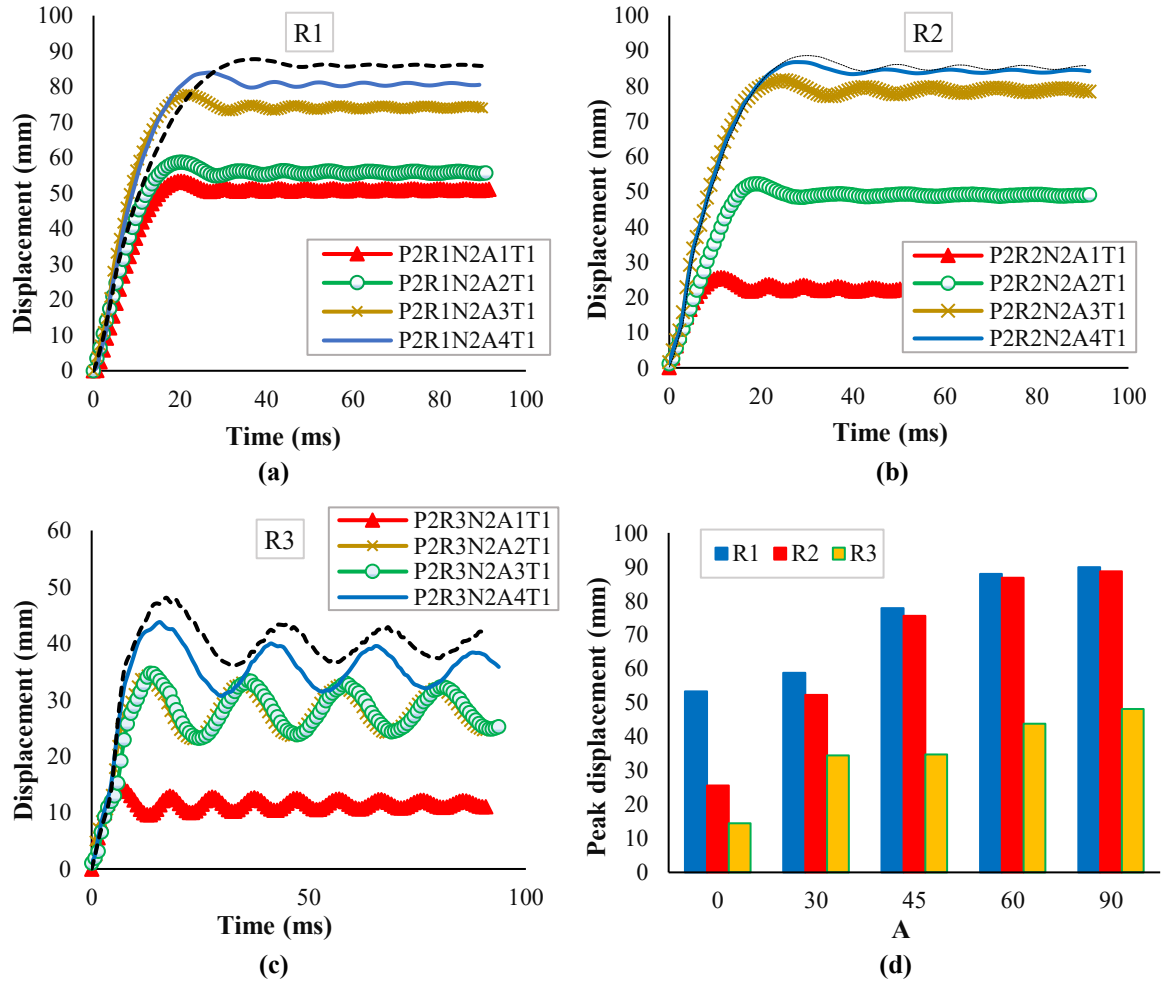

Fig. 12. The displacement - time curves of columns with different impact angles: a) Aspect ratio R1; b) Aspect ratio R2; c) Aspect ratio R3; and d) Comparison of peak displacements

From the bar chart of Figure 13d, the correlation between the maximal impact force and the impact angle and aspect ratio is apparent. The failure modes of specimens with an R1 aspect ratio for the five different impact angles are revealed in Figure 14. It is evident from Figure 14 that the maximum displacement is related to the impact angle of A5 (90°). The impact angle A2, the filling ratio P2, and the aspect ratios R1, R2, and R3 are considered.

Therefore, it can be said that for each aspect ratio, four specimens have been analyzed. The findings from the analysis of displacement-time curves are presented in Figure 15, while the impact force-time curves are depicted in Figure 16.

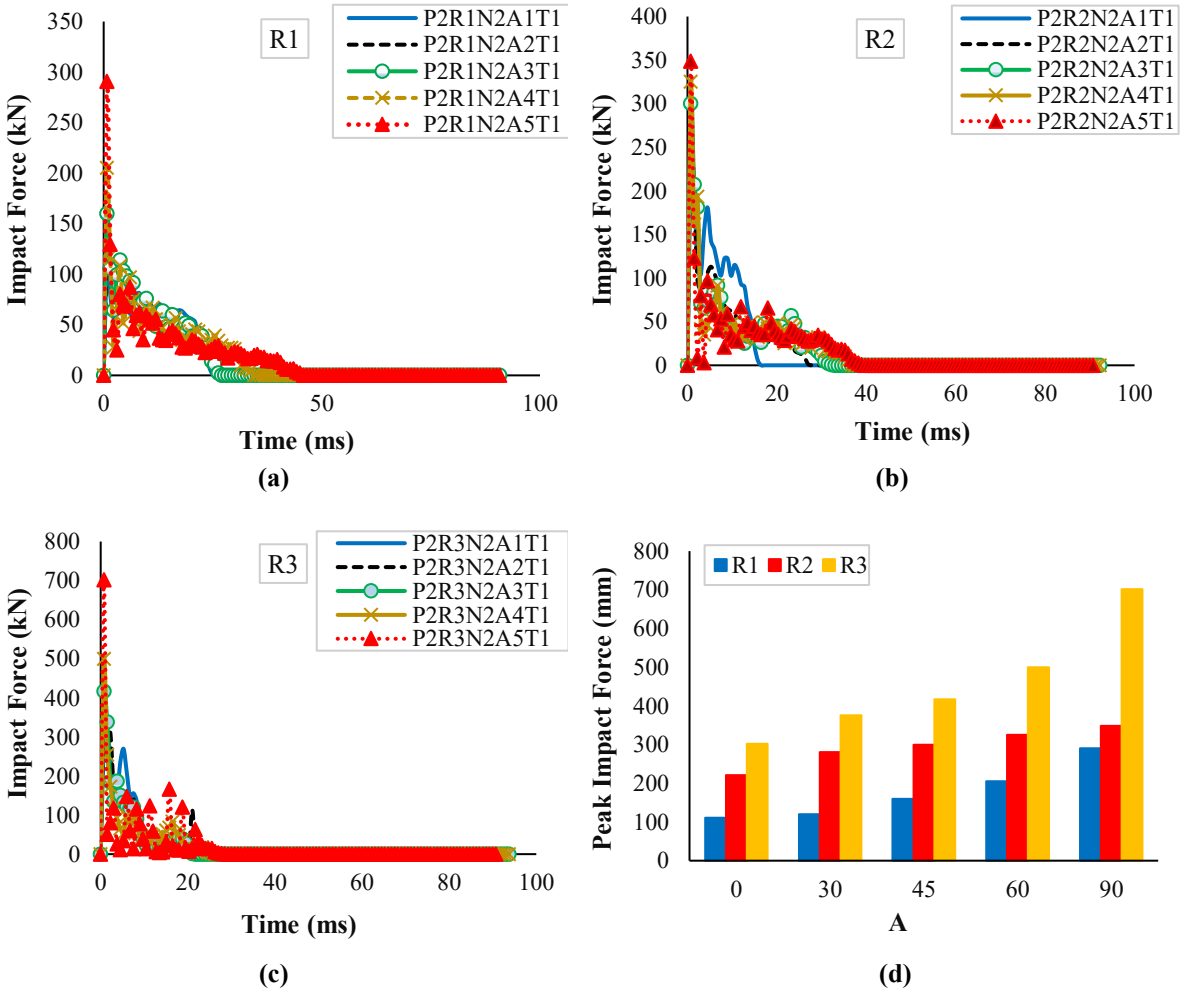

Fig. 13. The impact force-time curves of columns with different impact angles: a) Aspect ratio R1; b) Aspect ratio R2; c) Aspect ratio R3; and d) Comparison of peak impact forces

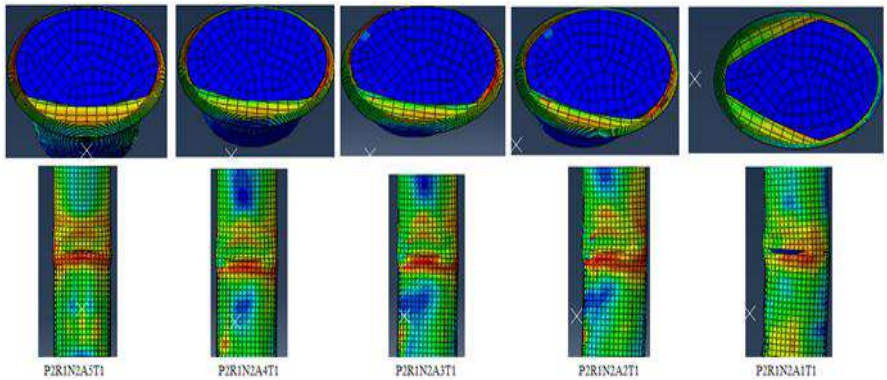

Fig. 14. The failure modes of the columns with the R1 aspect ratio with different impact angles

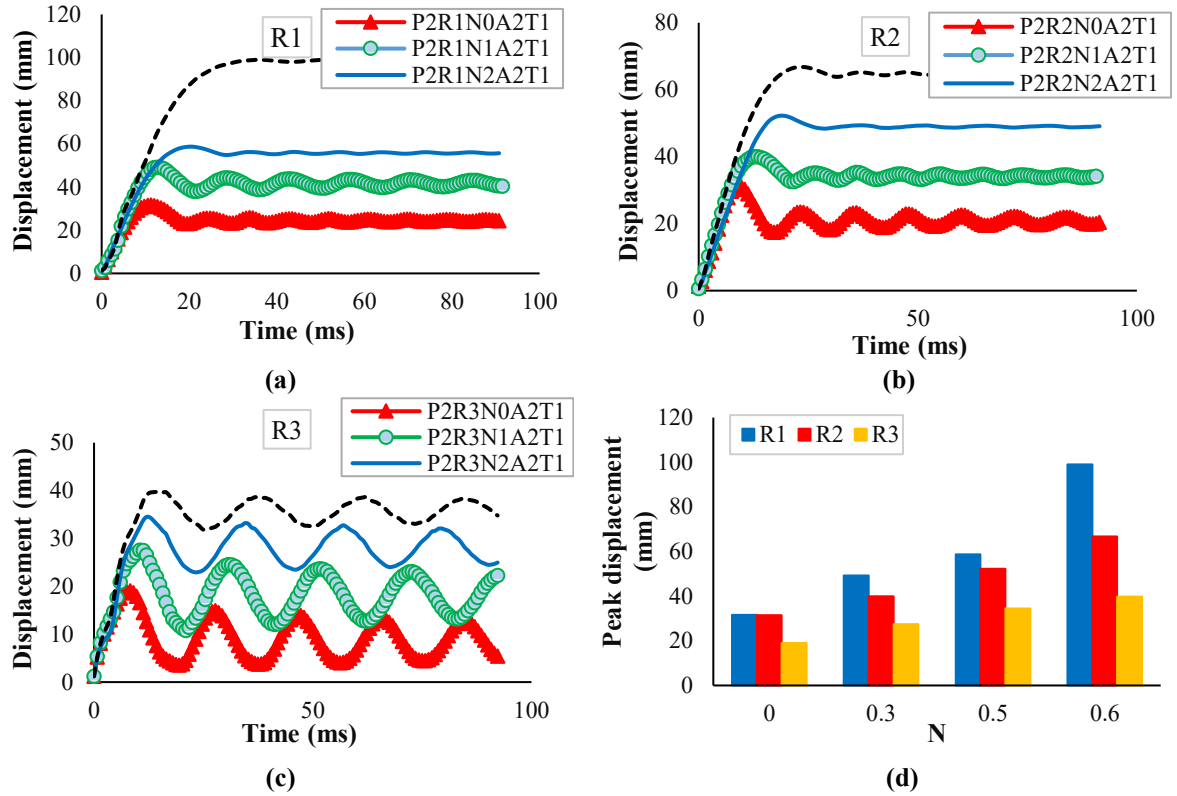

Fig. 15. The displacement - time curves of columns with different axial load ratios: a) Aspect ratio R1; b) Aspect ratio R2; c) Aspect ratio R3; and d) Comparison of peak displacements

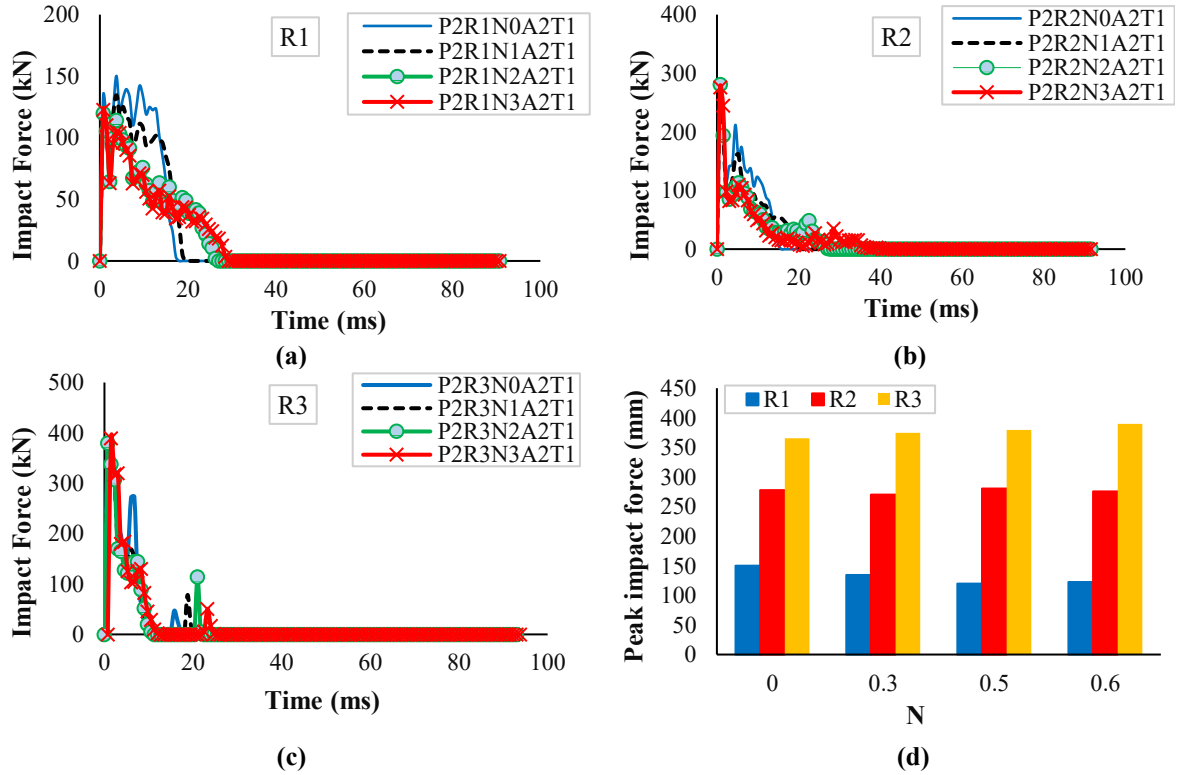

Fig. 16. The impact force-time curves of columns with different axial load ratios: a) Aspect ratio R1; b) Aspect ratio R2; c) Aspect ratio R3; and d) Comparison of peak impact forces

Additionally, the failure modes are illustrated in Figure 17. Based on Figure 15, the data clearly indicates that the curves exhibit an upward tendency starting from

the time of collision of the impact block t_d. As is observed in Figure 15, the displacements in the column increase with increasing axial load ratio, and in the R1 and R2 aspect ratios, upon the separation of the hit block from the column, the displacements stabilize at a relatively consistent magnitude with a minor oscillation. But in the R3 aspect ratio after the peak point, the displacements are accompanied by more oscillation. The maximum contact time is 34.5 ms, specifically for the P2R1N3A2T1 sample.

The P2R1N3A2T1 specimen exhibits the greatest displacement of 99 mm, while the P2R3N0A2T1 model has the lowest displacement of 19.03 mm. Figure 16 shows the impact force-time curves subjected to an impact load. As depicted in this diagram, when the axial load ratio is increased, the duration of contact between the column and the impact block following the collision is extended, which can be explained by the rise in impact kinetic energy when the axial load ratio is more significant, in which case the column indicates more plastic energy dissipation capacity throughout the impact procedure.

The aspect ratio significantly influences the magnitude of the impact force and by increasing the aspect ratio, can be seen a 69% increase in impact force. The maximal impact force of 518/389 kN is associated with the P2R3N3A2T1 specimen. The bar chart in Figure 16d demonstrates that there is minimal impact on the maximum impact force when the axial load ratio is rose. The failure modes of the specimens with the R1 aspect ratio for different axial load ratios are illustrated in Figure 17. The figure clearly demonstrates that increasing the axial load ratio increases the specimens' deformation.

4.5. The Effect of Steel Tube Wall Thickness

The primary purpose of this section is to search the influence of the steel tube wall thicknesses (T) on the performance of elliptical hollow and partially concrete-filled cold-formed steel columns under the influence of lateral impact loading. Four thicknesses of 2.25, 2.75, 3.25, and, 4 mm have been selected for the steel tube. The analysis of specimens has been performed by considering the impact angle A2, the filling ratio P2, and the aspect ratios R1, R2 and R3.

The results of the analyses are presented in the procedure of displacement-time curves in Figure 18, impact force-time curves in Figure 19, and failure modes in Figure 20. Based on Figure 18, it is clear that by raising the steel tube's wall thickness, the columns' displacement decreases under the impact load. In the current work, the maximum displacement is related to the P2R1N2A2T0 column with a value of 844.289 mm, and the minimum amount is related to the P2R3N2A2T3 column with a value of 16.065 mm. It is clear from the diagrams in Figure 18d that by increasing the aspect ratio, the columns highest displacement decreases for diverse steel tube wall thicknesses.

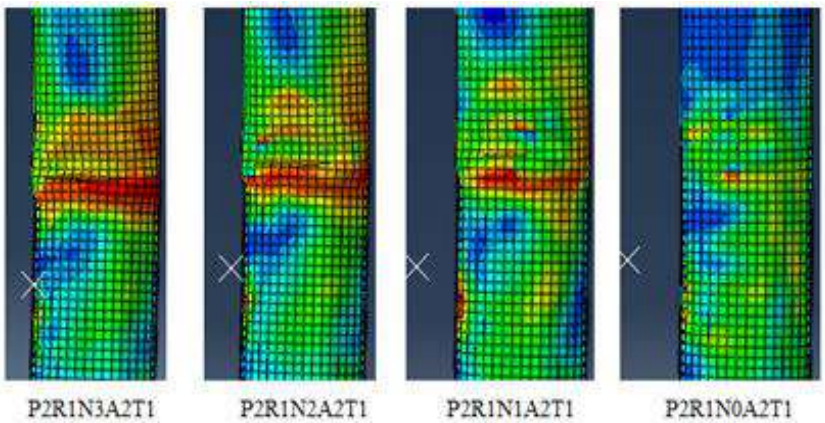

Fig. 17. The failure modes of the columns with R1 aspect ratio for different axial load ratios

At low wall thicknesses of steel tubes, the duration of contact time between the impact block and the column extends after the collision, so the maximum contact time of the P2R1N2A2T0 specimen is 27.751 ms. From the diagrams in Figure 19, it is evident that as the steel tube wall thickness surges, the amount of impact force increases, also the time of complete unloading of the impact load decreases.

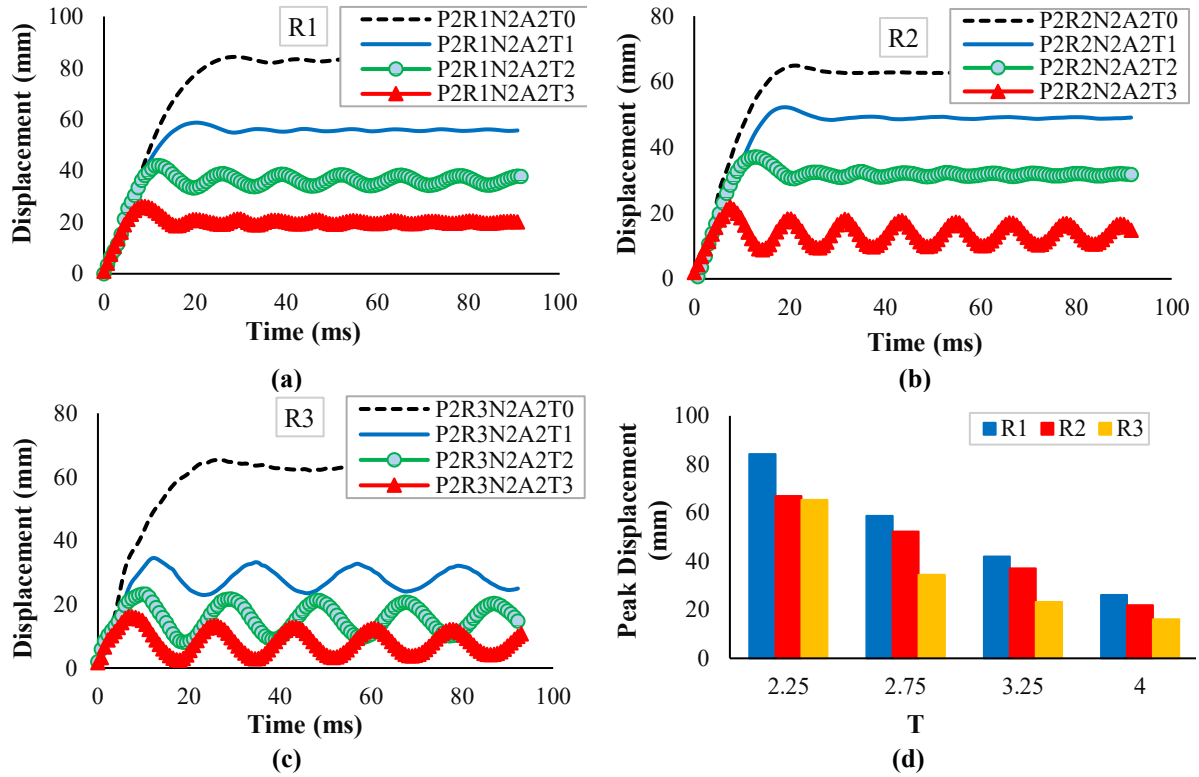

Fig. 18. The displacement - time curves of columns with different wall thicknesses of steel tube: a) Aspect ratio R1; b) Aspect ratio R2; c) Aspect ratio R3; and d) Comparison of peak displacements

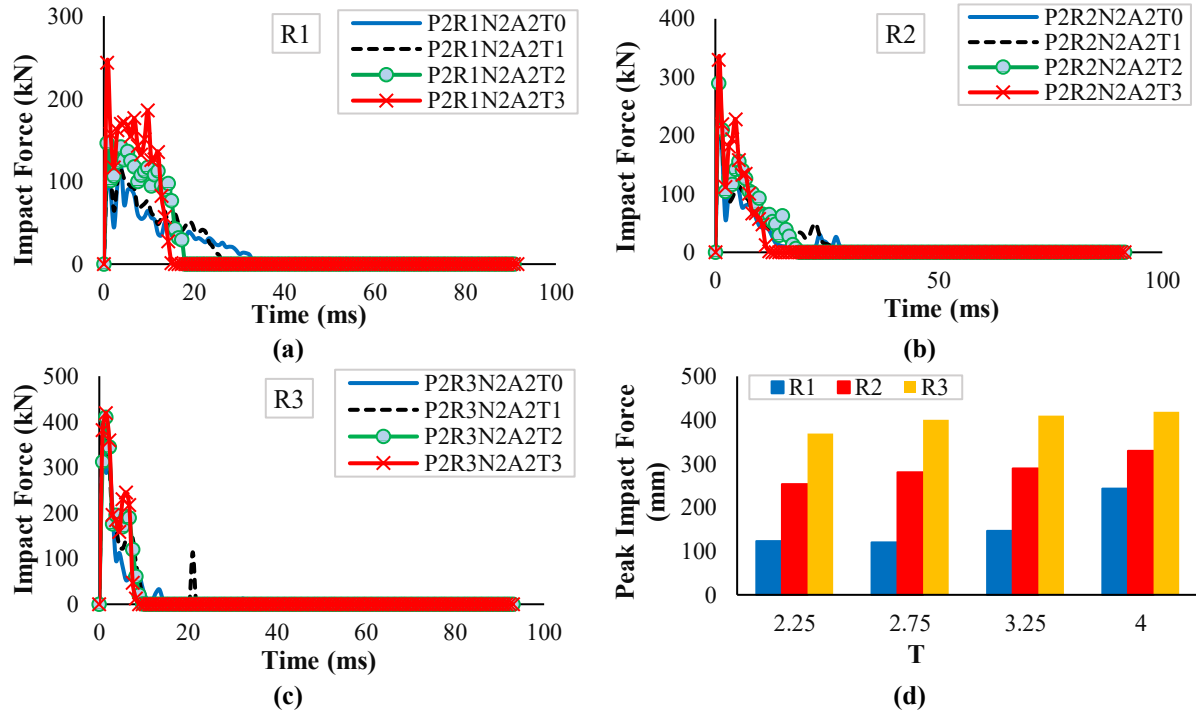

Fig. 19. The impact force-time curves of columns with different wall thicknesses of steel tube: a) Aspect ratio R1; b) Aspect ratio R2; c) Aspect ratio R3; and d) Comparison of peak impact forces

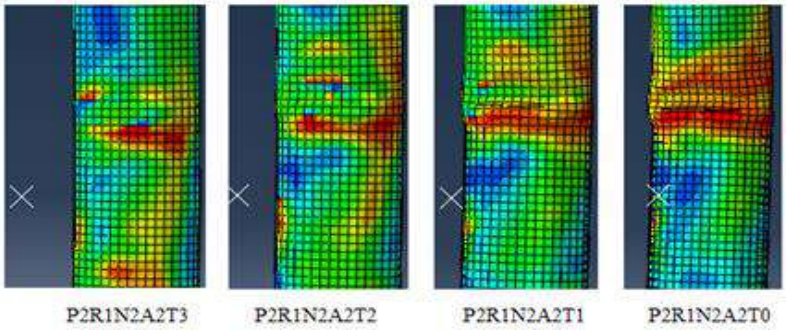

Fig. 20. The failure modes of the columns with the R1 aspect ratio for different thicknesses of steel sections

According to Figure 19d, it can be seen that for different wall thicknesses of steel tubes, the impact force surges with rising the aspect ratio. The maximum impact force of 403.27 kN is associated with the P2R3N2A2T3 specimen. Based on the columns failure modes with the R1 aspect ratio for steel tubes with diverse wall thicknesses in Figure 20, it is evident that more deformation has happened in the columns with low wall thickness.

4.6. The Influence of the Aspect Ratio

The main goal of this section is to investigate the influence of diverse aspect ratios on the performance of elliptical PCFCFST columns. In the current study, the three different aspect ratios (R) 1.66, 2, and 2.5 are considered. In the previous sections, for each variable parameter, all three aspect ratios are considered. The numerical outcomes of total the considered parameters in this study are assumed in Table 5. On the basis of the outcomes of Table 5, it is clear that in PCFCFST specimens, for changing different parameters, increasing the aspect ratio is associated with decreasing the maximum displacement (Δ_{max}). So the maximum and minimum Δ_{max} are, in turn, related to the aspect ratios R1 and R3, respectively. It can also be seen from the above table that increasing the aspect ratio is associated with decreasing t_d and increasing impact force.

Table 5. The ultimate capacity of the columns with different aspect ratios and filling ratios

Constants		Peak displacement (mm)			t_d (ms)			Impact force (KN)		
		R1	R2	R3	R1	R2	R3	R1	R2	R3
A2, P2, N2	T0	84.2888	66.9254	65.3192	25.7513	19.5011	24.0019	115.6227	253.1291	369.1759
	T1	58.74308	52.2372	34.5086	19.5013	17.2503	9.7501	119.902	280.0948	379.5418
	T2	37.0851	42.0099	23.1753	11.250	10.5013	7.5019	146.0654	289.3365	410.2768
	T3	26.1073	21.8783	16.0648	8.2508	6.0018	3.7517	243.3309	329.6792	419.2018
A2, N2, T1	P0	96.16862	81.02753	86.80809	36.1768	26.2503	24.7523	54.1212	69.0789	75.2334
	P1	91.12152	78.71799	84.81627	33.001	24.7514	24.7507	58.0085	74.7438	72.2073
	P2	58.74308	52.2372	34.50862	19.5013	17.2503	17.2519	119.902	280.6948	379.5418
	P3	35.53408	23.46794	15.67315	12.0003	10.5005	9.7507	177.233	313.7162	408.43
A2, P2, T1	N0	31.57454	31.40822	19.02924	10.5012	7.5016	6.0013	150.2893	280.6948	405.5418
	N1	40.00309	49.21735	27.52239	12.0009	11.2517	8.2502	134.608	277.9797	389.5178
	N2	58.74308	52.2372	34.50862	19.5013	17.2503	9.7501	119.902	275.773	379.5418
	N3	66.79286	98.99415	39.86795	22.5008	34.5007	12.7504	112.5448	270.3577	374.405
P2, N2, T1	A0	53.32463	25.57191	14.49871	18.7502	10.5011	6.0028	110.9875	221.3038	302.3992
	A1	58.74308	52.2372	34.50862	19.5013	17.2503	9.7501	119.902	280.6948	379.5418
	A2	77.79389	75.58222	34.71507	21.7503	23.2501	9.7516	159.902	300.0512	416.8431
	A3	87.89511	86.80803	43.7639	27.7517	26.2503	12.002	205.2967	325.0398	499.8987
	A4	89.85444	88.65604	48.08018	36.7520	29.2504	16.5004	290.6437	348.6568	701.6393

4.7. Discussion

Figure 21 provides the abbreviated numerical results of all the specimens analyzed in. The outcomes of numerical investigations could be succinctly categorized into five sections based on the parameters under examination.

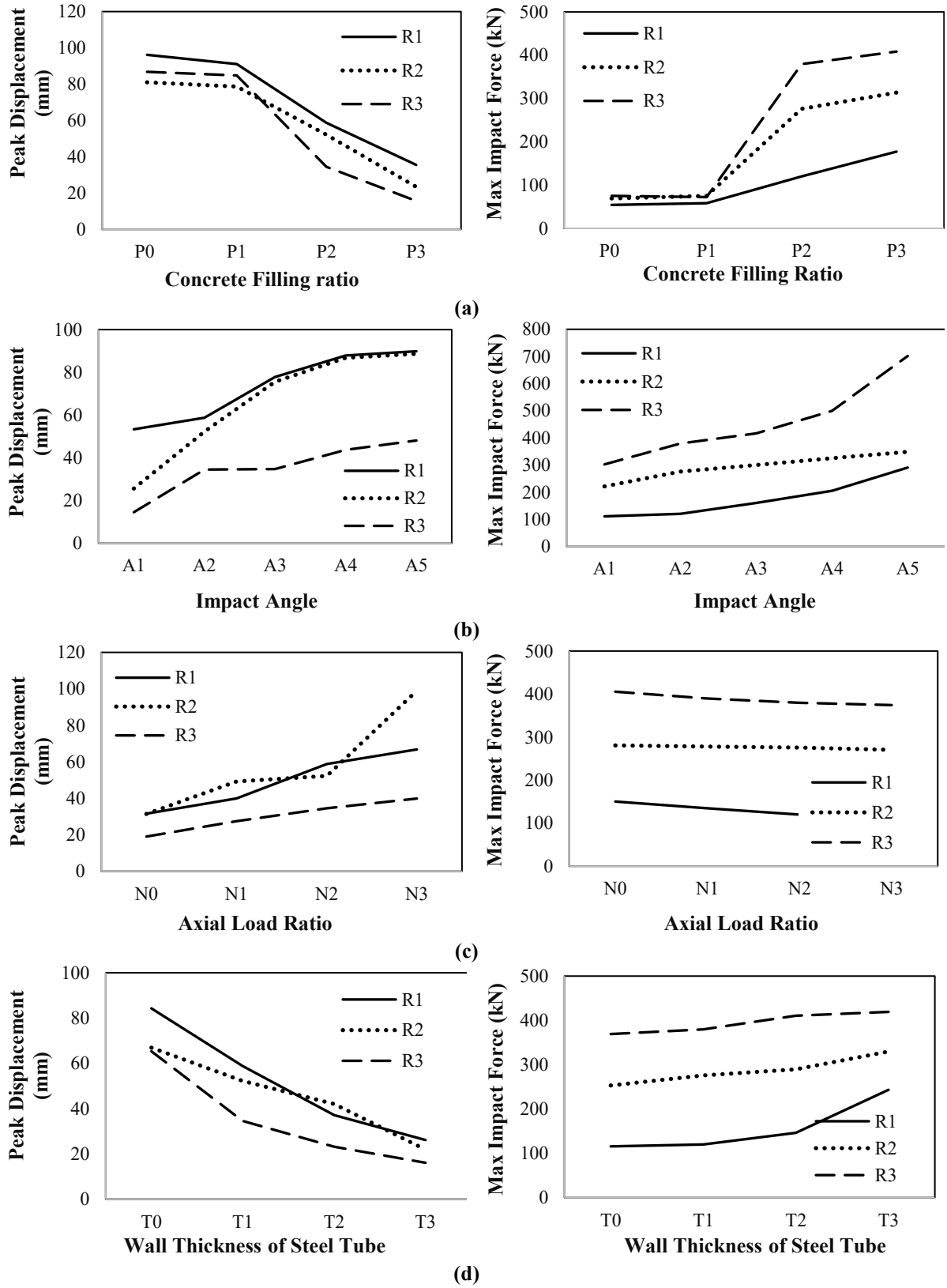

Fig. 21. Numerical results of all the studied specimens

Filling ratio effect: Hollow columns have the highest Δ_{max} for the different aspect ratios and columns with the highest filling ratio (0.6) have the lowest Δ_{max}.

Given that the impact height is 0.4 of the column height, the column's performance with a filling ratio of 0.2 is similar to the behavior of an empty column, and the greatest impact force and displacement are approximately the same. By increasing the filling ratio by 0.4, the maximum displacement reduces, and the impact force surges significantly. Swelling the maximum displacement and decreasing the impact force continue with surging the filling ratio to 0.6 with a smooth slope. The outcomes indicate that the lower the filling ratio, the duration of contact between the column and the impact block is longer and the lower the impact load. By surging the filling ratio, the maximum impact force also increases. The maximum displacement in the lower aspect ratio is more significant and gradually reduces with the increasing aspect ratio.

Also, the highest impact force at a lower aspect ratio has the lowest value, which increases with a surging aspect ratio. The difference in the maximum impact force responses for different aspect ratios increases with increasing filling ratio. At larger filling ratios, the influence of the aspect ratio on increasing the maximum impact force is more noticeable.

Impact angle effect: A surge in the greatest amount of displacement and greatest impact force is noticed when the impact angle is altered from zero (along with the big diameter of the ellipse) to 90 degrees (along with the small diameter of the ellipse). It is also observed that by altering the impact angle from A1 (0°) to A5 (90°), the increase in displacement in the R3 aspect ratio is much less than the R1 and R2 aspect ratios. The maximum amount of displacements occurs at the impact angle A5 (90°) along the small diameter of the elliptical section. It is evident that for all impact angles, the impact force rises with a surging aspect ratio, and for a fixed aspect ratio, the impact force also rises with a rising impact angle from A1 (0°) to A5 (90°).

Load ratio effect: As the axial force rises, the maximum displacement increases and the impact force decreases linearly with a smooth slope. By surging the axial force from zero to 60% of the ultimate load capacity, at the aspect ratio R3, the maximum impact force decreases by about 8%. This reduction is 4% for the R2 aspect ratio and 25% for the R1 aspect ratio.

Steel tube wall thickness effect: As the wall thickness rises from T0 to T3, the maximum impact force increases and the maximum displacement decreases by approximately 70%. For different wall thicknesses of steel tubes, the impact force surges with rising the aspect ratio.

Aspect ratio effect: In a column with a lower aspect ratio, the maximum displacement is more significant, and the highest impact force is lower. In general, as the cross-sectional aspect ratio rises, the maximum impact force increases, and the greatest displacement decreases. Figure 22 depicts the maximum displacement against the time to reach the maximum displacement.

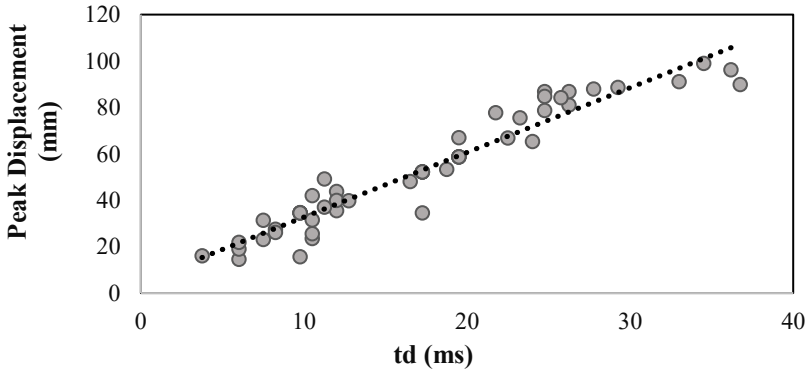

Fig. 22. Scatter of the studied specimen is analysis results

Based on the diagram, it can be determined that there is a nearly linear correlation between the greatest displacement and the time it takes to attain that maximum displacement which follows Eq. (2).

$$\Delta_{max} = 2.8\, t_d + 4.85 \quad (2)$$

5. Conclusions

This research investigated the lateral impact behavior of elliptical PCFCFST columns with axial compression load. The influences of aspect ratio, axial load ratio, impact angle, concrete filling ratio, and wall thickness of steel tubes were examined. The primary findings can be succinctly described as follows:

- Hollow columns have the highest Δ_{max} for the different aspect ratios, and columns with the highest filling ratio (0.6) have the lowest Δ_{max}. If an impact is put on the column's hollow part, the behavior of the filled column is the same as that of the empty column. As the filling ratio increases, the greatest displacement decreases, and the highest impact force increases. At larger filling ratios, the effect of the aspect ratio on increasing the highest impact force is more noticeable.
- By changing the impact angle from zero (along with the large diameter of the ellipse) to 90 degrees (along with the small diameter of the ellipse), a surge in the highest displacement and maximum impact force is observed. The maximum amount of displacements occurs at the impact angle A5 (90°) along the small diameter of the elliptical section. For all impact angles, the impact force rises with a surging aspect ratio.
- As the axial force rises, the highest displacement surges and the impact force diminishes linearly with a smooth slope.
- As the wall thickness surges, the highest impact force increases, and the highest displacement decreases. For different wall thicknesses of steel tubes, the impact force increases with the aspect ratio.
- In a column with a lower aspect ratio, the highest displacement is greater, and the highest impact force is lower. In general, as the cross-sectional aspect ratio rises, the maximum impact force increases, and the highest displacement decreases.
- There is a close correlation between the time and maximum displacement it takes to attain that maximum displacement, which can be approximated as a linear relationship.

6. References

Aghdamy, S., Thambiratnam, D.P., Dhanasekar, M. and Saiedi, S. (2015). "Computer analysis of impact behavior of concrete-filled steel tube columns", *Advances in Engineering Software*, 89, 52-63, https://doi.org/10.1016/j.advengsoft.2015.06.015.

Alam, M.I., Fawzia, S. and Zhao, X.L. (2016). "Numerical investigation of CFRP strengthened full-scale cfst columns subjected to vehicular impact", *Engineering Structures*, 126, 292-310, https://doi.org/10.1016/j.engstruct.2016.07.058.

Baltay, P. and Gjelsvik, A. (1990). "Coefficient of friction for steel on concrete at high normal stress", *Journal of Materials in Civil Engineering*, 2(1), 46-49, https://doi.org/10.1061/(ASCE)0899-1561(1990)2:1(46).

Craveiro, H.D., Rahnavard, R., Henriques, J. and Simões, R.A. (2022). "Structural fire performance of concrete-filled built-up cold-formed steel columns", *Materials*, 15(6), 2159, https://doi.org/10.3390/ma15062159.

Du, G., Andjelic, A., Li, Z., Lei, Z. and Bie, X. (2018). "Residual axial bearing capacity of concrete-filled circular steel tubular columns after transverse impact", *Applied Sciences*, 8(5), 793, https://doi.org/10.3390/app8050793.

Han, L.H., Xu, C.Y. and Tao, Z. (2019). "Performance of concrete-filled stainless steel tubular columns and joints: Summary of recent research", *Journal of Constructional Steel Research*, 152, 117-131, https://doi.org/10.1016/j.jcsr.2018.02.038 .

Liu, F., Wang, Y. and Chan, T.M. (2017). "Behavior of concrete-filled cold-formed elliptical hollow sections with varying aspect ratios", *Thin-walled Structures*, 110, 47-61, https://doi.org/10.1016/j.tws.2016.10.013.

Mohammadi Rana, N., Ghandi, E. and Niari, S.E. (2021). "Lateral impact response of elliptical hollow and partially concrete-filled cold-formed steel columns under static axial compression

load", *International Journal of Structural Stability and Dynamics*, 2250048, https://doi.org/10.1142/S0219455422500481.

Moradi, M., Tavakoli, H.R. and Abdollahzadeh, G.R. (2021). "Comparison of steel and reinforced concrete frames' durability under fire and post-earthquake fire scenario", *Civil Engineering Infrastructures Journal*, 54(1), 145-168, 10.22059/CEIJ.2020.292639.1628.

Rahnavard, R., Craveiro, H.D., Simões, R.A., Laím, L. and Santiago, A. (2022a). "Fire resistance of concrete-filled cold-formed steel built-up short columns", *Journal of Building Engineering*, 48, 103854, https://doi.org/10.1016/j.jobe.2021.103854.

Rahnavard, R., Craveiro, H.D., Lopes, M., Simões, R.A., Laím, L. and Rebelo, C. (2022b). "Concrete-filled cold-formed steel built-up columns under compression: Test and design", *Thin-Walled Structures*, 179, 109603, https://doi.org/10.1016/j.tws.2022.109603.

Rahnavard, R., Craveiro, H.D. and Simões, R.A. (2023). "Analytical prediction of the axial capacity of concrete-filled cold-formed steel built-up columns", *In Proceedings of the Annual Stability Conference*, Charlotte, North Carolina, 188, 110792, https://doi.org/10.1016/j.tws.2023.110792.

Rondal, J. (2000). "Cold-formed steel members and structures: general report", *Journal of constructional steel research*, 55(1-3), 155-158, https://doi.org/10.1016/S0143-974X(99)00083-8.

Shakir, A.S., Guan, Z.W. and Jones, S.W. (2016). "Lateral impact response of the concrete-filled steel tube columns with and without cfrp strengthening", *Engineering Structures*, 116, 148-162, https://doi.org/10.1016/j.engstruct.2016.02.047.

Wan, J., Chen, Y., Wang, K. and Han, S. (2017). "Residual strength of chs short steel columns after lateral impact", *Thin-Walled Structures*, 118, 23-36, https://doi.org/10.1016/j.tws.2017.04.027.

Wang, Y., Qian, X., Liew, J.R. and Zhang, M.H. (2015). "Impact of cement composite filled steel tubes: an experimental, numerical and theoretical treatise", *Thin-Walled Structures*, 87, 76-88, https://doi.org/10.1016/j.tws.2014.11.007.

Wang, J., Shen, Q., Jiang, H. and Pan, X. (2018). "Analysis and design of elliptical concrete-filled thin-walled steel stub columns under axial compression", *International Journal of Steel Structures*, 18(2), 365-380, https://doi.org/10.1007/s13296-018-0002-5.

Xu, W., Zhu, A.Z. and Gao, K. (2018). "Parameter analysis on the anti-impact behavior of pcfst columns under lateral impact load", *In MATEC Web of Conferences*, 206, 01020, https://doi.org/10.1051/matecconf/201820601020.

Yang, Y.F., Zhang, Z.C. and Fu, F. (2015). "Experimental and numerical study on square racfst members under lateral impact loading", *Journal of Constructional Steel Research*, 111, 43-56, https://doi.org/10.1016/j.jcsr.2015.04.004.

Yang, H., Liu, F., Chan, T.M. and Wang, W. (2017). "Behaviors of concrete-filled cold-formed elliptical hollow section beam-columns with varying aspect ratios", *Thin-Walled Structures*, 120, 9-28, https://doi.org/10.1016/j.tws.2016.10.013.

Yousuf, M., Uy, B., Tao, Z., Remennikov, A. and Liew, J.R. (2014). "Impact behavior of pre-compressed hollow and concrete filled mild and stainless steel columns", *Journal of Constructional Steel Research*, 96, 54-68, https://doi.org/10.1016/j.jcsr.2013.12.009.

Yu, W.W. (2000). "Cold-formed steel design", Ph.D. Thesis, University of Missouri-Rolla, https://www.wiley.com/en-us/cold-formed+steel+design%2c+5th+edition-p-9781119487418.

Zhang, X., Chen, Y., Shen, X. and Zhu, Y. (2019). "Behavior of circular cfst columns subjected to different lateral impact energy", *Applied Sciences*, 9(6), 1134, https://doi.org/10.3390/app9061134.

Zhu, A.Z., Xu, W., Gao, K., Ge, H.B. and Zhu, J.H. (2018). "Lateral impact response of rectangular hollow and partially concrete-filled steel tubular columns", *Thin-Walled Structures*, 130, 114-131, https://doi.org/10.1016/j.tws.2018.05.009.

Civil Engineering Infrastructures Journal 2025, 58(1): 71- 86
DOI: 10.22059/ceij.2024.360893.1928

RESEARCH PAPER

Comparison of Conventional and Energy Method in Evaluating the Seismic Fragility of Reinforced Concrete Frames

Javaheri Tafti, M.[1] and Haji Safari, M.[2*]

[1] Assistant Professor, Department of Civil Engineering, Taft Branch, Islamic Azad University, Taft, Iran.
[2] Ph.D. Candidate, Structural and Earthquake Research Center, Taft Branch, Islamic Azad University, Taft, Iran.

Received: 15 Jun. 2023; Revised: 20 Oct. 2023; Accepted: 08 Nov. 2024

ABSTRACT: This investigation aims at studying the energy method in calculating the exceedance probability of structures under seismic loads in reinforced concrete frames and its comparison with the conventional approach based on maximum story drift in structures. To do so, two reinforced concrete moment resisting frames with six and ten stories are designed based on the Iranian seismic code of practice and modeled nonlinearly with Perform software. Twenty near-fault earthquake records have been utilized to conduct the fragility analysis. The Incremental Dynamic Analysis (IDA) approach is used for the analysis and the IDA curves obtained from two methods are extracted and compared. The IDA curves resulted from the energy method provide this ability to calculate the elastic and plastic behavior zone and the instability point of the structure accurately. The output of the fragility analysis in reinforced concrete frames illustrates that the energy method can be utilized as an applicable approach in estimating the seismic fragility of the structures. The exceedance probability calculated in this approach is lower than the conventional method. The conventional method provides more conservative results in comparison to the energy method.

Keywords: Reinforced Concrete Moment Resisting Frame, Fragility Analysis, IDA Curve, Energy Method.

1. Introduction

There are various parameters to evaluate the behavior of structures. Parameters of displacement, rotation of plastic hinge, base shear, energy, etc., quantitatively and one-dimensionally express a seismic behavior. Fragility curves probabilistically express the behavior of the structure and exceed their performance levels.

The fragility curve defines the probability of exceeding an engineering demand parameter (such as drift) under specified boundary conditions (such as life safety) at different intensities of seismic loads (such as peak acceleration (Giordano et al., 2021; Hosseinlu et al., 2025).

Iteration of these operations for various seismic intensities or other single parameters would lead to normalized curves so-called fragility curves (Ge et al., 2021). Eq. (1) proposed by Barron-Corvera (2000) is used to demonstrate the conditional probability of exceeding the seismic

* Corresponding author E-mail: hs_m44@yahoo.com

response of the structure (R) from a particular performance limit state which is depicted by r_{lim} and is dependent on earthquake intensity (I):

$$\text{Fragility} = P\{R \geq r_{lim}|I\} \quad (1)$$

After choosing a few records in the IDA analysis approach, each of these records is scaled to specific intensities with equal steps and is exerted to the structure (Moradpour and Dehestani, 2021). The maximum dynamic response of the structure (usually the maximum drift) is extracted and creates the IDA curves with the maximum intensity corresponding to the earthquake records (Liu et al., 2021).

In a specific seismic load intensity (e.g. spectral acceleration, Sa) IDA curve suites illustrate the number of records by which the intended limit state is secured and the records by which the structural response has exceeded the limit state (Tavakoli et al., 2022). Fragility curves for structures have been developed with this argument (Afsar Dizaj and Kashani, 2022; Mesr and Behnamfar, 2023). In most previous studies, the maximum story drift parameter is considered as (R) or the Engineering Demand Parameter (EDP) and Immediate Occupation (IO), Life Safety (LS) and Collapse Prevention (CP), and limit states are assumed as r_{lim} (Moradi et al., 2022).

For instance, Xu and Gardoni (2016) probabilistically investigated the seismic fragility of reinforced concrete structures based on the maximum story drift and in various Sa intensities. Jalayer et al. (2015) developed the fragility of various structures using maximum story drift and PGA parameters as the structural response and seismic load intensity based on the linear regression method. Hancilar and Caktı (2015) conducted a research on the most suitable pair of earthquake intensity-engineering parameters in reinforced concrete structures. They concluded that the earthquake intensity-maximum story drift has better efficiency than other pairs of parameters. Del Gaudio et al. (2019) studied the drift fragility functions equation by estimating the damage in reinforced concrete structures under seismic load. They proposed a damage function based on the drift fragility approach. Hosseinpour and Abdelnaby (2017) studied the fragility of reinforced concrete structures under consecutive earthquakes using maximum story drift.

As it is obvious from the aforementioned studies, using story drift parameter as the EDP and limit states criteria proposed by regulations such as HAZUS and FEMA is a common and simple method in evaluating the fragility of structures (FEMA-356, 2000; Kircher et al., 2006). Moradi and Abdolmohammadi (2020) proposed an energy-based method in their study in which the dissipated plastic strain energy was used in the structure instead of using drift as EDP. They proposed that the Housner method can also be used to secure the limit states related to collapse prevention and life safety levels.

It was also illustrated that the elastic limit state and instability point can be determined by the energy method (Housner, 1960; Moradi and Abdolmohammadi, 2020).

Although the method of Moradi and Abdolmohammadi (2020) has been presented for a tall steel structure, the current study intends to assess this method on reinforced concrete structures and compare the fragility curves proposed by Moradi and Abdolmohammadi (2020) with the maximum story drift method to study whether it is possible to use this approach to evaluate the fragility curves of moderate and tall reinforced concrete structures or not. To do so, two reinforced concrete frames including six and ten stories are considered and the IDA curves from the maximum drift and strain energy are extracted and compared.

Eventually, the fragility curves for various limit states are calculated and compared through conventional and energy methods for these structures to evaluate the efficiency of the energy method in

determining the fragility of reinforced concrete frames.

2. Energy Balance

Earthquake is energy and in fact, during an earthquake, a large amount of energy reaches the structure. This energy, which is associated with ground shaking, causes vibration in the structure. Although force-displacement relationships (force balance) can also be used to investigate the dynamic response of the structure, but considering that earthquakes have an energetic nature, investigating this phenomenon with energy methods can be more useful. Nowadays, various methods are available for the analysis and design of structures, which one of them is the energy method. A structure would remain stable in case that the input energy (E_i) makes a balance with the internal energies in that structure (Moradi and Tavakoli, 2020). The internal energy in a structure consists of various energies including kinetic energy (E_k), dissipated energy through damping (E_i) and strain energy resulted from deformations.

The strain energy in a structure can be separated into potential energy (absorbed energy) (E_e) and dissipated energy (E_{in}) with respect to the deformation values (Goodarzi et al., 2023). The strain energy in the structure would be in form of absorbed energy if the deformations are within the elastic range and the strain energy would be the sum of potential and dissipated energy in the case that the deformations are within the plastic range.

Therefore, the energy balance in a structure can be defined as Eq. (2):

$$\begin{aligned} E_i &= E_k + E_{£} + E_e + E_{in} \\ E_k &= \frac{1}{2m\dot{u}^2} \\ E_{£} &= \int C\dot{u}^2 dt \\ E_e + E_{in} &= \int f_s du \\ E_i &= -\int m\ddot{u}_g du_g \end{aligned} \quad (2)$$

where C: is related to the damping coefficient, m: is mass, f_s: is the force, $\dot{u}$: is the velocity, u: is the displacement of structure, $\ddot{u}$: is the acceleration of the mass, and t: is time. Moradi and Abdolmohammadi (2020) proposed that the (E_{in}) parameter can be utilized as an EDP to assess the fragility of a structure. The dissipated energy in a structure has a direct relationship with the destruction level in the structure. The more the dissipated energy resulted from the plastic deformations in the structure is, the more damage the structure would experience during the seismic load. They proposed that in the case of using the plastic strain energy as EDP, the Housner (1960) method can be used for computing the limit states. This method is described in Section 4.

3. Model Properties

Reinforced concrete frames are used to achieve the goals of this investigation. For this purpose, concrete structures with moment resisting frame system with moderate ductility are considered with six and ten stories exposed to gravity loads according to loading guidelines and lateral loads according to the Iranian seismic code of practice (Standard No. 2800) with the aid of equivalent static method (Moradi et al., 2019). The specifications of gravity loads are depicted in Figure 1 and it is considered that the structure is located in a region with a high level of seismicity (A = 0.3 g) and on a soil type III.

It is assumed for 3D modeling and design of the structure that the structure has 4 spans with a length of 5 m each in both directions. The plan of the studied structure is demonstrated in Figure 1.

Table 1. Gravity load specifications (Moradi et al., 2020)

Parameter	Value	Unit
Dead load	600	Kg/m^2
Live load	500	Kg/m^2
Roof dead load	650	Kg/m^2
Snow	150	Kg/m^2
Roof live load	200	Kg/m^2

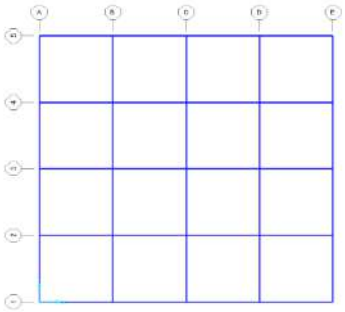

Fig. 1. Structural plan

After determination of gravity and lateral loads, the structure is modeled in SAP2000 v17 software and designed based on the Iranian concrete regulations and the required structural elements are achieved.

After computing the structural sections, the structure is controlled by checking some parameters such as relative inter-story drift. Furthermore, the materials specifications are illustrated in Table 2.

Table 2. Specifications of concrete and steel materials

Parameter	Value	Unit
Fc	2400000	Kg/m^2
Fy	34000000	Kg/m^2
Special weight	2400	Kgf/m^3

The structure is analyzed and designed after the modeling procedure and the specifications of sections for structural elements are depicted in Tables 3 and 4.

Table 3. Specifications of sections in the ten-story building

Story	Beam section	Column section
1-3	55×55	70×70 20 T 24
4-7	50×50	60×60 20 T 18
8-9	40×40	50×50 20 T 14

Table 4. Specifications of sections in the six-story building

Story	Beam section	Column section
1-3	50×50	60×60 20 fi 22
4-6	40×40	55×55 20 fi 16

After designing the structure and obtaining the sections, the middle frame of the plan is selected for conducting the nonlinear analysis and then the structure is modeled in Perform 3D software. The concentrated plastic hinge is used in defining the nonlinear behavior of the structure. It is considered that the structure has concentrated plasticity in critical regions and is elastic in other regions. The Iranian Guideline No. 360 is used for nonlinear modeling and the modeling values and acceptance criteria are selected based on this guideline. The behavior of structural elements in this model is according to the type of their internal work and the resulted force displacement curve is in form of force-controlled or displacement controlled condition. The force displacement curve can be an indication of ductile, semi-ductile or fragile behavior. The force-displacement curve in ductile behavior has four zones according to Figure 2a.

Finally, elastic and plastic values are combined and elements with elastic properties containing concentrated plasticity at the two ends are created. The modeled frames for six and ten-story structures are illustrated in Figure 3.

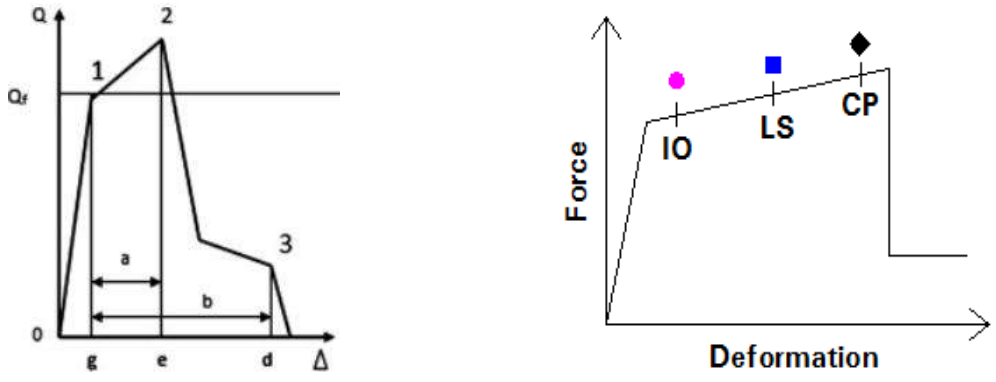

(a) **(b)**

Fig. 2. Force-deformation curve of the ductile element (Tavakoli and Afrapoli, 2018; Ugalde et al., 2019)

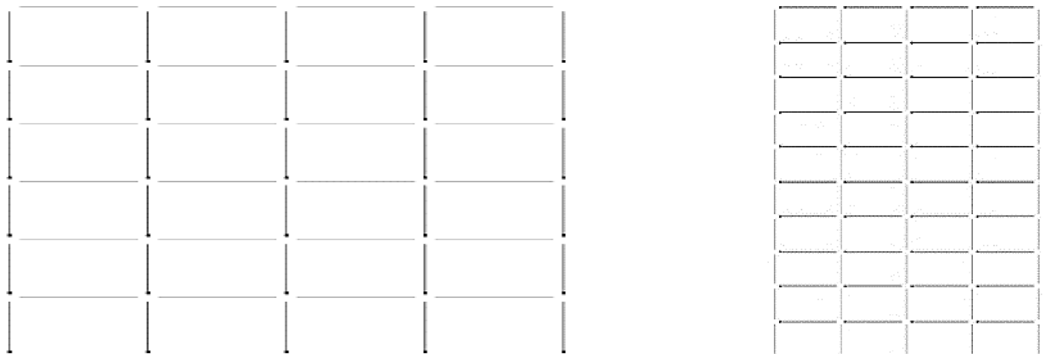

(a) **(b)**

Fig. 3. The modeled frames: a) Six-story frame; and b) Ten-story frame

4. Energy Method in Fragility Evaluation of the Structure

The steps of the approach proposed by Moradi and Abdolmohammadi (2020) for assessing the fragility of structures based on the plastic strain energy in the structure are presented in the following. In these steps, the required parameters for six and ten-story buildings are computed.

In various researches, many records have been used for IDA analysis. Generally, there are two methods for fragility analysis. Time history analysis and IDA analysis. In time history analysis, a larger number of records are used to perform the analysis and obtain the engineering demand parameter distribution.

In IDA analysis, a more limited number of records are used, but each record is scaled to many seismic intensities. IDA method has been used in this research. For this purpose, twenty seismic records have been used according to different references.

The AC parameter can be calculated based on Eq. (3) (Moradi and Abdulmohammadi, 2020).

$$E_t = \frac{1}{2}MS_v^2 = \frac{1}{2}M\left(\frac{T}{2\pi}S_a g\right)^2 \quad (3)$$

where M: is the structural mass, T: is period, S_a: is the spectral acceleration and g: is the gravity acceleration.

In various studies such as the report prepared by EERC in 1998, it was declared that the external work done by the system is equal to the elastic input energy multiplied by the energy modification factor (γ). γ: is dependent on ductility ratio (μ_s), ductility reduction factor (R_μ) and structural period (T) and is calculated as Eq. (4).

$$\gamma = \frac{2\mu_s - 1}{R_\mu^2} \quad (4)$$

where T_1 =0.57 and $T' = T_1.\sqrt{2\mu_s - 1}/\mu_s$ since all the parameters in Eq. (3) are constant except S_a, the value of (E_t) can be readily determined if a specific S_a can be defined for each performance level. μ_s and R_μ are shown in Table 5.

Table 5. Ductility reduction factor and the corresponding structural period range (Moradi and Abdolmohammadi, 2020)

Period range	Ductility reduction factor
$0 \le T < \frac{T_1}{10}$	$R_\mu = 1$
$\frac{T_1}{10} \le T < \frac{T_1}{4}$	$R_\mu = \sqrt{2\mu_s - 1}.\left(\frac{T_1}{4T}\right)^{2.513\log\left(\sqrt{2\mu_s-1}\right)^{-1}}$
$\frac{T_1}{4} \le T < T'_1$	$R_\mu = \sqrt{2\mu_s - 1}$
$T' \le T < T_1$	$R_\mu = \frac{T\mu_s}{T_1}$
$T_1 \le T$	$R_\mu = \mu_s$

Since tall buildings period range is more than (T_1), the ductility reduction factor is considered equal to the ductility factor. According to the Iranian seismic code of practice, the S_a can be considered as AB for LS performance level wherein A is the maximum design acceleration and B is the building response factor. The S_a value in CP performance level can be considered as 1.5 times of the Spectral Acceleration (SA) in LS performance level. Parameter of calculating AC for six and ten-story buildings in LS performance level is illustrated in Table 6.

For the CP performance level, the (E_{in}) values for six and ten-story buildings are calculated as 72325 and 129011 kg.m, respectively. Assessing the exceedance probability by comparing Steps 3 and 4. For each performance level, the value of dissipated strain energy in a specific intensity of seismic load in the structure is compared to the amount of allowable strain energy and its exceedance probability is calculated. Returning to Step 3 and computing the exceedance probability for other seismic load intensities. There are measures such as SA, Spectral Displacement (SD), Maximum Displacement Velocity (PGV) and Maximum Ground Acceleration (PGA) to measure intensity. Each of these parameters has its own characteristics.

Since in the past research in the field of fragility assessment with energy method, spectral acceleration and spectral displacement criteria have been used, in this research, it has been tried to calculate fragility from the perspective of ground acceleration. There is many research in the field of fragility curve that evaluated the fragility based on the maximum acceleration of the ground.

5. Seismic Load

The incremental time-history analysis is used in the current study. Twenty near-fault earthquake records is selected based on the recommendation of FEMA P695 for IDA analysis (Council, 2009). The specifications of these records are illustrated in Table 7. Near field earthquakes refer to the points of the earth whose distance from the surface center of the earthquake is less than a certain limit? The characteristics of this type of earthquake include the effect of progression, relative amplitude, pulse period and the number of pulses in the speed record (Sharma et al., 2020).

6. Assessing the Seismic Performance of the Structure

After the initial modeling, the seismic performance of two frames is studied in this section. The horizontal displacement curve of the roof in six and ten-story frames in various maximum accelerations of the Loma earthquake record is illustrated in Figure 4. According to this Figure, as it is expected, maximum rood horizontal displacement in the structure increases by increasing the maximum acceleration imposed to the structure. Residual displacement is one of the most important parameters that can be achieved from the roof horizontal displacement curve.

Table 6. Parameters of calculating ac for six and ten-story buildings for the ls performance level

Parameters	Unit	10-Story	6-Story
Period	s	1.2	0.75
A	-	0.35	0.35
B	-	1.75	2.5
Sa	-	0.6125	0.875
μ_s	-	1.85	1.52
R_μ	-	1.85	1.52
M	Kg	105000	63000
E_t	Kg.m	71914.21	37204
γ	-	0.788897	0.88
$E_{in(LS)}$	Kg.m	56732.9	33070

Table 7. Records specifications (Moradi and Abdolmohammadi, 2020)

ID No.	Lowest frequency (Hz.)	Record information	PGA max (g)
1	0.13	IMPVALL/H-E06_233	0.44
2	0.13	IMPVALL/H-E07_233	0.46
3	0.16	ITALY/A-STU_223	0.31
4	0.15	SUPERST/B-PTS_037	0.42
5	0.13	LOMAP/STG_038	0.38
6	0.13	ERZIKAN/ERZ_032	0.49
7	0.07	CAPEMEND/PET_260	0.63
8	0.10	LANDERS/LCN_239	0.79
9	0.11	NORTHR/RRS_032	0.87
10	0.12	NORTHR/SYL_032	0.73
11	0.13	KOCAELI/IZT_180	0.22
12	0.08	CHICHI/TCU065_272	0.82
13	0.06	CHICHI/TCU102_278	0.29
14	0.10	DUZCE/DZC_172	0.52
15	0.06	GAZLI/GAZ_177	0.71
16	0.13	IMPVALL/H-BCR_233	0.76
17	0.06	IMPVALL/H-CHI_233	0.28
18	0.13	NAHANNI/S2_070	0.45
19	0.13	LOMAP/BRN_038	0.64
20	0.25	LOMAP/CLS_038	0.51

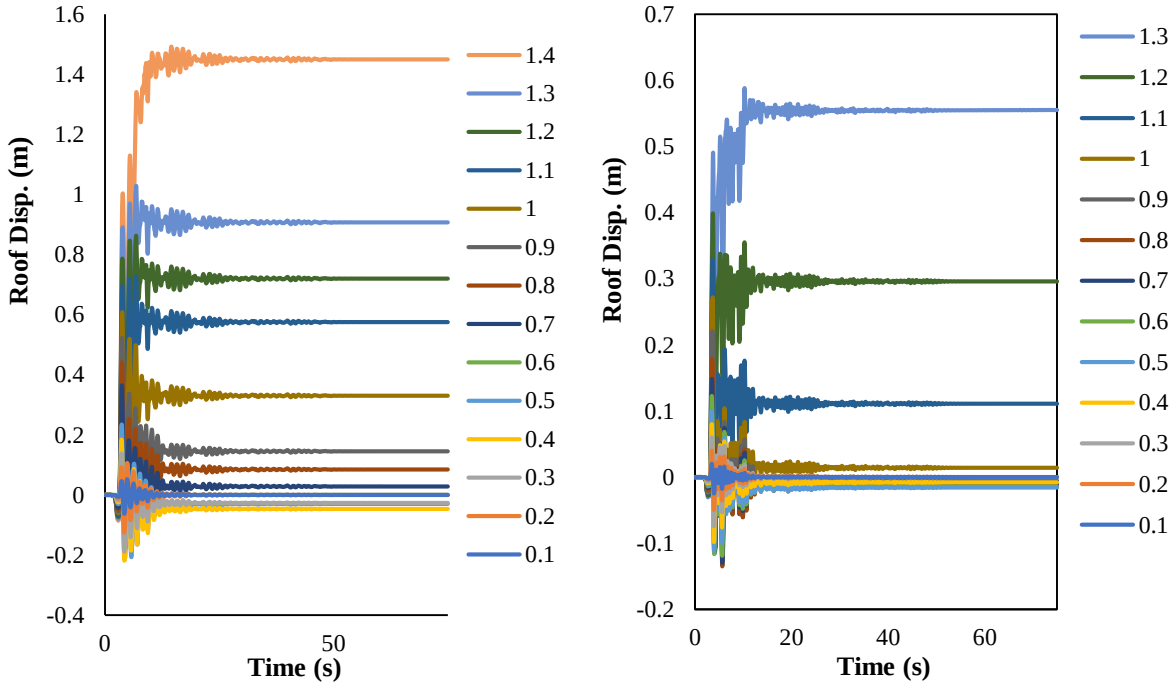

Fig. 4. Roof horizontal displacement: a) Ten-story building; and b) Six-story building

In the ten-story structure, the horizontal residual displacement remains zero until PGA = 0.6 g and increases hereafter. In the six-story building, the residual displacement remains zero until PGA = 0.5 g. Rising the residual displacement in the structure implies the growth of the dissipated plastic strain energy and damage in the structure.

The analyses results indicate that the residual displacement in the structures designed based on the Iranian seismic code of practice (standard 2800) occurs in the six-story building in a lower PGA in comparison to the ten-story structure. The time-history curve of the base shear in six and ten-story buildings is illustrated in Figure 5. Base shear is an indication of

structural capacity against seismic loadings. According to Figure 5, the base shear imposed to the ten-story structure is higher than that of the six-story structure and the maximum base shear of the structure increases by rising the PGA. The maximum drift curve of six and ten-story frames under Loma earthquake record is illustrated in Figure 6. In IDA analyses, the more the maximum story drift the structure has, the higher amount of response and performance would be in the structure. Based on the FEMA guideline, the values of 0.01, 0.02 and 0.04 as the drift limit are considered in IO, LS and CP performance levels. According to Figure 6, the amount of drift rises in the stories by increasing the maximum acceleration applied to the structure.

The maximum drift does not necessarily take place in a specific story in various maximum accelerations. For instance, in Figure 6a, the maximum story drift in the ten-story building occurs in stories 2-5 in various maximum accelerations while the maximum drift has taken place in stories 2 and 3 in the six-story building.

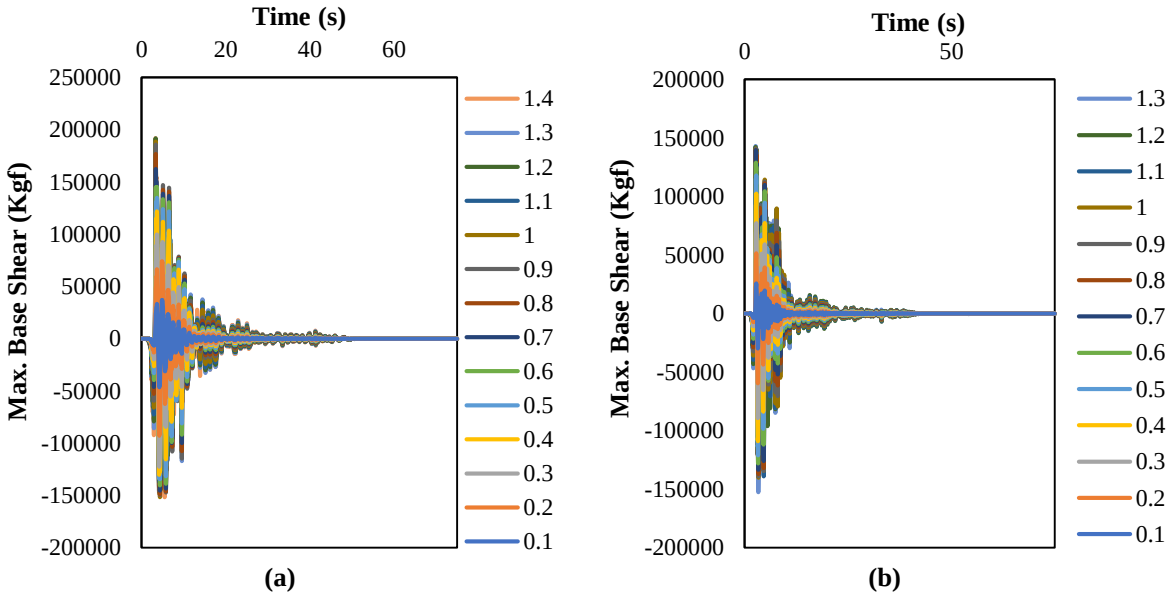

Fig. 5. Time-history curve of the base shear in the structure: a) Ten-story building; and b) Six-story building

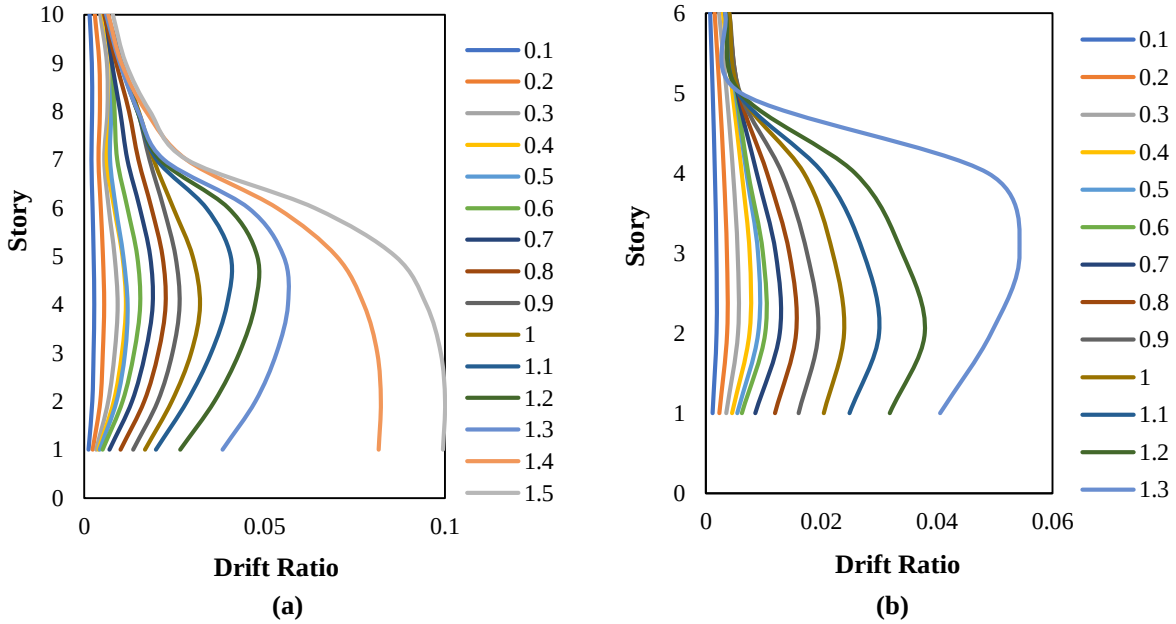

Fig. 6. The maximum drift curve of the structure: a) Ten-story building; and b) Six-story building

By applying the seismic load to the structure, the input energy should be equal to the internal energies in order to keep the stability of the structure. The input energy of the structure includes kinetic energy, absorbed strain energy, dissipated strain energy, and dissipated energy due to damping. The time-history curve of the energies for the six-story building in the maximum acceleration of 0.6 g is illustrated in Figure 7. The elastic strain energy starts from non-zero values with respect to this figure. This energy exists in the structure due to the gravity load and elastic deformations that occurred in the structure in form of potential energy before applying seismic load and increases by applying seismic load and making higher elastic deformations and its value fluctuates as far as the kinetic energy exists in the structure.

According to Figure 7, since the six-story building was not able to establish a balance in this maximum acceleration by kinetic and elastic energies and damping against the input energy due to the seismic load, the structure has employed its plastic strain energy capacity to create plastic deformations and the plastic strain energy has been formed in the structure. Based on Figure 7, the structure has been able to establish an energy balance against the input energy due to the seismic load by dissipating 8250 kg.m energy through plastic deformations, 3820 kg.m dissipated energy through damping, 5584 kg.m of elastic strain energy and 7027 kg.m of kinetic energy. To make the values of the dissipated strain energy in the structure meaningful, the plastic hinge rotation performance in the six-story structure under the Loma earthquake record in the maximum acceleration of 0.6 g is illustrated in Figure 8. According to this figure, no rotation is formed in the LS performance level in the structure and only a few beams have reached or exceeded the IO performance level (between IO and LS performance level).

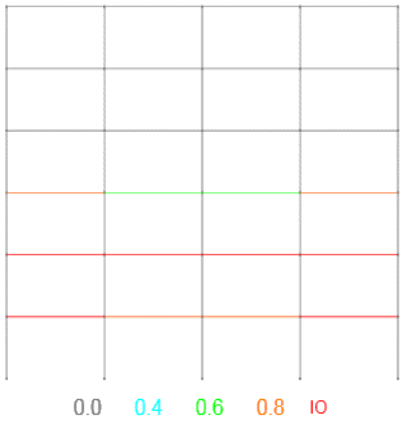

Fig. 7. Structural performance of the six-story building under Loma record with 0.6 g maximum acceleration

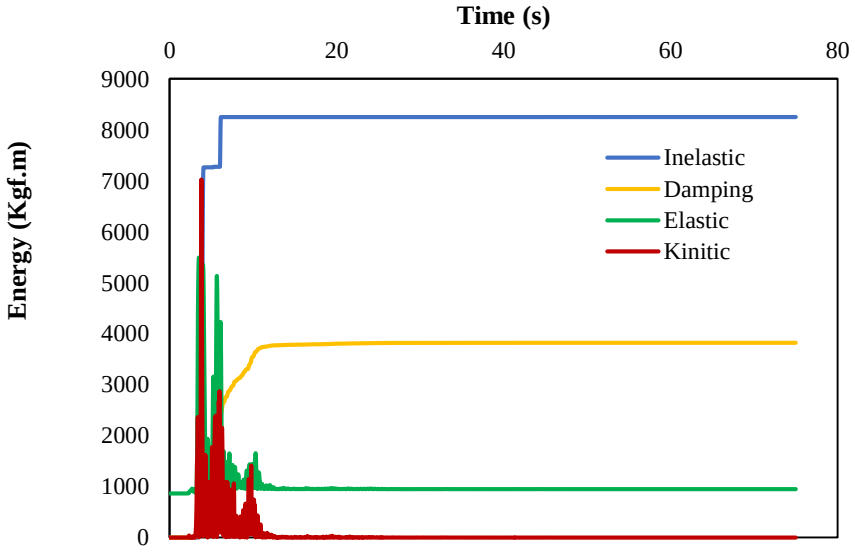

Fig. 8. Time-history curve of the internal energy in the six-story building under Loma record with PGA = 0.6 g

The time-history curve and performance of plastic hinges of the ten-story structure under the Loma earthquake record with the maximum acceleration of 0.7 g are also illustrated in Figures 9 and 10. The plastic strain energy in the structure indicating the measure of nonlinear deformations and damage exerted to the structure. The more the plastic strain energy is in the structure, the higher the damage and plastic hinge rotation would be in the structure. The time-history curve of plastic strain energy in six and ten-story buildings under the Loma earthquake record in various maximum accelerations is demonstrated in Figure 11.

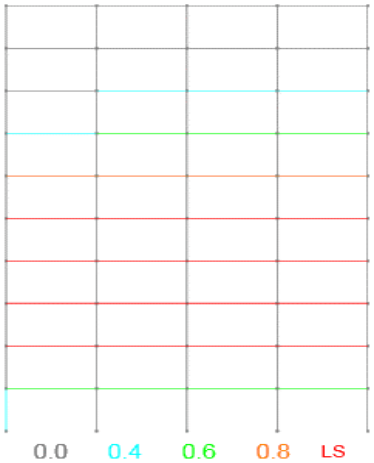

Fig. 9. Structural performance of the ten-story building under loma record with 0.7 g maximum acceleration

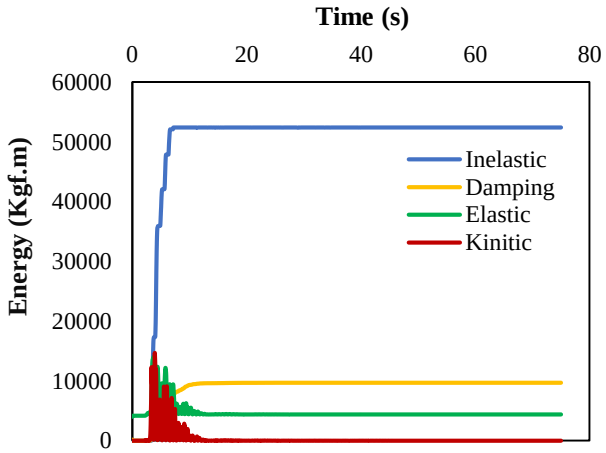

Fig. 10. Time-history curve of the internal energy in the ten-story building under Loma record with PGA = 0.7 g

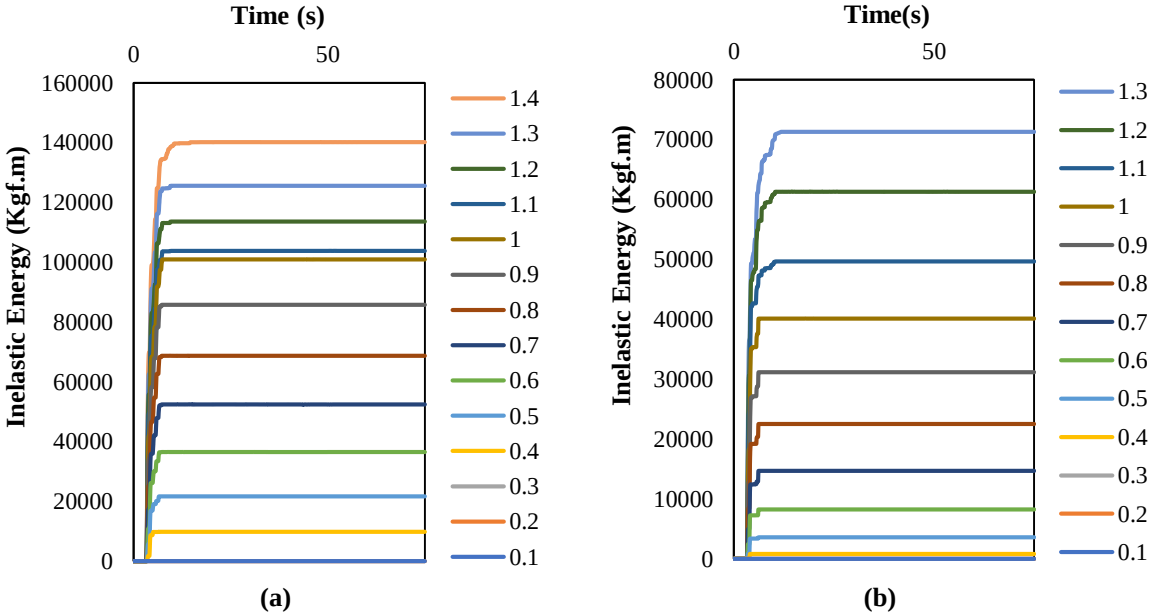

Fig. 11. Time-history curve of the plastic strain energy under Loma earthquake record in: a) Ten story; and b) Six story structures

According to Figure 11, the plastic strain energy measure in the structure increases by the rise of the acceleration value applied to the structure. These curves depict the amount of cumulative dissipated strain energy in the structure indicating the amount of energy dissipated in the structure until the x moment. Therefore, the time-history curve of the plastic strain energy in the structure has an ascending trend showing the amount of energy dissipated in a particular moment in the structure.

Roof displacement, base shear, maximum story drift and plastic strain energy parameters are studied in the structure, each of which can be used as EDP in assessing the fragility of the structure. The IDA and fragility curves of six and ten-story structures are calculated and compared in the following by considering the maximum base shear and plastic strain energy as EDP.

7. Incremental Dynamic Analysis

The IDA curves of six and ten-story buildings under specific earthquake records are illustrated in Figure 12 for the case that the maximum drift is considered as EDP. The PGA is used as IM with 0.1 g steps to conduct the IDA analysis and the analysis process continues if the drift reaches 0.1.

This form of presenting the IDA curves is a common method that is generally investigated before the fragility curve. This curve represents the variation trend of the structural maximum drift from lower values of IM until the instability moment. The IDA curves are presented in this section by considering the plastic strain energy as EDP for the studied structures. These curves are presented for six and ten-story buildings in Figure 13.

For a better evaluation of the IDA curves resulted from drift and energy methods, the curves achieved from the Imperial Valley earthquake record in the ten-story structure are separately compared (Figure 14). The IDA curves obtained from these two methods have the following differences:

- The IDA curve of the energy method starts from zero points however does not increase by the rise of acceleration and remains constant until a specific amount of acceleration. The zero value of the plastic strain energy in the structure illustrates that the structure has a perfectly elastic behavior and nonlinear deformations have not taken place in the structure while the IDA curve resulted from the drift method starts from zero and rises by increasing the acceleration. This curve has a linear behavior until a specific acceleration and exits the linear behavior hereafter.

Exceeding the linear state does not mean the exit of the elastic condition for this curve because the structure can become roughly nonlinear before this point but this curve cannot show the acceleration in which the structure enters the nonlinear condition.

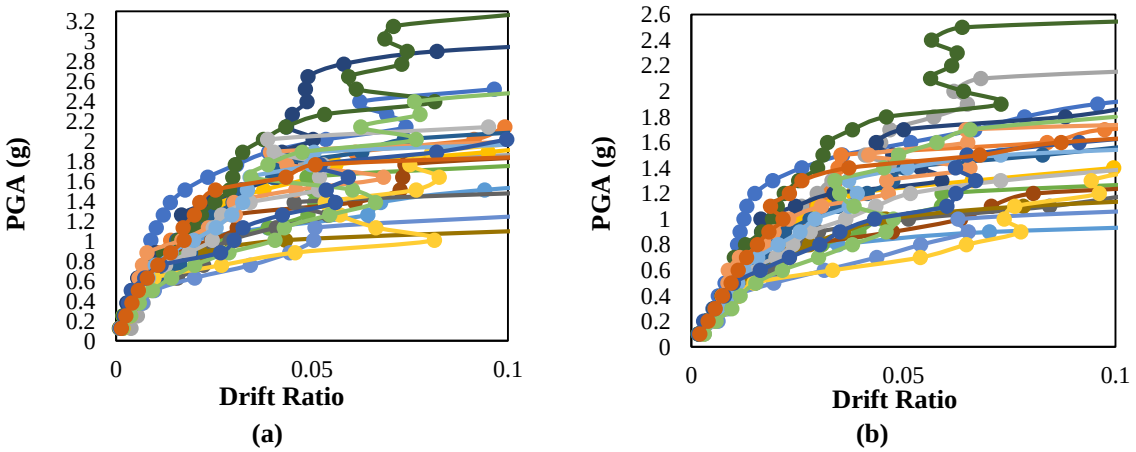

Fig. 12. IDA curve of the structures by considering the maximum drift as EDP: a) Ten-story building; and b) Six-story building

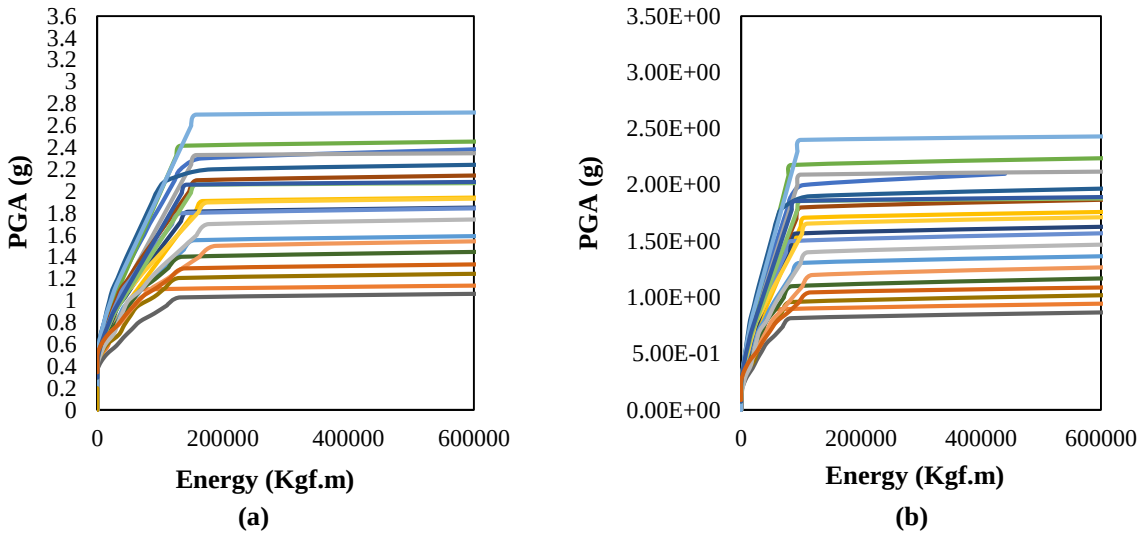

Fig. 13. IDA curve of the structures by considering the plastic strain energy as EDP: a) Ten-story building; and b) Six-story building

- The IDA curve obtained from the energy method after the elastic region (zero value) illustrates that the structure enters plastic deformations. After the elastic point, this curve would have an ascending trend and would never be constant or descending because by increasing the input energy, the structure is obliged to dissipate more plastic strain energy to reach equilibrium.

However, the IDA curve achieved from the drift method may not have an upward trend after the linear region and remain constant or have a downward trend. The reason for this phenomenon might be the occurrence of soft-story or changing the maximum drift of the structure from one story to another. However, these two curves in high accelerations in which the structure would reach the instability have a similarity. The energy and drift values would surge in the structure by increasing one or few acceleration steps. This immediate increase in drift or plastic strain energy can be described as the global instability of the structure. In most earthquakes selected in this study, instability point in two IDA curves corresponds with each other; however, there have been some records in which this point has discrepancies.

In this situation, the drift value has net reached 0.1 with an abrupt increase of the energy; in other words, the energy has not increased abruptly by reaching the drift to 0.1 value. Elastic points, performance levels calculated with drift and energy methods for the ten-story building and the instability point of the structure are illustrated in Figure 14.

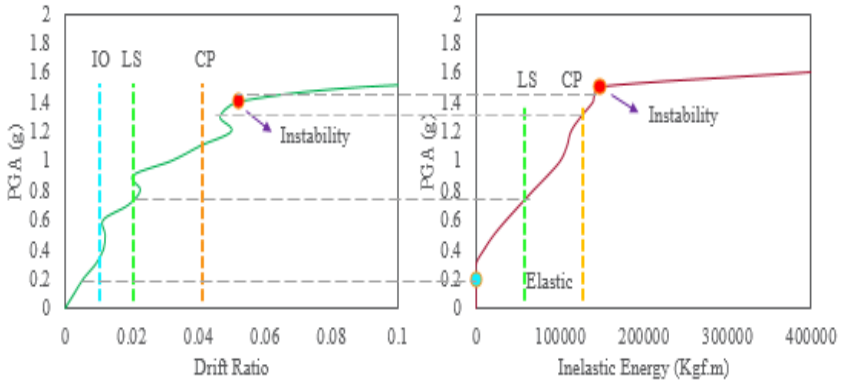

Fig. 14. Comparison of IDA curve under Imperial Valley record in ten-story building with drift and energy methods

The horizontal gray dash line in Figure 14 shows the comparison of elastic, LS, CP and instability points compared to the drift approach. These two methods present the same instability point in this specific record. The elastic performance level occurs in acceleration lower than the IO performance level. The highest difference in IDA curves in this record has taken place in CP performance level.

This level occurs in 1.3 g acceleration in the energy method and in 1.1 g in the drift method in the structure. The fragility curves of six and ten-story buildings with two different methods are compared in the following in order to examine the differences of these two methods in various performance levels.

8. Fragility Analysis

Fragility curves of the 2D frame of the ten-story reinforced concrete frame with two methods of drift and dissipated strain energy are illustrated in Figure 15. In this figure, the points are related to the exceedance probabilities which are calculated in various performance levels and the lines are related to the fitted curves with normal distribution function. The exceedance probability from elastic, LS, CP and instability are presented in the energy method while the exceedance probability from IO, LS, CP and instability is calculated in the drift approach.

For a better comparison, maximum acceleration values related to the 50% exceedance probability in various performance levels are compared. Maximum accelerations that show the 50% exceedance probability in three levels LS, CP and instability in drift method are 0.95 g, 1.35 g and 1.8 g, respectively. In this research, which is based on the energy method, it has been tried to express IDA curves based on the maximum acceleration of the ground (as a measure of intensity) and the plastic strain energy dissipated in the structure (as a parameter of engineering demand). In both methods, intensity measure is considered based on the maximum acceleration of the ground. This parameter is common in both methods.

For example, the IDA curve starts from zero by the drift method and increases immediately with the increase in the intensity of the seismic load. But in the energy method, up to a certain intensity, the value of the IDA curve is equal to zero. On the other hand, the performance levels obtained from two methods (such as LS and CP) have also been compared, which can be considered as a benchmark for comparison.

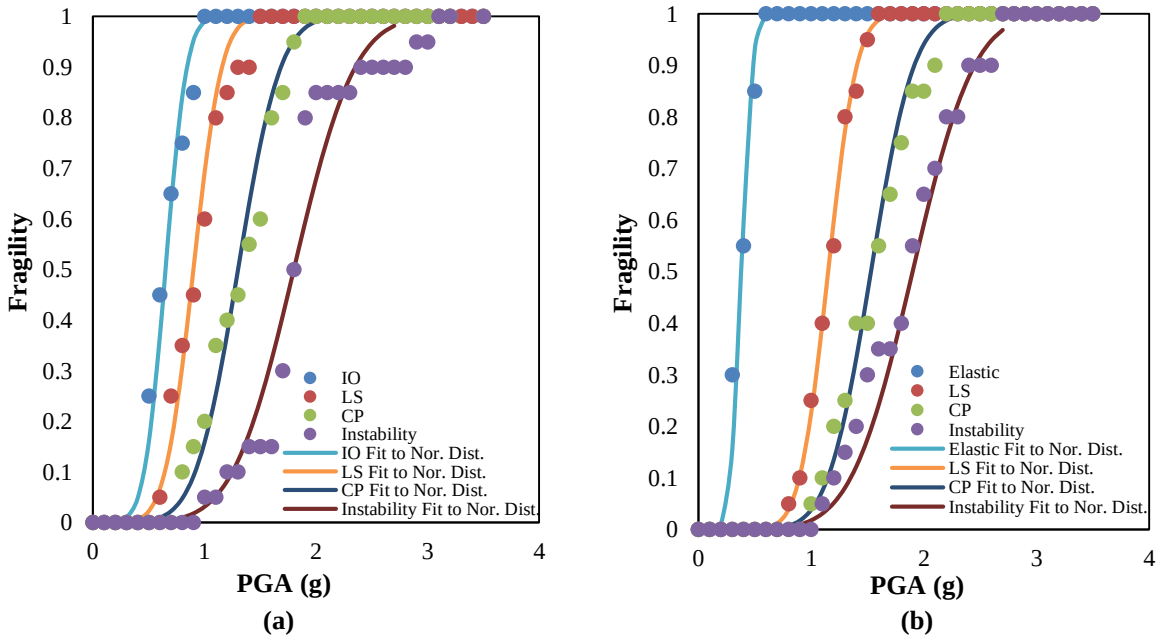

Fig. 15. Fragility curve of the ten-story structure with: a) Drift method; and b) Energy method

These values in the energy method are equal to 1.15 g, 1.52 g and 1.85 g, respectively. As it can be observed, the results achieved from the drift approach are more conservative than the energy approach. The fragility curves for the six-story building with drift and plastic strain energy have been illustrated in Figure 16. The maximum accelerations that show the 50% exceedance probability from three performance levels of LS, CP and instability point in the drift method are calculated as 0.7 g, 1.05 g and 4.5 g, respectively. These values for the energy approach are 0.85 g, 1.35 g and 1.55 g, respectively. As it is depicted, the exceedance probability resulted from the energy approach presents higher values in comparison to the drift method in the six-story building.

One of the advantages of the energy method compared to the drift method is that the exceedance probability from the elastic level can be calculated in the structures. Therefore, this method can be used for the structures for which the design seismic load is required to remain within the elastic range. For instance, the maximum exceedance probability (100%) from the elastic performance level in six and ten-story buildings takes place in the maximum acceleration of 0.4 g and 0.6 g, respectively, whereas the maximum exceedance probability from the IO performance level in these structures occurs in maximum accelerations of 0.7 g and 0.9 g, respectively. The ability to calculate the exceedance probability from the elastic level in structures is one of the advantages of this approach. The main limitation of this method is in evaluating the boundary conditions related to different performance levels.

Although the energy method is considered an excellent and perfect method in evaluating the probability of exceedance the elastic level, it can be associated with errors in other levels. In past research, Housner (1960) relationship has been used to calculate different levels of performance. Although this method is known as a definite and well-known method in the design of structures with energy methods, it can also be associated with errors in the evaluation of fragility curves. This method provides the amount of plastic strain energy at the design level. The main hypothesis of the energy method is that this input energy can make the structure reach the LS performance level. The same issue can be considered uncertainty in fragility assessment with the energy method.

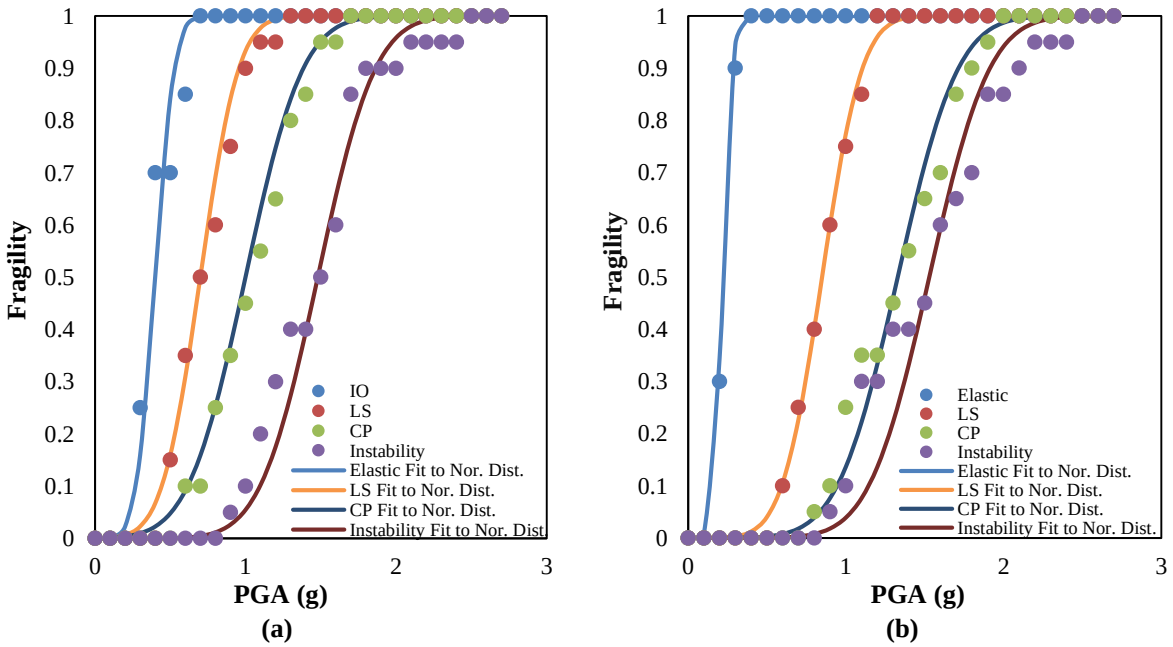

Fig. 16. Fragility curve of the six-story structure with: a) Drift method; and b) Energy method

The energy method has been proposed as a new method in assessing the fragility of structures. Structural design methods are changing from force methods to performance methods (Gardner, 2019). One of these performance methods is energy-based design. When the energy-based design method, which is considered as an efficient method, is included in the regulations, the energy-based fragility assessment method will be the most important tool for fragility analysis.

9. Summary and Conclusion

The aim of this study was to compare the fragility of six and ten-story reinforced concrete frames with the conventional and energy methods and to evaluate the possibility of using the energy method for reinforced concrete structures with moderate and short height. To do so, the seismic performance of frames was firstly studied. Then, the energy balance of internal and input energy due to seismic load was investigated. Afterward, the IDA curves based on energy method and inter-story drift were calculated and presented and their differences were discussed. At the end, the fragility of the frames was calculated for elastic, LS, CP and global instability damage levels in the energy method and compared with IO, LS, CP and global instability levels in the drift method.

The summary of the results are presented as follows:

- The maximum exceedance probability (100%) from the elastic performance limit in six and ten-story frames occurred in the maximum acceleration of 0.4 g and 0.6 g, respectively.
- Using the energy method represents higher values of fragility in a particular maximum acceleration compared to the drift method. In other words, the seismic fragility of the structures in the conventional method is more conservative than the energy method.
- The IDA curve resulted from the energy method is a curve with an ascending trend. This curve can obviously represent the performance point of the structure in the elastic zone.
- Since the drift value is the criterion of most guidelines in assessing the fragility of the structures, Ls and CP performance levels in the energy method can be transmitted to the drift method by modifying the Housner (1960) method and applying reduction factors which can be considered for further investigations.

10. References

Afsar Dizaj, E. and Kashani, M.M. (2022). "Nonlinear structural performance and seismic fragility of corroded reinforced concrete structures: modelling guidelines", *European Journal of Environmental and Civil Engineering*, 26(11), 5374-5403, https://doi.org/10.1080/19648189.2021.1896582.

Barron-Corvera, R. (2000). "Spectral evaluation of seismic fragility of structures" , State University of New York at Buffalo, Corpus ID: 15798216, http://civil.eng.buffalo.edu/~reinhorn/PUBLICATIONS/Reinhorn-Barron%20(2001)-%20ICOSSAR2001SpectP1.pdf.

Council, A.T. (2009). *Quantification of building seismic performance factors*, US Department of Homeland Security, FEMA, https://www.atcouncil.org/pdfs/FEMA-P695TOC.pdf.

Del Gaudio, C., De Risi, M.T., Ricci, P. and Verderame, G.M. (2019). "Empirical drift-fragility functions and loss estimation for infills in reinforced concrete frames under seismic loading", *Bulletin of Earthquake Engineering*, 17, 1285-1330, https://doi.org/10.1007/s10518-018-0501-y.

FEMA 356, F.E. (2000). "Prestandard and commentary for the seismic rehabilitation of buildings", Federal Emergency Management Agency: Washington, DC, USA, https://www.atcouncil.org/pdfs/FEMA356toc.pdf.

Gardner, L. (2019). "Stability and design of stainless steel structures-review and outlook", *Thin-Walled Structures*, 141, 208-216, https://doi.org/10.1016/j.tws.2019.04.019.

Ge, F.W., Tong, M.N. and Zhao, Y.G. (2021). "A structural demand model for seismic fragility analysis based on three-parameter lognormal distribution", *Soil Dynamics and Earthquake Engineering*, 147, 106770, https://doi.org/10.1016/j.soildyn.2021.106770.

Giordano, N., De Risi, R., Voyagaki, E., Kloukinas, P., Novelli, V., Kafodya, I., Ngoma, I., Goda, K.

and Macdonald, J. (2021). "Seismic fragility models for typical non-engineered URM residential buildings in Malawi", *Structures*, 32, 2266-2278, https://doi.org/10.1016/j.istruc.2021.03.118.

Goodarzi, M., Moradi, M., Jalali, P., Abdolmohammadi, M. and Hasheminejad, S. (2023). "Fragility assessment of an outrigger structure system based on energy method", *The Structural Design of Tall and Special Buildings*, 32(11-12), e2017, https://doi.org/10.1002/tal.2017.

Hancilar, U. and Caktı, E. (2015). "Fragility functions for code complying RC frames via best correlated im–edp pairs", *Bulletin of Earthquake Engineering*, 13, 3381-3400, https://doi.org/10.1007/s10518-015-9775-5.

Hosseinpour, F. and Abdelnaby, A. (2017). "Fragility curves for RC frames under multiple earthquakes", *Soil Dynamics and Earthquake Engineering*, 98, 222-234, https://doi.org/10.1016/j.soildyn.2017.04.013.

Housner, G.W. (1960). "The plastic failure of frame during earthquake", *Proceedings of 2nd WCEE*, VI, 997-1011, https://cir.nii.ac.jp/crid/1571135649126791296.

Jalayer, F., De Risi, R. and Manfredi, G. (2015). "Bayesian cloud analysis: Efficient structural fragility assessment using linear regression", *Bulletin of Earthquake Engineering*, 13, 1183-1203, https://doi.org/10.1007/s10518-014-9692-z.

Kircher, C.A., Whitman, R.V. and Holmes, W.T. (2006). "Hazus earthquake loss estimation methods", *Natural Hazards Review*, 7(2), 45-59, https://doi.org/10.1061/(ASCE)1527-6988(2006)7:2(45).

Liu, C., Fang, D. and Yan, Z. (2021). "Seismic fragility analysis of base isolated structure subjected to near-fault ground motions", *Periodica Polytechnica Civil Engineering*, 65(3), 768-783, https://doi.org/10.3311/PPci.15276.

Moradi, M. and Abdolmohammadi, M. (2020). "Seismic fragility evaluation of a diagrid structure based on energy method", *Journal of Constructional Steel Research*, 174, 106311, https://doi.org/10.1016/j.jcsr.2020.106311.

Moradi, M. and Tavakoli, H. (2020). "Proposal of an energy based assessment of robustness index of steel moment frames under the seismic progressive collapse", *Civil Engineering Infrastructures Journal*, 53(2), 277-293, https://doi.org/10.22059/ceij.2019.283574.1591.

Moradi, M., Tavakoli, H. and AbdollahZade, G. (2020). "Sensitivity analysis of the failure time of reinforcement concrete frame under postearthquake fire loading", *Structural Concrete*, 21(2), 625-641, https://doi.org/10.1002/suco.201900165.

Moradi, M., Tavakoli, H. and Abdollahzadeh, G. (2019). "Probabilistic assessment of failure time in steel frame subjected to fire load under progressive collapses scenario", *Engineering Failure Analysis*, 102, 136-147, https://doi.org/10.1016/j.engfailanal.2019.04.015.

Moradi, M., Tavakoli, H. and Abdollahzadeh, G.R. (2022). "Collapse probability assessment of a 4-story RC frame under post-earthquake fire scenario", *Civil Engineering Infrastructures Journal*, 55(1), 121-137, https://doi.org/10.22059/ceij.2021.313241.1718.

Moradpour, S. and Dehestani, M. (2021). "Probabilistic seismic performance of steel structures with FVDs designed by DDBD procedure", *Journal of Building Engineering*, 43, 102581, https://doi.org/10.1016/j.jobe.2021.102581.

Sharma, V., Shrimali, M.K., Bharti, S.D. and Datta, T.K. (2020). "Behavior of semi-rigid steel frames under near-and far-field earthquakes", *Steel and Composite Structures, an International Journal*, 34(5), 625-641, https://doi.org/10.12989/scs.2020.34.5.625.

Tavakoli, H. and Afrapoli, M.M. (2018). "Robustness analysis of steel structures with various lateral load resisting systems under the seismic progressive collapse", *Engineering Failure Analysis*, 83, 88-101, https://doi.org/10.1016/j.engfailanal.2017.10.003.

Tavakoli, H., Moradi, M., Goodarzi, M. and Najafi, H. (2022). "Outrigger braced system placement effect on seismic collapse probability of tall buildings", *Civil Engineering Infrastructures Journal*, 55(2), 259-276, https://doi.org/10.22059/ceij.2022.319629.1744.

Ugalde, D., Parra, P.F. and Lopez-Garcia, D. (2019). "Assessment of the seismic capacity of tall wall buildings using nonlinear finite element modeling", *Bulletin of Earthquake Engineering*, 17, 6565-6589, https://doi.org/10.1007/s10518-019-00644-x.

Xu, H. and Gardoni, P. (2016). "Probabilistic capacity and seismic demand models and fragility estimates for reinforced concrete buildings based on three-dimensional analyses", *Engineering Structures*, 112, 200-214, https://doi.org/10.1016/j.engstruct.2016.01.005.

Civil Engineering Infrastructures Journal 2025, 58(1): 87-102
DOI: 10.22059/ceij.2024.365671.1966

RESEARCH PAPER

Forecasting Bearing Capacity, Error Analyses and Parametric Analysis of Circular Footing Seating on the Limited Thick Sand-Layer with Eccentric-Inclined Load

Gnananandarao, T.[1*], Naik, C.S.[2], Onyelowe, K.[3] and Panwar, V.[4]

[1] Ph.D., Department of Civil Engineering, Aditya College of Engineering and Technology, Surampalem, Andhra Pradesh, India.
[2] Ph.D. Candidate, Department of Civil Engineering, Indian Institute of Technology Roorkee, Uttarakhand, India.
[3] Associate Professor, Department of Civil Engineering, Michael Okpara University of Agriculture, Umudike Umuahia, Nigeria.
[4] Ph.D., Department of Civil Engineering, National Institute of Technology, Hamirpur, Himachal Pradesh, India.

Received: 22 Sep. 2023; Revised: 13 Dec. 2023; Accepted: 14 Jan. 2024

ABSTRACT: Bearing Capacity (BC) of the soil is one of the crucial parameters to construct any structure. A consistent soft computing models can reduce the cost and time by swiftly generate the required experimental data. This research presents, M5P model tree and feedforward backpropagation ANN model have been used to predict the BC of the circular footing resting on the limited thick sand-layer with eccentric-inclined load. To generate the proposed model, a set of 120 data are gathered from the literature. The results of M5P model tree achieved a coefficient of determination (R^2) of 0.96 for both training and testing phases. The Mean Absolute Percentage Error (MAPE) was 19.83% for training and 21.46% for testing. Whereas, for ANN model, R^2 is 0.98 and 0.97; MAPE is 18.20 and 16.29 for training and testing, respectively. The R^2 and MAPE results reveals that, the ANN model is better substitute method for predict the BC of the Circular Footing (CF) resting on the limited thick sand-layer with eccentric-inclined load than the M5P model. Further, model equations are developed to calculate the BC of the circular footing for the both the methods. Finally, sensitivity analysis concludes that the input parameter ratio of depth of the rigid rough base to width of footing (H/B) is the most influencing parameter to predict the desired output.

Keywords: Circular Footing, Sand, Bearing Capacity, Eccentric-Inclined Load, M5P Model Tree, ANN, Sensitivity Analysis.

1. Introduction

Shallow footings are most commonly used foundations in the construction of the buildings due to its low cost. The Bearing Capacity (BC) of uniform soil with normal/eccentric/eccentric-inclined load on all regular shaped footings (strip, square, circular and rectangular) was well established (Terzaghi, 1973; Vesic, 1973).

* Corresponding author E-mail: anandrcwing@gmail.com

However, a significant effect on the bearing capacity can be observed as the hard soil strata within a limited depth below the footing. In some real-time conditions, a limited thick soil stratum can be observed beneath the bedrock. In such situations, load carrying capacity of the shallow footing situated on the soil strata can be influenced by the boundary of the rigid bedrock.

A Finite Element Analysis (FEA) performed on the strip footing was positioned on sand under eccentric inclined load to determine the BC by Loukidis and Ygeionomaki (2017). Later, Sethy and Patra (2019) reported about the shallow circular footings resting on the limited thick sand-layer with eccentric-inclined load. Further, Sethy et al. (2020) conducted a simulation study on the same footing of Sethy and Patra (2019) by using FEA and Plaxis3D software. However, the process of physical and FEA needs enormous specialties and time. Now a days soft computing techniques playing a major role in reducing the time and cost.

From the past decade, machine learning techniques play a significant role in geotechnical engineering for forecasting, planning, and management of the non-linear data sets. As an example, Dutta et al. (2015) used an artificial neural network to forecast the deviator stress of sand blended with waste plastic strips (strip thickness: 0-5 mm thick). Initially, for forecasting the deviator stress eight input parameters were considered, after conducting the sensitivity analysis lest effected three input parameters were excluded and forecasted with five input parameters. The model having five input parameters forecast the deviator stress better than the previous eight input parameters model. The cohesion of limestone following Artificial Neural Networks (ANN) and ANN with Genetic Algorithm (GA) estimated by Ebid et al. (2021) and Khandelwal et al. (2018). The study concludes that, the GA-ANN model predicts the cohesion of the limestone more precisely than the ANN and multiple regression. ANN approach was used for the forecasting the resilient modulus of granular material (Saha et al., 2018). In this study seven physical properties of the granular material were used as an input parameter to predict the resilient modulus. The study concludes that; the developed ANN model is much superior than the regression model in predicting the resilient modulus.

A research on the forecasting the BC of square footing resting on c-ϕ soil slope was done by Acharyya et al. (2020), where, two ANN model equations were proposed for predicting the BC and settlement of multi edges structural skirted footing positioned on the sand. Similarly, different studies performed on the forecasting the BC of rectangular footing on layered sand under inclined loading (Panwar, 2022); under-reamed piles compression capacity on sand and clay (Thottoth et al., 2024); cyclic load-induced settlement of strip footing on granular soil (Sasmal and Behera, 2021); BC for strip footing situated near sloping ground (Acharyya and Dey, 2019); unconfined compressive strength of fly ash stabilised organic clay (Gnananandarao et al., 2022); quarry dust modified unsaturated soil erodibility (Onyelowe et al., 2021) and erodibility of stabilized unsaturated lateritic soil (Onyelowe et al., 2022) using different soft computing techniques such as random forest regression, M5P model tree, SVM with different kernels and Artificial Neural Networks; the settlements of a raft reinforced with geogrid and geocell were predicted using ANN modelling with the help experimental data by Kumar et al. (2023).

The purpose of this article is to offer a strategy for forecasting the BC of circular footing resting on the limited thick sand-layer with eccentric-inclined load. The M5P model tree and ANN are utilized for present study. The data utilized in this study is collected from the published literature containing BC of circular footing and some other parameters. The total collected data sets are 120. This wide-ranging set of data

can be sufficient for developing a model and predicting the desired output (Acharyya and Dey, 2019).

2. M5p Model Tree

The M5 tree algorithm was proposed by Quinlan (1992) and it had been refined and renamed as a M5P algorithm (Wang and Witten, 1997). The major advantage of the model trees is that, they are having capability to handle the large sets of data, each with a different set of variables and dimensions. They are renowned for their ability to deal with missing data as well.

The M5P model architecture has depicted schematically in Figure 1. The M5P model begins with separating the input data into distinct sub sets, each sub-set has data records with a sharing feature (Figure 1a).

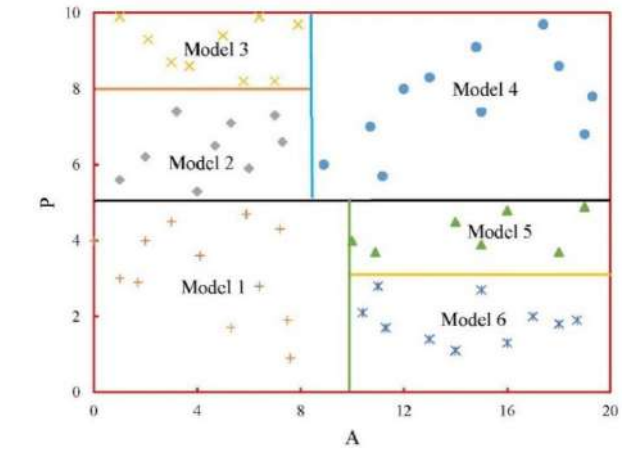

(a)

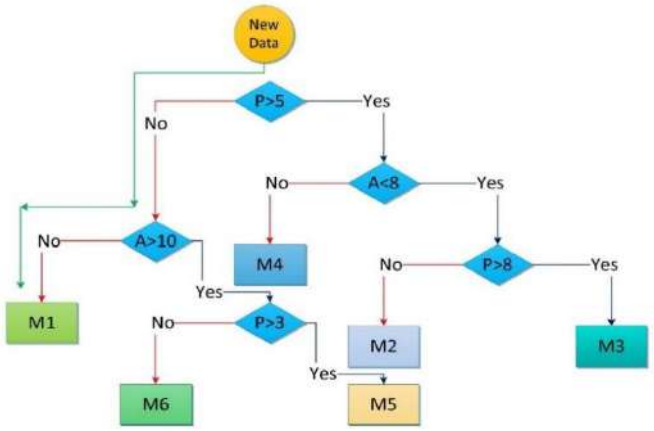

(b)

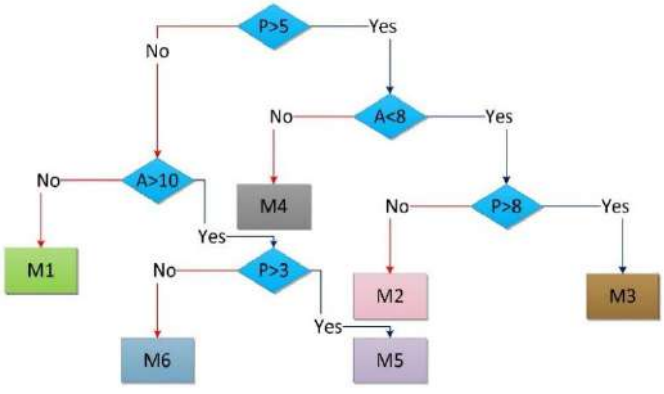

(c)

Fig. 1. The schematic view of the M5P model tree algorithm

To overcome the difference within the defined sub-set, Linear Regression Models (LRM) might be employed in this procedure. The information gathered in the preceding stage is then utilized to generate numerous nodes, each of which is segregated accord with the certain attribute (Figure 1b). This phase leads to construct a structure as like tree with the roots and leaves presented as top and bottom, respectively. New datasets are added to the tree. It progresses from the roots through the nodes until they reach to each leaf (Figure 1c). A math logical algorithm at every node helps the set of data to make its way to reach a leaf by validating a specified given set's value of data file containing the split value. This procedure enables the knowledge to be extracted from the tree model.

The M5P technique, which is an enhanced version of the M5 technique, has four basic phases. To form a tree, the input sets are dividing into multiple sub-sets in the first stage. The splitting criterion is used to reduce intra-subspace variation from the roots to the nodes. The variability is measured by the Standard Deviation (Stan. Dev.) values that reach the nodes. The Stan. Dev. reduction factor is used to develop the tree, which maximizes the expected reduction in error at each node, as shown in Eq. (1).

$$S.D.R = sd(S\ ) - \sum_i \frac{S_i}{|S|} \times sd(S_i) \qquad (1)$$

where *S.D.R*: Stan. Dev. reduction; *S*: A group of data that is received by the node; S_i: Splitting the node based on an attribute generated set; and *sd*: is standard deviation.

The SDR equation was proposed by Wang and Witten (1997). However, having constructed the tree, when it comes to phase two, using the data related to each sub-space, in each sub-space, a LRM is constructed. At the time, to overcome the problem of overtraining, a pruning strategy is used. When the SDR for a LRM at the root of a subtree is lower than the predicted error for the subtree, an overtraining problem emerges. However, the pruning procedure can result in severe incompatibilities among neighboring LRM.

The smoothing technique is performed in the final phase to correct for this issue. To develop the final model for the leaf, the smoothing procedure integrates all of the models from the leaf to the root. The anticipated result of the leaf is processed as it returns to the root in this procedure. This value is combined with the LRM's anticipated value as follows for that node.

$$E' = \frac{ne\ + ka}{n\ + k} \qquad (2)$$

where *E*: is the estimated value, forwarded to the next higher node; *e*: is the estimated forwarding from below to the current node; *a*: is the model's estimated value for this node; *n*: is the number of training samples; and *k*: is a constant.

3. Artificial Neural Networks

An artificial neural network is comprised of multiple layers of neurons, where each layer is connected to the subsequent layer. The neurons in each layer receive inputs from the previous layer, and then calculate an output based on those inputs and their own weights and biases. The outcome from the resulted layer i.e., last layer is the final network output. In this research, the backpropagation algorithm is employed to train feedforward neural networks. This method involves iteratively fine-tuning the network's weights and biases to minimize the disparity between its output and the intended outcome. The process involves transmitting the error in reverse through the network, starting from the output layer and moving towards the input layer. The error at each neuron is then used to adjust the weights and biases of that neuron, in order to reduce the error in the next layer. The backpropagation algorithm is a powerful tool for training feedforward neural networks. It is comparably straightforward to put into practice, and it can be employed

for training networks containing a substantial quantity of neurons. However, the algorithm can be slow to converge, especially for large networks. The flow of the ANN is presented in the Figure 2.

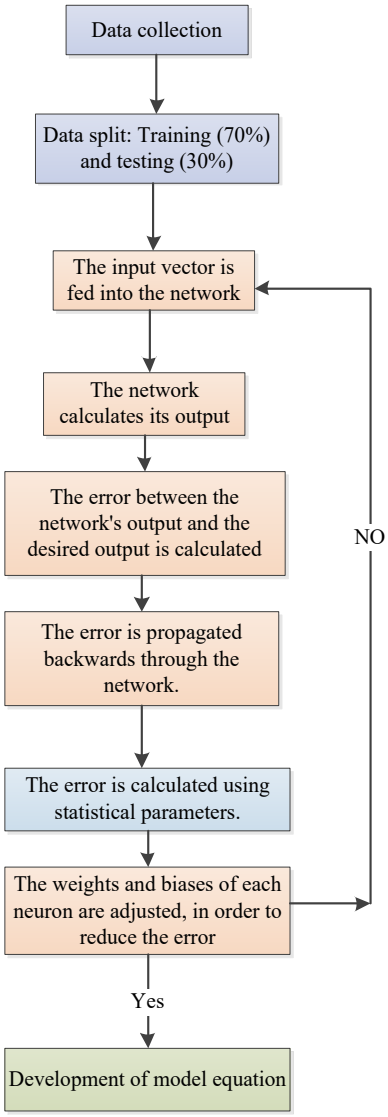

Fig. 2. Flowchart of the ANN model

4. Data Set

In the present research the total of 120 data points were collected from peer-reviewed literature (Sethy et al., 2020b). The data used in this study was generated through Plaxis3D software, employing both the Mohr-Coulomb (MC) model and the Hardening Soil (HS) model in the Finite Element Method (FEM). These FEM results were then compared to the laboratory experimental results conducted by Sethy et al. (2019). The outcomes from both the MC and HS models showed good agreement with the experimental results as reported by Sethy et al. (2020b). The differences between the results obtained in that study and those from previous research were found to be within a range of ± 20%. This compared comprehensive dataset was employed to predict the Bearing Capacity (BC) of a circular footing placed on a sandy layer with limited depth. The footing was subjected to eccentric-inclined loading during the analysis. The data consists of four attributes such as *H/B*, *a/f*, *e/B* and q_u where *H, B, a, f, e* and q_u: are depth of the rigid rough base, width of footing, load of inclination, angle of internal friction of soil, load eccentricity, and ultimate bearing capacity, respectively. The first three non-dimensional parameters (*H/B, a/f* and *e/B*) were used as an input parameter (q_u) in both the M5P model tree and ANN and the fourth parameter was used as an output parameter.

The range of data for the parameters for input and output are shown in Table 1. Further, typical input as well as output parameter ranges are depicted in the Figure 3 in terms of the histogram. Nevertheless, out of the entire dataset, 70% of the data was employed for training purposes, while the remaining 30% was allocated for testing.

Table 1. Data set for M5P and ANN modelling

Range of data	Input and output parameters			
	H/B	***α/ϕ***	***e/B***	***q_u* (kN/m^2)**
Minimum	0.3	0	0	42.5
Maximum	5.5	0.489	0.15	880
Stan. Dev.	1.80	0.17	0.06	190.07

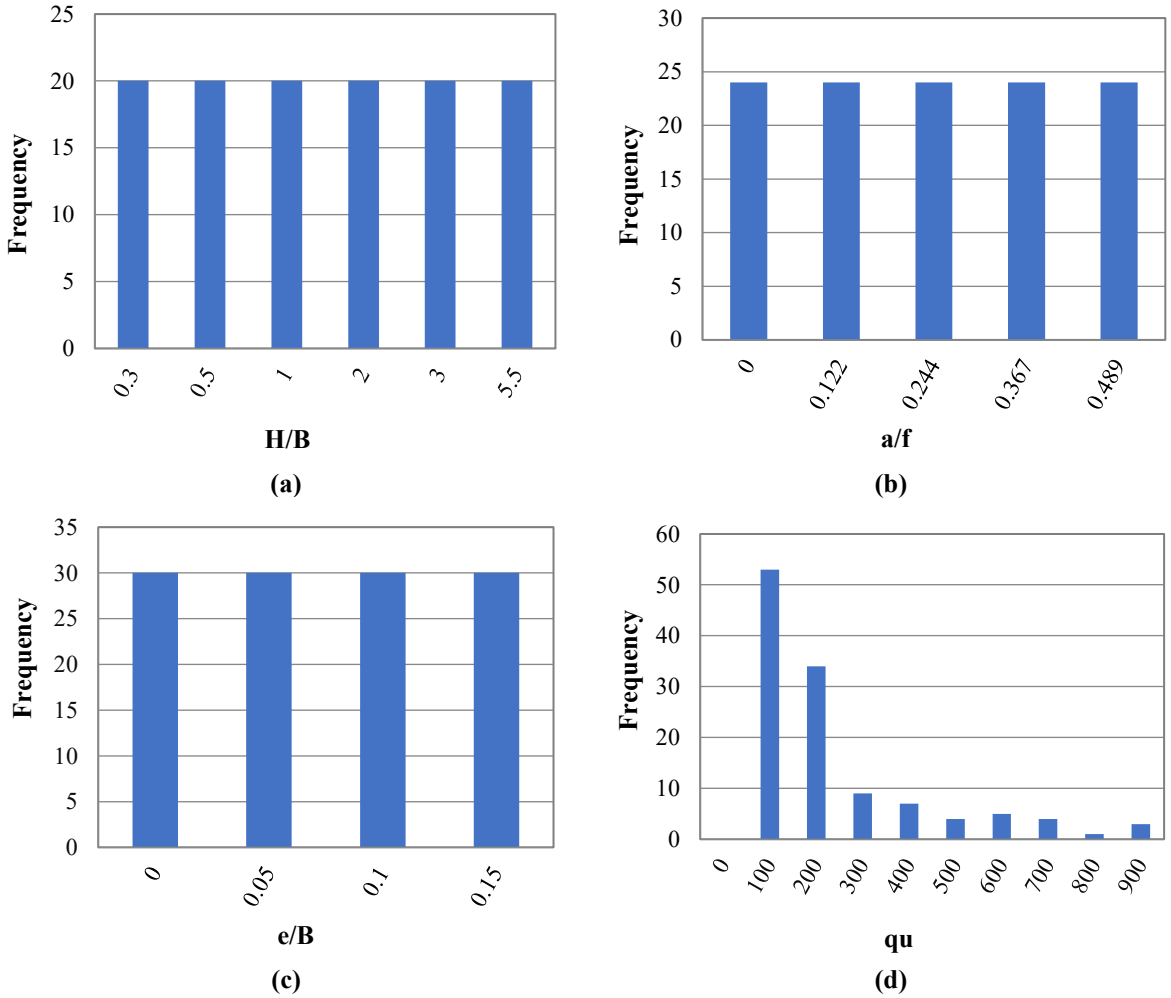

Fig. 3. Histograms of the data set: a) H/B: b) a/f; c) e/B; and d) q_u

5. Development of M5p Model Tree

To forecast the circular footing's BC on the limited thick sand-layer with eccentric-inclined load, many factors that may affect such as relative density, unit weight, soil friction angle, footing width, footing depth, sand layer limited thickness depth, type of footing material and so on. To attain the precise model, all these parameters need to be considered. However, it is exceedingly difficult to consider each specific attribute in the model in order to attain the desired output. Hence, majorly effecting parameters are converted in to the non-dimensional and used as an input parameter.

These non-dimensional parameters can also avoid the scaling impact of the circular footing. In the initial stage of this research, the function for estimating ultimate BC can be written as follows:

$$q_u = f\left(\frac{H}{B}, \frac{\alpha}{\phi}, \frac{e}{B}\right) \tag{3}$$

where, *H/B*, *a/f* and *e/B*: are no-dimensional parameters and the parameters already defined in the previous section.

6. Statistical Parameters of Error Analysis

The developed prediction model in the present study to forecast the BC of circular footing on the limited thick sand-layer with eccentric-inclined load developed by 120 data points gathered from the literature. There is no harmony among scholars when it comes to determining the desired level of prediction accuracy. Then, the quality prediction accuracy has become a major criterion. It was accomplished only after minimizing the error in the prediction (Ito,

1994; Sarle, 1995). In this paper, six statistical parameters were used such as: Mean Absolute Percentage Error (MAPE); Mean Square Error (MSE); Root Mean Square Error (RMSE); Mean Absolute Error (MAE); coefficient of correlation (r); and coefficient of determination (R^2).

MAPE can measure the relative performance among the various methods. Based on the calculated MAPE value the prediction accuracy is said to be good (MAPE between 10 to 20%), poor (MAPE between 20 to 50%) and inaccurate (MAPE over 50%) (Dutta et al., 2015). It is, not only provides the prediction quality, but also independent on the units of the measurements of the variable.

The calculated MSE gives accuracy measures as well as indications of the degree of dispersion; larger errors were given extra weight (Dutta et al., 2015). The squared difference among anticipated and actual observed data is taken into account by MSE in order to calculate the difference among predicted and observed data (Dutta et al., 2015). The root of MSE is the RMSE. It has the advantage of measuring within the same unit as the forecasted variables.

The MAE is one of the statistic parameters that determines overall accuracy and indicates the extent of the spread. All errors were also given the same importance when trying to calculate MAE. MAE is minimal (≈ 0) for perfect data fit and considerable for poor data fitting (Dutta et al., 2015). In comparison to MAE, MSE aggressively penalizes significant errors. MAE is determined by calculating from the same unit as MSE and RMSE, but large prediction errors are given less weight.

Further, the effectiveness of soft computing models is generally deciphered by coefficient of correlation 'r' and coefficient of determination 'R^2'. The evaluation of this method is skewed. As a result, in addition to the unbiased statistical criteria, extra unbiased statistical criteria should be utilized. The predictive models with a 'r' and a 'R^2' closer to one stand for good predictions.

The intensity of the forecasting errors can be measured using the MAPE, MSE, RMSE, and MAE. RMSE and MSE have historically been popular due to their theoretical importance in statistical modelling. Nonetheless, certain researchers caution against utilizing them for assessing predictive precision due to their heightened susceptibility to deviations compared to MAE. Moreover, MAE and RMSE can also be utilized in tandem to discern the spread of errors within a prediction set. Always, the RMSE shall outweigh or be equivalent to the MAE.

As the gap between RMSE and MAE widens, the variance in individual errors within the dataset also increases. Moreover, when RMSE is equivalent to MAE (both ranges 0 to ∞), all errors share the same magnitude. RMSE and MAE can be called as negative score's, with lower values being preferable. Besides, MAE can be regarded as a 'strong' measure for the output accuracy i.e. for prediction. The choice of an error measure has a significant impact on the results, which forecasting approaches are the generally accurate.

The mentioned statistical parameters and their mathematical is expressed as follows:

$$MAPE = \left[\frac{1}{n}\sum_{i=1}^{n}\left|\frac{q_{u_{ti}} - q_{u_{pi}}}{q_{u_{ti}}}\right|\right]\times 100 \tag{4}$$

$$MSE = \frac{1}{n}\sum_{i=1}^{n}\left(q_{u_{ti}} - q_{u_{pi}}\right) \tag{5}$$

$$RMSE = \sqrt{\frac{1}{n}\sum_{i=1}^{n}\left(q_{u_{ti}} - q_{u_{pi}}\right)} \tag{6}$$

$$MAE = \frac{1}{n}\sum_{i=1}^{n}\left|q_{u_{ti}} - q_{u_{pi}}\right| \tag{7}$$

$$r = \frac{q_{u_t}.q_{u_p} - n\overline{q_{u_t}.q_{u_p}}}{(n-1)\mathrm{S}_{q_{u_t}}\mathrm{S}_{q_{u_p}}} \tag{8}$$

$$R^2 = 1 - \frac{\sum_i\left(q_{u_{pi}} - \frac{1}{n}\sum_{i=1}^{n}q_{u_{ti}}\right)^2}{\sum_i\left(q_{u_{ti}} - \frac{1}{n}\sum_{i=1}^{n}q_{u_{ti}}\right)^2} \tag{9}$$

where $q_{u_{ti}}$: is target bearing capacity, $q_{u_{pi}}$: is predicted bearing capacity, q_{u_t}: is mean of targeted bearing capacity, q_{u_p}: is mean of predicted bearing capacity, $s_{q_{ut}}$: is standard deviation of the target bearing capacity, s_{qu_p}: is standard deviation of the predicted bearing capacity, and n: is number of observations.

7. Developed M5P Model Equation

The training and testing technique is a most widely used technique to develop the learning algorithms to establish the model (Behnood et al., 2017). For training and testing the model, the train and test datasets are divided into two subsets using random partitioning. The model is trained using 70% of the data and then tested using the remaining 30% for evaluation of the desired model. Table 1 provides the minimum, maximum and Standard Deviation values for the total data for each of the individual parameters used to create the M5P model.

The model tree that was created using the M5P technique is displayed in Eqs. (10-14). Theses equations can be used to determine the Bearing Capacity (BC) based on the conditions illustrated in Figure 4. Now, the statistical parameter results were used to see the prediction precision of the developed M5P model for forecasting the BC of CF is seating on the limited thick sand-layer with eccentric-inclined load. From the model M5P, the predicted results and the actual results were used to solve Eqs. (10-14). The calculated results are shown in the Table 2 for training as well as for testing.

$$BC = -510.84 \times \frac{H}{B} - 585.19 \times \frac{\alpha}{\phi} - 1274.64 \times \frac{e}{B} + 861.01 \quad (10)$$

$$BC = -545.73 \times \frac{H}{B} - 464.09 \times \frac{\alpha}{\phi} - 996.34 \times \frac{e}{B} + 732.08 \quad (11)$$

$$BC = -18.45 \times \frac{H}{B} - 161.30 \times \frac{\alpha}{\phi} - 404.40 \times \frac{e}{B} + 232.55 \quad (12)$$

$$BC = -17.26 \times \frac{H}{B} - 114.08 \times \frac{\alpha}{\phi} - 348.25 \times \frac{e}{B} + 207.89 \quad (13)$$

$$BC = -15.98 \times \frac{H}{B} - 170.40 \times \frac{\alpha}{\phi} - 321.93 \times \frac{e}{B} + 217.25 \quad (14)$$

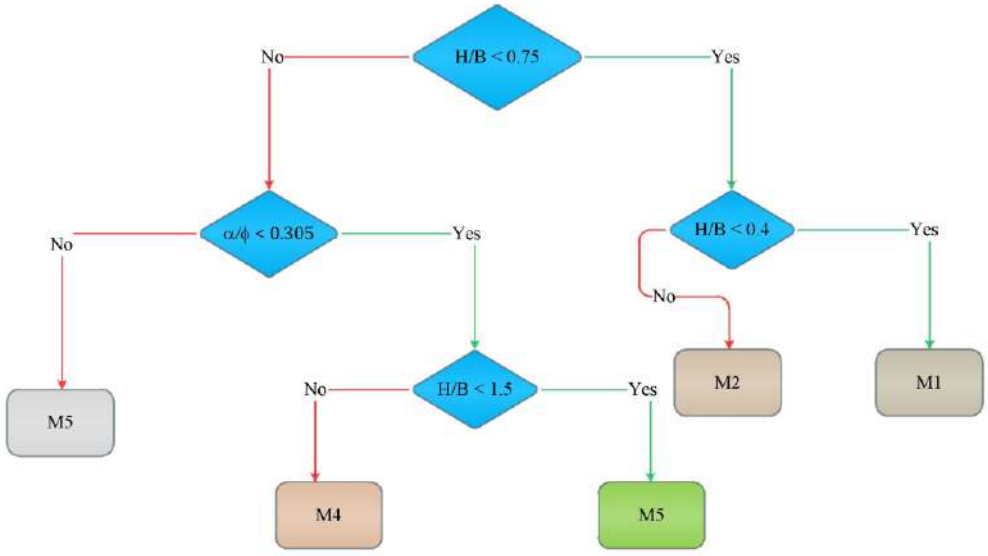

Fig. 4. Proposed M5P model tree to forecast the bearing capacity (q_u)

Table 2. Statistical parameters values for testing and training by M5P model

Statistical parameters	Training	Testing
R	0.99	0.99
R^2	0.96	0.96
MSE (kPa)	2273.72	1795.07
RMSE (kPa)	47.68	42.37
MAE (kPa)	32.13	28.57
MAPE (%)	19.83	21.46

Analyzing Table 2 reveals that, (keeping the above section in view-statistical parameters) the calculated MAPE value is lower than 20%, it reflects good accuracy of the present proposed prediction model (Behnood et al., 2017). Further, MSE, RMSE and MAE calculated results are small enough to represent the proposed model as good to predict the BC of the circular footing resting on the limited thick sand-layer with eccentric-inclined load.

Finally, r and R^2 calculated results (≈1) also represent the proposed model as good enough to predict the desired output (Behnood et al., 2017). The predicted versus (vs) actual values were compared in terms of the plot as demonstrated in Figures 5 and 6 for training and testing, respectively.

Close examination of Figures 5 and 6 unveils that, a comparison of predicted vs targeted values is within the 20% of the deviation line as reference to line of equality. The proposed soft computing model (M5P model tree) offers significant advantages. It excels at generating mathematical equations and enhances understanding of their formulation. Additionally, these models are easy to refine and apply. Besides, it is easier to improve and use these models. The model's limitation lies in its lack of high accuracy for higher values of the bearing capacity. Likewise, the modelling relies solely on experimental values for the data, and the inclusion of field data would significantly enhance its significance.

8. Preparation of ANN Model

The ANN technique is a dynamic method of information processing that develops connections between input variables (X_i) and output variables (Y_j) through interconnected neurons (represented by weight factor, w_j).

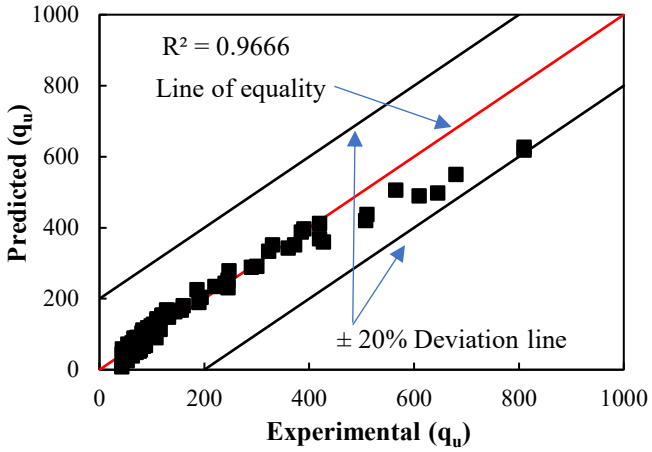

Fig. 5. M5P predicted vs experimental plot for training data

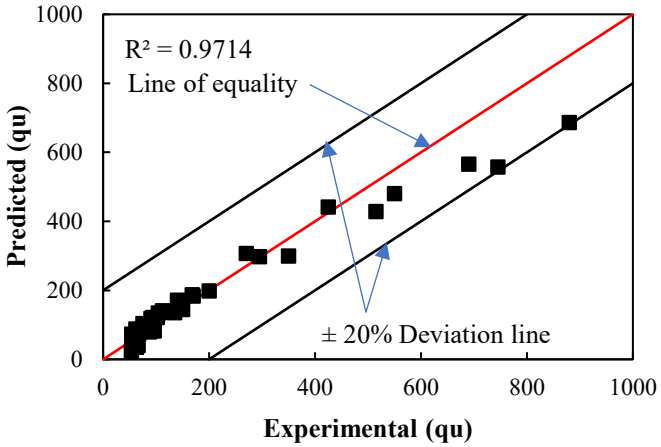

Fig. 6. M5P predicted vs experimental plot for testing data

It is crucial to emphasize that the input variables (X_i) and the output variables (Y_j) are typically normalized to x_i and y_j, respectively. The ANN models establish a relationship between the normalized input parameters x_i and the normalized output variables y_j as follows:

$$y_j = f\left(\sum_{i=1}^{n} w_{ji} x_i\right) + b_j \tag{15}$$

where f: is the transfer function employed which follows a form of sigmoidal function, w_{ji}: is the undetermined weight factors, b_j: is a bias.

A neural network model precisely adapts the weight factors (w_{ji}) and bias (b_j) in Eq. (15) by minimizing error function. Within the field of geotechnical engineering, the utilization of the ANN approach is extensive in the creation of prediction models. This involves harnessing comprehensive datasets derived from both experimental studies and numerical analyses. Overall, the creation of an ANN model encompasses a pivotal stage is the construction of the ANN architecture.

8.1. Selection of ANN Architecture

In this study, a three-layered ANN model was constructed, as depicted in Figure 7. The ANN model comprises of three layers: the input layer, the hidden layer, and the output layer. Determining the suitable quantity of hidden layers and neurons for each of these hidden layers constitutes an intricate undertaking within the design of ANNs. As outlined by Boger and Guterman (1997), a proposition has been made that the quantity of neurons in the hidden layer could be set at 70% of the data of the input layer. Besides, they indicated that if the number of hidden layer neurons is insufficient, supplementary neurons can be subsequently incorporated into the output layer. Conversely, it is advised by Linoff and Berry (1997) that the ideal count of neurons within the hidden layer should be kept below twice the quantity of neurons in the input layer.

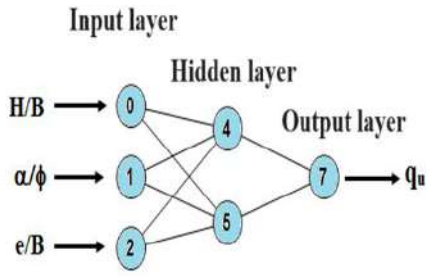

Fig. 7. Architecture of ANN model

Meanwhile, Blum (1992) put forth the notion of an intermediate size for the hidden layer neurons, lying between the size of the input and output layers. Given these observations, it was resulted at the recommended method for ascertaining the quantity of neurons in the hidden layer (70% of input layer), which is based on simple guidelines presented by Boger and Guterman (1997). This approach is also endorsed by Ito (1994) and Kůrková (1992) who have adopted a similar strategy.

For this study, single hidden layers were utilized to reduce the complexity of the ANN model, which was a crucial factor for this research to develop the model equations. A hidden layer in a neural network serves a crucial role in enabling the network to learn and represent complex patterns and relationships within the input data. The success of the neural network model depends significantly on knowing when to stop the training process. Overtraining the neural network can lead to noisy results, while insufficient training can result in poor predictions and a lack of generalization for new data.

Hence, a trial-and-error technique was employed to adjust the number of iterations for both training and testing datasets. In the present study the mean square error was calculated between the real and forecasted values across various iterations, ultimately pinpointing the iteration that yielded the lowest mean square error. This served as the optimal reference for identifying the neural network structure, as illustrated in Figure 8. The training process was halted upon reaching a low value for the average error function to avoid potential overfitting effects caused by further iterations.

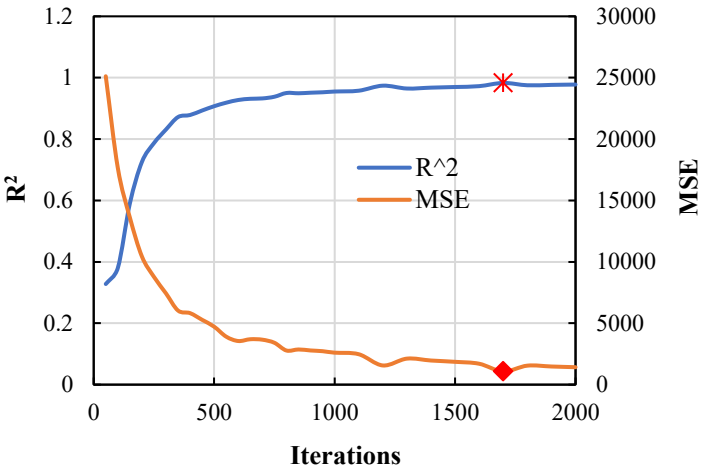

Fig. 8. Optimal hidden layer neurons

After careful consideration, the number of iterations was set to 1700 for this experiment. As a result, the neural network model selected for this experiment followed a configuration of 3-2-1, which denotes the count of neurons in the input, hidden, and output layers, respectively, for the purpose of constitutive modelling.

8.2. Prediction of Baring Capacity Using ANN

After successful construction of architecture for ANN model, it was fed with desired input parameters in order to calculate the output. In this process weights and bias was generated as presented in Table 3. The predicted output is compared with the original data for training (Figure 9) and testing (Figure 10).

Further, to understand the prediction accuracy of the proposed ANN model, performance measures were used (as discussed in section "statistical parameters"). The calculated values of performance measures are tabulated in Table 4.

Table 3. ANN model connection weights and biases

Hidden neurons	Weights (w_{jk})				Biases	
	H/B	α/ϕ	e/B	q_u	b_{hk}	b_0
1	12.14	1.10	1.03	-5.04	0.28	9.47
2	15.98	0.54	0.23	-7.74	0.45	-

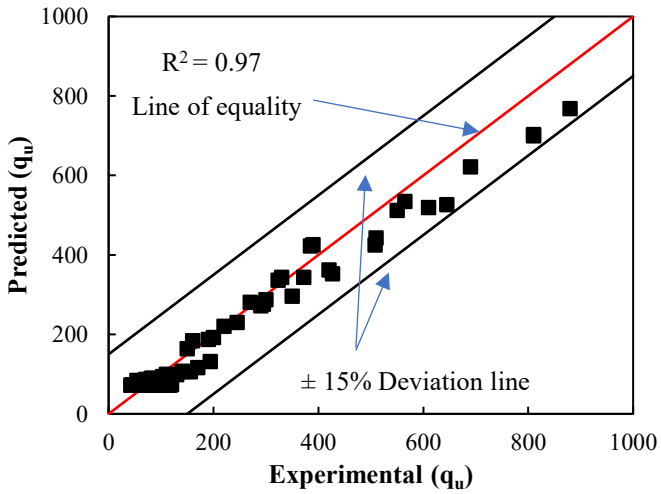

Fig. 9. Comparing actual q_u with ANN predicted q_u on training data

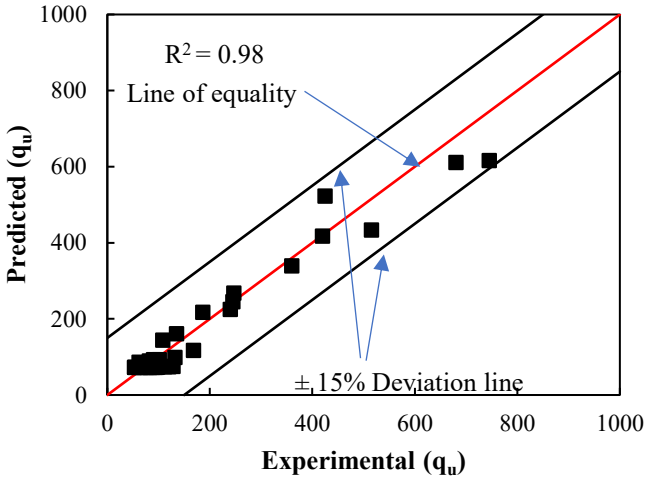

Fig. 10. Comparing actual q_u with ANN predicted q_u on testing data

Table 4. The statistical metrics for both the training and testing datasets by ANN model

Statistical parameters	Training	Testing
R	0.99	0.98
R^2	0.98	0.97
MSE	1567.96	1394.23
RMSE	39.60	37.34
MAE	28.98	24.88
MAPE (%)	18.20	16.29

9. The Equation of the ANN Model for 'Qu' Based On the Trained Neural Network

The fundamental mathematical equation of the ANN connecting the input variables and the output can be expressed as follows:

$$q_u = f\left\{b_0 + \sum_{k=1}^{h}\left(w_k \times f\left[b_{hk} + \sum_{j=1}^{m}\left(w_{jk} \times X_j\right)\right]\right)\right\} \quad (16)$$

As a result, the model equation for the output may be formed using the ANN model's training weights. In this work, a model equation for circular footing bearing capacity was created utilising the values of the weights and biases presented in Table 2 as per the equations below.

$$A = 0.28 + 12.13\frac{H}{B} + 1.1\frac{\alpha}{\phi} + 1.03\frac{e}{B} \quad (17)$$

$$B = 0.45 + 15.98\frac{H}{B} + 0.54\frac{\alpha}{\phi} + 0.23\frac{e}{B} \quad (18)$$

$$E = 9.46 - \frac{5.04}{(1+e^{-A})} - \frac{7.74}{(1+e^{-B})} \quad (19)$$

$$q_u = \frac{1}{(1+e^{-E})} \quad (20)$$

The bearing capacity value produced from Eq. (9) is in the range of [-1, 1] and must be denormalized as Eq. (21):

$$q_{u\,actual} = 0.5(q_u + 1)(q_u\,\max - q_u\,\min) + q_u\,\min \quad (21)$$

where q_u *max* and q_u *min*: are the maximum and minimum values of bearing capacity, respectively, as used in the data set.

10. Sensitivity Analysis for M5P Model

Sensitivity analysis was used to determine which input parameter had the most influence for predicting the q_u of circular footing resting on the limited thick sand-layer with eccentric-inclined load by M5P model. With the use of statistical measures (r, R^2, MSE, RMSE, MAE and MAPE), one input parameter was removed for each case and its influence on the bearing capacity of the soil was measured as shown in Table 5.

Table 5. M5P model's parametric analysis on training data

Input combinations	Input parameters removed	r	R^2	MSE	RMSE	MAE	MAPE (%)
H/B, α/ϕ, e/B	--	0.99	0.97	2117.38	46.02	29.30	18.93
α/ϕ, e/B	H/B	0.76	0.23	30083.37	173.45	134.61	91.28
H/B, e/B	α/ϕ	0.97	0.88	6508.77	80.68	51.93	31.08
H/B, α/ϕ	e/B	0.99	0.92	4091.38	63.96	39.36	25.39

Study of the Table 5 demonstrates that *H/B* is the most effective input parameter on forecasting the bearing capacity. This is because variations in the thickness of the rigid soil affect pressure distribution, which can lead to either an increase or decrease in the footing's bearing capacity. Second one is the ratio of the load of eccentricity to the angle of internal friction (*α/ϕ*) followed by the ratio of load of inclination to width of the footing (*e/B*). Finally, from the Table 5, it can be concluded that removing the other parameter has no significant impact on forecasting the BC of the layered soil with limited thickness, in contrast to *H/B*. It should be mentioned that the ratio H/B had a significant part in predicting the q_u of the layered soil with limited thickness.

10.1. Sensitivity Analysis for ANN Model

In this section, an examination is conducted to analyze the influence of individual variables on the bearing capacity (output) via parametric analysis. To conduct the sensitivity analysis, two methods were employed based on the weight configuration, as outlined by David (1991) and Olden and Jackson (2002).

In the initial method (David, 1991; Kůrková, 1992), the connection weights of each neuron in the hidden layer were divided into several (based on the type of modeling) components, a concept later verified by Onyelowe et al. (2021, 2022). These components were subsequently connected to each corresponding input neuron. On the other hand, the second method, as proposed by Olden and Jackson (2002), entailed the computation of the cumulative product of the ultimate weights of connections (spanning from input neurons to hidden neurons and from hidden neurons to output) across all input neurons (Onyelowe et al., 2022). To determine the contribution of individual variables corresponding to a given input, the procedures presented by David (1991) and Olden and Jackson (2002) was followed. The outcomes derived from these procedures are shown in Figure 11.

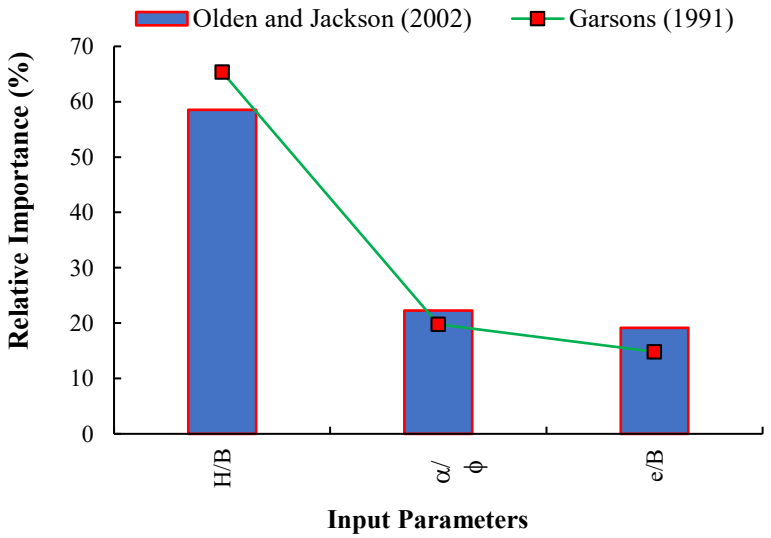

Fig. 11. Parametric analysis for ANN model

Figure 11 clearly indicates that the dominant influential factor (H/B) is followed by (a/f), and (e/B) based on the both methods of David (1991) and; Olden and Jackson (2002). Finally, it can be concluded that, both methods yielded identical results from the parametric analysis.

11. Comparison of M5P Tree and ANN Models

After successfully completing the M5P model tree and ANN modelling, a comparison is made among these models to assess their competency, along with an examination of the parametric analysis results. The outcome of the proposed M5P model tree and ANN model is visualized on scatter plots, depicting the measured versus predicted values for both training (Figures 5 and 6) and testing (Figures 9 and 10) datasets. Representing the data points of predicted versus measured outputs along with a line of equality and a ± 15% error line serves as an appropriate method for illustrating the model's predictive capacity.

The results of the statistical parameter from the M5P model tree (Table 2) and ANN model (Table 4) reveals that, both modes are good in prediction the desired q_u as r, R^2 are close to 1 and remaining MSE, RMSE, MAE and MAPE are small values (as discussed in Section 6).

But, the M5P model tree is inferior than the ANN model as evidence from the comparison of Tables 2 and 4. A comparison was made among the models using line diagram as data number vs q_u as depicted in Figure 12. This figure shows that both M5P and ANN models representing lines are overlapped with the experimental data. Hence, both models can be useful to predict the desired q_u. In conclusion, the parametric analysis conducted to assess the influence of individual variables on the output q_u highlights that (H/B) emerges as the primary contributing independent factor, followed by (α/ϕ) and (e/B). The influence of independent parameter on predicting the q_u was found same in both methods (M5P and ANN) as per the Table 5 and Figure 11.

12. Conclusions

This paper deals with the problem of prediction of bearing capacity of a circular footing subjected to an eccentric-inclined load placed on sand with a limited thick.

The objectives of this paper were:

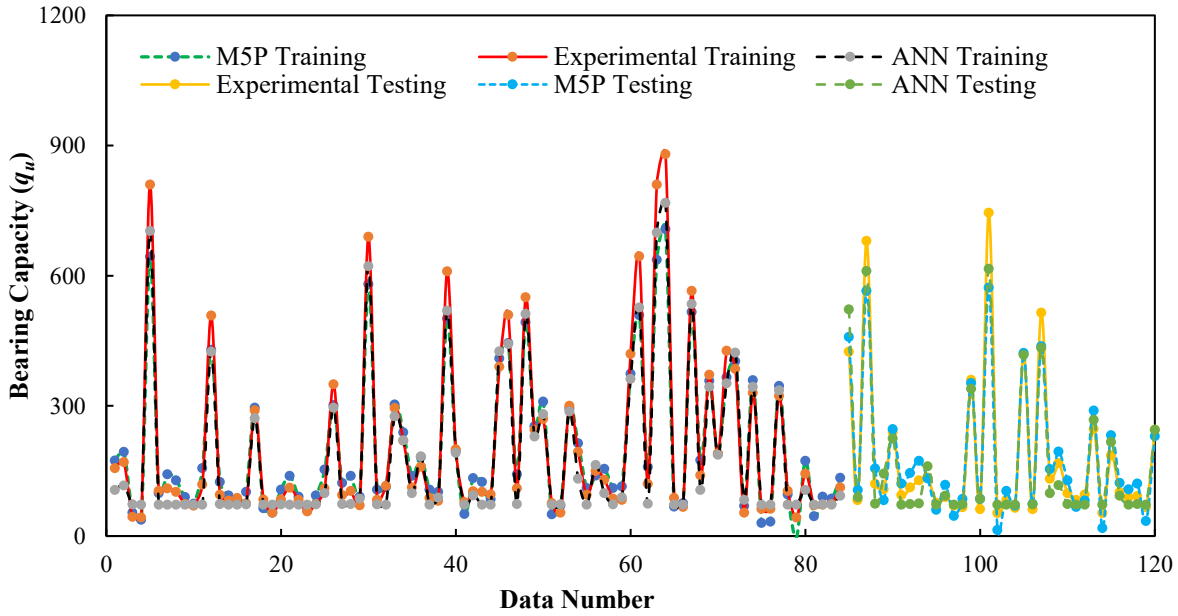

Fig. 12. Comparison of experimental vs M5P tree and ANN models training and testing data

- To evaluate how well the M5P tree model and ANN model can predict the load-bearing capacity of a circular footing on sand under specific conditions, like an eccentric-inclined load with limited thickness of sand.
- To conduct a comparison between the developed M5P model tree and ANNs.
- To develop the model equations based on both M5P tree and ANN models.
- To perform sensitivity analysis to see the influence of each input parameter on the output prediction.

The results show that the ANNs model is effective in predicting the bearing capacity of a circular footing under an inclined load on sand with limited thickness. It performs much better than the M5P model. With the ANN model, data can be inputed after training to predict outcomes. On the other hand, the M5P model requires the entire process each time a prediction is to be made. To evaluate the performance of both models, measures like MSE, RMSE, MAE, MAPE, R^2 and r used. In both models, MSE, RMSE, MAE and MAPE had low values, while r and R^2 were close to 1 for both models. This suggests that both models can predict the bearing capacity of a circular footing under an inclined load on sandy ground with limited thickness, but the ANN model is considered the best.

A sensitivity analysis was performed to understand the importance of each input parameter on bearing capacity (q_u). The results indicated that *H/B* is the most significant input parameter, followed closely by α/ϕ and *e/B*. The benefit of utilizing M5P and ANNs techniques is their ease of updating when new data becomes available.

13. References

Acharyya, R. and Dey, A. (2019). "Assessment of bearing capacity for strip footing located near sloping surface considering ANN model", *Neural Computing and Applications*, 31, 8087-8100, https://doi.org/10.1007/S00521-018-3661-4/FIGURES/22.

Acharyya, R., Dey, A. and Kumar, B. (2020). "Finite element and ANN-based prediction of bearing capacity of square footing resting on the crest of c-φ soil slope", *International Journal of Geotechnical Engineering*, 14, 176-187, https://doi.org/10.1080/19386362.2018.1435022.

Behnood, A., Behnood, V., Modiri Gharehveran, M. and Alyamac, K.E. (2017). "Prediction of the compressive strength of normal and high-performance concretes using M5P model tree algorithm", *Construction and Building Materials*, 142, 199-207, https://doi.org/10.1016/J.CONBUILDMAT.2017.03.061.

Blum A. (1992). *Neural network in C++*, Wiley, New York, https://www.scirp.org/reference/referencespapers?referenceid=3084639.

Boger, Z. and Guterman, H. (1997). "Knowledge extraction from artificial neural networks models", *Proceedings of the IEEE International Conference on Systems, Man and Cybernetics*, 4, 3030-3035, https://doi.org/10.1109/ICSMC.1997.633051.

Garson, G.D. (1991). "Interpreting neural network connection weights", *AI Expert*, 6, 47-51, https://www.semanticscholar.org/paper/Interpreting-neural-network-connection-weights-Garson/d5e392035d5f4b1ae37027cabfd1bfdf6733015b.

Dutta, R.K., Dutta, K. and Jeevanandham, S. (2015). "Prediction of deviator stress of sand reinforced with waste plastic strips using neural network", *International Journal of Geosynthetics and Ground Engineering*, 1, 1-12, https://doi.org/10.1007/s40891-015-0013-7.

Ebid, A.M., Onyelowe, K.C. and Arinze, E.E. (2021). "Estimating the ultimate bearing capacity for strip footing near and within slopes using AI (GP, ANN and EPR) techniques", *Journal of Engineering*, 2021(1), 3267018, https://doi.org/10.1155/2021/3267018.

Gnananandarao, T., Dutta, R.K., Khatri, V.N. and Kumar, M.S., (2022). "Soft computing based prediction of unconfined compressive strength of fly ash stabilized organic clay", *Journal of Soft Computing in Civil Engineering*, 6, 43-58, https://doi.org/10.22115/SCCE.2022.339698.1429.

Ito, Y. (1994). "Approximation capability of layered neural networks with sigmoid units on two layers", *Neural Computation*, 6, 1233-1243, https://doi.org/10.1162/NECO.1994.6.6.1233.

Khandelwal, M., Marto, A., Fatemi, S.A., Ghoroqi, M., Armaghani, D.J., Singh, T.N. and Tabrizi, O. (2018). "Implementing an ANN model optimized by genetic algorithm for estimating cohesion of limestone samples", *Engineering with Computers*, 34, 307-317, https://doi.org/10.1007/S00366-017-0541-Y/FIGURES/8.

Kumar, V., Priyadarshee, A., Chandra, S., Jindal, A. and Rana, D. (2023). "Behavioral study of raft reinforced with geogrid and geocell through experiments and neural models", *Civil Engineering Infrastructures Journal*, 56, 321-332, https://ceij.ut.ac.ir/article91785.html.

Kůrková, V. (1992). "Kolmogorov's theorem and multilayer neural networks", *Neural Networks*, 5, 501-506, https://doi.org/10.1016/0893-6080(92)90012-8.

Linoff, G.S. and Berry, M.J.A. (1997). *Data mining techniques: For marketing, sales, and customer Relationship management*, Wiley, New York, https://www.researchgate.net/publication/271077515_Data_Mining_Techniques_For_Marketing_Sales_andCustomerRelationshipManagement.

Loukidis, D. and Ygeionomaki, N. (2017). "Bearing capacity in sand under eccentric and inclined loading using a bounding surface plasticity model", *Springer Series in Geomechanics and Geoengineering*, 267-273, https://doi.org/10.1007/978-3-319-56397-834.

Olden, J.D. and Jackson, D.A. (2002). "Illuminating the "black box": A randomization approach for understanding variable contributions in Artificial Neural Networks", *Ecological Modelling*, 154, 135-150, https://doi.org/10.1016/S0304-3800(02)00064-9.

Onyelowe, K.C., Gnananandarao, T. and Ebid, A.M. (2022). "Estimation of the erodibility of treated unsaturated lateritic soil using support vector machine-polynomial and -radial basis function and random forest regression techniques", *Cleaner Materials*, 3, 100039, https://doi.org/10.1016/J.CLEMA.2021.100039/REFERENCES.

Onyelowe, K.C., Gnananandarao, T. and Nwa-David, C. (2021). "Sensitivity analysis and prediction of erodibility of treated unsaturated soil modified with nanostructured fines of quarry dust using novel artificial neural network", *Nanotechnology for Environmental Engineering*, 6(2), 1-11, https://doi.org/10.1007/S41204-021-00131-2.

Quinlan, J.R. (1992). "Learning with continuous classes", In: *Australian Joint Conference on Artificial Intelligence*, (pp. 343-348), https://www.semanticscholar.org/paper/Learning-With-Continuous-Classes-Quinlan/ead572634c6f7253bf187a3e9a7dc87ae2e34258.

Saha, S., Gu, F., Luo, X. and Lytton, R.L. (2018). "Use of an artificial neural network approach for the prediction of resilient modulus for unbound granular material", *Transportation Research Record: Journal of the Transportation Research Board*, 2672, 23-33, https://doi.org/10.1177/0361198118756881.

Sarle, W.S. (1995). "Stopped training and other remedies for overfitting", In: *Proceedings of the 27th Symposium on the Interface of Computing Science and Statistics*, (pp. 352-360), https://www.semanticscholar.org/paper/Stopped-Training-and-Other-Remedies-for-Overfitting-Sarle/851743cc8d65f0f6004a2a2279025f8377fc124c.

Sasmal, S.K. and Behera, R.N. (2021). "Prediction of combined static and cyclic load-induced settlement of shallow strip footing on granular soil using artificial neural network", *International Journal of Geotechnical Engineering*, 15, 834-844, https://doi.org/10.1080/19386362.2018.1557384.

Sethy, B.P., Patra, C.R., Das, B.M. and Sobhan, K. (2020). "Behavior of circular foundation on sand layer of limited thickness subjected to eccentrically inclined load", *Soils and Foundations*, 60, 13-27, https://doi.org/10.1016/j.sandf.2019.12.005.

Sethy, B.P., Patra, C.R., Das, B.M. and Sobhan, K. (2019). "Bearing capacity of circular foundation on sand layer of limited thickness underlain by rigid rough base subjected to eccentrically inclined load", *Geotechnical Testing Journal*, 42, 597-609, https://doi.org/10.1520/GTJ20170420.

Terzaghi, K. (1973). *Theoretical soil mechanics*, 1st Edition, John Wiley and Sons, Inc., https://doi.org/10.1002/9780470172766.

Thottoth, S.R., Das, P.P. and Khatri, V.N. (2024). "Prediction of compression capacity of under-reamed piles in sand and clay", *Multiscale and Multidisciplinary Modeling, Experiments and Design*, 2024, 1-17, https://doi.org/10.1007/S41939-023-00331-0.

Vesic, A.S. (1973). "Analysis of ultimate loads of shallow foundations", *Journal of the Soil Mechanics and Foundations Division*, 99, 45-73, https://doi.org/10.1061/JSFEAQ.0001846.

Vishal, P. and Dutta, R.K. (2022). "Application of machine learning technique in predicting the bearing capacity of rectangular footing on layered sand under inclined loading", *Journal of Soft Computing in Civil Engineering*, 6, 130-152, https://www.jsoftcivil.com/article158236.html.

Wang, Y. and Witten, I.H. (1997). "Induction of model trees for predicting continuous classes", In: *Proceedings of the 9th European Conference on Machine Learning Poster Papers*, (pp. 128-137), https://www.researchgate.net/publication/33051395_Induction_of_model_trees_for_predicting_continuous_classes.

Civil Engineering Infrastructures Journal 2025, 58(1): 103-121
DOI: 10.22059/ceij.2024.365637.1963

RESEARCH PAPER

Investigation of a Loaded Pile Responses Due to Proposed Deep Excavation in Sand Soil: Finite Element Analysis Using Plaxis3D Program

Hakeem, B.M.[1*]

[1] Associate Professor, Civil Engineering Department, Higher Institute of Engineering and Technology, New Minia, Egypt.

Received: 20 Sep. 2023; Revised: 16 Dec. 2023; Accepted: 14 Jan. 2024

ABSTRACT: Geotechnical design engineers are giving increasing attention to how piles respond to soil movements brought on by nearby braced excavations. This study investigates the effect of deep excavation on an adjacent loaded single pile on sand soil using the PLAXIS 3D finite element program. Leung et al. (2006) centrifuge test results were employed to verify the numerical model. The different parameters in this study were the excavation depth, type of pile head, diameter of pile, and the distance between the pile and the excavation. The results of the investigation demonstrated that the excavation depth (He) in proportion to the pile's length (Lp) has an important effect on pile responses. The case of (He/Lp = 2.0) leads a maximum lateral deflection at the pile toe of 24.80% from the diameter of pile. However, the lowest lateral deflection at the pile-0.85% of the pile diameter-occurs in the case where He/Lp = 0.5, which reduces. When He/Lp = 0.5, 1.0, the maximum value of bending moment of the pile occurs at around 0.70% normalized depth of the pile, or 230 and 298 kN.mm, respectively. Furthermore, the pile's response is greatly affected by the distance between it and the excavation site; after 10 meters, the value of bending moment in the pile is insignificant. Furthermore, it was found that while the maximum pile lateral deflection reduces as pile diameter increases, the bending moment along the pile remains constant. In this paper, the type of pile head was also discussed.

Keywords: PLAXIS 3D, Deep Excavation, Pile, Deflection, Bending Moment.

1. Introduction

Pile foundations are recommended when heavy structural loads have to be transferred from soil of lower-bearing capacity to a stratum of high bearing capacity. The influence of generated ground movement on the lateral response of an existing pile was investigated by Madhumathi and Ilamparuthi (2018) using 1 g model experiments on a single pile implanted in sandy soil. Depending on the pile's Lp/dp ratio, deflection reduces with spacing, and a decrease in deflection is noticeable for the shorter pile (Lp/dp = 10). Regardless of the placement of the pile, the deflection is less for piles with Lp/dp < 20. According to Zhang et al. (2018) the maximum values of the pile's lateral deflection and bending moment decrease noticeably as the pile gets farther away from the excavation edge.

Furthermore, the type of pile head greatly affects the pile's response, and an increase in axial force has a minimal impact

* Corresponding author E-mail: civileng_beshoy@mhiet.edu.eg

on the pile's behavior. Shakeel and Ng (2017) examined the behavior of a 2 × 2 pile group adjacent to a deep excavation in soft clay using a three-dimensional coupled consolidation analysis. Among the subjects covered were the effects of working load, soil permeability, pile length, pile group location from excavation, stiffness of the supporting system, and soil condition.

Ashour (2021) introduced research to study the value of bending moment, settlement, and lateral deflection of a loaded pile adjacent to a propped deep excavation using a Finite Element (FE) program. He concluded that the excavation depth behind the retaining wall considerably affects the ground surface settlement, and the settlement curve deepens as the excavation depth rises. Additionally, the ground movement increases significantly with increasing excavation depth and reduces noticeably with decreasing wall distance.

The ABAQUS program was utilized in a parametric analysis by Nishanthan et al. (2016) to investigate the pile responses caused by deep excavation in clay. They concluded that the stiffness, fixity, and distance of the pile head in the wall support system all significantly affected the behavior of the pile. Lateral movements in the surrounding soil are certain to occur as a result of stress reduction from the development of underground infrastructure and the excavation needed for basement construction adjacent to existing buildings.

It is necessary to consider both the buildings' safety and the stability of the foundations supporting them in this situation (Soomro et al., 2019). Li and Yang (2023) presented a study to examine the influence of pile groups to combined horizontal soil loading from excavation and surcharge. The results reveal that, in terms of pile group lateral displacement, capped-head pile groups can offer greater constraint than free-head pile groups. A 2-D finite element numerical model is used to examine the behavior of pile groups adjacent to deep sand excavations (Shafee and Fahimifar, 2018). The results show that excavation-induced alterations to adjacent pile groups can be accurately simulated using a basic 2-D plane strain model. They found that additional bending moments are imposed on piles as excavation depth is increased, and this should be taken into account while establishing the pile's structural design. Also, the result indicates that for pile groups adjacent to an excavation, incline loading causes additional lateral deformations and bending moments. Simultaneous vertical and horizontal loading, which primarily affects the upper half of piles, can result in severe lateral deformation, structural damage to piles, and serviceability issues.

In the study of Yi (2022), a three-dimensional Finite Difference Technique (FDM) was utilized to simulate a single pile that was exposed to loading of passive effect due to a new embankment in soil that was primarily composed of soft clay. He found that the lateral earth pressure at the pile increased with decreasing pile stiffness, while it increased with increasing embankment height and cushioning thickness. The behavior of a single pile behind a stable retaining wall in clay that is subjected to excavation-induced soil movements has been studied using a series of centrifuge model tests. The results show that the soil and wall continue to move even after the earth has been removed, causing the adjacent pile to bend and deflect (Leung et al., 2006). Additionally, once the excavation is complete, extra pore pressure is released, which eventually results in the wall and soil sliding.

Through extensive numerical parametric research, the interaction behavior between currently loaded piles and braced excavation design factors was examined in saturated sand (Shabban et al., 2023). They discovered that by raising the strut axial rigidity, the induced pile group settlement and tilting can be lessened because of the lowered soil motions during the excavation. A negligible difference in the pile group settling occurs as the wall embedded depth grows when the excavation depth is very

small. It has been found that reducing pile group tilting and settlement for deeper excavations can be achieved by increasing the wall penetration depth to excavation depth ratio.

According to Le and Nguyen (2021) an extensive excavation was done in the deep layer of soft soil in order to establish the basement floor and pile cap foundation for the 15-story skyscraper in Ho Chi Minh City. Due to the thick, weak soil (clay loam), a large embankment load (70 kN/m^2) far from the pit and a load from nearby construction and the construction machinery (10 kN/m^2) away from the excavation's side of 2.6 m caused a large displacement of bending moments inside the pile, which exceeded the pile's bending resistance moment and resulted in pile failure.

Soomro et al. (2020) stated that in order to estimate the deformation mechanism of a twenty-story building situated on a (4 × 4) piled raft to an adjacent twenty-five-meter-deep basement excavation, a 3D numerical parametric research was carried out. The excavation caused the raft to settle differently. The result was a persistent interstate drift in the 20-story skyscraper as it was displaced laterally towards the excavation. The building's structural components may experience strain due to interstate drift.

According to Shaban et al. (2023), there is a possibility that the adjacent piled buildings will tilt and settle as a result of varying levels of excavation for the new constructions. Accurately forecasting soil movement and pile response is critical to preventing damage to neighboring structures Finite Element numerical models are used to calculate the responses of the pile groups. The parametric research has changed pile group configurations, new building load, and center-to-center pile spacing. The groups of 2, 4, and 6 capped head piles next to excavation sites were all investigated.

Alielahi et al. (2014) assessed the effectiveness of under-reamed piles in clayey soils. Their research aimed to compare the performance of full and half bulbs under piles and conventional piles of the same length and volume in clayey soils. Using Plaxis 3D foundation software with a finite element base, bearing capacity diagrams were plotted for this purpose, and the outcomes were compared. Half-bulb under-reamed piles performed better than other piles, exhibiting reduced displacements, and higher compressive bearing capacities, according to analysis and computation results. Additionally, under piles demonstrated a smaller uplift and a higher ultimate tensile bearing capacity in comparison to conventional piles of the same length and different volume.

In the current study, the 3D PLAXIS finite element program will be employed to perform computational analyses in three dimensions in order to acquire new understanding of how piles respond to nearby deep excavation in sand. The most significant influences on pile response (i.e., excavation depth, type of pile head, pile diameter, and distance from pile to excavation) will be studied using the validated model. The value of bending moment, later deflection, and settlement of the pile will be considered the pile response in this research.

2. Using Centrifuge Test Results to Verify the Plaxis3D Finite Element Model

2.1. Current Study Objectives

The objectives of this study is:

a) Verifying the viability of the selected computational procedures by comparing the centrifuge test results obtained by Leung et al. (2006) with those obtained by the PLAXIS (3D) finite element model software.

b) To find out how a loaded pile responds in sand soil to a propped deep excavation.

c) The effect of excavation depth, type of pile head pile diameter, and distance

from pile to excavation on the influence of pile.

2.2. Centrifuge Model Setup (Leung et al., 2006)

Centrifuge Model of Leung et al. (2006) was used in this study. They used the centrifuge test to evaluate the 3D finite element numerical model employed in this parametric analysis. To investigate the behavior of the piles as a result of nearby soft clay excavation, a centrifuge test with 50 g centrifuge acceleration was conducted in the instance of a stable retaining wall.

The stainless steel model container's inside dimensions are 200 mm in width, 470 mm in height, and 540 mm in length. The container was first filled with 120 mm of Toyoura sand (in prototype scale equal to 6 m), and then with 130 mm of Malaysian kaolin clay (6.5 m in prototype scale). The wall model for the centrifuge test was a 3 mm thick aluminium plate, while the pile model was made from a hollow square aluminium tube. After the model of pile and wall were set in location, the clay layer in the excavation zone was carefully taken out and replaced with a latex bag filled with a solution of ZcCl2 that has the same density as the clay that was taken out. The centrifuge physical model established by Leung et al. (2006) is shown in Figure 1. The centrifuge model built at prototype scale by Leung et al. (2006) is shown in Figures 2 and 3 in cross section and a plane view, respectively.

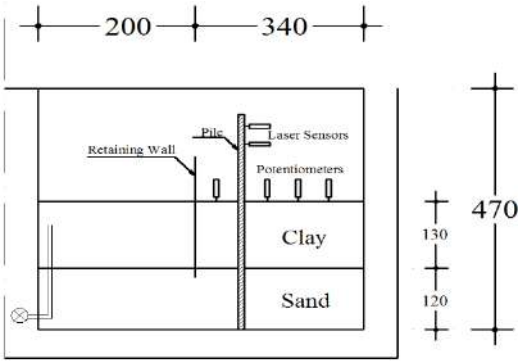

Fig. 1. Centrifuge model setup, all dimensions in mm (Leung et al., 2006)

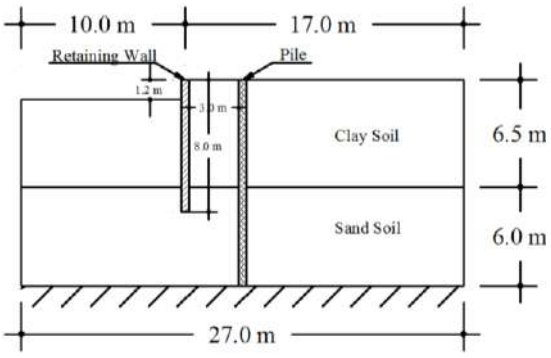

Fig. 2. Cross section of the prototype-scale centrifuge model (Leung et al., 2006)

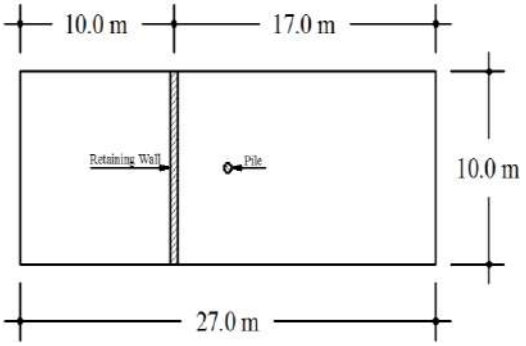

Fig. 3. Plane view of the prototype-scale centrifuge model (Leung et al., 2006)

2.3. Material Characteristics Used in Centrifugal Testing

Based on the Leung et al. (2006) the PLAXIS 3D program was employed to simulate the centrifuge test. The kaolin clay used in the centrifuge test was modelled using the Modify Cam Clay model (MCC), which has been used to investigate the behaviour of usually soft soils (PLAXIS 3D Material Models V21). In order to simulate the behaviour of the sand used in the centrifuge test, the Hardening Soil Model (HS) (PLAXIS 3D Material Models V21) was used. The kaolin clay, the sand parameters employed in the finite element study are listed in Tables 1 and 2 (Leung et al., 2006).

Using a hollow square aluminium tube, the pile model for the centrifuge test was constructed, a bending rigidity, EI of 2.2×10^5 kN.m^2. This value corresponds to a 600 mm diameter cast-in-situ Grade 35 concrete bored pile with a length of 12.5 m in prototype scale. The prototype bending moment for the model of retaining wall, which was made of a 3 mm thick aluminium plate, was 24×103 kN.m^2/m. The pile characteristics employed in the analysis are listed in Table 3.

2.4. Centrifuge Test Simulation in Three Dimensions Using Finite Elements

The centrifuge test was modelled in PLAXIS 3D at prototype scale (Figures 2 and 3). Because of the model's symmetry, only half of the model was simulated. The Modify Cam Clay model (MCC), which is appropriate for simulating the behaviour of usually consolidated soft soils, and the Hardening soil model were used for modelling the sand soil. The mesh size was determined to be 27, 10 and 12.5 m in the X, Y, and Z axes. The model's bottom side was restricted in all directions, but the model's vertical sides were restrained from moving in a horizontal manner. Any movement in the top half was possible. Using a 10-node element, the soil was simulated. Three-node line beam components were used to model the pile as an embedded beam.

Table 1. Geotechnical parameters of the kaolin clay that was used in this verification

Dry properties	Value	Unit	Reference
Unit weight (γ_{dry})	15.21	kN/m^3	
Coefficient of permeability (μ)	1.36×10^{-8}	m/s	
K_0 Value for normal consolidation (K_0^{nc})	0.60	-----	Leung et al. (2006)
Cam-clay compression index (λ)	0.64	-----	
Cam-clay swelling index (k)	0.14	-----	
Tangent of the critical state line (M)	0.90	-----	Teh et al. (2005)
Friction Internal Angle (Ø)	23	º	Leung et al. (2006)
Poisson's ratio (ν)	0.30	-----	Bowles (1997)

Table 2. Geotechnical parameters of the toyoura sand that was used in this verification

Properties	Value	Unit	Reference
Dry Unit weight (γ_{dry})	15.78	kN/m^3	
Triaxial compression stiffness (E_{50}^{ref})	30×10^3	kN/m^2	
Primary oedometer stiffness (E_{oed}^{ref})	24×10^3	kN/m^2	Nishanthan et al. (2016)
Unloading/reloading stiffness (E_{ur}^{ref})	99×10^3	kN/m^2	
K_0 value for normal consolidation (K_0^{nc})	0.318	-----	
Reference stress for stiffness (p^{ref})	100	kN/m^2	
Friction Internal Angle (Ø)	43	º	Leung et al. (2006)
Dilatancy angle (ψ)	15	º	
Poisson's ratio (ν)	0.30	-----	Bowles (1997)

Table 3. Geotechnical parameters of the pile that was used in this verification

Properties	Value	Unit	Reference
Bending rigidity (EI)	2.2×10^5	kN.m^2	Nishanthan et al. (2016)
Diameter	0.6	m	
Length	12.5	m	

A specific interface element explained the interaction between the earth surrounding the foot and skin of the pile. To represent the real contact between the soil and the wall, a 12-node interface element was used. The default mesh refinements value was utilized to refine the soil surrounding the elements. The wall was modelled as a triangular plate element with six nodes. As shown in Figure 4, the mesh was constructed of 12770 nodes and 7017 soil elements.

2.5. Comparison Between Experimental and Theoretical Results

Figures 5 and 6 show the generated bending moment as a result of the adjacent excavation and the computed and experimental lateral deflection profile along the pile. It was found from both measuring and numerical analysis that the pile head suffers the greatest lateral deflection. However, because of the pile's free head, the induced Bending Moment (BM) was zero in both the computed and observed measurement. The numerical and experimental results were found to be in very good agreement, having a maximum difference as shown in Figures 5 and 6.

The results of the centrifuge test revealed the same trend for the lateral deflection and bending moments. In general, there is high agreement between the computed and measured results, as shown in Figures 5 and 6.

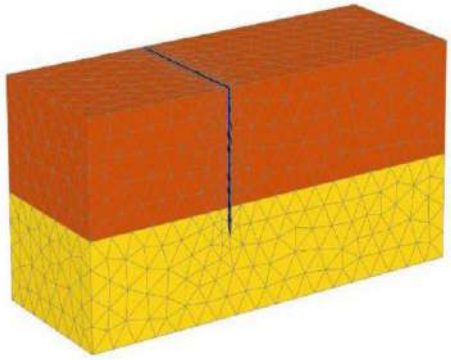

Fig. 4. 3D view of the used finite element mesh in modelling the centrifuge test

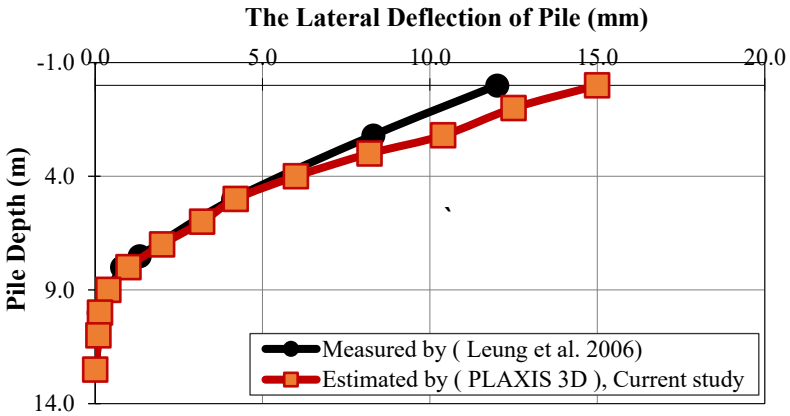

Fig. 5. Comparison of experimental and numerical induced lateral deflection along the pile length

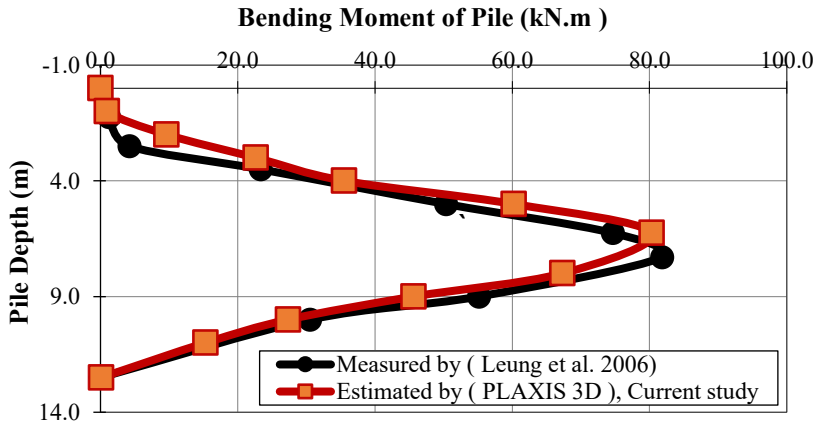

Fig. 6. Comparison of experimental and numerical induced bending moment along the pile length

Therefore, it can be used in the finite element analysis (PLAXIS 3D) that follows in this investigation.

3. Estimation the Bearing Capacity of Pile

Using the PLAXIS 3D program, a loaded pile test was carried out to determine the pile bearing capacity. A point load was applied gradually to a single bored concrete pile with a diameter of one meter, a length of twenty meters, and a modulus of elasticity of 30 GPa (with increments of 500 kN). The model's dimensions were chosen to be 40 × 40 × 40 m in the X, Y, and Z axes, respectively. The boundary condition effect was prevented by the larger dimensions in the same way as Nishanthan et al. (2016). Sand parameters are listed in Table 2, which was used to model the sandy soil. In this study, the pile was embodied in the simulation by an embedded 3-node line element. The curve for load-settlement is shown in Figure 7. Using the settlement-based failure criterion for large-diameter piles provided by Ng (2001), the pile's ultimate capacity was calculated. Eq. (1) provides the failure criterion.

$$\Delta_{ph.max} \cong 0.045\, d_p + \frac{1}{2}\frac{P_h\ L_p}{A_p E_p} \quad (1)$$

where d_p: is the diameter of pile, P_h: is the load placed on pile, L_p: is the pile length, A_p: is the pile area, E_p: is modulus of elasticity of pile, $\Delta_{ph,\ max}$: is maximum head settlement at the ultimate capacity of the pile. Based on this equation, the ultimate value of pile bearing capacity was estimated to be about 5000 kN, and the working load was determined to be 1600 kN tacking a factor of safety of 3.

4. Numerical Modelling Using PLAXIS 3D

4.1. Geometry of the 3D Problem

A typical three dimensional finite elements numerical model was employed to carry out the parametric investigation, as shown in Figure 8.

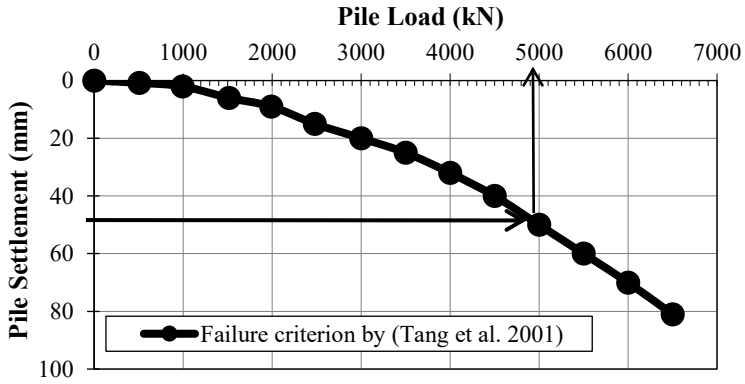

Fig. 7. Load versus settlement curve estimated by PLAXIS 3D program

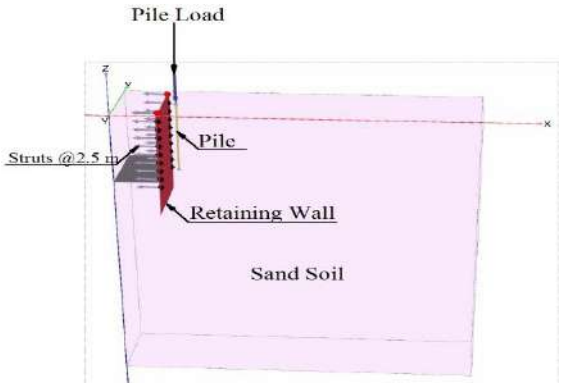

Fig. 8. Typical used finite element model

The dimensions of the model were determined to be 60, 20 and 80 m in the X, Y, and Z axes, respectively. According to Nishanthan et al. (2016) these dimensions were adequate to avoid boundary conditions from having an effect.

4.2. Boundary Conditions

The model's boundary conditions were identical to those used in centrifuge test modelling, as shown in Figure 9. In the analysis, medium-type mesh was employed. The mesh that was used for the analysis as shown in Figure 10.

4.3. Different Parameters Used in This Study

The models used for these analyses with various He/Lp conditions are shown in Figures 11 to 14. In each analysis condition, the depth of retaining wall to excavation depth ratio was 1.5 in the same way as in (Hsiung, 2009). The length of pile was kept constant at twenty meters. An embedded beam was used to model the pile.

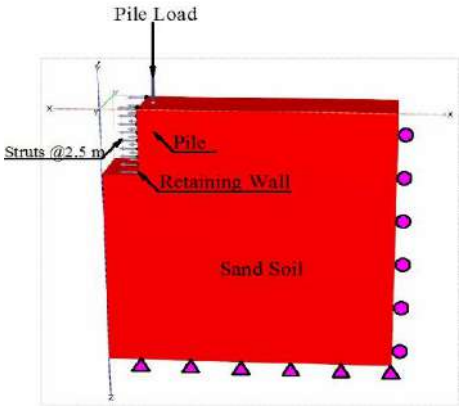

Fig. 9. Boundary conditions used in finite element model

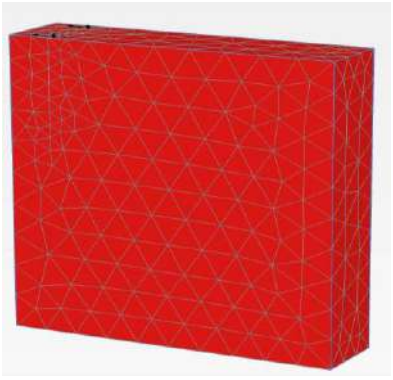

Fig. 10. Finite element mesh

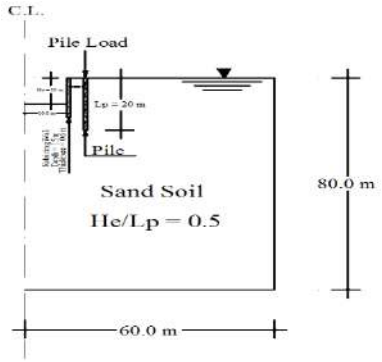

Fig. 11. Cross section of 3D model for (He/Lp = 0.5) case

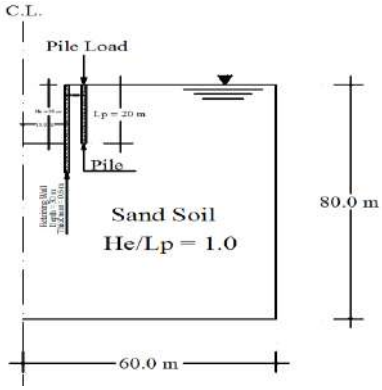

Fig. 12. Cross section of 3D model for (He/Lp = 1.0)

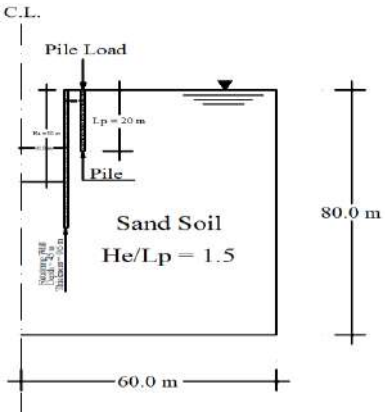

Fig. 13. Cross section of 3D model for (He/Lp = 1.5) case

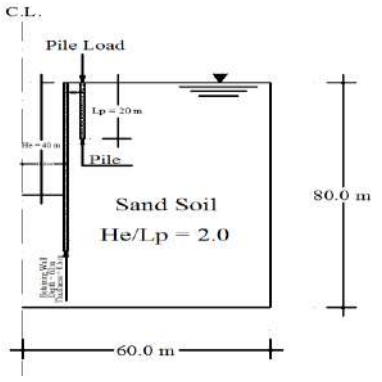

Fig. 14. Cross section of 3D model for (He/Lp = 2.0) case

Table 4 summarizes all the parameters taken into consideration in the present study. The program's flexible graphical interfaces make it simple for users to create a geometry model. The user interface consists of two subprograms: the input and output programs (PLAXIS 3D Reference Manual, 2020). Joint pieces called interfaces are used to simulate how soil and structure interact.

In order to approximate the area where a plate connects with the surrounding soil, they can also be formed adjacent to a plate, between two soil volumes, or between geogrid elements.

4.4. Material Models Parameters

Hardening Soil model (HS) was used for modeling the sand. Table 5 lists the sand characteristics that were used in the analysis. The characteristics of the sand were taken from the research of Unsever (2015). It was supposed that the groundwater table was at the surface in the same way as Nishanthan et al. (2016). In the vertical and horizontal planes, the struts were separated at 2.5 and 10 m, respectively. The pile properties are listed in Table 6.

Table 4. All cases have been studied in this research

Excavation depth, (He) (m)	He/Lp	Distance from the pile to the excavation, (X), (m)	Pile head type	Pile dia. (m)
10	0.5	3.0 = 15 % (He)	Free	0.5
20	1.0	5.0 = 25 % (He)	Hinged	1.0
30	1.5	10.0 = 50 % (He)	Rigid	1.5
40	2.0	20.0 = 100 % (He)		

Table 5. Geotechnical properties of the sand that was used in this study (Unsever, 2015)

Properties	Value	Unit
Dry unit weight (γ_{dry})	14.52	kN/m^3
Saturated unit weight (γ_{sat})	19.00	kN/m^3
Relative density (D_r)	70	%
Initial void ratio (e_{inital})	0.83	-----
Triaxial compression stiffness (E_{50}^{ref})	29.56 × 10^3	kN/m^2
Primary oedometer stiffness (E_{oed}^{ref})	24.65 × 10^3	kN/m^2
Unloading/reloading stiffness (E_{ur}^{ref})	99.59 × 10^3	kN/m^2
K_0 value for normal consolidation (K_0^{nc})	0.318	-----
Reference stress for stiffness (p^{ref})	100	kN/m^2
Cohesion (C)	0.1	kN/m^2
Friction internal angle (Ø)	43	º
Dilatancy angle (ψ)	15.8	º
Poisson's ratio (ν)	0.19	-----
Interface reduction factor	0.75	-----

Table 6. Geotechnical properties of the embedded pile that was used in this study (Unsever, 2021)

Properties	Value	Unit
Dry unit weight (γ_{dry})	25	kN/m^3
Young's modulus (E)	30 × 10^6	kN/m^2
Pile length (Lp)	20	m
Skin resistance	Layer dependent	-----
Max. skin resistance (T_{max})	380	kN/m^2
Max. base resistance (F_{max})	1598	kN/m^2

Table 7. Geotechnical properties of the diaphragm wall was used in this study (Unsever, 2021)

Properties	Value	Unit
Dry unit weight (γ_{dry})	25	kN/m^3
Young's modulus (E)	30 × 10^6	kN/m^2
Poisson's ratio (ν)	0.3	-----
Thickness	0.6	m

Table 8. Geotechnical properties of the strut (fixed end anchor) was used in this study (Unsever, 2021)

Properties	Value	Unit
Axial rigidity	374.85×10^3	-----
Area	17.85×10^{-4}	m^2
Young's modulus (E)	210×10^6	kN/m^2

The values used for the bearing capacity characteristics are based on the research of Nishanthan et al. (2016). The analysis's diaphragm walls and strut parameters are displayed in Tables 7 and 8, respectively. Based on the failure criterion, a working load of 1600 kN was applied to the pile head.

4.5. The Standard Model Follows the Steps of Finite Element Modelling

The process of using finite elements can be outlines as follows:

- Soil model: Soil stratigraphy and the geometry model were created. Additionally, a data set for soil layers was developed.
- Structure model: All structural components, including the levels of excavation, the pile, the diaphragm walls, the loads, and the struts, were created. Next, it is necessary to define each element's structural characteristics.
- Mesh mode: A mesh has been created.
- Flow conditions: The groundwater level was assigned in this step.
- Staged construction: In this step, the building phases were specified as follow:
- Initial phase: It is a stage that PLAXIS automatically generates to start the initial stresses.
- Stage 1 Pile Construction: A 20 m long pile is constructed in this stage.
- Stage 2 Applying the load: At the pile's head, a load of 1600 kN was applied.
- Stage 3 Wall Construction: This stage included the installation of the diaphragm wall.
- Stage 4 Excavation: The top 2.5 m of earth have been excavated (deactivated).
- Stage 5 Strut Installation: The strut installation until reaching the final depth of excavation.

5. Results and Discussion

5.1. Effect of the Depth of Excavation on the Pile Response

To examine the influence of the depth excavation on the response of pile, four various case studies of excavation depth to a constant value of the pile length (i.e., 20 m) were studied. The excavation above, and below the pile toe is illustrated by these cases (He / Lp = 0.5, 1.0, 1.5 and 2).

5.1.1. The Induced Settlement Along the Length of Pile Due to the Excavation

Figure 15 illustrates how excavation causes the loaded pile to settle along its length in four different cases of (He/Lp).

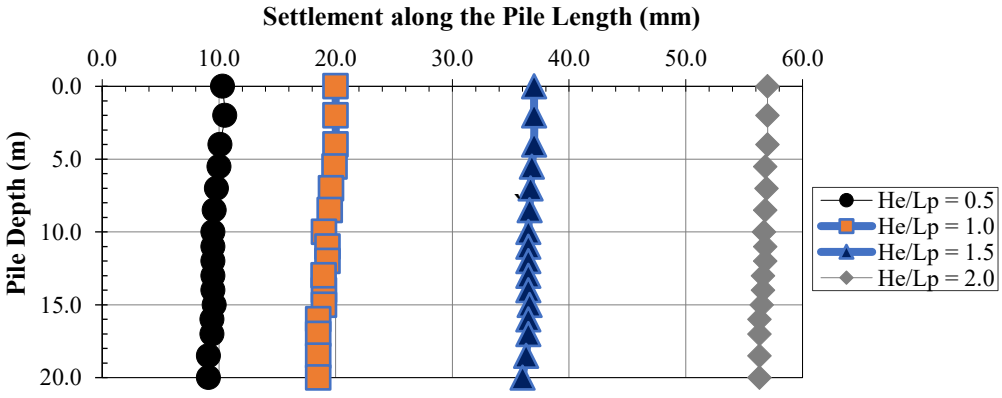

Fig. 15. The induced settlement along the pile length due to the excavation in four cases of (He/Lp)

Results indicate that as excavation depth increases, pile settlement also increases. Settlement is constant along the pile's axis. For the cases of (He/Lp = 0.5, 1, 1.5 and 2.0, respectively), the maximum pile settlement is 1, 2, 3.7, and 5.7% from pile diameter (= 1.0 m). This occurs due to the decrease in frictional resistance as the He/Lp increases, causing an increase in the settlement value.

5.1.2. The Lateral Deflection Induced Along the Length of Pile Due to the Excavation

The lateral deflection profile of the pile as a result of the excavation is shown in Figure 16 for four case of (He/Le). The pile is moving in the direction of excavation if the values are negative. The results indicate that in four different cases of (He/Lp), the pile deflected towards the excavation side, as would be predicted given that excavation causes soil to be displaced in that direction and reduces stress. When He/Lp = 0.5, the maximum lateral deflection value is 8.5 mm, (0.85% of the pile diameter), at the pile head, then the deflection decrease until 12 m of the pile length.

As shown in Figure 17, the lateral deflection value increases from the pile head and reaches a maximum value of 12.7 mm (1.27% of the pile diameter) at 11.0 m of the pile length. After that, the deflection starts to decrease according to the case of (He/Lp = 1.0). The pile toe shows the largest lateral displacement when He/Lp = 1.5, reaching a maximum of 22.7 mm (22.75% from the pile diameter).

Additionally, in the case of (He/Lp = 2.0), the pile toe experiences the greatest lateral displacement, which reaches a maximum of 24.8 mm (24.80 % of the pile diameter). It means that when He/Lp = 2.0, the pile toe obtains the most lateral deflection. While the pile toe experiences the lowest lateral deflection when He/Lp = 0.5. In addition, whereas pile toe lateral displacements are dependent on excavation depth, head of pile settlements are similar in all four cases. The reason for the increase in lateral deflection is that by increasing the excavation depth, and the pile is loaded, it causes movement in the direction of the excavation due to the lack of soil surrounding the pile, causing a decrease in its bearing capacity.

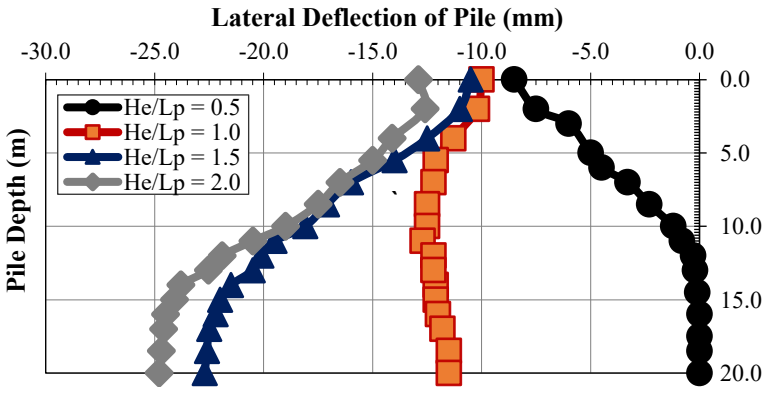

Fig. 16. The induced lateral deflection profile along the pile length due to the excavation in four cases of (He/Lp)

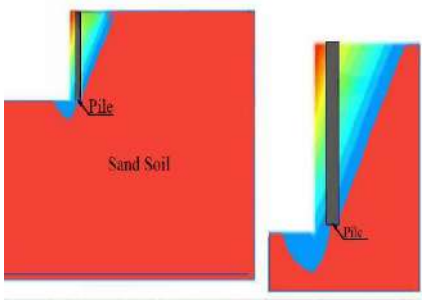

Fig. 17. The induced lateral deflection profile along the pile length. (He/Lp = 1.0)

5.1.3. Bending Moment Induced by Excavation Along the Pile Length

Figure 18 shows the generated bending moment profile at the pile as a result of the excavation in each of the four cases of (He/Lp). The pile is under tensile stress, which is toward the excavation, as illustrated by the negative values. The generated value of bending moment at the pile head is zero in all cases because of the pile's free head. According to the results, the upper length of the pile is where the negative bending moment always develops gradually. For case of (He/Lp = 0.5), the value of bending moment becomes positive in the portion below and then gradually decreases until the pile-toe bending moment, where it finally becomes zero. A similar bending moment behaviour exhibits for cases (He/Lp = 1, 1.5, and 2.0), where the full pile shaft experienced a negative bending moment, putting the pile shaft under tensile stress, and where the bending moment was zero at the pile toe. In all four cases, the maximum bending moment (positive or negative, depending on the excavation depth) occurs at a depth of roughly 0.70% of the normalized depth of the pile. For case of (He/Lp = 1), the pile toe was at the same level as the ultimate excavation depth, resulting in the highest moment. In contrast, for case of He/Lp = 0.5 produced a greater bending moment than the case of (He/Lp = 2.0) because the lower portion of the pile in the case of (He/Lp = 0.5) was subjected to higher levels of soil constrain. As a result, it may be said that the pile experiences the greatest bending moment when He/Lp = 1, and the least amount of bending moment when He/Lp = 2.0.

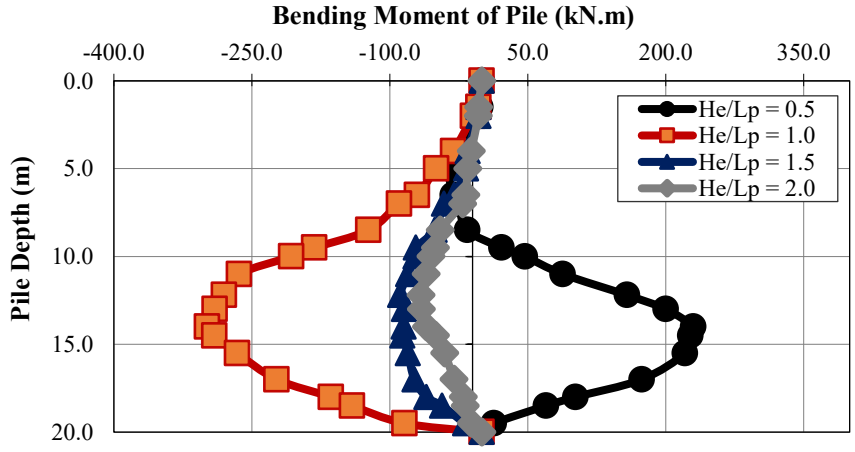

Fig. 18. The induced bending moment profile along the pile length due to the excavation in four cases of (He/Lp)

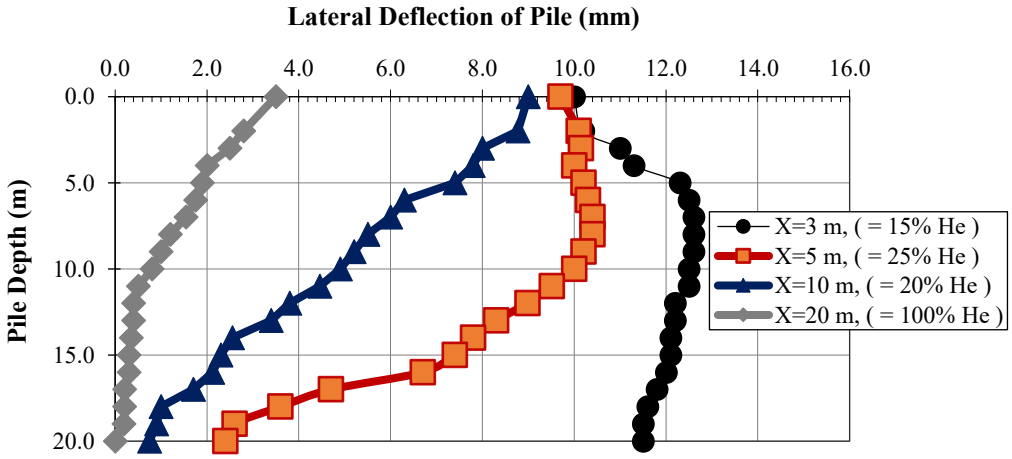

Fig. 19. Lateral deflection of the pile due to changing the distance from the pile to the excavation site (He/Lp = 1.0, He = 20 m)

5.2. The Influence of Excavation's Distance from the Pile on the Response of the Pile

The effect of the horizontal distance of the excavation site on pile reaction was investigated at four different distances: 5, 10, and 20 m (i.e., 15%, 25%, 50%, and 100% from the final excavation depth He). 20 m (He/Lp = 1) was the final excavation depth and pile length that kept constant. The results indicate that, as expected, the pile's lateral deflection decreases as the distance from the excavation (X) to the pile increases (see Figure 19). Additionally, it is obvious that, at a distance of 20 m, the value of lateral deflection of the pile head decreases significantly. In addition, the deflection of pile-toe decrease as the distance increases.

Furthermore, the bending moment along the pile length is clearly reduced as the distance from the pile to the excavation (X) increases, as shown in Figure 20. After a distance of 10 m between the excavation and the pile, it is found that the generated bending moments on the pile are neglected.

5.3. Influence of the Type of Pile Head on the Response of the Pile

The value of a pile's lateral deflection as a result of excavation for free, hinged, and rigid pile heads (He/Lp = 0.5, 1, 1.5, and 2.0, respectively) is shown in Figures 21 to 24. The hinged head indicates a pile group connected to a beam, whereas the stiff head represents piles restrained back by a rigid raft. The figures show that, in each of the three conditions, the deflection at the pile head was exactly zero due to the stiff head.

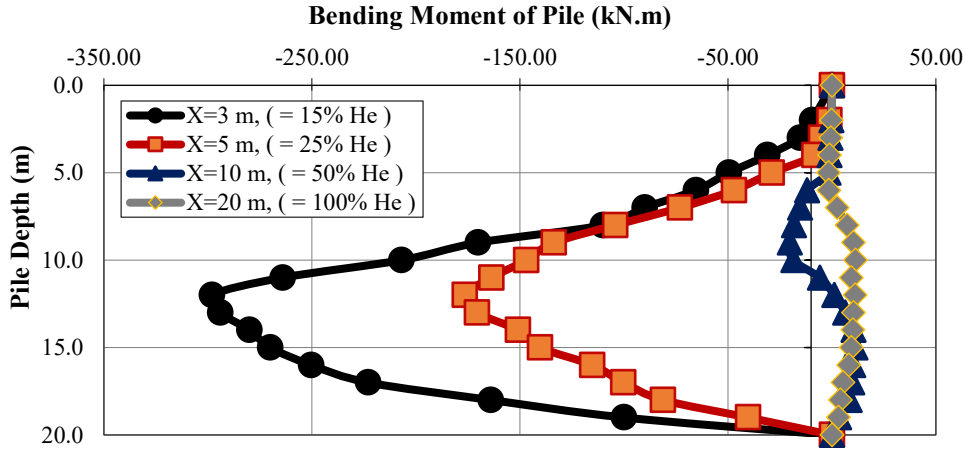

Fig. 20. Bending moment of the pile due to changing the distance from the pile to the excavation site (He/Lp = 1.0, He = 20 m)

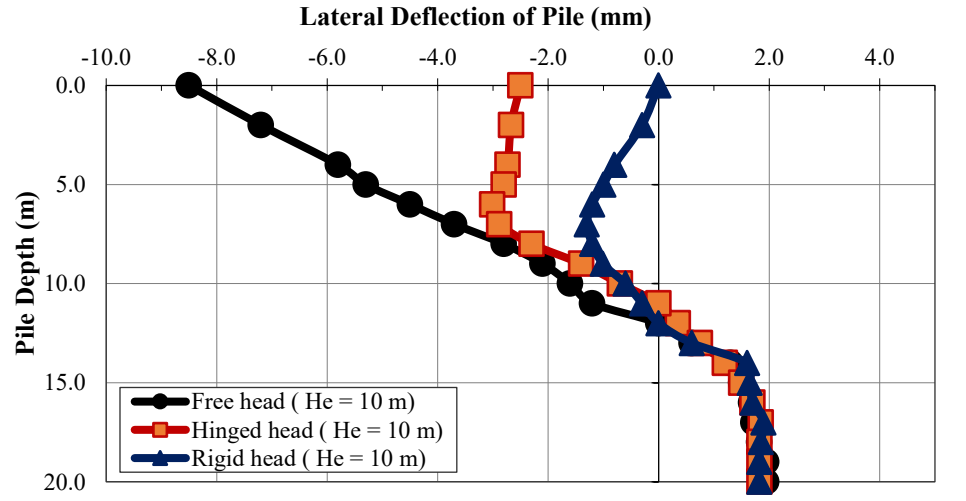

Fig. 21. Lateral deflection of the pile in case of free, hinged, and rigid pile head (He/Lp = 0.5)

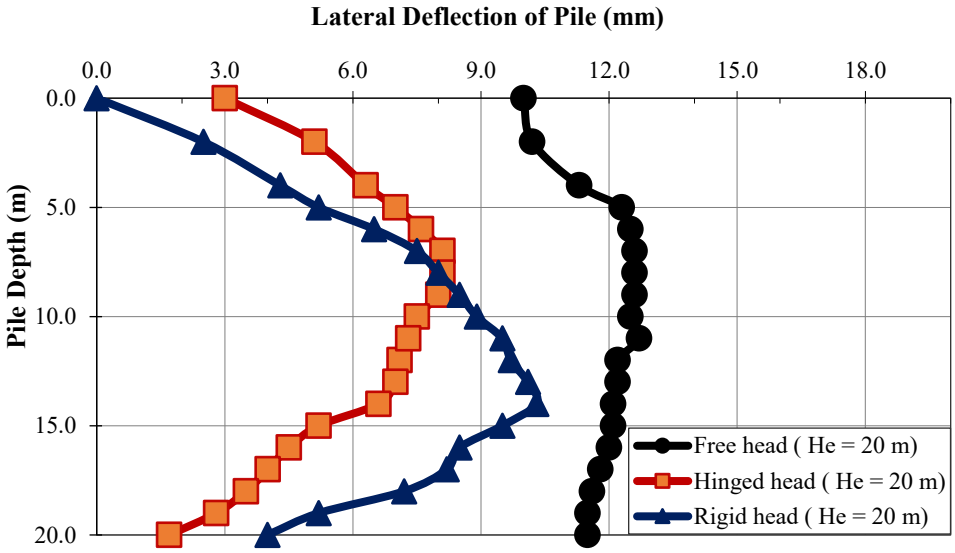

Fig. 22. Lateral deflection of the pile in case of free, hinged, and rigid pile head (He/Lp = 1.0)

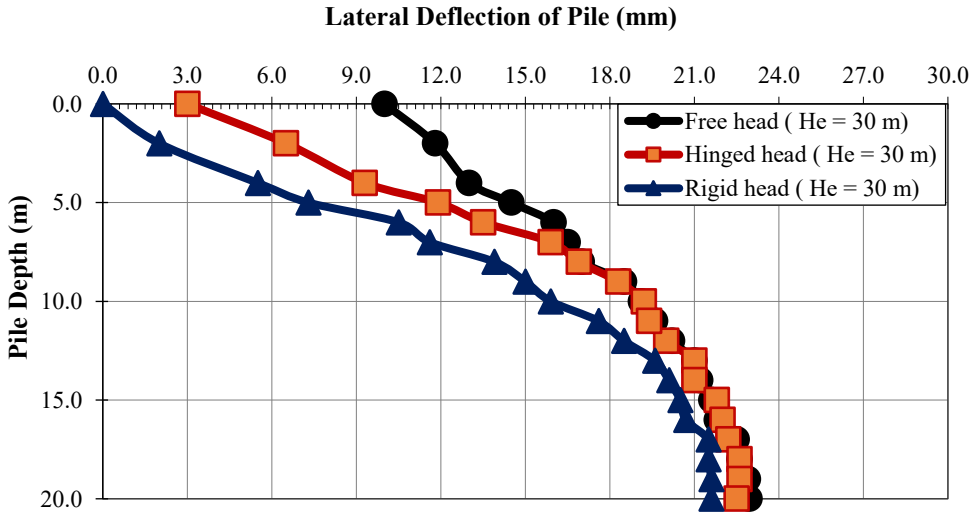

Fig. 23. Lateral deflection of the pile in case of free, hinged, and rigid pile head (He/Lp = 1.5)

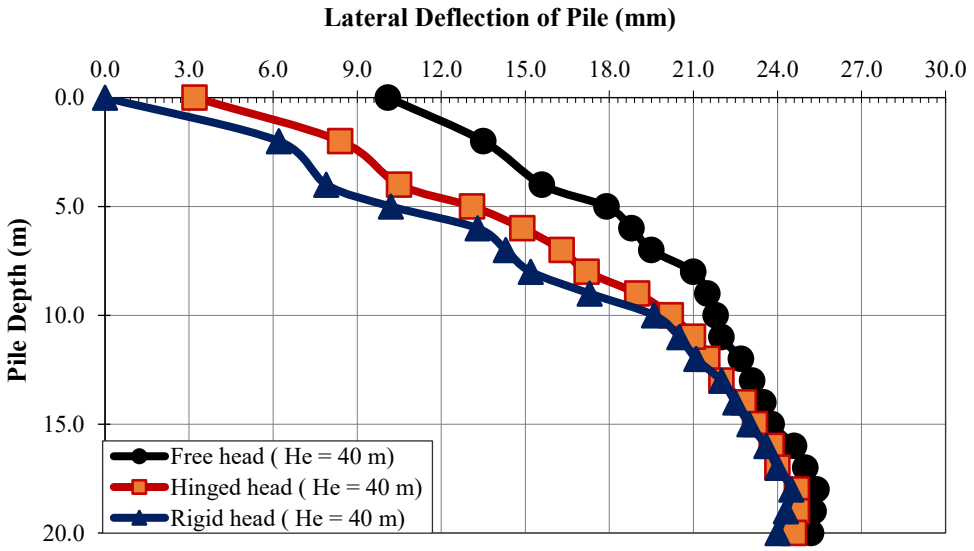

Fig. 24. Lateral deflection of the pile in case of free, hinged, and rigid pile head (He/Lp = 2.0)

This is due to the pile head's restrictions against both horizontal and vertical movement. Additionally, it should be mentioned that the maximum deflection for (He/Lp = 1.5) was about at the pile's mid-depth, but for (He/Lp = 2.0) the highest deflection for all pile head conditions was near the pile's toe. The generated pile bending moment for free, hinged, and rigid pile heads, respectively, are shown in Figures 25 to 28 for each of the four cases of (He/Lp = 0.5,1,1.5 and 2.0).

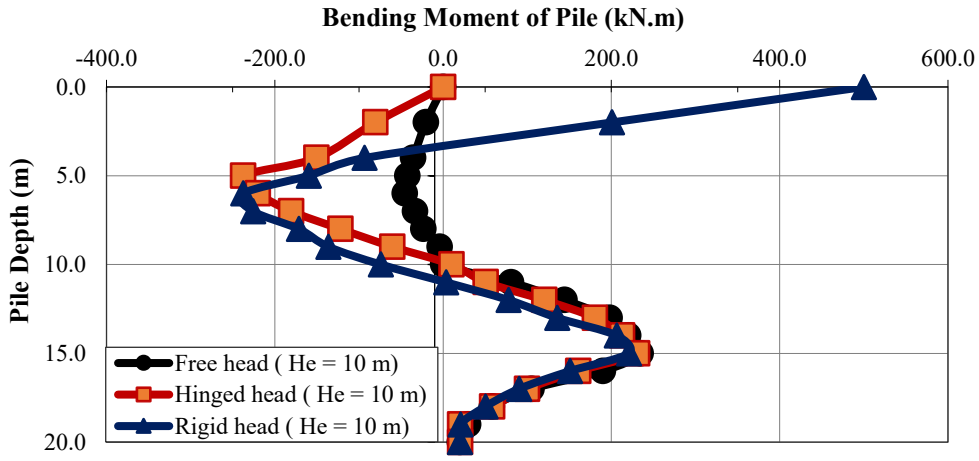

Fig. 25. Bending moment induced along the pile length in case of free, hinged, and rigid pile head (He/Lp = 0.5)

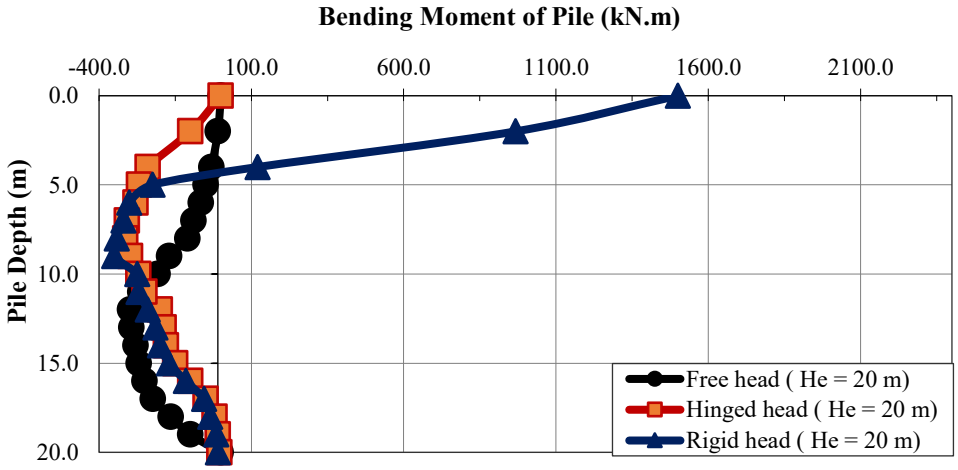

Fig. 26. Bending moment induced along the pile length in case of free, hinged, and rigid pile head (He/Lp = 1.0)

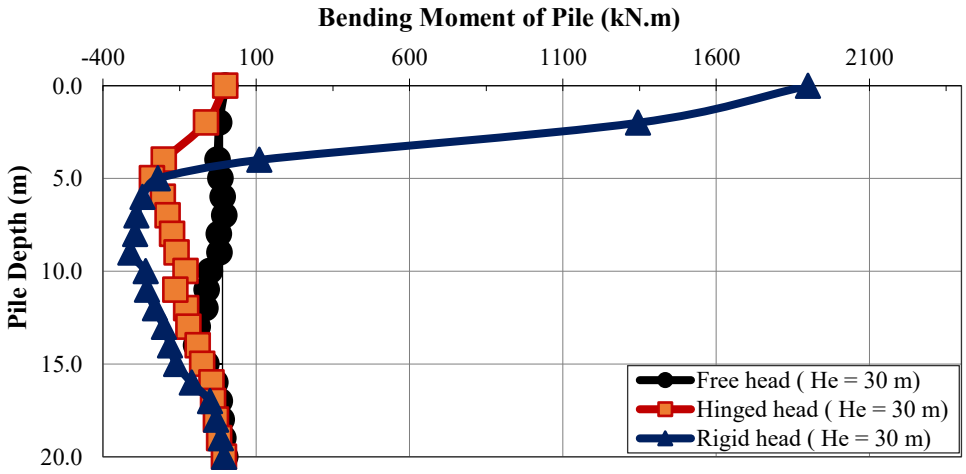

Fig. 27. Bending moment induced along the pile length in case of free, hinged, and rigid pile head (He/Lp = 1.5)

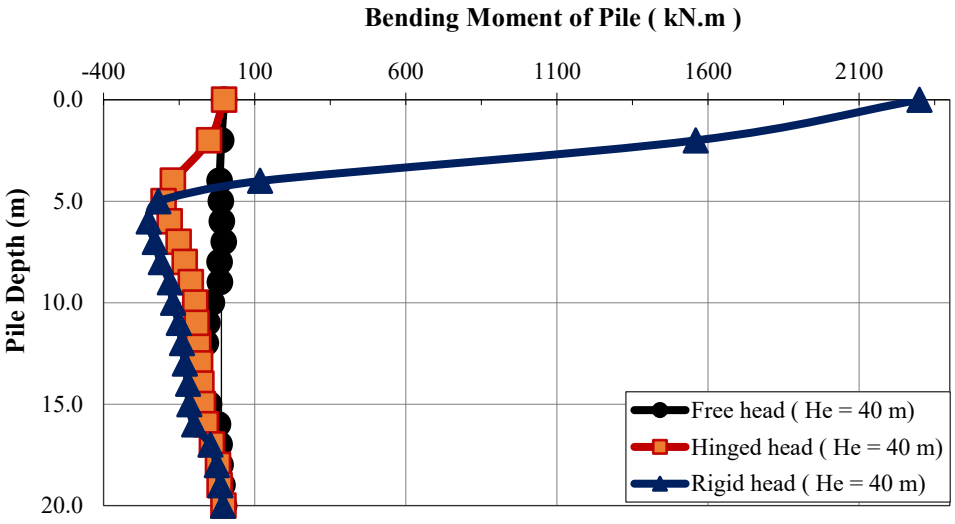

Fig. 28. Bending moment induced along the pile length in case of free, hinged, and rigid pile head (He/Lp = 2.0)

If the values are negative, there is tensile stress on the pile along its shaft. At the pile head, a significant positive bending moment was created because the movement of the pile head was restricted in the case of a rigid head. Figures 25 to 28 show how the generated positive BM at the pile head grows with increased excavation depth. Consequently, it might be considered that the type of pile head and the depth of the excavation have a significant role in determining how the pile responds to excavation, especially when the pile head is rigid and induces a substantial positive bending moment.

5.4. Effect of the Pile Diameter on the Pile's Response

Three varied diameters of 0.5, 1.0, and 1.5 m were investigated to examine the impact of pile diameter on the pile reaction. The excavation was limited to a depth of 20 m, and the pile length was kept at 20 m throughout these analyses. The lateral deflection of the pile due to variations in the pile's diameter is shown in Figure 29. For the case of (He/Lp = 1.0), the maximum values of lateral deflection are 1.05%, 1.27% and 3.16% from pile diameter, respectively.

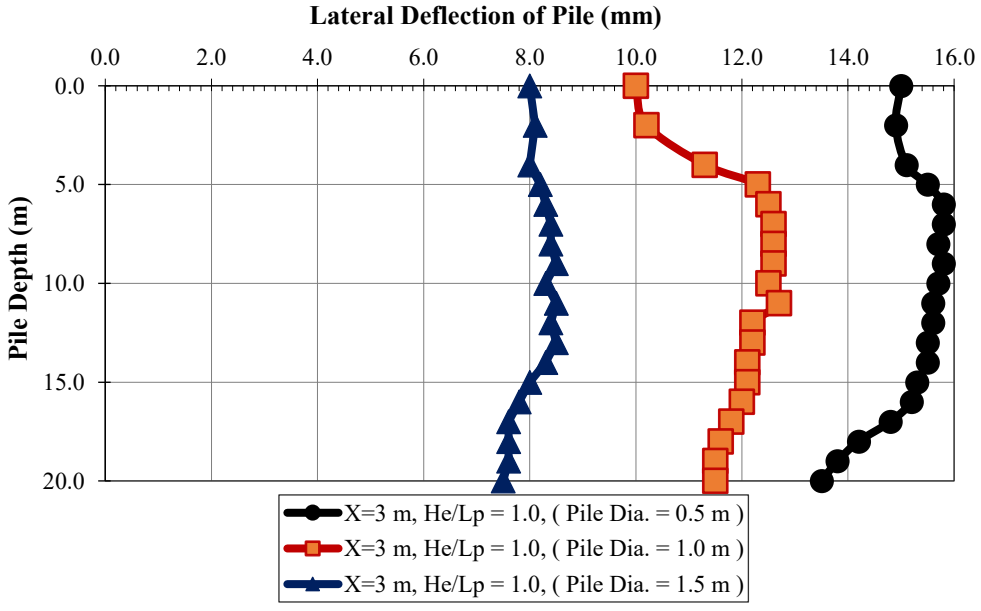

Fig. 29. Lateral deflection of the pile due to changing the pile diameter (He/Lp = 1.0)

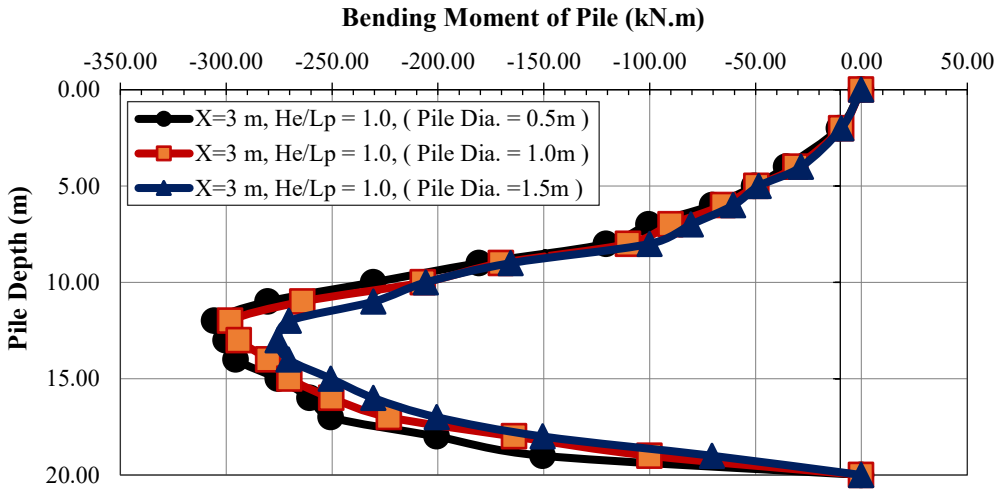

Fig. 30. The induced bending moment of the pile due to changing the pile diameter (He/Lp = 1.0)

Additionally, Figure 30 shows how the pile's bending moment changed as the pile's diameter increased. As a result, the results show that there are no appreciable differences between the three pile diameter scenarios. The results show that with increasing pile diameter, there is a decrease in the value of lateral deflection of the pile due to the increase in the contact area between the pile and surrounding soil; hence, the bearing capacity of the pile increases and there is a decrease in lateral deflection.

6. Conclusions

Using PLAXIS 3D software, a 3D finite element analysis was carried out in the present study to investigate how nearby deep excavation affected the behaviour of a loaded single pile in sand soil. A parametric study was carried out to determine the effect of different factors on pile behaviour, such as excavation depth, distance from pile to excavation site, pile head type, and diameter pile (after Leung et al., 2006), once the finite element model had been validated using previously presented centrifuge test results. Based on the results of the finite element analysis, the followings are the study's recommended conclusions:

- The maximum pile settlement for each case of He/Lp = 0.5, 1, 1.5 and 2.0 is 10, 20, 37 and 57 mm, or 1, 2, 3.7 and 5.7% from the diameter of pile (= 1.0 m).
- The pile toe is where the largest lateral deflection occurs when He/Lp = 2.0, whereas the pile toe is where the lowest lateral deflection occurs when He/Lp = 0.5.
- The maximum magnitude of the bending moment occurs at roughly 0.70% of the normalized depth of the pile. When the pile toe and the final excavation depth were at the same level, the maximum moment was generated for He/Lp = 1. As a result of increased soil restraint on the lowest part of the pile for He/Lp = 0.5 the bending moment in that scenario was larger than He/Lp = 2.0 case.
- The lateral displacement of the pile significantly reduces with increasing distance from the excavation site (X). However, the bending moments in the pile become negligible at ten meters of distance between the excavation and the pile.
- A significant factor influencing the behaviour of the pile is the type of pile head. If the head of the pile is rigid, a large positive moment is created at the pile head. Therefore, it can be summarized that the type of pile head and the depth of the excavation have a major effect on the pile's response during excavation, particularly in the case of rigid pile heads where a strong positive value of bending moment is induced at the pile head.
- Additionally, the maximum deflection for He/Lp = 1.5 was about at the pile's mid-depth, but for He/Lp = 2.0 the highest deflection for all pile head conditions was

near the pile's toe.
- As pile diameter increases, the maximum pile lateral deflection decreases.
- Increased pile diameter has no effect on the pile's bending moment.
- Thus, it can be concluded that if the most important safety measures are not followed. Depending on the length and depth of the excavation as well as the characteristics of the soil and pile, a new excavation site can significantly alter the stability of the present pile structure.
- As a limitation, this study focused on the single pile, the pile subjected to axial force only, no bending moment allowed.

7. Suggestions for Future Studies

The following cases are possible for conducting research:
- PLAXIS 3D can be used for the study to examine how adjacent pile groups subjected to inclined loading are affected by deep excavation.
- In the present study, PLAXIS 3D was used to analyse how a single pile developed as a result of adjacent deep excavation. It is suggested to simulate such cases in future research using programs such ABAQUS, Midas, and Flac.
- To examine how pile group behaviour connected by a raft foundation is affected by deep excavation.
- The provision of high diaphragm wall thickness or high supporting system stiffness would influence all results, therefore this should be taken into account.
- Studying the effect of ground water table in this analysis.

8. Notations

A: The pile area
BM: Bending moment
D_r: Relative Density
EI: Bending rigidity
E: The elastic modulus of the pile
e_{inital}: Initial void ratio
E_{50}^{ref}: Triaxial compression stiffness
E_{oed}^{ref} : Primary oedometer stiffness
E_{ur}^{ref} : Unloading/reloading stiffness
FE: Finite element
F_{max}: The maximum base resistance
He: Final depth of excavation
HS: Hardening soil model
He/Lp: Excavation depth to pile length ratio
k: Cam-clay swelling index
Lp: Pile length
Lp/dp: Pile length to pile diameter ratio
LD: Lateral deflection
M: Tangent of the critical state line
MCC: Modify Cam Clay
T_{max}: Maximum skin resistance
X: Distance from the excavation to the pile (center to center)
γ_{dry}: Soil unit weight
γ_{sat}: Saturated unit weight
μ: Coefficient of permeability
K_0^{nc}: Value for normal consolidation
λ: Cam-clay compression index
Ø: Friction Internal Angle
ν: Poisson's ratio
p^{ref}: Reference stress for stiffness
ψ: Dilatancy angle
$\Delta ph,max$: Maximum pile head settlement at the pile ultimate capacity

9. References

Alielahi, H., Mardani, Z. and Daneshvar, S. (2014). "Influence of under-reamed pile groups arrangement on tensile bearing capacity using fe method", *Electronically Journal of Geotechnical Engineering (EJGE)*, 19, 1395-1410, https://www.researchgate.net/publication/271445649.

Ashour, S. (2021). "Analyses of the effect of deep excavation on behaviour of adjacent pile in sand using 3d finite element method", MSc. Thesis, Bursa Uludağ University, http://hdl.handle.net/11452/22363.

Bowles, J.E. (1997). *Foundation analysis and design*, The McGraw-Hill Companies, Inc., Fifth Edition, ISBN 0-07-912247-7, https://apilibrary.lqdtu.edu.vn/media/FoundationAnalysisAndDesign.pdf.

Hsiung, B.C. (2009). "A case study on the behaviour of a deep excavation in sand", *Computers and Geotechnics*, 36(4), 665-675, https://doi:10.1016/j.compgeo.2008.10.003.

Leung, C.E., Ong, D.E. and Chow, Y.K. (2006). "Pile behaviour due to excavation-induced soil movement in clay. i: stable wall", *Journal of*

Geotechnical and Geoenvironmental Engineering, 132(1), 36-44, https://doi:10.1061/(ASCE)1090-0241(2006)132:1(36).

Le, N.T. and Nguyen, T.A. (2021). "3D finite element analysis of pile behaviour inside the deep excavation in soft soil", *International Journal of Engineering Research and Technology (IJERT),* 10(1), 5-10, http://doi.org/10.17577/IJERTV10IS010007.

Li, T. and Yang, M. (2023). "Investigation of passive pile groups' responses induced by combined surcharge-induced and excavation-induced horizontal soil loading", *Buildings*, 13(11), 2775, 1-13, https://doi.org/10.3390/buildings13112775.

Madhumathi, R.K. and Ilamparuthi, K. (2018). "Laboratory study on response of single pile adjacent to supported cut", Geotechnical and Geological Engineering, 36, 3111-3133, https://doi.org/10.1007/s10706-018-0524-9.

Nishanthan, R., Liyanapathirana, D.S. and Leo, J. (2016). "Shielding effect in pile groups adjacent to deep unbraced and braced excavations", *International Journal of Geotechnical Engineering*, 11(2), 162-174, https://doi.org/10.1080/19386362.2016.1200270.

Ng, C.W., Yau, T.L., Li, J.H. and Tang, W.H. (2001). "New failure load criterion for large diameter bored piles in weathered geomaterials", *Journal of Geotechnical and Geoenvironmental Engineering*, 127(6), 488-498, https://doi.org/10.1061/(ASCE)1090-0241(2001)127:6(488).

PLAXIS 3D-Reference Manual. (2020). "CONNECT Edition V20.03", Bentley, June, https://www.scribd.com/document/516563012/FEM-2D-Reference.

Shafee, A. and Fahimifar, A. (2018). "Numerical investigation on the effects of deep excavation on adjacent pile groups subjected to inclined loading", *International Journal of Geotechnical and Geological Engineering*, 12(7), 489-49, https://www.scribd.com/document/707142821/10009284.

Shakeel, M. and Ng, C.W. (2017). "Settlement and load transfer mechanism of a pile group adjacent to a deep excavation in soft clay", *Computers and Geotechnics*, 96, 55-72, http://doi.org/10.1016/j.compgeo.2017.10.010.

Shabban, M.G., Abd El-Naiem, M.A., Senoon, A.A. and Kenawi, M.A. (2023). "Interaction analysis between existing loaded piles and braced excavation design parameters", *Journal of Engineering Sciences (JES)*, 51(3), 189-206, https://doi.org/10.21608/jesaun.2023.187262.1199.

Shabban, M.G., Abd El-Naiem, M.A., Senoon, A.A. and Kenawi, M.A. (2023). "Effects of excavation and construction sequence on behaviour of existing pile groups", *Innovative Infrastructure Solutions*, 8(223), 1-12, https://doi.org/10.1007/s41062-023-01193-8.

Soomro, M.A., Mangnejo, D.A., Bhanbhro, R., Memon, N.A. and Memon, M.A. (2019). "3D finite element analysis of pile responses to adjacent excavation in soft clay: Effects of different excavation depths systems relative to a floating pile", *Tunnelling and Underground Space Technology*, 86, 138-155, https://doi.org/10.1016/j.tust.2019.01.012.

Soomro, M.A., Mangi, N., Cheng, W. and Mangnejo, A. (2020). "The effects of multipropped deep excavation-induced ground movements on adjacent high-rise building founded on piled raft in sand", *Advances in Civil Engineering*, 2020(1), 8897507, https://doi.org/10.1155/2020/8897507.

Teh, K.L., Leung, C.F. and Chow, Y.K. (2005). "Spud can penetration in sand overlying clay", *Soil Mechanics | Geotechnical Engineering*, ISFOG 2005, Perth, Australia, 529-534, https://scholarbank.nus.edu.sg/handle/10635/74363.

Ünsever, Y.S. (2015). "An experimental study on static and dynamic behaviour of model pile foundations", Ph.D. Thesis, Middle East Technical University, Turkey, https://open.metu.edu.tr/bitstream/handle/11511/24493/index.pdf.

Yi, S. (2022). "Parametric study of passive piles subjected to adjacent surcharge load in extensively deep soft soil", *Frontiers in Materials*, 9, 1080547, http://doi.org/10.3389/fmats.2022.1080547.

Zhang, R., Zhang, W. and Goh, A.T. (2018). "Numerical investigation of pile responses caused by adjacent braced excavation in soft clays", *International Journal of Geotechnical Engineering*, 15(7), 783-797, https://doi.org/10.1080/19386362.2018.1515810.

Civil Engineering Infrastructures Journal 2025, 58(1): 123-145
DOI: 10.22059/ceij.2024.366834.1975

RESEARCH PAPER

Structural Failure of Masonry Arch Bridges Subjected to Seismic Action

Bagherzadeh Azar, A.[1*] and Sari, A.[2]

[1] Ph.D. Candidate, Institute of Earthquake Engineering and Disaster Management (ITU Graduate School), Istanbul Technical University, Istanbul, Turkey.
[2] Professor, Faculty of Civil Engineering, Istanbul Technical University, Istanbul, Turkey.

Received: 18 Oct. 2023; Revised: 04 Dec. 2023; Accepted: 25 Dec. 2023

ABSTRACT: This study investigates the seismic response of a historical arch bridge using a macro-modelling technique in Finite Element (FE) software ABAQUS. A comprehensive investigation involving documentary sources and on-site assessments has facilitated a thorough understanding of the case study, the Halilviran bridge. 3D finite element models incorporating damage plasticity behavior were constructed for the FE model. The masonry units were modelled with the Concrete Damage Plasticity (CDP) material model, and the backfill was developed with the Mohr-Coulomb (M-C) material model. Nonlinear dynamic analysis was utilized to predict the progression of damage to the bridge and determinate the most susceptible structural components. The seismic performance of the case study was evaluated through an examination of the outcomes utilizing contour plots depicting tensile damage, maximum displacements, and energy calculated from the tensile damage. The findings indicate that the spandrel walls, which are interconnected with the pier, and the inner section of the arches represent the most vulnerable components of masonry bridges, the failure of which heightens the risk of progressive collapse of the bridge.

Keywords: Masonry Arch Bridges, Seismic Behavior, Strengthening Techniques, Collapse, Bridge Failure.

1. Introduction

The breakdown of infrastructure can result in significant economic and social consequences and impede rescue and recovery efforts. It is crucial to assess the effectiveness of historical masonry structures and provide detailed and accurate data to inform maintenance decisions for reinforcing them against seismic forces.

The earthquakes that have taken place in the last 25 years have clearly shown the high vulnerability of masonry structures to seismic events (Milani, 2019b) owing to their distinctive characteristics and susceptibility to lateral forces. Research conducted post-earthquakes has shown that the main reason for the susceptibility of buildings is the presence of local failure modes, which are a result of the out-of-plane response of structural components.

Hence, it is imperative to introduce a sufficiently thorough methodology capable of accurately representing the actual structural reaction of intricate structures to lateral forces and precisely identifying the

* Corresponding author E-mail: azar19@itu.edu.tr

most vulnerable elements. Post-earthquake assessment of the structure along with Nonlinear Dynamic Analysis (NDA) is a comprehensive approach for studying the structural behavior, which involves analyzing force redistribution, ductility, damage and collapse mechanisms. Various methods have been suggested, utilizing sophisticated numerical and experimental tools to generate three-dimensional models of the structures, analyze failure mechanisms and design effective strengthening techniques (Castellazzi et al., 2017; Clementi et al., 2017; Valente and Milani, 2019). The research conducted by Li and Chen (2023) aimed to examine the seismic vulnerability of a reinforced concrete girder bridge. The investigation involved the integration of nonlinear vulnerability analysis techniques with numerical and probabilistic modeling methods. The study selected 1069 reinforced concrete bridges that had been impacted by the Wenchuan earthquake for vulnerability assessment. The vulnerability of the damaged bridges was evaluated using the Chinese seismic intensity scale. A new approach was devised to compare vulnerabilities by considering both the failure ratio and the likelihood of exceeding certain thresholds. Furthermore, a model was established to compute the average damage index of reinforced concrete girder bridges across various intensity zones. This model uses matrix calculations and compares vulnerability parameters using matrices and curves.

Li (2023) examined the seismic vulnerability characteristics of buildings and evaluates the seismic capacity of different types of structures during real seismic events. This research employed probabilistic damage model analysis techniques. Additionally, a nonlinear regression-based approach was presented for analyzing prediction models. A predictive model was created to assess structural vulnerability, taking into account failure rates and the probability of exceeding certain intensity levels in different areas. The model was validated using data from an earthquake damage database. Moreover, a vulnerability matrix predictive model was introduced, which involveed updating the mean vulnerability index parameter. A comparative model was also developed to predict the vulnerability matrix of typical structures in specific regions.

Pelà et al. (2013) performed a seismic evaluation of an existing masonry bridge consisting of three curved segments. The seismic capacity of the bridge was evaluated using time history and pushover analysis techniques. Altunısık et al. (2015) performed a research investigation on the impact of arch thickness on the load-bearing capacity of arch bridges, and evaluated the seismic resilience of such bridges. To accomplish this goal, artificial acceleration records were generated, considering the seismic characteristics of the location where the bridge is located.

Li et al. (2023) developed metrics and probability indicators to assess the resilience and vulnerability of group formations in both urban and rural settings. Their research comprised a statistical analysis of seismic damage data gathered during field surveys after the Jiuzhaigou earthquake in Sichuan Province, China. The researchers developed a methodology for comparing and analyzing multidimensional modal resilience and probability metrics. They suggested a quantitative approach to improve the precision and rationality of structural resilience evaluations in the context of macro intensity measurement. This model was based on maximizing the macro intensity index and refining the lognormal distribution. Additionally, comparative models were formulated to appraise group structure resilience against established macro intensity benchmarks. The study also encompassed on-site damage assessments and analyses of the mechanisms of destruction, considering the unique attributes of regional structural seismic resilience and the actual vulnerabilities exposed during the

earthquake event.

The current research presents the results of sophisticated numerical analyses performed on 3-D finite element models. In order to enhance the precision of evaluating the behavior of macro-elements at both local and global levels, and to qualitatively evaluate the mechanical properties of the masonry, data is incorporated from comprehensive surveys, laser scanning, and non-destructive testing.

This paper is succinctly divided into three main components. Firstly, a 3-D finite element model of the bridge is constructed. Following this, non-linear dynamic analyses are carried out, beginning with a material model. The final stage involves a detailed and meticulous analysis of the results, requiring a comprehensive understanding and significant theoretical expertise. The primary objective of the initial modeling phase is to achieve a high level of accuracy and consider various factors that significantly impact the structure's behavior in the event of a collapse. This examination encompasses several factors, including the interconnection between the spandrel walls and the condition of them, the degradation of the masonry and the stiffness of the backfill.

2. Case Study

The Halilviran Bridge is about 20 km from the city of Diyarbakir in Turkey and is located near the Devegecidi stream. The architectural composition of the bridge is made of uniform limestone. Its most important structural feature is a semi-circular arch that rises from the rocky base in both directions of the river channel.

The stone structure, consisting of seven arches, was designed to facilitate the crossing of the river obstacle. The bridge has a total length of 132 m, with a documented roadway width of 5.10 m and a height of 8.50 m above the ground. The spans of the arches range from 5.95 m to 7.00 m, increasing from west to east.

The seventh arch to the east has a special shape compared to the previous arches. It has a pointed shape that resembles the round arch, but is lower in height. Figures 1 and 2 show the architectural design, cross-sectional views and vertical views as well as the main geometric dimensions of the Halilviran bridge.

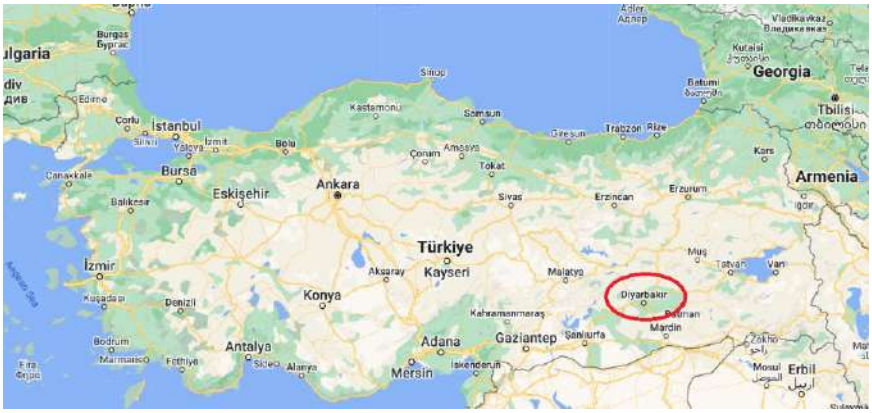

(a)

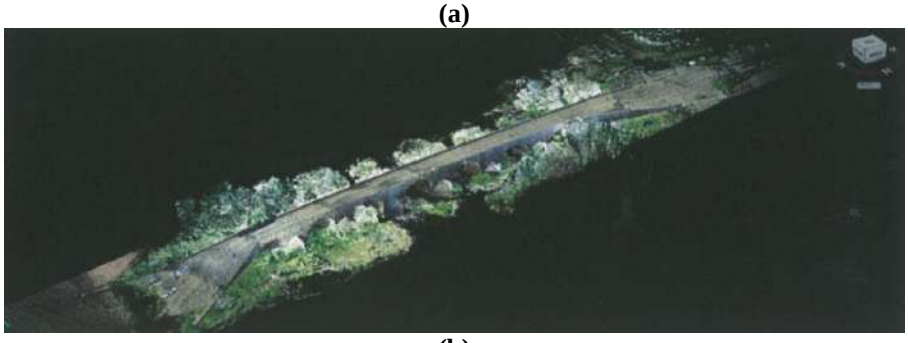

(b)

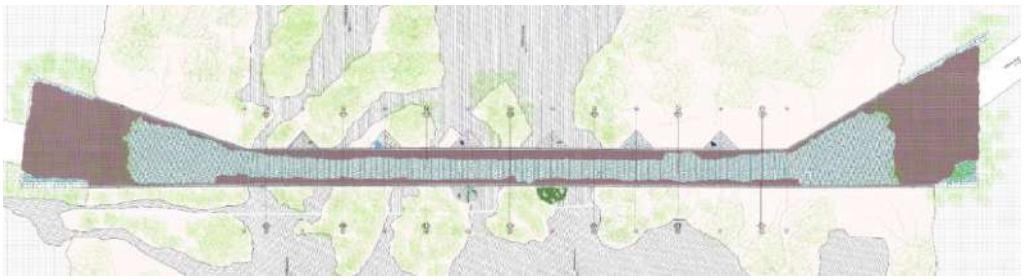

(c)

Fig. 1. Halilviran bridge: a) Location; b) 3D Scanning cloud image; and c) CAD drawing (Azar and Sari, 2023)

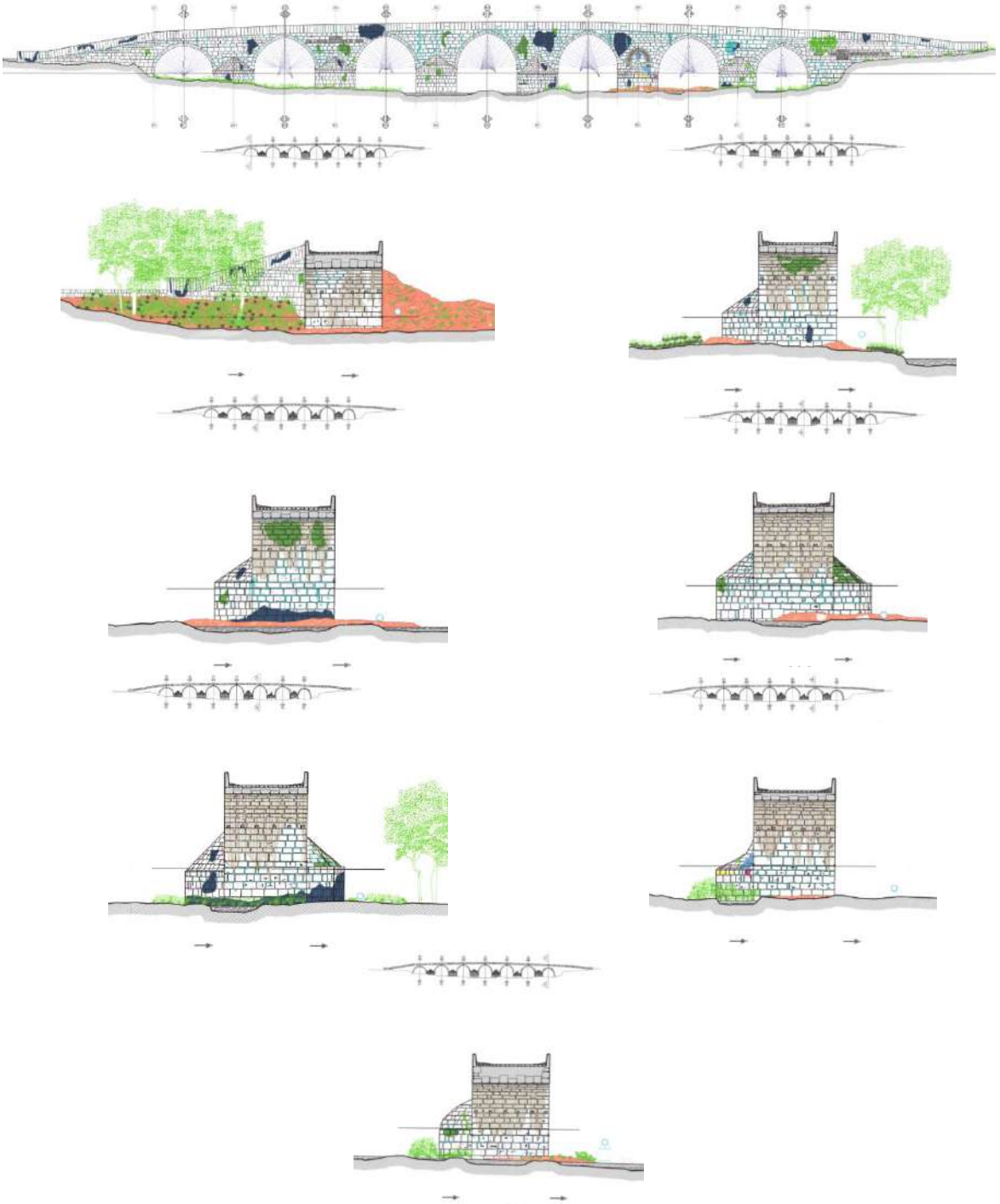

Fig. 2. Halilviran Bridge: Section and elevation views with indication of the main geometrical dimensions (Azar and Sari, 2023)

3. FE Models and Material Model Adopted

The 3D finite element discretization was applied using C3D8R, which denotes 8-node reduced integration elements. The selection of the element size was determined to achieve precise outcomes and computational effectiveness within the framework of non-linear dynamic analyses.

Figure 3 depicts the viewpoints of the geometric representations of the bridge, which were generated within the commercial software ABAQUS. These representations consist of separate structural elements known as macro-elements, as shown in Figure 4. In order to ensure the accurate modeling of the bridge's response, it is essential to consider the interplay among its different components.

This study focuses on examining the interaction between the masonry-masonry and masonry-backfill elements. The analysis assumes a zero-thickness contact, employing a hard contact model to depict the interaction between the surfaces. In this context, "hard" contact denotes an interaction where there is no softening or penetration of the surfaces within the model. Furthermore, a friction coefficient of 0.78 is adopted to characterize the tangential behavior.

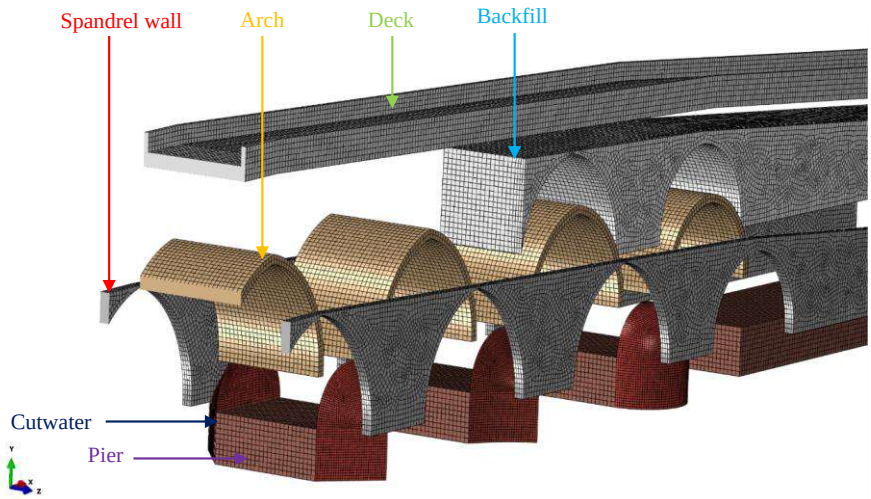

Fig. 3. Finite element model of the bridge

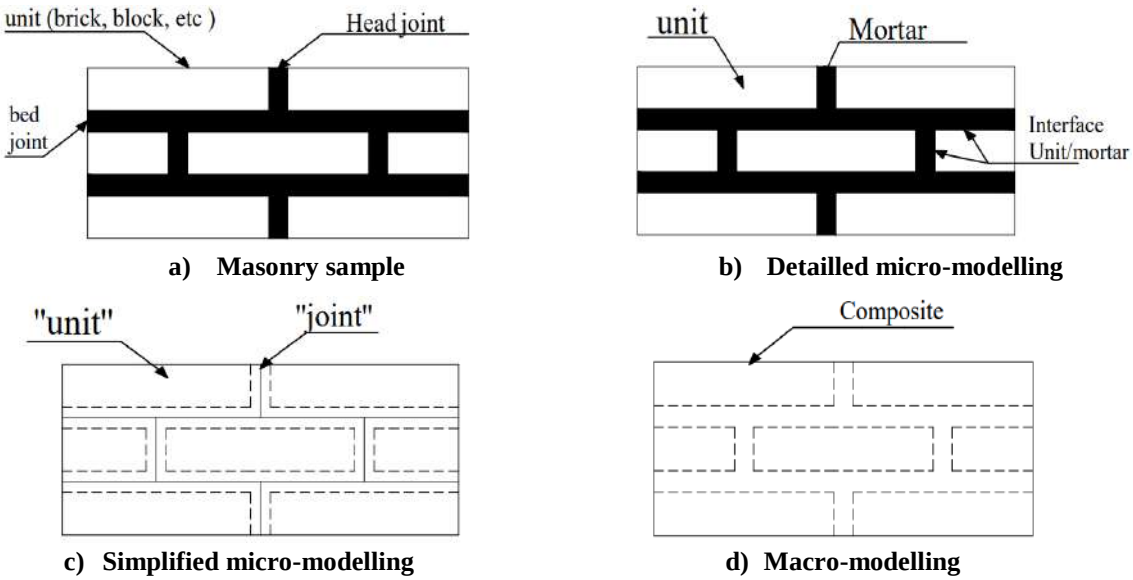

a) Masonry sample **b) Detailled micro-modelling**

c) Simplified micro-modelling **d) Macro-modelling**

Fig. 4. Material modeling techniques (Hokelekli and Yilmaz, 2019)

The mechanical material parameters for the interfaces and masonry units are determined based on relevant literature sources (Borlenghi et al., 2023; Pepi et al., 2021; Ashayeri et al., 2021; Güllü and Özel, 2020; Alpaslan et al., 2023; Gaetani et al., 2021; Gönen and Soyöz, 2022; Stockdale et al., 2019; Ferrero et al., 2021). The material characteristics for masonry and backfill are shown in Tables 1 through Table 4 (Azar and Sari, 2023, 2024, 2025).

4. Material Properties

4.1. Material Model

Concrete Damage Plasticity (CDP) presents a commendable approach for accurately representing two common types of failure, namely tensile cracking and compressive crushing. This modeling technique efficiently integrates the deterioration of materials under cyclic stress conditions.

Figure 5 illustrates the inherent behavior of masonry when subjected to both tensile and compressive loads. Within the context of tensile behavior, the material exhibits a linearly elastic response until it reaches a point known as σ_{t0}. Micro fracture is the result of a material reaching its maximum stress.

Table 1. Plasticity parameters of the CDP model

Parameter	Value
Dilation angle (ψ)	20°
Eccentricity (ε)	0.1
f_{b0}/f_{c0}	1.16
K_c	0.667
Viscosity parameter	0.01

Table 2. Basic material properties

Part	ρ (Kg/m^3)	E (Mpa)	υ
Pier	2200	3500	0.2
Cutwater	2200	2800	0.2
Arch	2200	3360	0.2
Backfill	2000	500	0.2
Spandrel wall	1900	1500	0.2
Deck	2000	1500	0.2

Note: E: isYoung's modulus; ρ: is density; υ: is poisson's coefficient.

Table 3. Input parameters for backfill material

ρ (Kg/m^3)	E (N/mm^2)	υ	c (MPa)	∅ (°)
1900	500	0.2	0.05	35

Table 4. Inelastic material parameters

Part	f_t (Mpa)	f_c (Mpa)	G_f (Mpa)
Pier	0.71	7.06	45
Arch	0.84	8.4	54
Spandrel wall	0.32	3.15	20.3

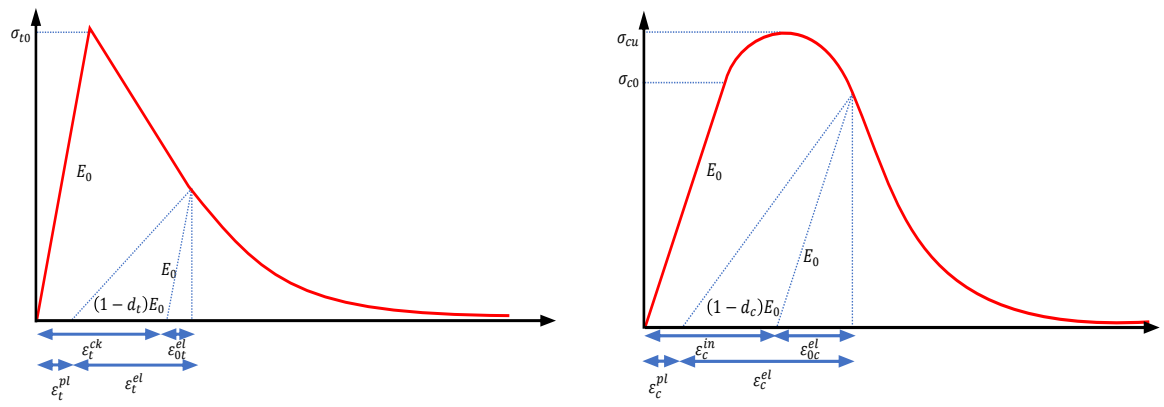

(a) **(b)**

Fig. 5. Representation of the masonry constitutive behavior in: a) Tension; and b) compression

After reaching its maximum point, the material exhibits a softening behavior in relation to the stress-strain relationship, as depicted in Figure 5a. Material undergoes deformation when it is compressed, and this deformation is observed at the point where the stress is at its maximum. At the point of maximum stress, the material demonstrates a softening behavior, as shown Figure 5b.

The CDP model may be characterized in terms of stress and strain, as follows.

$$\sigma_t = (1 - d_t) D_0^{el} : (\varepsilon - \varepsilon_t^{el}) \quad (1)$$

$$\sigma_c = (1 - d_c) D_0^{el} : (\varepsilon - \varepsilon_c^{el}) \quad (2)$$

where t: stands for tension, c: is denoted as compression, σ_t: is tensile stress and σ_c : compressive stress. ε_t^{el}: is plastic strain in tension and ε_c^{el}: is denoted as compression strain. Additionally, d_t and d_c; are variables that signify damage, and D_0^{el}: stands for undamaged initial elastic modulus.

4.2. Mohr-Coulomb Constitutive Model

The fill material commonly comprises soil, unbounded masonry, or rubble. The current study utilizes this material model to integrate the infill (Table 3). The Mohr-Coulomb criterion states that the yield point of a material is determined by the linear correlation between the shear stress acting on any point in the material and the normal stress acting on the corresponding plane (Figure 6).

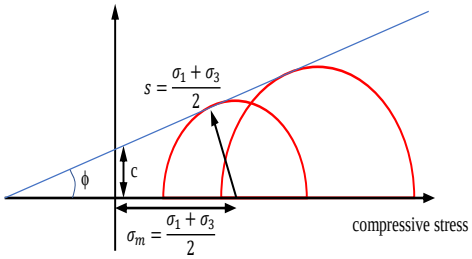

Fig. 6. Mohr–coulomb material model

In the Mohr-Coulomb material model shear stress (τ) can be characterized as a function of normal stress (σ), cohesion (c) and internal friction angle (φ) (Eq. (3)).

$$\tau = c + \sigma \tan \emptyset \quad (3)$$

The M-C model may be stated by three stress invariants, which are equivalent to pressure stress as Eq. (4).

$$p = -\frac{1}{3} trace(\sigma) \quad (4)$$

Eq. (5) represent the Mises equivalent stress.

$$q = \sqrt{\frac{3}{2}(S:S)} \quad (5)$$

where S: is stress deviator.

Eq. (6) states deviatory stress (R_{mc}) as follows.

$$R_{mc}(\Theta.\varphi) = \frac{1}{\sqrt{3}\cos\varphi} \sin\left(\Theta + \frac{\pi}{3}\right) + 1/3 \cos\left(\Theta + \frac{\pi}{3}\right) \tan\varphi \quad (6)$$

5. Verification of FE Model

A verification study was carried out on masonry arch bridges by Fanning and Boothby (2001) to establish the appropriate material properties required for accurately simulating this specific structural type. The bridges were subjected to tests in which a reference frame was placed under the bridge, Linear Variable Differential Transformers (LVDT) were attached to measure the structural displacements and a vehicle was loaded with a specific weight.

Modeling parameters such as support conditions, properties and masonry stiffness were determined by fitting the finite element model to the test results. The behavior of masonry was replicated by utilizing a solid component modeled in terms of rigidity, incorporating features such as cracks and crushing.

The infill material was characterized using a Drucker-Prager material model, while the interface between masonry and infill was defined as a friction contact surface. The bridges were subjected to operational loads in a simulation, and the results of the model were compared with the results of on-site tests of the structures. By

considering the relevant material properties and visually inspecting the material and construction of the structure, a three-dimensional nonlinear finite element analysis program can be used to accurately predict the performance of an arch bridge.

Griffith bridge has a span of 9.49 m, a height above the abutments of 2.67 m, a width of 7.85 m and an arch ring thickness of 45 cm. The front segment of the arch ring is made of granite, while the rest of the arch ring is made of limestone, with joints around 0.5 cm thick.

The spandrel walls are made of limestone blocks with a joint thickness of around 1 cm. The examination and computational analysis of the Griffith bridge in Dublin, Ireland, are showcased in Figure 7. Figure 8 displays the finite element simulation of the deformation of the arch barrel and spandrel walls under the scenario where a fully loaded truck places its rear axle at the center of the span. Figure 9 exhibits the comparative data derived from numerical simulations and physical experiments conducted at the midpoint of the bridge's central axis during the passage of the fully loaded truck.

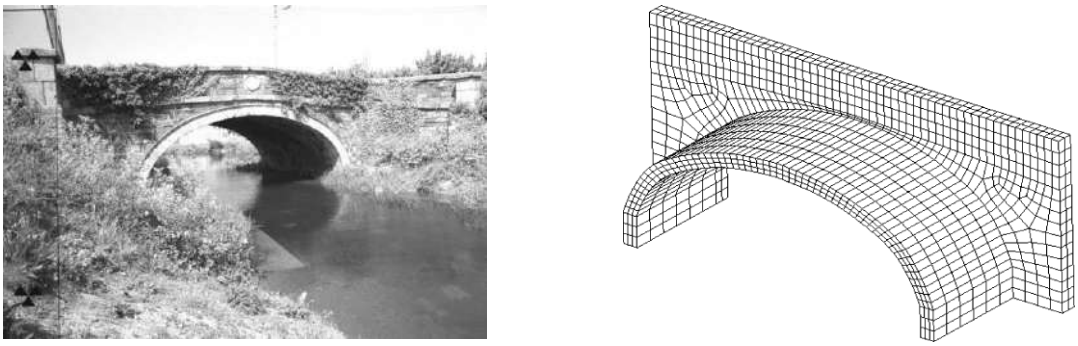

Fig. 7. Griffith bridge in Dublin, Ireland

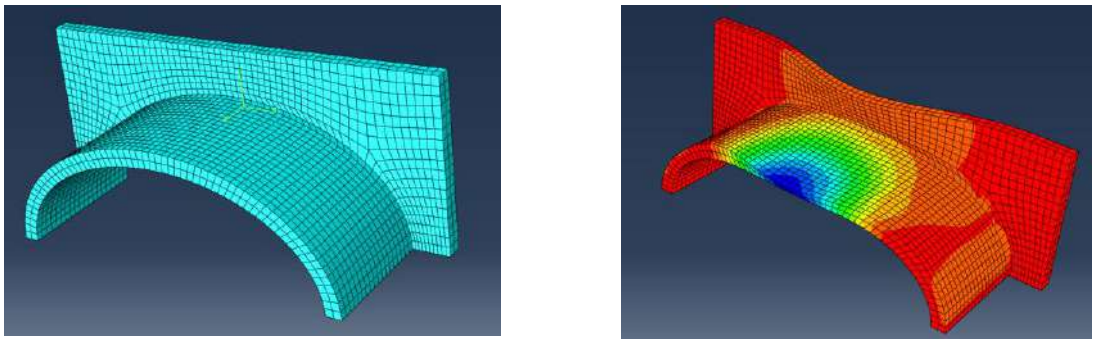

Fig. 8. Deformation of the arch barrel and spandrel walls

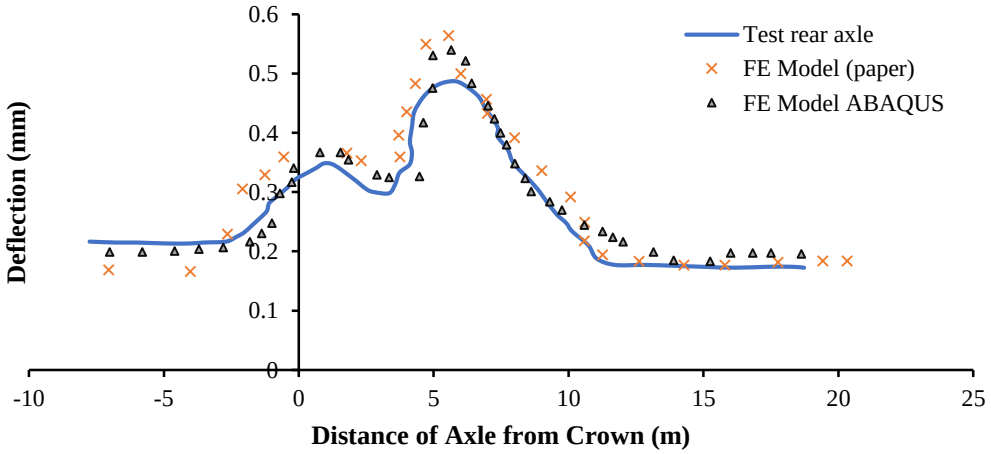

Fig. 9. Numerical and test crown displacements for fully loaded truck

The study indicated a maximum deflection of 0.43 mm in the experimental results, while the finite element model predicted a deflection of 0.54 mm.

6. Modal Analysis

The structural behavior of masonry bridges is influenced by various characteristics that have been shown to have significant effects. Factors such as the overall length, the number of spans, the maximum length, the height, the arch type and the material properties are essential in this context. The accurate assessment of structural performance requires the application of finite element modelling. The validation of the initial finite element model in masonry structures requires the use of tests or empirical equations. In a study by Bayraktar et al. (2022) statistical methods were used to establish a quantitative correlation between the maximum arch span and the initial natural frequencies of eight masonry bridges. This correlation was determined by analyzing the respective natural frequencies by using Eq. ().

$$y = -3.935 \ln(x) + 16.824 \quad (7)$$

where x and y: denote the maximum arch span (measured in meters) and the first frequency (expressed in Hertz), respectively. Table 5 displays the theoretical frequency values calculated using Eq. (7) and the experimentally determined first frequency values. The results indicate a strong agreement between the experimentally observed and theoretically predicted values.

Consequently, it is proposed that Eq. (7) is suitable for validating the analytical model of masonry bridges. Given the minimal discrepancy between the experimentally obtained and theoretically calculated initial frequency values, the authors suggest that the finite element model constructed accurately reflects the real structural response. The mass contribution ratio and the analysis of the mode motions show that the first and third as well as the fifth mode shape significantly influence the behavior of the model.

Table 5. Correlation between the dynamic characteristics of the bridges

Bridge type	Span number	Length of span	The first natural frequency (Hz)	
			Experimental	Empirical, Eq. ()
Stone Masonry	Seven	16	5.890	5.914
Stone Masonry	Single	16	5.279	6.123
Stone Masonry	Single	19.5	6.063	5.137
Stone Masonry	Two	25	4.640	4.126
Stone Masonry	Single	25	4.045	4.189
Stone Masonry	Eight	15	4.730	6.168
Stone Masonry	Two	10	8.853	7.763
Stone Masonry	Two	12	6.970	7.046

Table 6. Numerical natural frequencies and ratios of the effective mass to the total mass in the three main directions

Mode	f (Hz)	$m_{eff,x}/m_{tot}$ (%)	$m_{eff,y}/m_{tot}$ (%)	$m_{eff,z}/m_{tot}$ (%)
1	8.8076	0	0	24.02
2	9.3167	0	0	0.1
3	9.8325	0.1	0	12.7
4	10.470	0.4	0	0
5	11.010	35.4	0	0
6	11.196	0.1	0	6.55
7	12.067	0	0	0.4
8	12.943	0	0	0.2
9	13.092	0	0	4.60
10	14.078	0	0	0.1

Table 6 shows the distribution of the initial 10 modes of the Halilviran bridge in both longitudinal and transverse directions. In addition, the deformed shapes of the primary modes are shown together with their respective periods and the mass ratio involved (PMR) in the main directions. The first mode (with a period of 0.11 s) involves the deck, with the transverse direction having a PMR value of 24.02%.

The third mode, with a period of 0.10 s, affects the upper part of the piers and the parapet walls. The PMR in the transverse direction is 12.72%. The fifth mode with a period of 0.09 s (T = 0.09 s) concerns the filling and the deck of the bridge. It has the highest PMR of 35.4% in the longitudinal direction. The sixth vibration mode with a period of 0.08 s concerns the parapet wall of the bridge. It has the highest PMR of approx. 6.55% in the transverse direction.

7. Nonlinear Analyses

In the subsequent phase, the model is subjected to two horizontal components of ground motion for dynamic analysis. The full Newton-Raphson method is used to solve the nonlinear equilibrium equations by a stepwise integration approach with a time step of 0.005 s. Rayleigh damping refers to the dissipation of energy resulting from phenomena that are not explicitly accounted for in the constitutive law of the material. The viscous damping coefficients for masonry are typically between 2% and 10%.

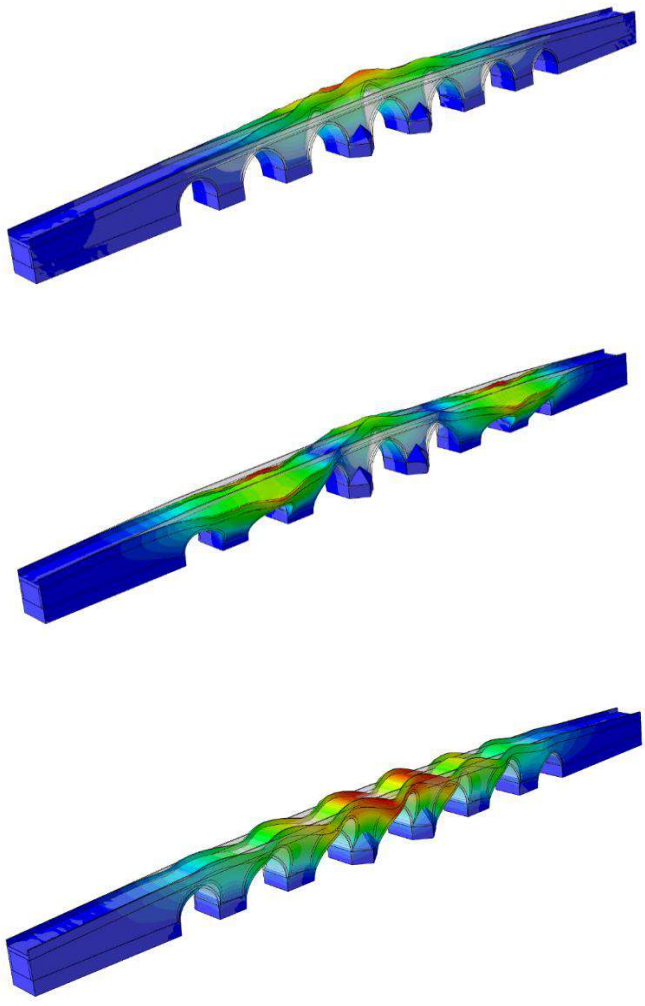

Fig. 10. Distribution of the modes in the longitudinal and transversal directions. Deformed shapes of the first main modes, corresponding periods and participating mass ratios

In this research, the model is exposed to a damping ratio of 3%, which is established through an analysis of the first frequency and the frequency at which the modal mass contribution ratio surpasses 90%. This study uses acceleration data that was recorded during the Düzce earthquake sequence on August 17, 1999. Figure 11 depicts the time history of acceleration, specifically the two horizontal components, with respect to the Peak Ground Acceleration (PGA) of 0.36 g in the longitudinal and transverse directions. The decision was made to restrict the duration of the accelerograms to 5 s (between the 7th and 12th second of the graph) in order to manage the substantial computational resources needed for the analyses.

8. Results

An evaluation of the overall performance of the masonry bridge is carried out through a comparative analysis of results. Initially, this comparison involves an assessment of the amount of energy absorbed by the model. The energy equilibrium of the system under seismic activity can be elucidated by Eq. (8). Within this equation, various variables are defined; (EI) the energy input from the earthquake $(W\xi)$, represents the energy dissipated as a result of viscous effects (Wp), accounts for the hysteretic energy encompassing plasticity and damage (We), signifies the elastic-strain energy and (Wk), stands for the kinetic energy.

$$EI = W\xi + Wp + We + Wk \quad (8)$$

The overall elastic vibrational energy, represented as Wev, is the combination of the elastic strain energy (We) and the kinetic energy (Wk). Eq. (8) can be reformulated in a different manner.

$$EI - Wev = W\xi + Wp \quad (9)$$

The cumulative energy absorption in Eq. (9) is delineated on the right-hand side. Specifically, $W\xi$ comprises the dissipated energy from viscous effects, which includes the dissipation of soil through dashpots denoted by $W(\xi.s)$ and $W(\xi.r)$ the portion attributed to the structure through Rayleigh damping.

Conversely Wp represents the energy dissipation by the structure through plasticity and damage. The computation of $W(\xi.s)$ involves the integration of dashpot coefficients and the square of velocities across the dashpots over time. To ensure reproducibility of results, the variable EI, signifies the external work in the analysis.

Additionally, $W\xi$ denotes the energy dissipated due to viscous effects, while Wp, represents the combined energy dissipated by plastic deformation and damage. The variable We, signifies the recoverable strain energy, and Wk represents the kinetic energy. In the base-fixed model, $W\xi$ and $W(\xi.r)$, coincide due to the absence of dashpots.

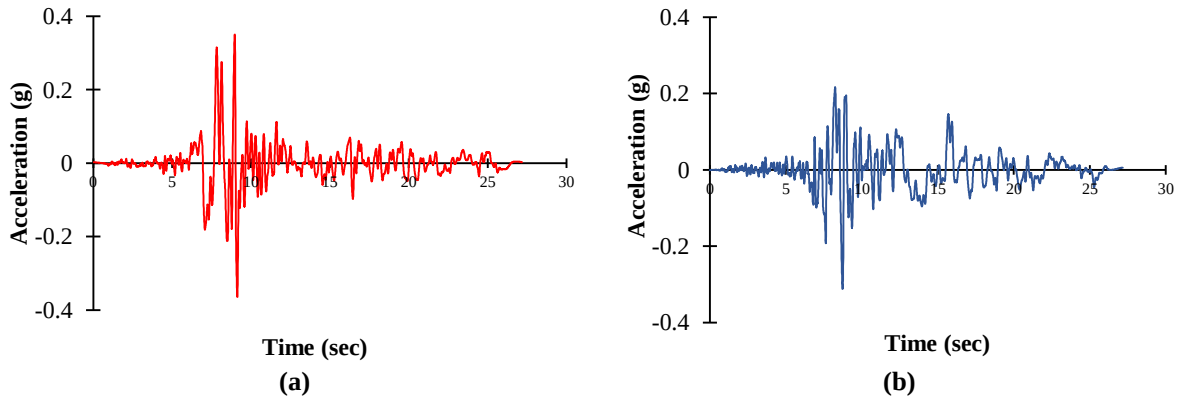

Fig. 11. Horizontal components of the real accelerograms used in the non-linear dynamic analyses: a) Longitudinal direction; and b) Transversal direction

Figure 12 illustrates the variations over time in the energies (EI). (Wξ). (Wp). (We) and (Wk). within the model. The primary dissipation of input energy occurs due to plastic deformation. This phenomenon is attributed to the localized damage in a limited number of elements, thus validating the suitability of the selected CDP parameters. The study investigates the impact of tension and compression-induced damages on masonry materials, particularly in the context of seismic damage assessment for masonry bridges. Tensile cracks and compressive crushing are the two main forms of damage observed in masonry materials, with tension being a significant factor due to the lower tensile strength compared to compressive strength. The research focuses on analyzing the effects of tension and pressure-induced damages on masonry bridges during seismic events. Tensile fractures in bridges occur when the predicted plastic strains and main stresses in tension surpass specified threshold values.

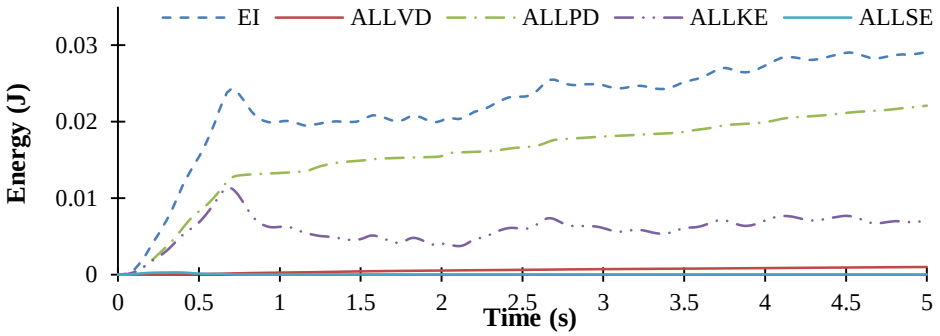

Fig. 12. Total input energy (EI), energy dissipated by viscous effects (Wξ), hysteretic energy (Wp), kinetic energy (Wk) and elastic-strain energy (We)

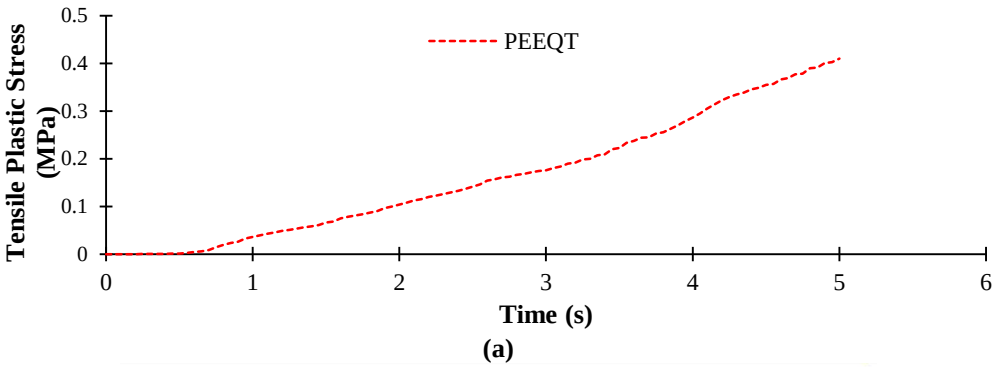

(a)

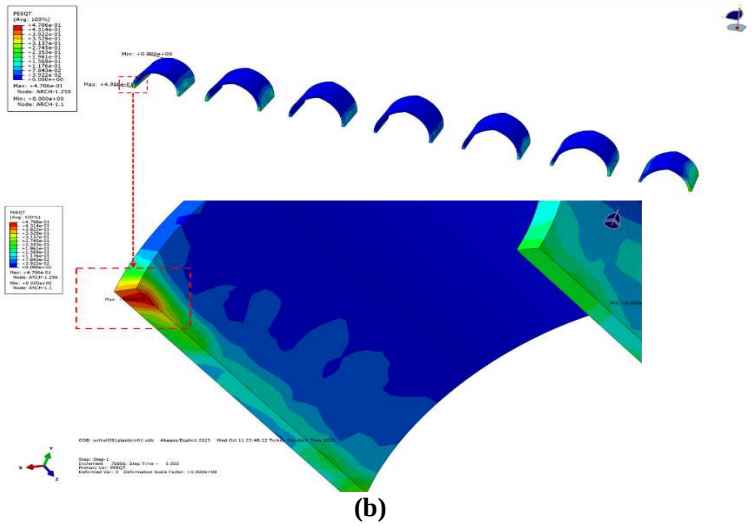

(b)

Fig. 13. a) Time histories; and b) Maximum principal (tension) strain contour maps of the arch

The study utilizes Figures 13 and 14 to present the maximum values and patterns of equivalent plastic tensile strains (PEEQT) in masonry arches and spandrel walls under the influence of longitudinal and transverse strong ground motions. The distribution of equivalent plastic tensile strain (PEEQT) after 5 s of earthquake records reveals concentrated tensile plastic deformations around the bearing portion connecting the arches of the wall.

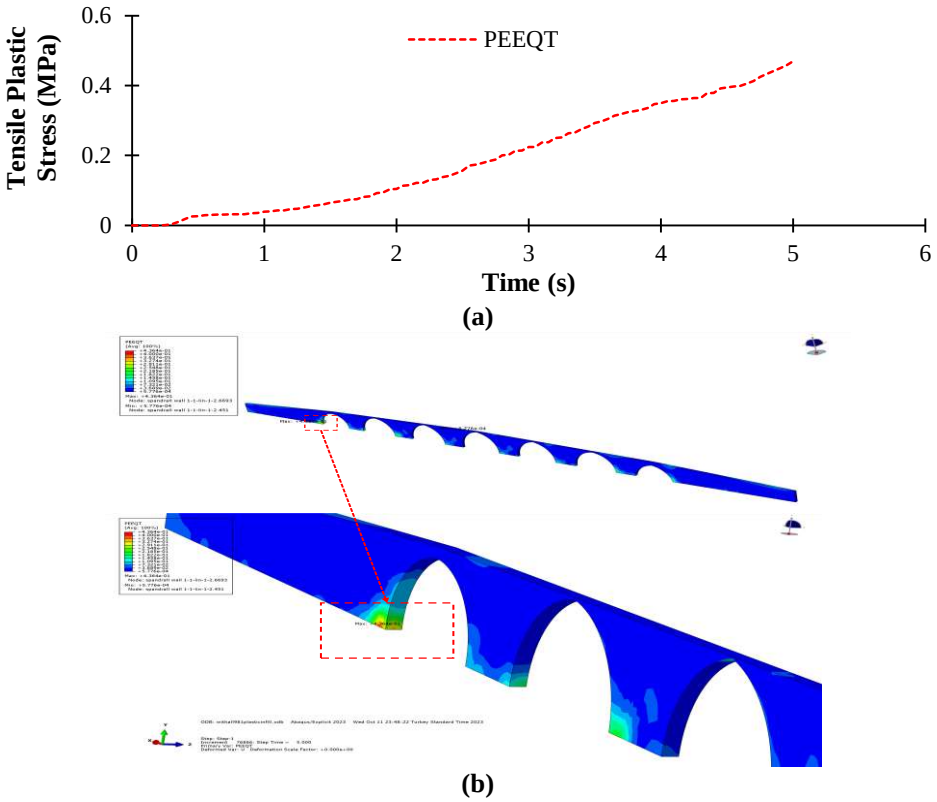

Fig. 14. a) Time histories of the spandrel wall; and b) Maximum principal (tension) strain contour maps

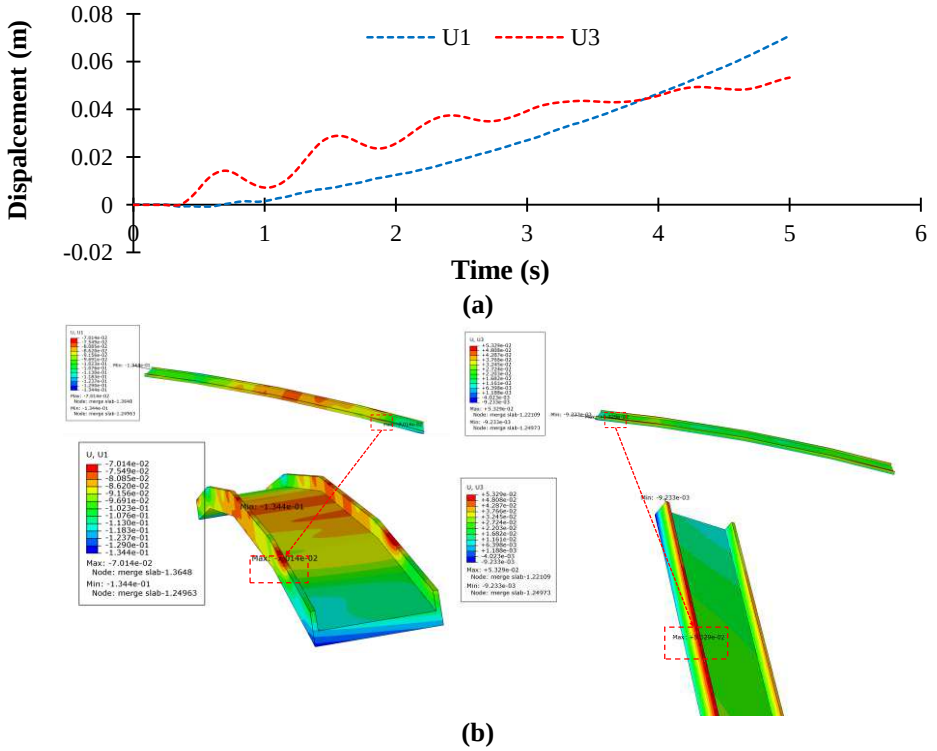

Fig. 15. A) Transverse displacement; and b) Longitudinal of the bridge deck

The masonry arches and spandrel walls exhibit peak plastic tensile strains of $4.7e^{-1}$ and $4.36e^{-1}$, respectively, with the strains predominantly localized in the lower interior sections of both structures. Additionally, the study highlights the maximum displacements of the bridge deck in the longitudinal and transverse directions, as depicted in Figure 15. Figure 16 illustrates the dynamic displacements graphed in the horizontal directions at the upper and lower ends of the spandrel walls of the bridge. This graph illustrates the significance of the structural response in masonry bridges that takes place out of the plane.

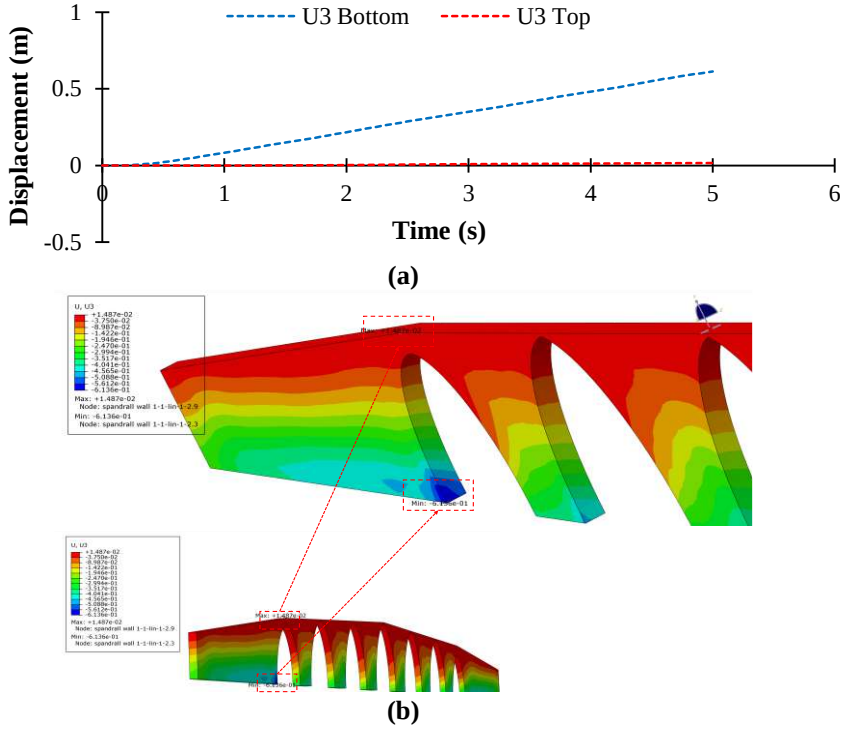

Fig. 16. a) Time histories of the spandrel wall; and b) Displacements in the transverse directions at the bottom contour maps

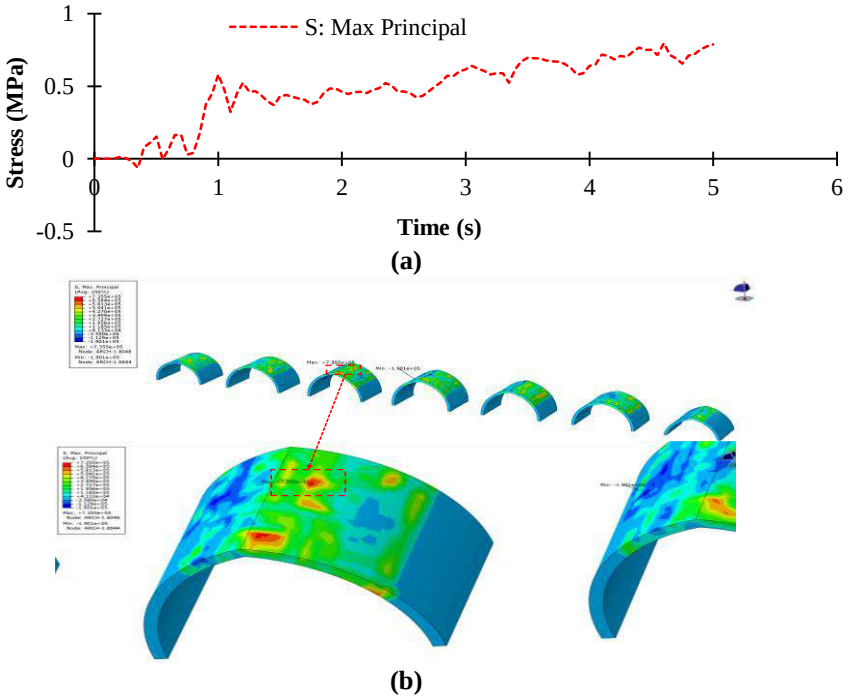

Fig. 17. a) Time histories; and b) Maximum principal (tension) stress contour maps of the arches

The measurements are carried out to determine the horizontal displacements of the spandrel wall, leading to the manifestation of out of plane characteristics in the wall. The longitudinal displacements of the spandrel wall are assessed to establish its in-plane behavior. The stability of the spandrel walls and their relationship with the arch barrel are crucial elements influencing the various challenges observed in masonry arch bridges. Figures 17-19 illustrate that the masonry unit undergoes peak principal stresses when exposed to intense ground motion along the arch interface.

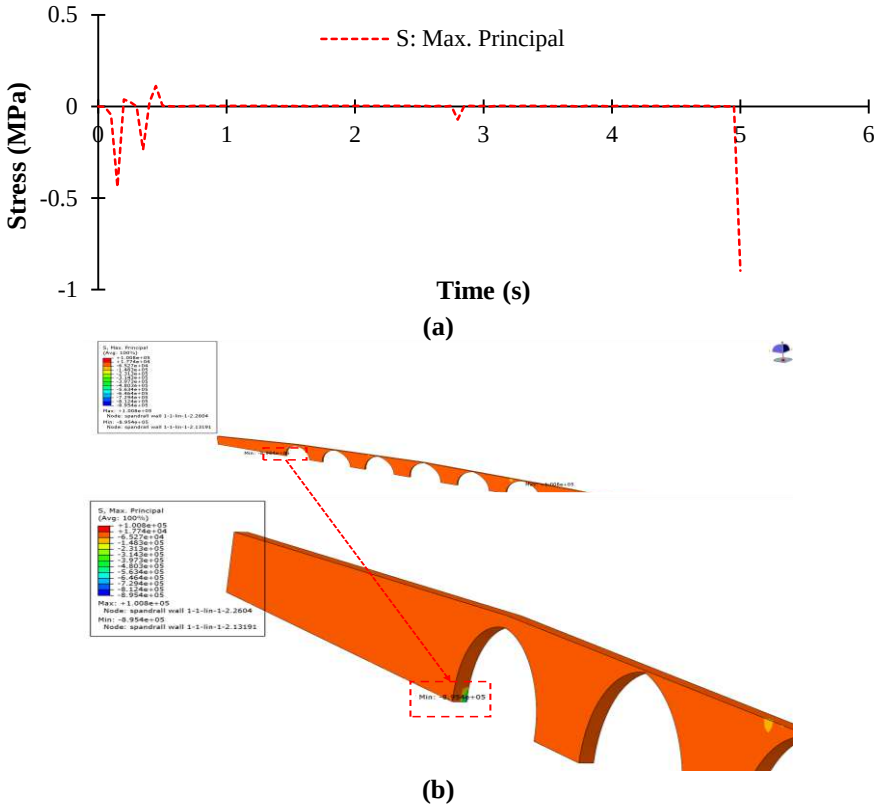

Fig. 18. a) Time histories; and b) Maximum principal (compression) stress contour maps of the spandrel wall

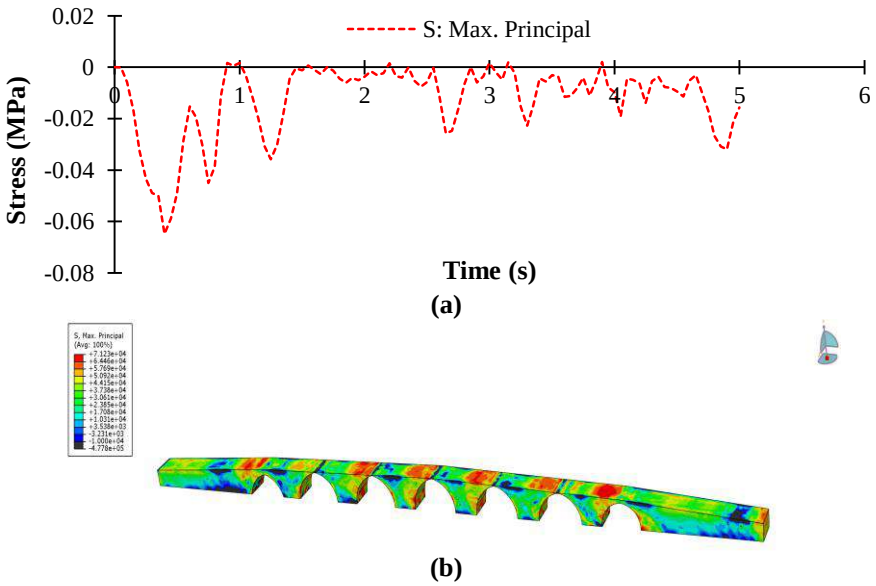

Fig. 19. a) Time histories; and b) Maximum principal (compression) stress contour maps of the infill

Figures 20 and 21 illustrate the changes over time in the minimum principal stresses and the specific stress regions. The minimum principal stresses determined in the analysis were below 3.15 MPa, which is the upper limit for compressive stresses in masonry walls and vaults. However, the model showed increased stresses in certain segments of the bridge that approached the maximum allowable value.

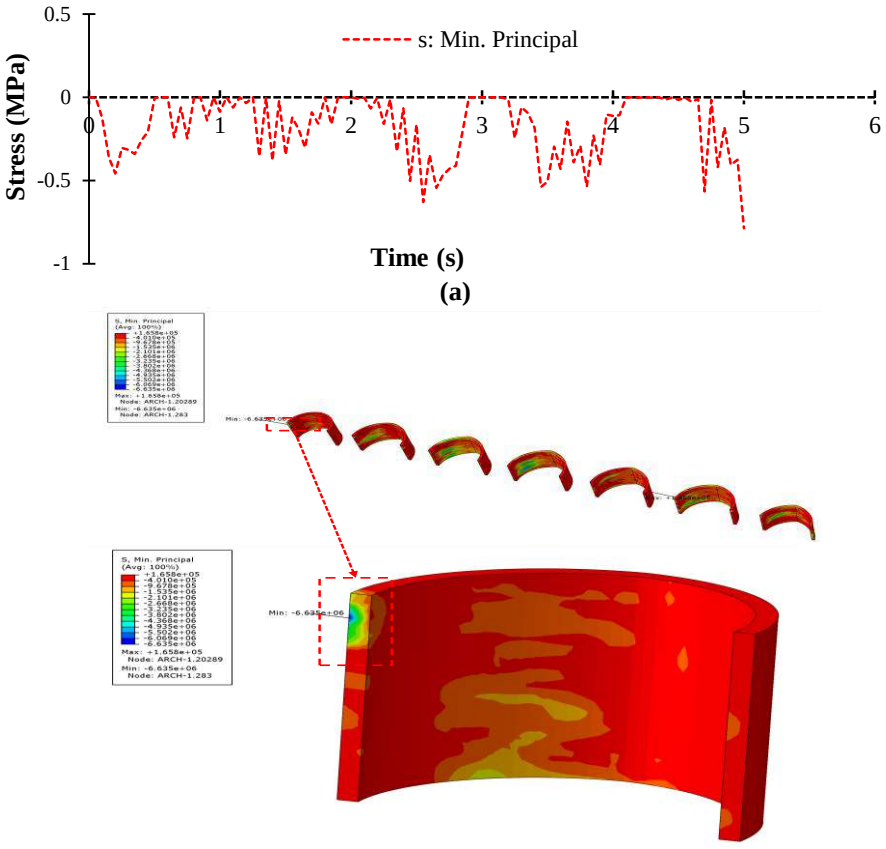

Fig. 20. a) Time histories; and b) Minimum principal (compression) stress contour maps of the arches

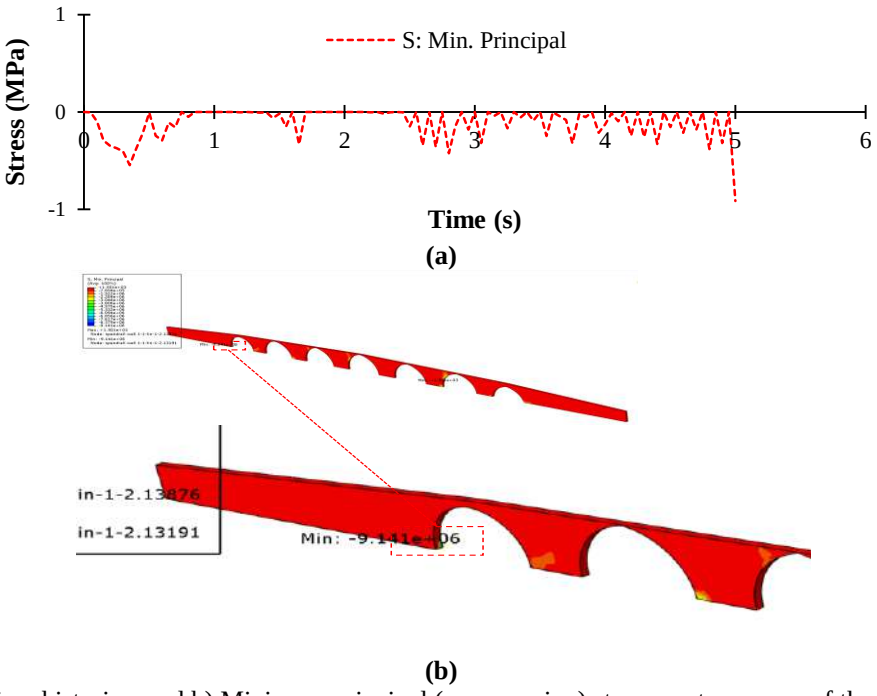

Fig. 21. a) Time histories; and b) Minimum principal (compression) stress contour maps of the spandrel wall

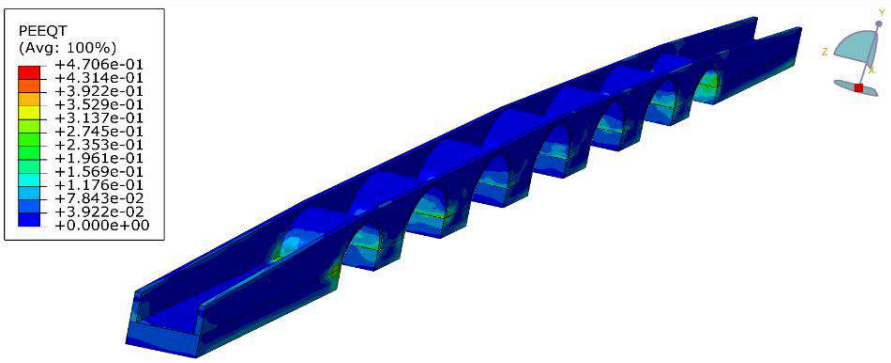

Fig. 22. Maximum principal (tension) strain contour maps of the bridge

9. Post-Earthquake Survey

In this section the findings of the prompt evaluation conducted after an earthquake on a total of five bridges situated within or near the city of Glina. A visual inspection was conducted by Perković et al. (2021), Novak et al. (2020), Miranda et al. (2021), Korbar et al. (2021), and Cassese et al. (2020) for the assessment, using a pre-established process.

Two significant earthquakes struck North-western Croatia. The earthquake occurred in March 2020 and the second one took place in December 2020. After Petrinja earthquake for bridges in and around the town of Glina started.

9.1. Matija Gubec Street Bridge

The cross-sectional design of the bridge consists of three steel elements, along with an 18 cm thick concrete surface. The superstructure has a width of 4 m. The seismic activity had a noticeable effect on the stone wall connections, resulting in cracks and openings of various centimeters.

The absence of mortar and displacement of the stone blocks were observed. The abutment exhibited indications of both lateral shifting and rotational motion towards the bridge opening due to ground movements. Evidence of soil erosion was observed at the abutment wings.

9.2. Roviška Bridge

The bridge is built with reinforced concrete and comprises more than three spans. The superstructure is composed of a reinforced concrete slab directly supported by substantial columns projecting outward at the upper end. The asphalt connection linking the abutment and superstructure sustained no damage, and there were no discernible movements at the superstructure supports. The columns and abutments showed no notable indications of cracks, rotations, or settlements. Subsequent to the earthquake, the bridge continued to operate as intended.

9.3. Svracica Bridge

The superstructure of the bridge consists of two continuous composite girders spanning four evenly distributed sections. It is constructed with a composite cross-section comprising multiple steel girders. Despite the earthquake, no significant damage, such as permanent deformations or displacements, was observed in the superstructure or substructure components. Consequently, regular maintenance was conducted to ensure the bridge's unrestricted operation. However, further examination and upkeep are advised due to the deterioration of the steel girders and indications of corrosion in the column reinforcement.

9.4. Nikola Tesla Street Bridge

The bridge is a truss structure with three continuous girders spanning across. The superstructure of the construction is composed of steel girders and concrete ribs, which are filled with concrete and positioned between two sets of steel girders.

The steel girders are partially embedded

within these ribs, serving as a formwork for the concrete. The bridge did not exhibit significant structural damage as a result of the earthquake, neither in the upper structure, lower structure, nor the inclined surfaces surrounding the supports.

Fractures were observed in the region where the superstructure connects to the abutment, specifically at the point where the abutment wall intersects with the cross girder and provides support for the superstructure.

9.5. Hader Bridge

The bridge consists of a continuous slab girder with multiple spans and a simply supported girder that extends across. The structure sustained damage from an earthquake on various structural elements.

The movement of the bridge superstructure in both the longitudinal and transverse directions was clearly noticeable at a significant pace. Extensive review of literature and in-depth analysis of design experience consistently indicate that columns are widely recognized as the most critical element in the seismic evaluation of reinforced concrete road bridges. The main factors contributing to structural defects in columns include inadequate dispersion of longitudinal and transverse reinforcement, poor concrete quality, insufficient seismic design, concrete degradation, reinforcement and steel girder corrosion, railing and bearing deterioration, obstruction of expansion joints, asphalt cracking, and erosion of abutment slopes (Kassem et al., 2022). The ability of columns to deform is essential in dissipating seismic energy.

Assessing the ductility of older bridges that do not meet current seismic design standards is a challenging task. Earthquakes often lead to shear critical brittle fracture in columns due to the limited shear capacity of short piers, while tall pillars may collapse due to flexural failure. To extend the applicability of the findings to other ancient masonry multi-span arch bridges, it is important to consider the influence of differential settlements on their structural capacity. Accurate estimation can only be achieved through the use of a sophisticated model that accounts for the interaction between soil and structure, known as Soil-Structure Interaction (SSI).

Several bridges have been recognized as significant structures requiring maintenance through proper restoration methods and suitable construction materials (Samadi et al., 2021). Therefore, understanding the composition of construction materials, different structural components, and their overall structural integrity is essential. To fully comprehend the structural behavior of masonry arch bridges, it is crucial to have knowledge about the fundamental structural elements that constitute them. Understanding the performance of masonry bridges and their ability to withstand changes in structural components requires an appreciation of their load-carrying capacities and an evaluation of the structural integrity and intensity of the load they support.

10. Conclusions

This study showed that it is possible to perform a seismic assessment with a simplified method using a limited data set, even in a complex environment with different modelling factors. A detailed three-dimensional FE model was created to investigate the dynamic properties of the bridge. This model effectively represented the complex geometric details obtained from laser scanning and photogrammetric surveys. The material properties of the bridge components were evaluated by diagnostic and geognostic investigations and by consulting the relevant literature. By using acceleration diagrams consisting of two horizontal diagrams showing the longitudinal and transverse alignment of the bridge, the study provided the following results:

- This research showed that the point cloud generated by terrestrial laser scanning technology provides fast and highly accurate data to determine the essential

structural geometry required for structural analysis. The point cloud data was used to create a computerized solid element model of the building. Once the modeling process was completed, load and material assumptions were determined and then static and dynamic evaluations of the structure were performed.

- Bridge failure primarily happened at the junction between the parapet walls and the barrels, as well as with the masonry arch, which are the most susceptible elements of the bridge (see Figure 22).
- The bridge exhibited dynamic properties, as the first analysis of its natural frequency showed. Furthermore, the results of the non-linear dynamic simulations underlined the vulnerability of the bridge to seismic forces and indicated a significant vulnerability. A comprehensive understanding of the behavior of the various macro elements that make up the bridge was achieved by comparing contour plots showing tensile damage, displacements and dissipated energy.
- The preliminary results of the natural frequency analysis provided valuable insights into the dynamic properties of the bridge. The Halilviran bridge exhibited three predominant modes, each characterized by a significant PMR. The presence of masonry affected the fundamental behaviors of the bridge and thus influenced its overall structural integrity. The primary vibration patterns of the bridge had a short duration, leading to a significant increase in spectral accelerations and subsequent remarkable structural deterioration.
- In model, the 1st and 3rd mode shapes occurred in the transverse direction, whereas the 4th and 5th mode shape occurred in the longitudinal direction (Figure 10).
- Figure 12 showed the overall energy dissipation of the bridge as part of a non-linear dynamic analysis. Most of the energy introduced into the system was dissipated by structural plasticity mechanisms. In accordance with the existing literature, the generalization of these results should be taken with caution, as the response of a bridge structure to seismic events depends on various factors, including the dynamic properties of the system, the choice of foundation model, soil type, and frequency spectrum of seismic waves.
- Examination of the contour plots of the plastic strain damage showed that the bridge shows signs of degradation, particularly in the parapet wall, the upper sections of the arches and the infill. The choice of infill material played a crucial role in improving the structural stability of bridges, especially when considering the specific reinforcement method used. This strategy has the potential to improve the reinforcement of masonry bridges.
- Prior studies in the literature, specifically by Seker et al. (2014) have recommended the utilization of the subsequent equation to determine the maximum relative displacement requirement for masonry structures. Consequently, this investigation also incorporates Eq. (10) for the evaluation of displacement values.

$$\Delta_{imax} \leq \frac{0.02 * h_i}{R} \tag{10}$$

wher h_i and R: denote the height of the structure and the behavior factor related to the ductility of the structure, respectively. Low bridge $h_i = 9$ m, $R = 2$ and the corresponding maximum allowable top displacement is 0.09 m. The study revealed that the displacements observed at the interlock points between the arches and spandrel wall with the piers are greater in analyses compared to the values computed using the provided formula. Consequently, it can be inferred that the displacements exceed the permissible thresholds.

- The inclusion of fill material in a masonry arch bridge provides several beneficial effects that enhance its load-bearing capacity. Firstly, the additional weight of the infill material applies

compressive stresses on the arch, thereby improving its stability. Additionally, it assists in distributing dynamic loads from the roadway to the upper section of the arch.

Moreover, it prevents horizontal movements of the arch by utilizing passive ground pressures. Nonetheless, the study indicated that improving the mechanical properties of the backfill could significantly enhance the seismic response of the bridge (Martinelli et al., 2018). This is particularly evident in the cases of elastic modulus and increases in cohesion.

- The investigation revealed that the primary stresses caused by both out of plane and in-plane seismic forces exceeded the critical tensile stress threshold of 0.32 MPa for masonry walls. The potential collapse of the bridge could be significantly affected by the out-of-plane behavior of these elements under lateral seismic forces. Specific retrofitting measures would be essential to ensure consistent structural performance. In addition, the parapet walls are highly susceptible to seismic and train traffic loads, especially with regard to their out of plane behavior. It is therefore crucial to prioritize the repair and reinforcement of dilapidated parapet walls exposed to these loads. The most severely damaged coatings of the Halilviran bridge are obviously those exposed to significant transverse displacements or located near sections exposed to significant horizontal displacements. Figure 19 illustrated the vertical displacement of the parapet wall of the Halilviran bridge perpendicular to the bridge plane. To prevent failure in the vertical plane of the parapet walls, the tensile areas can be reinforced using various techniques. The specific configuration of the strengthening system depends on factors such as the classification of the building, cultural significance and mechanical requirements. Several techniques have been commonly proposed to improve the structural integrity of parapet walls.
- Various techniques can be employed to address issues with spandrel walls, such as using transverse tie bars, substituting backfill with concrete, reconstructing with a tapered section, grouting if needed, applying a thin concrete cover, and utilizing a Fabric-Reinforced Cementitious Matrix (FRCM) composite (Figure 23). Mokrini et al. (2012) extensively studied these methods. In cases where a spandrel wall with a tapered section is considered beyond repair, an alternative approach involves demolishing the existing walls and reconstructing them with a tapered section instead of a straight one. Additionally, adding a layer of reinforced concrete to an existing one can protect the arch and inner surfaces by applying a thin coating of reinforced concrete. Concrete filling can also be used to replace part or all of the backfill material. Transverse tie bars, known as rots, stitching, or anchoring, can be used to connect and restrain the lateral movement of spandrel walls.
- The macro modeling technique was employed to calculate the collapse loads and potential hinge mechanisms of multi-span masonry arch bridges when the micro modeling technique is deemed too intricate.

This approach is advantageous for determining the highest tensile stresses that exceed the tensile strength and identifying potential hinge mechanisms in multi-span brick arch bridges.

- The analysis of the findings indicated that the structural response and damage levels of the various macro-elements in the case study wre influenced by both their geometric characteristics and potential interactions with neighboring components.
- The absence of bending moment in arches is a widely acknowledged phenomenon, attributed to their inherent curvature properties. However, due to the interaction with other components and the inherent lack of symmetry in the load, the presence of a bending moment is inevitable.

Complex arch constructions experience both bending moments and horizontal thrusts, resulting in tensile strains being applied to the cross sections of the arch construction.

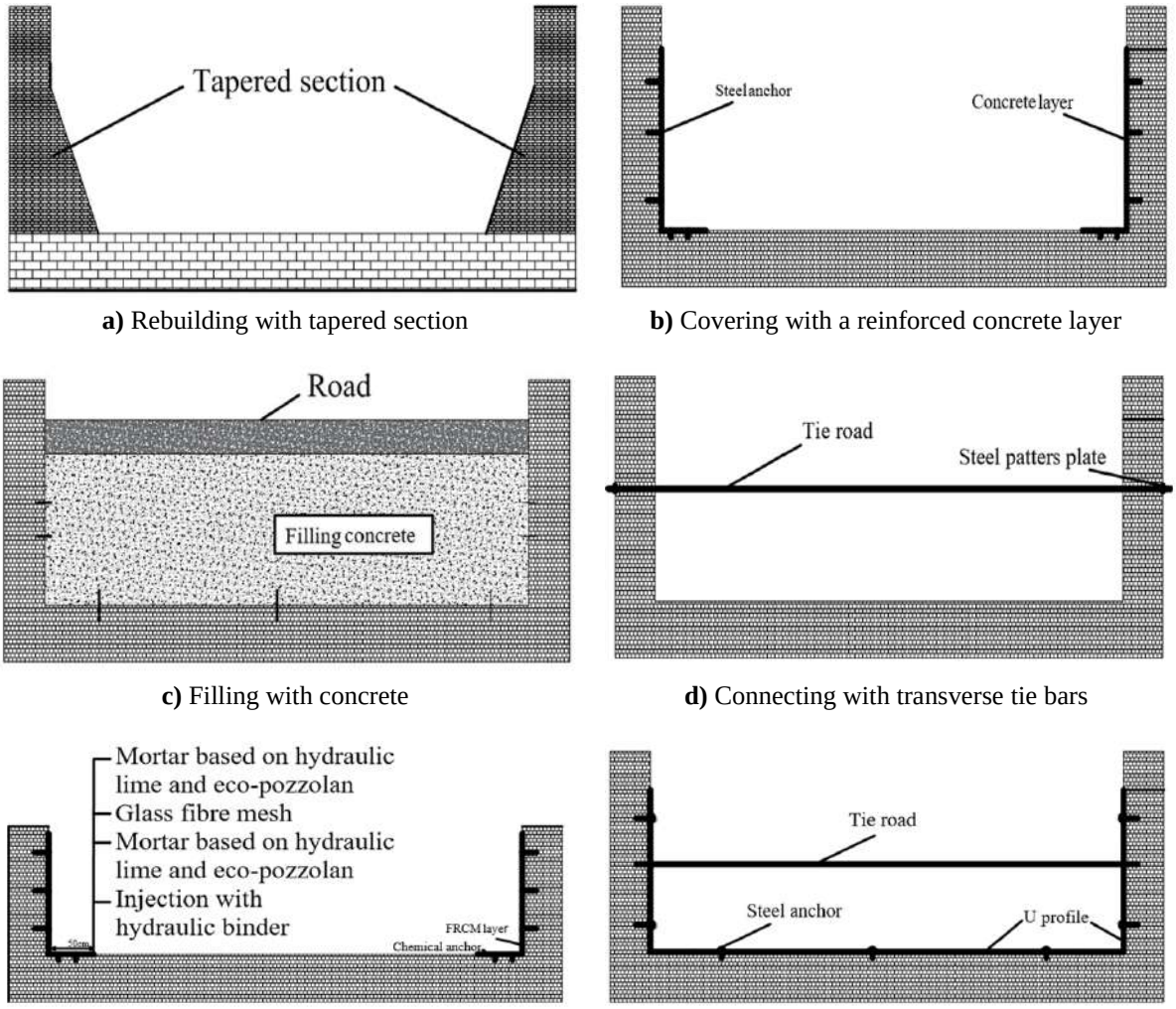

a) Rebuilding with tapered section

b) Covering with a reinforced concrete layer

c) Filling with concrete

d) Connecting with transverse tie bars

e) Covering with FRCM

f) Connecting with stainless steel U profiles

Fig. 23. Strengthening techniques for spandrel walls of masonry bridges (Bayraktar and Hökelekli, 2021)

Increasing the dead loads leads to a reduction in tensile stresses, often necessitating the use of larger cross-section dimensions for arches. This is particularly evident in old masonry structures, where engineers recognize the significant influence of the self-weight in maintaining the stability of arches. Therefore, it is crucial to consider the potential failures that may arise from geometric modifications due to retrofitting, as these adjustments can have detrimental and lasting effects on the structure.

11. Acknowledgment

The authors gratefully acknowledge the support of the YAP Project (Project ID: 43950, Project Code: MGA-2023-43950) in conducting this research.

12. References

Alpaslan, E., Yilmaz, M.F. and Sengönül, B.D. (2023). "Rating and reliability assessment of a historical masonry arch bridge", *Journal of Civil Structural Health Monitoring*,13(4-5), 1-19, https://doi.org/10.1007/s13349-023-00692-7.

Ashayeri, I., Biglari, M., Formisano, A. and D'Amato, M. (2021). "Ambient vibration testing and empirical relation for natural period of historical mosques, Case study of eight mosques in Kermanshah, Iran", *Construction and Building Materials*, 289, 123191, https://doi.org/10.1016/j.conbuildmat.2021.123191.

Azar, A.B. and Sari, A. (2025). "Reinforcement of arch structures under blast loads: A sustainable approach to structural enhancement", *Journal of Structural Integrity and Maintenance*, 10(1), 2457913, https://doi.org/10.1080/24705314.2025.2457913.

Azar, A.B. and Sari, A. (2024). "Damage identification of masonry arch bridge under

blast loading using smoothed particle hydrodynamics (SPH) method", *Structural Engineering and Mechanics*, 91(1), 103, https://doi.org/10.12989/sem.2024.91.1.000.

Azar, A.B. and Sari, A. (2023). "Historical arch bridges-deterioration and restoration techniques", *Civil Engineering Journal*, 9(7), https://doi.org/10.28991/CEJ-2023-09-07-010.

Bayraktar, A., Çalik, I. and Türker, T. (2022). "A simplified fundamental frequency formulation based on in-situ tests for masonry stone minarets", *Experimental Techniques*, 46(2), 225-238, http://doi.org/10.1007/s40799-021-00474-0.

Bayraktar, A. and Hökelekli, E. (2021). "Seismic performances of different spandrel wall strengthening techniques in masonry arch bridges", *International Journal of Architectural Heritage*, 15(11), 1722-1740, https://doi.org/10.1080/15583058.2020.1719234.

Borlenghi, P., Saisi, A. and Gentile, C. (2023). "ND testing and establishing models of a multi-span masonry arch bridge", *Journal of Civil Structural Health Monitoring*, 1-17, https://re.public.polimi.it/handle/11311/1227342.

Cassese, P., De Risi, M. T. and Verderame, G.M. (2020). "Seismic assessment of existing hollow circular reinforced concrete bridge piers", *Journal of Earthquake Engineering*, 24(10), 1566-1601, http://doi.org/10.1080/13632469.2018.1471430.

Castellazzi, G., D'Altri, A.M., de Miranda, S. and Ubertini, F. (2017). "An innovative numerical modelling strategy for the structural analysis of historical monumental buildings", *Engineering Structures*, 132, 229-248, https://doi.org/10.1016/j.engstruct.2016.11.032.

Chalajour, S. and Hataf, N. (2023). "The comparison of tunnel convergence from numerical analysis with monitoring data based on different constitutive models in rock medium", *Civil Engineering Infrastructures Journal* 56(2), 301-319, https://doi.org/10.22059/CEIJ.2022.343391.1843

Clementi, F., Pierdicca, A., Formisano, A., Catinari, F. and Lenci, S. (2017). "Numerical model upgrading of a historical masonry building damaged during the 2016 Italian earthquakes: The case study of the Podestà palace in Montelupone (Italy)", *Journal of Civil Structural Health Monitoring*, 7, 703-717, https://link.springer.com/article/10.1007/s13349-017-0253-4.

Fanning, P.J. and Boothby, T.E. (2001). "Three-dimensional modelling and full-scale testing of stone arch bridges", *Computers and Structures*, 79(29-30), 2645-2662, https://doi.org/10.1016/S0045-7949(01)00109-2.

Ferrero, C., Calderini, C., Portioli, F. and Roca, P. (2021). "Large displacement analysis of dry-joint masonry arches subject to inclined support movements", *Engineering Structures*, 238, 112244, https://doi.org/10.1016/j.engstruct.2021.112244.

Gaetani, A., Bianchini, N. and Lourenço, P.B. (2021). "Simplified micro-modelling of masonry cross vaults: stereotomy and interface issues, *International Journal of Masonry Research and Innovation*, 6(1), 97-125, http://doi.org/10.1504/IJMRI.2021.112076.

Gönen, S. and Soyöz, S. (2022). "Reliability-based seismic performance of masonry arch bridges", *Structure and Infrastructure Engineering*, 18(12), 1658-1673, https://doi.org/10.1080/15732479.2021.1918726.

Güllü, H. and Özel, F. (2020). "Micro tremor measurements and 3D dynamic soil-structure interaction analysis for a historical masonry arch bridge under the effects of near-and far-fault earthquakes", *Environmental Earth Sciences*, 79, 1-29, https://link.springer.com/article/10.1007/s12665-020-09086-0.

Jindal, A., RN, G.D., Kumar, P., Kumar, V. and Rana, D. (2023). "Rehabilitation prospects of concrete pavements with self-compacting concrete containing wollastonite micro-fiber." *Civil Engineering Infrastructures Journal* 56(2), 221-233, https://doi.org/10.22059/CEIJ.2023.341456.1828.

Kassem, M.M., Nazri, F.M., Farsangi, E.N. and Ozturk, B. (2022). "Development of a uniform seismic vulnerability index framework for reinforced concrete building typology", *Journal of Building Engineering*, 47, 103838, https://doi.org/10.1016/j.jobe.2021.103838.

Korbar, T., Markušić, S., Stanko, D. and Penava, D. (2021). "Petrinja M6.2 earthquakes in 2020 damaged also solid linear infrastructure: are there similar active faults in Croatia", *1st Croatian Conference on Earthquake Engineering*, March 2021, http://doi.org/10.5592/CO/1CroCEE.2021.253.

Martinelli, P., Galli, A., Barazzetti, L., Colombo, M., Felicetti, R., Previtali, M., Roncoroni, F., Scola, M. and di Prisco, M. (2018). "Bearing capacity assessment of a 14th century arch bridge in Lecco (Italy)", *International Journal of Architectural Heritage*, 12(2), 237-256, http://doi.org/10.1080/15583058.2017.1399482.

Miranda, E., Brzev, S., Bijelic, N., Arbanas, Ž., Bartolac, M., Jagodnik, V., Lazarević, D., Mihalić Arbanas, S., Zlatović, S., Acosta Vera, A., Archbold, J., Bantis, J., Blagojevic, N.,

Borozan, J., Božulić, I., Cruz, C., Dávalos, H., Fischer, E., Gunay, S., Hadzima-Nyarko, M., Heresi, P., Lignos, T., Lin, T., Marinkovic, M., Messina, A., Miranda, S., Poulos, A., Scagliotti, G., Tomac, I., Tomic, I, Ziotopoulou, K., Žugić, Z. and Robertson, I. (2021). *Petrinja, Croatia December 29, 2020*, MW 6.4 Earthquake Joint Reconnaissance Report (JRR), https://doi.org/10.17603/ds2-1w0y-5080.

Mokrini, F., Waeyenberge, L., Viaene, N. and Moens, M. (2012). "First report of the cereal cyst nematode Heterodera latipons on wheat in Morocco", *Plant Disease*, 96(5), 774, https://doi.org/10.1094/PDIS-11-11-0999-PDN.

Novak, M.S., Uros, M., Atalic, J., Herak, M., Demsic, M., Banicek, M., Lazarevic, D., Bijelic, N., Crnogorac, M. and Todoric, M. (2020). "Zagreb earthquake of 22 March 2020-preliminary report on seismologic aspects and damage to buildings", *Gradevinar*, 72, 843-867, https://doi.org/10.14256/JCE.2966.2020.

Pelà, L., Aprile, A. and Benedetti, A. (2013). "Comparison of seismic assessment procedures for masonry arch bridges", *Construction and Building Materials*, 38, 381-394, https://doi.org/10.1016/j.conbuildmat.2012.08.046.

Pepi, C., Cavalagli, N., Gusella, V. and Gioffrè, M. (2021). "An integrated approach for the numerical modeling of severely damaged historic structures: Application to a masonry bridge", *Advances in Engineering Software*, 151, 102935, https://doi.org/10.1016/j.advengsoft.2020.102935.

Perković, N., Stepinac, M., Rajčić, V. and Barbalić, J. (2021). "Assessment of timber roof structures before and after earthquakes", *Buildings*, 11(11), 528, https://doi.org/10.3390/buildings11110528.

Samadi, D., Taghaddos, H., Nili, M.H. and Noghabaei, M. (2021). "development of a bridge maintenance system using bridge information modelling", *Civil Engineering Infrastructures Journal*, 54(2), 351-364, https://doi.org/10.22059/CEIJ.2020.298837.1661.

Seker, B.S., Cakir, F., Dogangun, A. and Uysal, H. (2014). "Investigation of the structural performance of a masonry domed mosque by experimental tests and numerical analysis", *Earthquakes and Structures*, 6(4), 335-350, https://doi.org/10.12989/eas.2014.6.4.335.

Stockdale, G., Milani, G. and Sarhosis, V. (2019). "Increase in seismic resistance for a full-scale dry stack masonry arch subjected to hinge control", *Key Engineering Materials*, 817, 221-228, https://doi.org/10.4028/www.scientific.net/KEM.817.221.

Valente, M. and Milani, G. (2019a). "Damage survey, simplified assessment and advanced seismic analyses of two masonry churches after the 2012 Emilia earthquake", *International Journal of Architectural Heritage*, 13(6), 901-924, https://doi.org/10.1080/15583058.2018.1492646.

Civil Engineering Infrastructures Journal 2025, 58(1): 147-157
DOI: 10.22059/ceij.2024.361393.1932

RESEARCH PAPER

Effect of Ferro-Cement Confinement on Compressive and Splitting Tensile Behavior of Plain Concrete

Al-Rafi, A.[1], Islam, T.[1], Ibtesham, K.R.[1] and Sen, D.[2*]

[1] B.Sc. Student, Department of Civil Engineering, Ahsanullah University of Science and Technology, Bangladesh.
[2] Associate Professor, Department of Civil Engineering, Ahsanullah University of Science and Technology, Bangladesh.

Received: 27 Jun. 2023; Revised: 30 Dec. 2023; Accepted: 12 Feb. 2023

ABSTRACT: This study aims to investigate the behavior of Ferro-cement confined plain concrete (i.e., ultimate load, failure mechanism, damages, and ductility) under both compression and split tension. The main motivation of this study was the research gap concerning the split tensile behavior of Ferro-cement confined concrete. In the experiment, Ferro-cement confinement method (i.e., monolithic and non-monolithic casting of Ferro-cement around concrete cylinders) and wire mesh content were the main variables. For each confinement method, Ferro-cement with wire mesh contents of 0.22%, 0.25% and 0.50% were considered. The test results demonstrated a notable capacity enhancement of concrete with Ferro-cement confinement under both compression and split tension. In the test, cracks were originated and propagated radially from the outer Ferro-cement shell towards the concrete core under compression, whereas cracks were generated and propagated in the opposite way under split tension. More damages, i.e., residual crack widths, were observed at the location of initial crack formation, irrespective of the parameters of this study, under both loadings. In addition, no distinct relationship was found between the displacement ductility and the parameters of this study.

Keywords: Strengthening, Performance, Retrofitting

1. Introduction

Concrete structures can deteriorate, which necessitates structural strengthening to achieve improved load-bearing capacity and durability. This structural strengthening involves the evaluation of the structure, identification of weaknesses, and implementation of a strengthening scheme on an existing building. Several strengthening schemes are available, including additional structural member insertion and modification of structural elements using different materials (Bahmani and Zahrai, 2023). Common approaches include Fiber Reinforced Polymer (FRP) wrapping, concrete jacketing, Carbon Fiber Reinforced Polymer (CFRP) and Ferro-Cement (FC) jacketing, etc. In the context of Bangladesh, where vulnerable buildings require attention, FC strengthening has a great prospect because of material availability, affordability, and strength enhancement

* Corresponding author E-mail: debasish.ce@aust.edu

potential. Ferro-cement strengthening of concrete may ensure upgraded structural performance, resilience, and safety of aging structures (Boban and John, 2021). Moreover, FC have also been utilized as a sustainable construction material (Minde et al., 2023). Therefore, several researchers have investigated the effect of FC, as a strengthening material, on the behavior of structural elements, e.g., RC beams, columns, slab, panels, water tank, unreinforced masonry wall, etc. (Ahsan et al., 2023; El-Sayed et al., 2023a; Shaheen et al., 2023; Aules et al., 2022; Jaraullah et al., 2022; Amala et al., 2021; Erfan et al., 2021; Surendra and Ravindra, 2021). In addition, several researchers have investigated the effect of FC on non-structural elements, e.g., masonry infill wall, water pipe, etc. (El-Sayed et al., 2023b; Sen et al., 2023). In this context, investigation of the behavior of plain concrete with FC confinement is important to properly understand the effect of FC on reinforced concrete. Previously, investigations on the FC strengthening technique of concrete cylinders have carried out by several researchers (Heng et al., 2017; Idris, 2016; Kaish et al., 2015; Xiong et al., 2011; Balaguru, 1989; Kaushik and Singh, 1997).

Most researchers have focused on the FC confinement of plain concrete only (Heng et al., 2017; Idris, 2016; Kaish et al., 2015; Balaguru, 1989). However, few researchers have focused on FC confined concrete cylinder specimens having longitudinal reinforcements (Xiong et al., 2011; Kaushik and Singh, 1997).

Heng et al. (2017) investigated the behavior of FC confined concrete cylinders under axial compression. A 25 mm thick FC layer with either one, two, or three layers of wire mesh was cast around the concrete cylinders (100 mm in diameter and 200 mm in height). The wire mesh was a non-galvanized, expanded metal mesh with a diamond-shaped opening and a strand thickness of 0.84 mm. The experimental result showed 18-40% load capacity improvement, where no delamination of the FC layer was observed.

Idris (2016) investigated different retrofitting methods, i.e., reinforced concrete confinement and FC overlay techniques for confining plain concrete cylinders (100 mm in diameter and 200 mm in height). Some concrete cylinders were retrofitted with an approximately 18-32 mm FC layer having either one or two layers of wire mesh (18-gauge woven wire mesh with a square opening of 12.5 mm). Ferro-cement retrofitted concrete cylinders exhibited 12-171% load capacity improvement under compression, where failure mode was reported as splitting for most of the retrofitted cylinders.

Kaish et al. (2015) investigated the axial behavior of FC confined concrete of different sizes (diameters of 150, 100 and 75 mm). Each concrete cylinder was confined with a 12.5 mm FC layer having either single or double layers of welded wire mesh (with a square opening of 12.5 mm and a wire diameter of 0.85 mm). Ferro-cement jacketed concrete cylinders demonstrated a load capacity improvement of 13 - 48%, where vertical cracks were observed along the height of the FC layer. It is to be noted that disintegration of the FC layer and core concrete was observed in the case of FC confinement with a single-layer wire mesh. The displacement ductility (i.e., a ratio of displacement at 0.85 of the ultimate load on the post-peak stage to displacement at the yield load) of all jacketed cylinders was higher than that of non-jacketed cylinders. The displacement ductility varied between 1.34 and 2.43.

Balaguru (1989) carried out an experimental investigation on concrete cylinders (150 mm in diameter and 300 mm in height) containing wire mesh layers. The main variables were concrete strength (i.e., 20 MPa and 40 MPa) and the number of layers of wire mesh (i.e., 2, 3, and 4 layers of wire mesh) in FC. The wire mesh was galvanized woven mesh with a square opening of 12.5 mm and a wire diameter of 1.09 mm. The experimental results showed an improvement in compressive strength of

11-33% and 18-30% (approximately) for normal and high-strength concrete, respectively, when wire mesh layers varied from 2-4 layers. The experimental observation showed that crack growth and crack network formation occurred in a much more controlled way in the case of the FC confined cylinders. The strain at peak compressive load was doubled by providing four layers of wire mesh in FC when compared to that of non-confined concrete cylinders.

In summary, previous experimental studies on the FC strengthening of plain concrete mainly have focused on the improvement of load-carrying capacity, the changes in ductility and/or displacement at peak strength, and the failure modes under compressive loading. However, load capacity improvement and failure mechanisms of FC confined concrete have not been studied under split tensile loading, to the author's best knowledge. Since concrete is relatively weak under tension, a study is required to investigate the behavior of FC confined concrete under split tensile loads. Therefore, the objective of this study is to comprehensively investigate the behavior of FC confined plain concrete under both compression and splitting tensile conditions. The investigated behavior includes ultimate load, failure mechanisms, damages, and displacement ductility.

2. Experimental Program

The experimental program includes two types of cylindrical specimens, i.e., unconfined and confined plain concrete, as shown in Figure 1. The unconfined specimens were cylinders of 100 mm diameter and 200 mm height. On the other hand, FC confined specimens had a 150 mm diameter, including a 25 mm FC shell, and a 200 mm height. A 25 mm mortar shell thickness, as suggested by Xiong et al. (2011) and Heng et al. (2017), was maintained at the outer edge of the core concrete. Two construction methodologies, namely, monolithic and non-monolithic casting, were adopted for FC shell construction. In monolithic construction, the core concrete and FC shell were constructed together. In contrast, the FC shell was constructed on hardened concrete in the case of non-monolithic construction.

Nine unconfined, i.e., control specimens were made, where a compression load test was conducted on five specimens and a split tensile test was conducted on four specimens following ASTM C 39/C 39M (2019) and ASTM C496 (2019), respectively.

Meanwhile, six FC confined specimens were constructed for each volume fraction of wire mesh using both monolithic and non-monolithic casting methods. Among them, the compression load test was conducted on three specimens, and the split tensile test was conducted on three specimens. The configuration of all the specimens (unconfined and confined) is shown in Table 1.

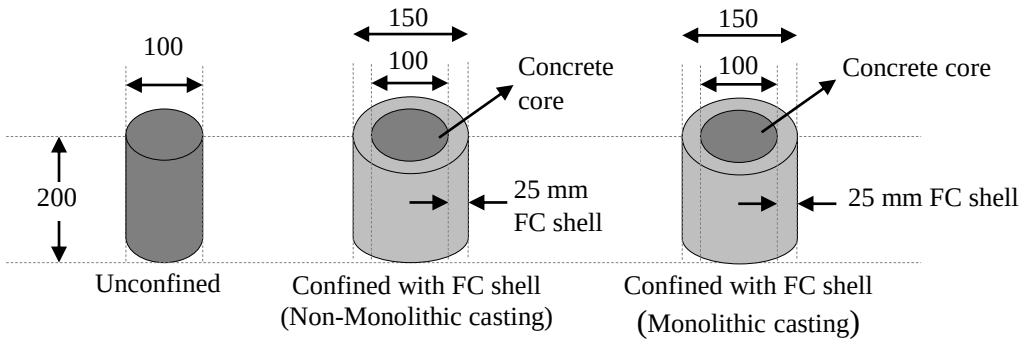

N.B.: Please refer to Figures 2 and 3 for non-monolithic and monolithic casting process

Fig. 1. Types of specimens in the current study (all dimensions are in "mm")

2.1. Materials and Mix Design

The cement utilized in this study meets BDS EN 197-1, 2003 standards and can be classified as CEM-II/B-M. As per specification, the used cement is Portland Composite Cement (PCC), which contains clinker (65-69%), blast furnace slag, pulverized fuel ash/limestone-slag (31-35%) and gypsum (0-5%).

The chemical composition of the clinker in the cement utilized in FC is given in Table 2. In concrete, 19 mm downgraded brick chips were used as coarse aggregate, and locally available river sand was used as fine aggregate. The material properties of the aggregates are given in Table 3. The concrete mix ratio was kept 1:2:4 (C: FA: CA) by volume, corresponding to M15 grade, with a water-cement ratio of 0.81.

For the outer shell mortar, the mortar mix ratio was kept at 1:2.5 (C: FA) by weight, and the water-cement ratio ranged from 0.64 to 0.75. Tap water was used during the mixing of constituent materials of concrete and mortar.

The mix proportions of concrete and FC mortar are given in Table 4. At 28 days, the average compressive strength of unconfined concrete cylindrical specimens was 6.73 MPa, while the mortar cube strength was 13.12 MPa. Two types of wire mesh, with different wire diameters and spacing, were used in this study to achieve the target volume fractions of mesh reinforcement. The wire diameter, spacing, and average ultimate tensile strength of Type-1 wire mesh were 1.02 mm, 12.8 mm, and 268.9 MPa, respectively. On the other hand, Type-2 wire mesh had a wire diameter of 1.24 mm, a spacing of 21.8 mm, and an average ultimate tensile strength of 334.5 MPa.

Table 1. Configuration of all types of specimens

Specimen type	Series name	Wire diameter (mm)	Wire spacing (mm)	Volume fraction, ρ (%)	No. of mesh layer, N	Shell thickness, t_s (mm)	Nominal diameter (mm)	Nominal height (mm)
Unconfined	C	-	-	-	-	-	100	200
non-monolithically confined (RA)	RA_22	1.24	21.82	0.22	Single	25	150	200
	RA_25	1.02	12.8	0.25	Single	25	150	200
	RA_50	1.02	12.8	0.50	Double	25	150	200
Monolithically confined (RB)	RB_22	1.24	21.82	0.22	Single	25	150	200
	RB_25	1.02	12.8	0.25	Single	25	150	200
	RB_50	1.02	12.8	0.50	Double	25	150	200

Table 2. Chemical composition of clinker

Constituent	Composition (%)
CaO	66.35
SiO_2	22.23
Al_2O_3	5.48
Fe_2O_3	3.47
MgO	0.85
SO_3	0.20

Table 3. Material properties of the aggregates

Aggregate	Fineness modulus	Absorption capacity (%)	Bulk sp. gravity (SSD)	Bulk sp. gravity (OD)	Apparent sp. gravity
Brick chips	3.3	23.6	1.8	1.5	2.3
River sand	1.4	5.0	2.3	2.2	2.5

Table 4. Mix proportion of concrete and Ferro-cement mortar

Specimen type	Concrete (Kg/m^3)			Ferro-cement mortar (Kg/m^3)	
	Cement	Ca [ssd]	Fa [ssd]	Cement	Fa [ssd]
Unconfined	205.7	1028.6	657.1	-	-
Non-monolithically confined (RA)				571.4	1428.6
Monolithically confined (RB)				-	-

2.2. Construction of Test Specimens

In this study, two types of construction methods were adopted to construct the confined specimens: non-monolithic (RA) and monolithic (RB) casting methods. In the non-monolithic casting method, 100 mm × 200 mm plain concrete cylinders were initially prepared.

After seven days, the hardened concrete was chipped off and inserted into a PVC mold along with a 125 mm diameter wire mesh ring. Then, the mortar was poured into the empty spaces around the plain hard concrete in such a way that a 25 mm thickness of mortar shell was maintained around the core concrete. The construction sequence of the non-monolithic casting is illustrated in Figure 2.

On the other hand, the concrete was directly poured into a PVC mold containing a 125 mm wire mesh ring in the monolithic casting method. The space between the mold and wire mesh ring was properly filled with the mortar matrix of the utilized concrete. The construction sequence of the monolithic casting is illustrated in Figure 3. During specimen casting, in both methods, the wire mesh ring was tried to keep at the center of the 25 mm FC shell.

Galvanized Iron (GI) wires were utilized to securely fasten the joints of the wire mesh ring, ensuring that its stability is maintained. It is to be noted that a 100 mm overlap of wire mesh was incorporated to prevent reinforcement debonding, which suggested by Kaushik et al. (1987).

3. Experimental Result and Discussion

3.1. Behavior Under Compression Load

The load-displacement relationship of both unconfined and confined specimens is depicted in Figure 4 for both non-monolithic and monolithic casting methods.

The confined specimens demonstrated notably enhanced load-carrying capacity compared to the unconfined specimens. The experimental results showed that the compressive load capacity increased between 95 ~ 187% and 62 ~ 115% for monolithic and non-monolithic casting methods, respectively, when compared to unconfined concrete. The unconfined specimens experienced a sharp drop in load-carrying capacity, while the confined specimens exhibited a gradual decrease in load-carrying capacity. Specimen failure became apparent upon wire mesh rupture, accompanied by significant cracks on the mortar shell and a drop in load-carrying capacity. Both unconfined and confined specimens showed vertical cracks on the outer side of the cylinder. Under the applied compressive load, the lateral expansion of the confined specimen's core concrete induced hoop tension in the FC shell due to Poisson's effect. Consequently, this led to the expansion and subsequent cracking of the shell. Upon reaching the maximum compressive load, rapid increases in crack widths were observed. After examining the damaged specimens, common failure patterns were observed, as shown in Figure 5. For both non-monolithic and monolithic specimens, it was observed that cracks originated from the outer edge of the shell in a radial pattern and extended towards the core concrete. Additionally, multiple vertical cracks were observed on the FC shell.

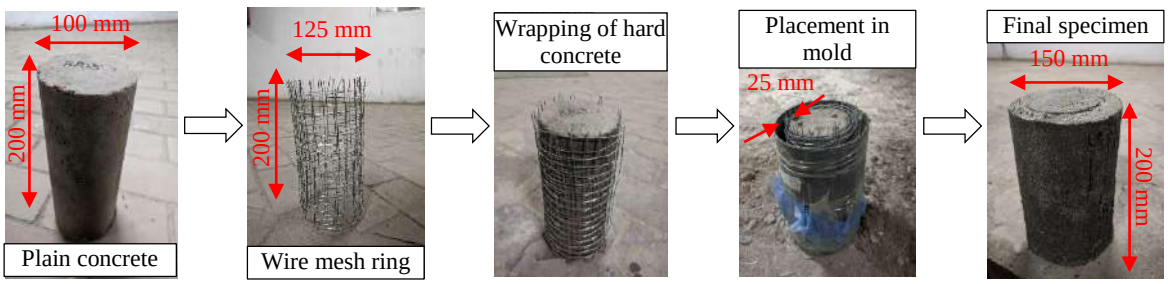

Fig. 2. Casting procedure of non-monolithically confined (RA) specimens

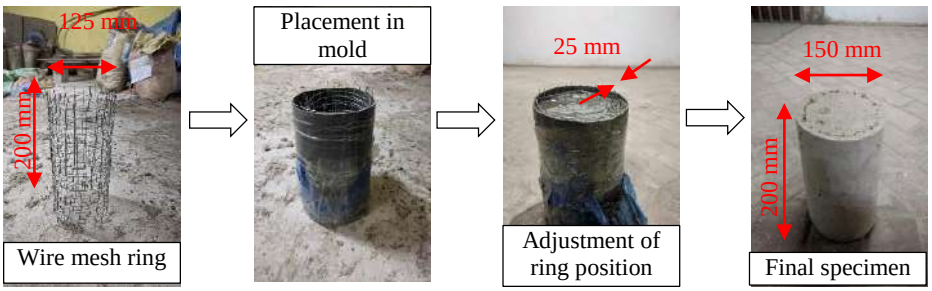

Fig. 3. Casting procedure of monolithically confined (RB) specimens

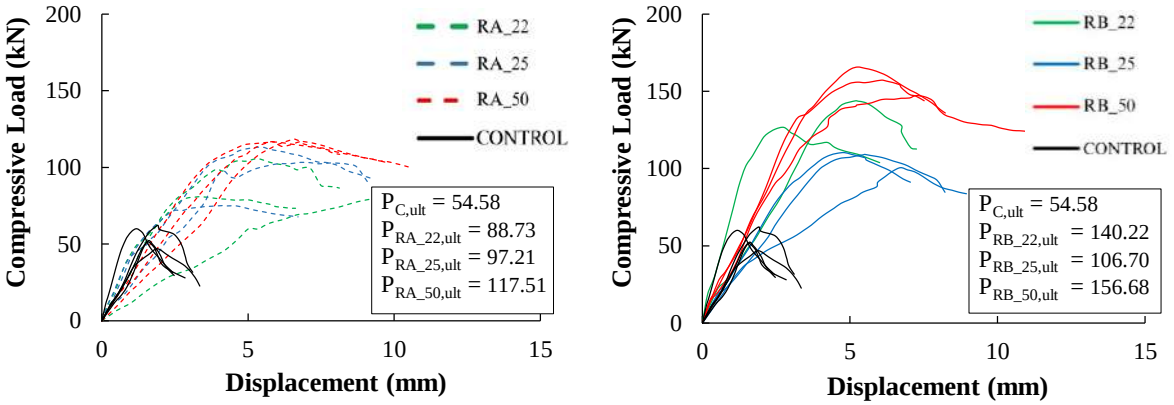

Fig. 4. Compressive load-displacement relationship of unconfined and Ferro-cement confined specimens: a) Non-monolithically confined; and b) Monolithically confined

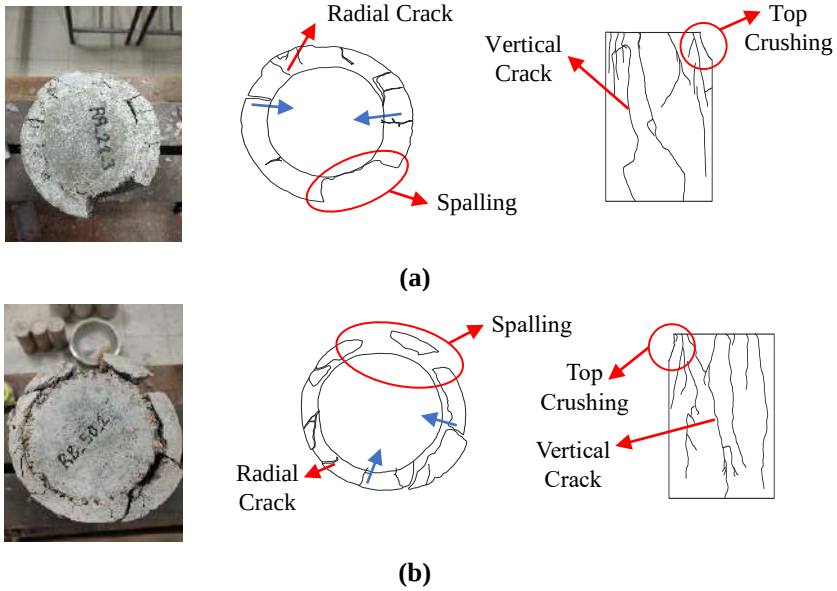

Fig. 5. Failure mode of: a) Non-monolithic; and b) Monolithic specimens under compressive load

Similar failures were reported by other researchers, for instance, Idris (2016) and Kaish et al. (2015). Furthermore, crushing was observed at the top of the specimens. Nevertheless, there was more mortar spalling on the shell of monolithically cast specimens compared to non-monolithically cast specimens.

3.2. Behavior Under Split Tension

The experimental split tensile load capacity, and average crack width on the concrete core and the FC shell are presented in Table 5. The experimental results indicate that the split tensile load-carrying capacity increased between 68 ~ 212% and 80 ~ 101% for monolithic and non-

monolithic casting methods, respectively, compared to unconfined concrete. Both unconfined and confined specimens showed splitting failure.

The split cracking originated from the core concrete and propagated towards the FC shell. This crack generation and propagation indicate that, at first, the core concrete failed under split tension, followed by cracking on the FC shell. Finally, the cracks in the core opened substantially, and loading was stopped. The rupture of the wire mesh was not observed. After examining the damaged confined specimens, common failure patterns were observed, as in Figure 6. It is to be noted that the split tensile behavior of FC confined plain concrete was found to be a research gap in the literature.

Therefore, these results would be helpful in understanding the efficacy of FC to improve the concrete split tensile capacity and in understanding the corresponding crack propagation of FC confined concrete.

3.3. Effect of Different Parameters on the Performance of FC Confined Concrete

3.3.1. On compression and split tensile capacity

Figure 7a represents the compressive load capacities of all the specimens. For non-monolithic specimens (RA), compressive load capacity increased linearly with the increase in wire mesh content, i.e., volume fraction in the FC shell. In the case of monolithic specimens (RB), wire mesh confinement was effective in increasing the compressive load capacity; however, the relationship of capacity enhancement with the increase of wire mesh content in FC was not conclusive. In this context, a non-linear trend of compressive capacity improvement with an increasing number of wire mesh layers was evident in other previous studies (e.g., Balaguru, 1989; Idris, 2016). In contrast, a linear trend was also found by Kaish et al. (2015) based on only two FC confined cylinders having one and two layers of wire mesh in the FC. Nonetheless, the monolithically confined (RB) specimens exhibited a relatively higher load-carrying capacity in comparison to the non-monolithically confined (RA) specimens.

Figure 7b represents the split tensile capacities of all the specimens. In the case of both non-monolithic specimens (RA) and monolithic specimens (RB), wire mesh confinement was effective in increasing the split tensile load capacity; however, capacity enhancement was not linearly varied with the volume fraction of wire mesh in FC. It is also evident that both non-monolithic (RA) and monolithic (RB) specimens exhibited comparable load-carrying capacity under split tension, except for specimens with a 0.50% volume fraction of wire mesh.

3.3.2. On Maximum Residual Crack Width

The maximum residual crack width of all of the specimens was measured using a crack scale after the completion of each specimen test. Under the compression load, cracks originated at the FC shell and propagated towards the core concrete. The FC shell was cracked within a range of approximately 1.8 ~ 5.8 mm on average, whereas the concrete core was cracked within a range of approximately 0.15 ~ 0.70 mm on average, which indicates that the FC shell was damaged more than the concrete core. The average core concrete crack width of all specimens under compression load is shown in Figure 8a. The core concrete crack width decreased with the increase in wire mesh volume fraction in FC for both the non-monolithic and monolithic casting methods.

Also, the residual crack widths were of similar order for both casting methods. Under split tension, cracks initiated at the core concrete center and propagated towards the FC shell mortar. The FC shell was cracked within a range of approximately 0.9 ~ 1.7 mm on average,

whereas the concrete core was cracked within a range of approximately 1.6 ~ 7.0 mm on average, which indicates that the concrete core was damaged more than the FC shell. The average FC shell crack width of all specimens under the split tensile load is shown in Figure 8b.

Table 5. Average experimental ultimate load and crack width of all specimens under split tension.

Specimen type	Series name	Average experimental ultimate load, P_{ult} (KN)	Average crack width (mm) On core	On shell
Unconfined	C	30.84	2.01	-
Non-monolithically confined	RA_22	62.02	2.47	1.72
	RA_25	55.52	1.80	1.57
	RA_50	60.80	1.57	1.40
Monolithically confined	RB_22	69.06	7.00	1.45
	RB_25	51.82	5.50	1.10
	RB_50	96.34	3.83	0.87

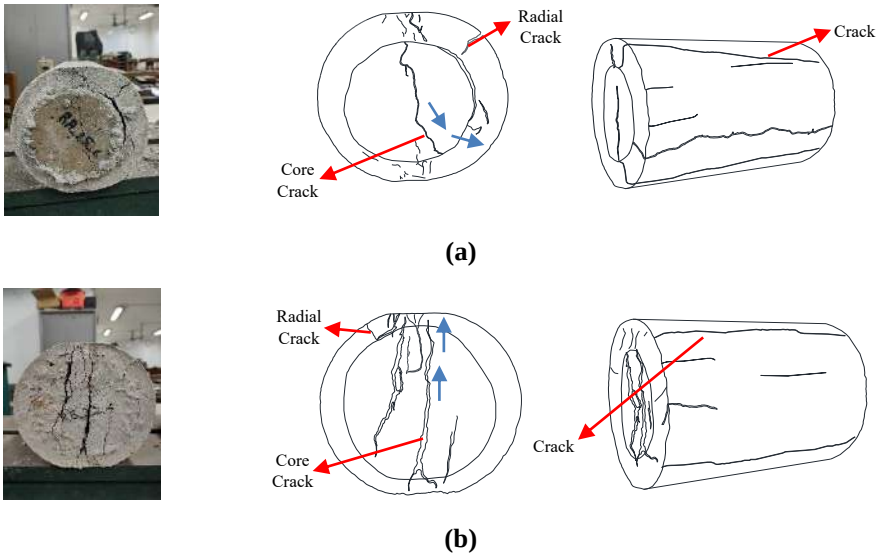

Fig. 6. Failure mode of: a) Non-monolithic; and b) Monolithic specimens under split tensile condition

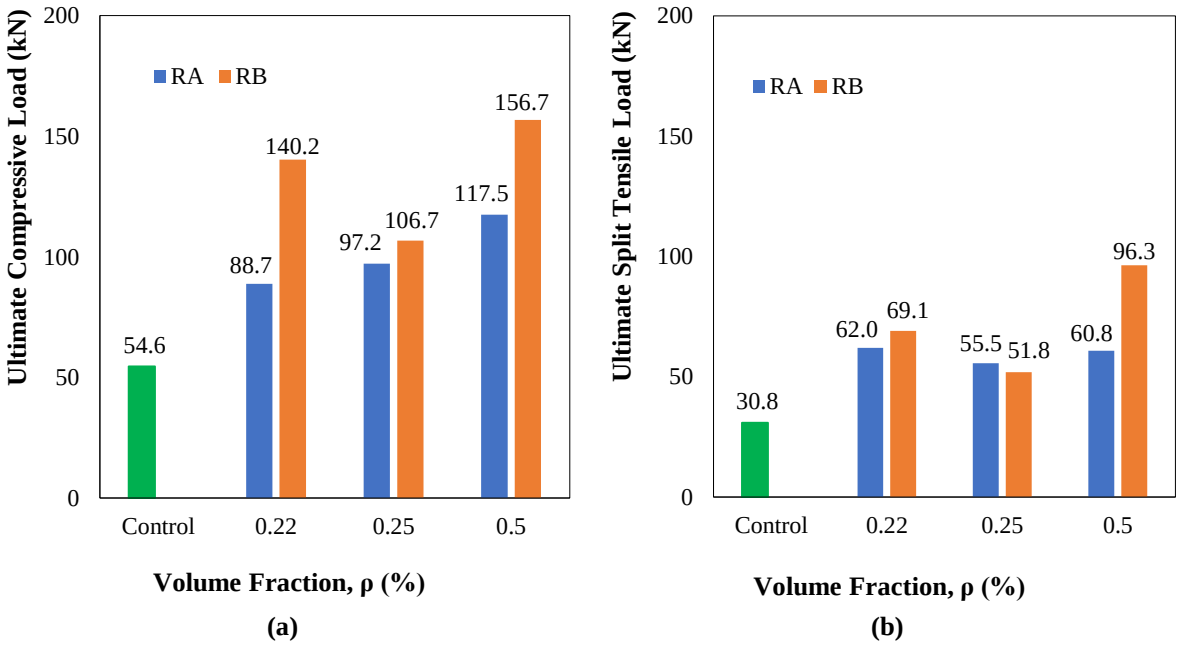

Fig. 7. Ultimate load capacity of unconfined and FC confined concrete under: a) Compression; and b) Split tensile condition.

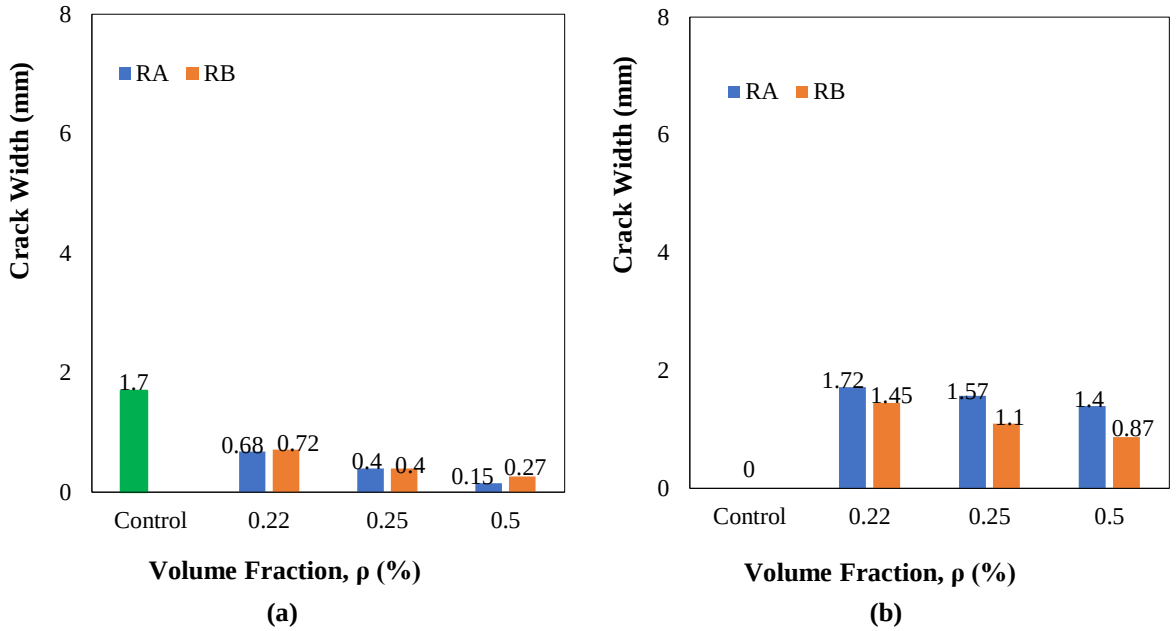

Fig. 8. Maximum crack width of: a) Core concrete under compression; and b) FC shell under split tension

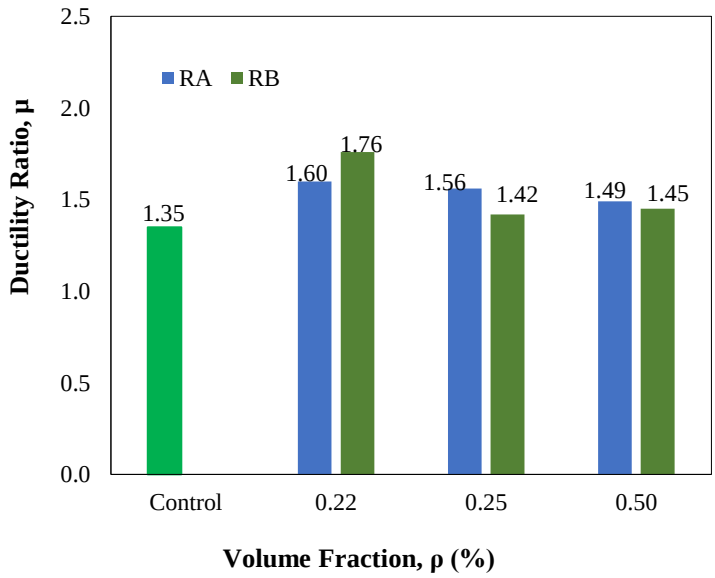

Fig. 9. Displacement ductility under compression load

It is evident that the FC shell crack width decreased with the increase in wire mesh volume fraction in FC for both the non-monolithic and monolithic casting methods. Also, the residual crack widths were relatively lower for monolithic specimens. In summary, the location of maximum damage varied under compression and split tension. However, under both loading conditions, more damages, i.e., residual crack widths, were observed at the location of initial crack formation, irrespective of the parameters of this study.

3.3.3. On Displacement Ductility

The displacement ductility was determined for specimens tested under compression loads as a ratio of displacement at 80% of the ultimate load after the post-peak and displacement at the maximum load. The average displacement ductility of all specimens (minimum 1.42 and maximum 1.76) under the compression load is shown in Figure 9. It is evident that wire mesh confinement marginally improved the ductility. In literature, Kaish et al. (2015) found displacement ductility (i.e., a ratio of displacement at 0.85 of the

ultimate load on the post-peak stage to displacement at the yield load) of all jacketed cylinders within a range of 1.34 to 2.43. The variation in the ranges of displacement ductility could be attributed to the differences between the definition of displacement ductility in this study and Kaish et al. (2015). Nevertheless, no remarkable relationship among displacement ductility, volume fraction of wire mesh in FC, and construction method was found in this study.

4. Conclusions

This study focused on the experimental behavior of unconfined and Ferro-Cement confined plain concrete cylinders under compression and split tension. Two construction methodologies, namely, non-monolithic and monolithic casting, were adopted for FC confinement. In addition, 0.22%, 0.25% and 0.50% volume fractions of wire mesh in FC were considered for each construction method.

The following conclusions were drawn within the limited scope of this study:

- Compression load carrying capacity improved by 62% to 115% for non-monolithic specimens and 95% to 187% for monolithic specimens, with an increase in wire mesh volume fraction from 0.22% to 0.50%.
- Split tensile load capacity increased by 80% to 101% for non-monolithic specimens and 68% to 212% for monolithic specimens, with an increase in wire mesh volume fraction from 0.22% to 0.50%.
- Under compression, cracks originated from the outer edge of the FC shell in a radial pattern and extended towards the core concrete, irrespective of the parameters of this study. Whereas cracks originated at the center of core concrete and propagated radially towards the FC shell under split tensile load.
- The location of maximum damage varied under compression and split tension. However, under both loading conditions, more damages, i.e., residual crack widths, were observed at the location of initial crack formation, irrespective of the parameters of this study.
- No notable relationship among displacement ductility, volume fraction of wire mesh in FC, and construction method was found.

6. References

Ahsan, R., Zahan, S. and Nahar, J. (2023). "Review of tests on Ferro-cement retrofitted unreinforced masonry", *ACI Special Publication*, *358*, 179-205, https://doi.org/10.14359/51740236.

Amala, M., Dhal, L., Gokul, V., Christi, S. and Dhanasekar, K. (2021). "Strengthening of compression member by Ferro-cement with high performance mortar-Jacketing technique", *Materials Today: Proceedings*, 43, 1810-1818, http://doi.org/10.1016/j.matpr.2020.10.495.

ASTM C 39/C 39M (2019). *Standard test method for compressive strength of cylindrical concrete specimens*, American Society for Testing and Materials (ASTM), USA, https://scribd.com/document/488623641/ASTM-C39-C39M-20-Standard-Test-Method-for-Compressive-Strength-of-Cylindrical-Concrete-Specimens.

ASTM C496 (2019). Standard test method for splitting tensile strength of cylindrical concrete specimens, American Society for Testing and Materials (ASTM), USA, https://pdfcoffee.com/astm-c-496-pdf-free.html.

Aules, W.A., Saeed, Y.M., Al-Azzawi, H. and Rad, F.N. (2022). "Experimental investigation on short concrete columns laterally strengthened with Ferro-cement and CFRP", *Case Studies in Construction Materials*, 16, e01130, https://doi.org/10.1016/j.cscm.2022.e01130.

Bahmani, M. and Zahrai, S.M. (2023). "Proposed methodology and comprehensive design process for seismic rehabilitation of steel structures with supplemental viscous dampers", *Civil Engineering Infrastructures Journal*, 56(1), 79-103, https://doi.org/10.22059/CEIJ.2022.330808.1793.

Balaguru, P. (1988). "Use of Ferro-cement for confinement of concrete", In: *Proceedings of the Third International Conference on Ferro Cement*, Rourke, India, 296-305.

BDS EN 197-1 (2003). *Composition, specifications and conformity criteria for common cements*, Bangladesh Standards and Testing Institution (BSTI), Bangladesh, https://scribd.com/doc/311860993/BDS-EN-

197-1-2003.

Boban, J.M. and John, A.S. (2021). "A review on the use of Ferro-cement with stainless steel mesh as a rehabilitation technique", *Materials Today: Proceedings*, *42*, 1100-1105, http://doi.org/10.1016/j.matpr.2020.12.490.

El-Sayed, T.A., Shaheen, Y.B., Mohamed, F.H. and Abdelnaby, R.M. (2023a). "Performance of Ferro-cement composites circular tanks as a new approach for RC tanks", *Case Studies in Construction Materials*, 19, e02228, https://doi.org/10.1016/j.cscm.2023.e02228.

El-Sayed, T.A., Shaheen, Y.B., AbouBakr, M.M. and Abdelnaby, R.M. (2023b). "Behavior of Ferro-cement water pipes as an alternative solution for steel water pipes", *Case Studies in Construction Materials*, 18, e01806, https://doi.org/10.1016/j.cscm.2022.e01806.

Erfan, A.M., Abd Elnaby, R.M., Elhawary, A. and El-Sayed, T.A. (2021). "Improving the compressive behavior of RC walls reinforced with Ferro--cement composites under centric and eccentric loading", *Case Studies in Construction Materials*, 14, e00541, https://doi.org/10.1016/j.cscm.2021.e00541.

Heng, K., Areemit, N. and Chindaprasirt, P. (2017). "Behavior of concrete cylinders confined by a Ferro-geopolymer jacket in axial compression", *Engineering and Applied Science Research*, 44(2), 90-96, https://ph01.tci-thaijo.org/index.php/easr/article/view/67564.

Idris, I.I. (2016). "Behavior and strength of concrete cylinders confined by reinforced concrete jacket and Ferro-cement overlay", *International Journal Science and Engineering Investigation*, 5(49), 19-23, http://www.ijsei.com/papers/ijsei-54916-04.pdf.

Jaraullah, M.N.A., Dawood, E.T. and Abdullah, M.H. (2022). "Static and impact mechanical properties of Ferro-cement slabs produced from green mortar", *Case Studies in Construction Materials*, 16, e00995, https://doi.org/10.1016/j.cscm.2022.e00995.

Kaish, A.B.M.A., Jamil, M., Raman, S.N. and Zain, M.F.M. (2015). "Axial behavior of Ferro-cement confined cylindrical concrete specimens with different sizes", *Construction and Building Materials*, 78, 50-59, https://doi.org/10.1016/j.conbuildmat.2015.01.044.

Kaushik, S.K., Gupta, V.K. and Rahman, M.K. (1987). "Efficiency of mesh overlaps of Ferro-cement elements", *Journal of Ferrocement*,17, 329-36, https://researchgate.net/publication/293124693_efficiency_of_mesh_overlaps_of_Ferrocemente lements.

Kaushik, S. and Singh, S. (1997). "Behavior of Ferro-cement composite columns in compression", *ACI Special Publications*, 172, 669-682. https://doi.org/10.14359/6158.

Minde, P., Bhagat, D., Patil, M. and Kulkarni, M. (2023). "A state-of-the-art review of Ferro-cement as a sustainable construction material in the Indian context", *Materials Today: Proceedings*, https://doi.org/10.1016/j.matpr.2023.03.250.

Sen, D., Alwashali, H., Islam, M.S., Seki, M. and Maeda, M. (2023). "Lateral strength evaluation of Ferro-cement strengthened masonry infilled RC frame based on experimentally observed failure mechanisms", *Structures*, 58, 105428, https://doi.org/10.1016/j.istruc.2023.105428.

Shaheen, Y.B., Eltaly, B.A., Yousef, S.G. and Fayed, S. (2023). "Structural performance of Ferro-cement beams incorporating longitudinal hole filled with lightweight concrete", *International Journal of Concrete Structures and Materials*, 17(1), 21, https://doi.org/10.1186/s40069-023-00579-3.

Surendra, B.V. and Ravindra, R. (2021). "A study of affordable roofing system using Ferro-cement and bamboo cement panels", *Journal of the Institution of Engineers (India): Series A*, *102*(3), 633-642, https://doi.org/10.1007/s40030-021-00533-0.

Xiong, G.J., Wu, X.Y., Li, F.F. and Yan, Z. (2011). "Load carrying capacity and ductility of circular concrete columns confined by Ferro-cement including steel bars" *Construction and Building Materials*, 25(5), 2263-2268, https://doi.org/10.1016/j.conbuildmat.2010.11.014.

Civil Engineering Infrastructures Journal 2025, 58(1): 159-171
DOI: 10.22059/ceij.2024.366170.1969

RESEARCH PAPER

Evaluation of Uncertainty in Shear-Wave Velocity Based on CPT Records Using the Robust Optimization Method

Hajitaheriha, M.M.[1*], Mola-Abasi, H.[2], Li, J.[3], Salahi, M.[4] and Ataee, O.[5]

[1] Ph.D. Candidate, Department of Civil Engineering, Memorial University of Newfoundland, Newfoundland, NL, Canada.
[2] Assistant Professor, Department of Civil Engineering, Gonbad University, Gonbad, Golestan, Iran.
[3] Assistant Professor, Department of Civil Engineering and Construction Management, California Baptist University, California, U.S.
[4] Professor, Department of Applied Mathematics, Faculty of Mathematical Sciences, University of Guilan, Rasht, Iran.
[5] Assistant Professor, Department of Geography and Urban Planning, University of Mazandaran, Babolsar, Mazandaran, Iran.

Received: 3 Oct. 2023; Revised: 16 Jan. 2024; Accepted: 12 Feb. 2024

ABSTRACT: Shear-wave velocity (V_s) is used to evaluate the soil shear modulus and classify the soil type in pseudo-static analysis. Empirical correlations are developed to relate V_s and Cone Penetration Test (CPT) records. However, uncertainty in the input parameter measurements is always a major concern. Therefore, the current research employs a novel method based on robust optimization to study the effect of such uncertainties. To measure the merits of the suggested method, 407 records were collected and categorized for several soil types. The identification procedure employed in this investigation is based on the robust model of least squares, solved using the interior point technique for second-order cone problems. The uncertainty definition is examined against correlation coefficients for empirical models, and optimum values are determined based on the frobenius norm of the data points. A diagram for calculating the shear wave velocity considering uncertainties is also presented. This study suggests that the robust method is the best pattern recognition tool for uncertain datasets compared to previous statistical models. Other power models also have good accuracy compared to the polynomial model, but when uncertainty is taken into account, the accuracy of the other models is lower compared to the polynomial model.

Keywords: CPT, Polynomial Model, Robust Optimization, Shear-Wave Velocity, Uncertainty.

1. Introduction

The Shear Wave Velocity (Vs) induced shear modulus is a main geotechnical property corresponding to small strains which is of importance in geotechnical research. Due to the constraints in gathering undisturbed samples, particularly in granular soils, in situ seismic tests, in place of laboratory measurements are the best

* Corresponding author E-mail: mhajitaherih@mun.ca

possible direct tests in achieving the Vs. To establish the Vs profile, the surface wave velocity assessment, as well as down-hole and cross-hole techniques can be conducted (Eslami et al., 2020; Mayne, 2007; Robertson, 2009). However, because of the limits of the noise level and space constraints in urban areas, seismic in situ investigations are not usually possible or appropriate. Therefore, it is convenient to estimate Vs indirectly by other common in situ tests, such as the Standard Penetration Test (SPT) for compacted soils and the Cone Penetration Test (CPT) for soft soils.

Among in situ tests, CPT is a more versatile and reliable test that is used in geotechnical site investigations (Anagnostopoulos et al., 2003). Zhang et al. (2021) proposed a Multilayer Fully Connected Network (ML-FCN) to optimize the training of the Deep Neural Network (DNN) using the Vs and SPT datasets. Zhao et al. (2021) developed a new PSO-KELM hybrid machine learning model to evaluate soil liquefaction potential and explore nonlinear relationships between Cyclic Resistance Ratio (CRR), CPT and Vs measurements. Wang et al. (2022) assessed thirteen alluvium sites in Taipei Basin, and measurements of shear wave velocity were concurrently obtained using the five common seismic methods.

Measurement discrepancies were quantified through statistical analysis of the data, offering guidance for method selection. Yang et al. (2023) integrated CPT-Vs data to create a simplified probabilistic assessment for liquefaction potential. Chala and Ray (2023) employed Machine Learning (ML) algorithms to predict V_s from CPT data, including Random Forests (RFs), Support Vector Machine (SVM), Decision Trees (DT) and eXtreme Gradient Boosting (XGBoost).

Zhou et al. (2022) presented two SVM models optimized with Genetic Algorithm (GA) and Grey Wolf Optimizer (GWO) to predict soil liquefaction potential, validated using CPT, SPT and VS test data with varying input variables. Several correlations and mathematical methods were suggested for estimating the V_s based on CPT records for loose sand, silt, clay, and all other soil types (Comina et al., 2022; Jakka et al., 2022; Meng and Pei, 2023; Zhao et al., 2022).Wang et al. (2022) investigated 13 alluvial sites in Taipei Basin and measured the velocity profiles employing each of the five most common seismic methods. Using test data and statistical models, differences in seismic methods were quantified as calibrated measurement uncertainties, which can be used as a reference for selecting an appropriate method to measure shear wave velocity. Zhai et al. (2024) aimed to develop a Bayesian framework that considered both in-situ test data (SPT, CPT) and prior information, to determine the probabilistic characteristics of V_s while accounting for transformation uncertainty. The study found out that the model which includes two in_situ tests accurately predicts shear wave velocity. Using different travel times (i.e., first arrival picks, peaks and troughs picks, crossover picks, and the peak response of the cross-correlation function) and different velocity analysis methods (i.e., pseudo-interval, true-interval, corrected vertical travel time slope-based, and raytracing), Stolte et al. (2020) developed a number of V_s profiles. Gilder et al. (2021) presented CPTu data related to the Kathmandu valley sediments and employed the established CPTu interpretation procedures to assess the in-situ soil properties. Previously, for the assessment of variability and seismic response of the subsoils in Kathmandu, SPT data and limited shear wave velocity measurements were predominantly used.

This study provided further data to supplement the existing SAFER/GEO-591 database, new shear wave velocity measurements, and initial estimates of CRR at the visited sites. It was concluded that liquefaction assessment mainly due to the presence of saturated silts in the valley demands a more detailed methodology.

Wang et al. (2022) examined the

performance of V_s-SPT and V_s-CPTU models and found that V_S has a strong correlation with the depth of soil (D) but weak correlation with SPT-N or CPT-q_c.

This indicates that most of the transformation models in previous studies are not suitable to these sites as they disregard soil depth in their formulation. In an attempt to confirm if the assumption about the consistency of depth is true for V_s data using models created in the CSR framework, Wang et al. (2022) created two models to assess the chances of liquefaction. These models use the V_s based probabilistic approach and consider the uncertainty of measurements. By assuming consistency in depth, it was found that the performance of the suggested models is similar to two commonly used models based on the CSR framework, and better than the Chinese code model.

Mohammadikish et al. (2023) utilized two different approaches, namely, the whole data strategy and partial distance strategy, in their study. Bayat et al. (2023) introduced an analytical approach to optimize the compaction pattern and dynamic compaction variables regarding regular constraints. They employed a metaheuristic approach (Genetic Algorithm) to find global optimum. Results indicated that the maximum allowed values of tamper mass and the number of tamper drops were required to minimize compaction energy. In this study, researchers examined the effectiveness of fuzzy c-means clustering in analyzing incomplete data to evaluate the probabilistic liquefaction. The data used for this analysis included CPT and V_s field data. This method compared the traditional deterministic and probabilistic liquefaction evaluation approaches, and it was found that the fuzzy c-means clustering model demonstrated a similar predictive capability compared to other methods. Thus, it is considered reliable for evaluating the liquefaction possibility. The main variables as input parameters are cone resistance (q_c), sleeve friction (f_s) and overburden pressure in effective form (σ'_{V0}) in the correlation functions, such as linear, logarithm, power, and polynomial functions. Some of the important correlations are presented in Table 1, in which, $a_i's$ are constant coefficients of the model and each researcher has estimated the coefficients using the data related to the study case.

Such empirical correlations (Table 1) are generally based on statistical regression analyses with notable modeling drawbacks. For example, inaccuracies enter into the field measurements of V_s in case histories similar to all other natural phenomena measurements (Ghose, 2004). Such inaccuracies may exist in other influencing parameters and can cause deviation. Therefore, proposing a formula capable of dealing with the uncertainties and inaccuracies in input parameters is required.

Accordingly, a novel optimization method is proposed in the present study to overcome the disadvantages of the previous empirical correlations by considering the uncertainties. The other main aim of this paper is to validate the previous models for V_s based on the CPT parameters, q_c, and f_s, via a database and to quantify the effect of uncertainties on the evaluation of the correlation parameters using the robust optimization model. The robust optimization model is the robust counterpart of the least-squares model that is reformulated as a Second-Order Cone Program (SOCP) in which possible uncertainties can be reasonably adjusted.

The SOCP has been widely used in optimization and could be applied in predicting V_s as an advancement in terms of assessment compared to previous regression methods. Also, SOCP considers the variation of inaccuracies and uncertainties. The novelty of this article is the consideration of data uncertainty, which was not taken into account in previous similar articles. Therefore, this article presents an uncertainty-tolerant model for use by researchers. In other words, a model that has very low uncertainty in the parameters of its influence on the result

output. It is worth noting that given the uncertainty of the data, the coefficients of the models are also revised. The rest of the paper is organized as follows: Section 2 analyzes the uncertainty and robust optimization model. Section 3 presents the database. In Sections 4 and 5, the modeling process and main results obtained from the present study are summarized, respectively.

2. Review of the Robust Optimization Framework

Robust optimization is a modeling method where significant uncertainties are presented. This model aims to discover ideal solutions for the worst-case scenario of uncertainties in a specific database (Ben-Tal et al., 2009). In real-world applications, it is common to assume that the data is available with a certain level of uncertainty.

Thus, classical algorithms may not meet the expectations of the modeler. Robust optimization is a framework for dealing with such situations. It should be noted that the robust approach normally involves computational complexity, such as, inaccuracies entered in the field measurements of V_s or depth (precision in measurement). Such inaccuracies may also exist in other influential parameters, which may cause prediction uncertainties.

Table 1. A list of the proposed correlations between V_s and CPT

Functional form	Proposed correlation (m/s)	Eq.	Author(s)	Soil type	Units q_c	Units f_s
$V_S = a_1 + a_2 q_c$	$V_s = 154 + 0.64 q_C$	1	Barrow (1983)	All	kgf/cm^2	-
	$V_s = 134 + 0.52 q_C$	2	Sykora (1983)	Sand	kgf/cm^2	-
	$V_s = 160 + 0.9 q_C$	3	Iyisan and Ansal (1993)	All	kgf/cm^2	-
	$V_s = 218 + 0.70 q_C$	4	Iyisan and Ansal (1993)	Sand	kgf/cm^2	-
$V_S = a_1 + a_2\, ln(q_c)$	$V_s = 109.29 + 52.674 ln(q_C)$	5-1	Tun (2003)	All	MPa	MPa
	$V_s = 109.29 + 52.674 ln(q_C)$	5-2	Tun and Ayday (2018)	All	MPa	MPa
$V_S = a_1 + a_2\, log(f_s)$	$V_s = 18.5 + 118.8 log(f_S)$	6	Mayne (2006)	All	-	kPa
$V_S = a_1 (q_c)^{a_2}$	$V_s = 54.8 (q_C)^{0.29}$	7-1	Sykora (1983)	Sand	kgf/cm^2	-
	$V_s = 45 (q_C)^{0.41}$	7-2	Iyisan and Ansal (1993)	All	kgf/cm^2	-
	$V_s = 1.75 (q_C)^{0.627}$	7-3	Mayne and Rix (1995)	Clay	kPa	kPa
	$V_s = 55.3 (q_C)^{0.377}$	7-4	Iyisan and Ansal (1993)	Clay	kgf/cm^2	-
	$V_s = 211 (q_C)^{0.23}$	7-5	Madiai and Simoni (2004)	All	MPa	MPa
$V_S = a_1 (q_c)^{a_2} f_s^{a_2}$	$V_s = 12.02 (q_C)^{0.319} (f_S)^{-0.0466}$	8-1	Hegazy and Mayne (1995)	Sand	kPa	kPa
	$V_s = 155 (q_C)^{0.29} (f_S)^{-0.10}$	8-2	Madiai and Simoni (2004)	All	MPa	MPa
$V_S = a_1 (q_c / Pa)^{a_2} + a_3$	$V_s = 50[(q_C/p_a)^{0.43} - 3]$	9	Paoletti et al. (2010)	Sand	kPa	-
$V_S = a_1 (q_c)^{a_2} (f_s)^{a_2} (\sigma_v)^{a_3}$	$V_s = 359 (q_C)^{0.119} (f_S)^{0.1} (\sigma'_v)^{0.204}$	10	Kruiver et al. (2021)	All	MPa	MPa
$V_S = a_1 (q_c)^{a_2} (f_s)^{a_2} (Z)^{a_3}$	$V_S = 18.4 (q_c)^{0.144} (f_s)^{0.0832} (Z)^{0.278}$	11	McGann et al. (2015b)	All	kPa	kPa
$V_S = a_1 + a_2 q_c + a_3 f_s + a_4 q_c^2 + a_5 f_s^2 + a_6 (q_c f_s)$	V_s (m/s) $= 100[1.36 - 0.35 f_s + 0.15 q_c - 0.05 f_s^2 - 0.018 q_c^2 + 0.39 (f_s)(q_c)]$	12-1	Mola-Abasi et al. (2015)	Clay	MPa	MPa
	V_s (m/s) $= 100[1.73 + 2.74 f_s + 0.03 q_c - 4.015 f_s^2 - 0.00026 q_c^2 + 0.007 (f_s)(q_c)]$	12-2		Sand	MPa	MPa
	V_s (m/s) $= 100[1.47 + 2.07 f_s + 0.10 q_c + 9.50 f_s^2 - 0.0023 q_c^2 - 0.034 (f_s)(q_c)]$	12-3		Mixed	MPa	MPa
	V_s (m/s) $= 100[1.40 + 1.59 f_s + 0.09 q_c - 1.33 f_s^2 - 0.002 q_c^2 + 0.05 (f_s)(q_c)]$	12-4		All	MPa	MPa

Suppose that such input-induced variations are considered boundaries of the central data point (Figure 1) and the true data point exists at every point within this boundary. In this case, robust optimization aims to minimize the maximum error with a certain level of uncertainty (Kalantary, 2013). Such input-induced deviations are considered the boundaries of the central data point (Figure 1). Evaluating constant coefficients (a_i) of empirical Eqs. (1-12) (a_1 to a_6) using regression analysis can be formulated as follows:

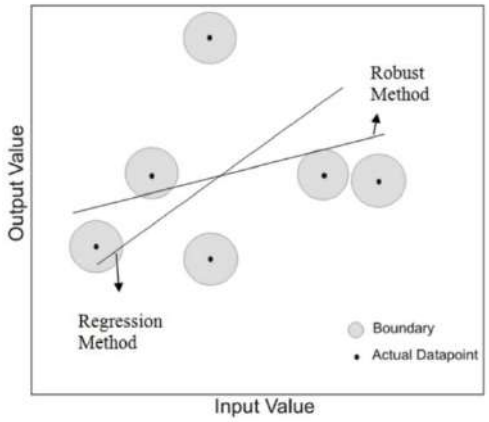

Fig. 1. Robust and regression methods

$$Ax = b. A \in R^{m\times n}. b \in R^{m\times 1} \; and \; x \in R^{n\times 1} \tag{13}$$

where A and b: are data matrices, and x: is the vector of variables. Also, m and n: are the number of case histories and input parameters, respectively, that show the over-determined set of equations in the case of ($m > n$). All models are first examined using a compiled database and simple least-squares regression analysis. The classic method for solving the least squares problem is as follows:

$$min_{x\in R^n} \|(Ax - b)\|^2 \tag{14}$$

Next, the robust least-squares model is presented in Eq. (15). If the level of uncertainty in the databases is known and is equal to ρ, the robust model for minimizing the worst-case residual is as follows (Alizadeh and Goldfarb, 2003):

$$min_x max_{\|[E.r\|_F\leq\rho} \|(A + E)x - (b + r)\|^2 \tag{15}$$

where, ρ, E and r: are the uncertainties in A and b, respectively, and the norm of the matrix, $\| \|_F$ is the Frobenius norm (Golub and Van Loan, 2013). Eq. (15) in its current form cannot be solved. However, it can be written in SOCP form (Sturm, 2002). First, for a given x:

$$r(A.b.x) \underset{\longrightarrow}{def} max\{\|(A + E)x - (b + r)\| \mid \|E.r\|_F \leq \rho\} \tag{16}$$

Eq. (17) is resulted from the triangular inequality.

$$\|(A + E)x - (b + r)\| \leq \|Ax - b\| + \left\|(E. -r)\begin{pmatrix} x \\ 1 \end{pmatrix}\right\| \tag{17}$$

Moreover,

$$\left\|(E. -r)\begin{pmatrix} x \\ 1 \end{pmatrix}\right\| \leq \|E.r\|_F \left\|\begin{pmatrix} x \\ 1 \end{pmatrix}\right\| \leq \rho \left\|\begin{pmatrix} x \\ 1 \end{pmatrix}\right\| \tag{18}$$

but for the choice $(E. -r) = uv^t$, where:

$$u = \begin{cases} \rho\dfrac{Ax - b}{\|Ax - b\|}. if \; Ax - b \neq 0 \\ \text{any vector } \in R^m \text{ of norm } \rho. \text{otherwise} \end{cases}$$

and (19)

$$\mathrm{v} = \frac{\begin{pmatrix} x \\ 1 \end{pmatrix}}{\left\|\begin{pmatrix} x \\ 1 \end{pmatrix}\right\|}$$

Eq. (20) is obtained.

$$\left\|(E. -r)\begin{pmatrix} x \\ 1 \end{pmatrix}\right\| = \|u\| \times \left\|\begin{pmatrix} x \\ 1 \end{pmatrix}\right\| = \rho \left\|\begin{pmatrix} x \\ 1 \end{pmatrix}\right\| \tag{20}$$

Therefore,

$$r(A.b.x) = \|Ax - b\| + \rho \left\|\begin{pmatrix} x \\ 1 \end{pmatrix}\right\| \tag{21}$$

Thus, min $r(A,b,x)$: is equivalent to the following SOCP:

$$\begin{matrix} min(t + \rho s) \\ \|Ax - b\| \leq t. \\ \sqrt{1 + \|x\|^2} \leq s \end{matrix} \tag{22}$$

The problem of Eq. (22) is a SOCP that can be solved using efficient interior point-based software packages such as SeDuMi (Sturm, 1999). It is solved for different values of uncertainty parameters, ρ. To account for the uncertainty, a new parameter of Eq. (23) is introduced.

$$\text{Uncertainty } (\%) = \frac{\rho}{2\|DATA\|_{fro}} \times 100 \quad (23)$$

The uncertainty parameter introduced in Eq. (23) means that each data point can have an extreme uncertainty up to half of its value. In other words, data are assumed to be in the form of Eq. (24).

$$\begin{aligned} \text{Data point} &= \text{actual value} \\ &\pm \text{uncertainty} \\ &= \text{actual value} \\ &\pm \left(\frac{\text{actual value}}{2}\right) \end{aligned} \quad (24)$$

One of the advantages of this method is to find the model coefficients and find a logical relationship between the uncertainty and the predicted value. In other words, by knowing the measurement accuracy associated with the data and determining the corresponding uncertainty, the corresponding uncertainty coefficient can be determined and the model output value can be predicted from the corresponding graphs. Of course, the models must be simple and straightforward enough so that they can be converted into linear and matrix models by changing parameters or mapping.

3. Database Compilation

This study utilizes the data from a project in Eskisehir, Turkey. From a combination of CPT logs and V_s profiles extracted from the SCPT data, 407 triple data (q_c, f_s and V_s) were obtained from 37 sites within the specified range where the V_s values come from approximately the same depth ranges.

The database was divided into four soil types. Figure 2 shows the CPT data as a sample and Figure 3 shows the scatter of q_c, fs and V_s as a function of depth. Also, in Table 2, a sample of the database is presented. Mola-Abasi et al. (2015) and Tun (2003) introduced more information about the site investigation and data process. In the mentioned articles, detailed explanations of the data and physical-mechanical conditions were given, and since this is not part of the main discussion of the article, the readers' attention was drawn to these articles for further research.

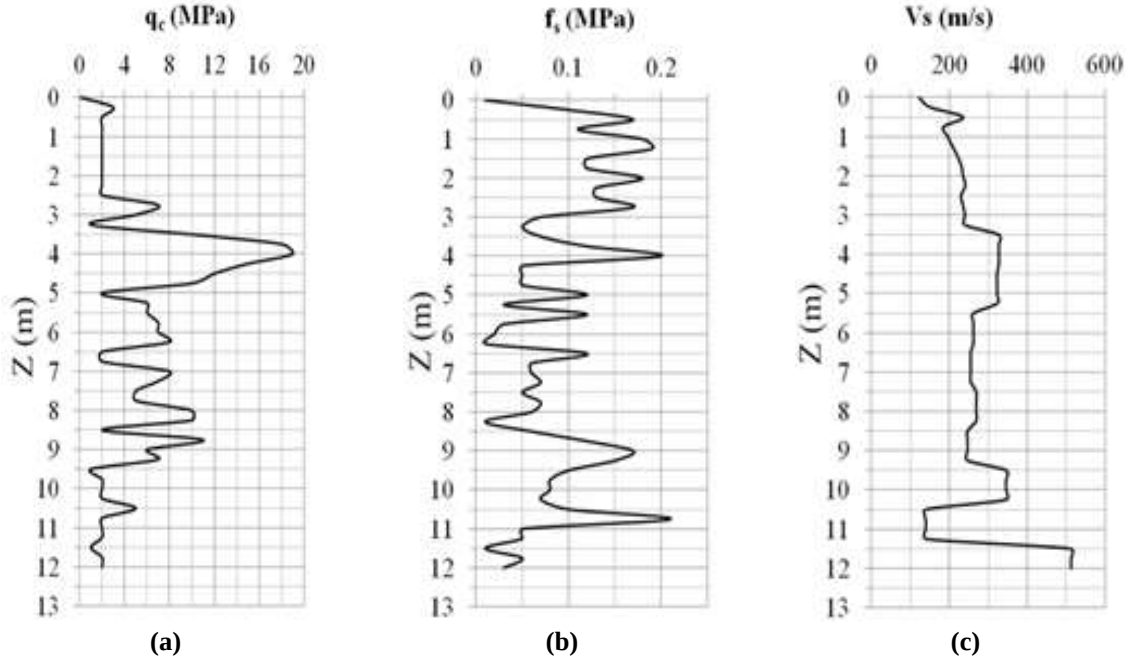

Fig. 2. An example of a CPT and V_s record: a) q_c; b) f_s and c) V_s

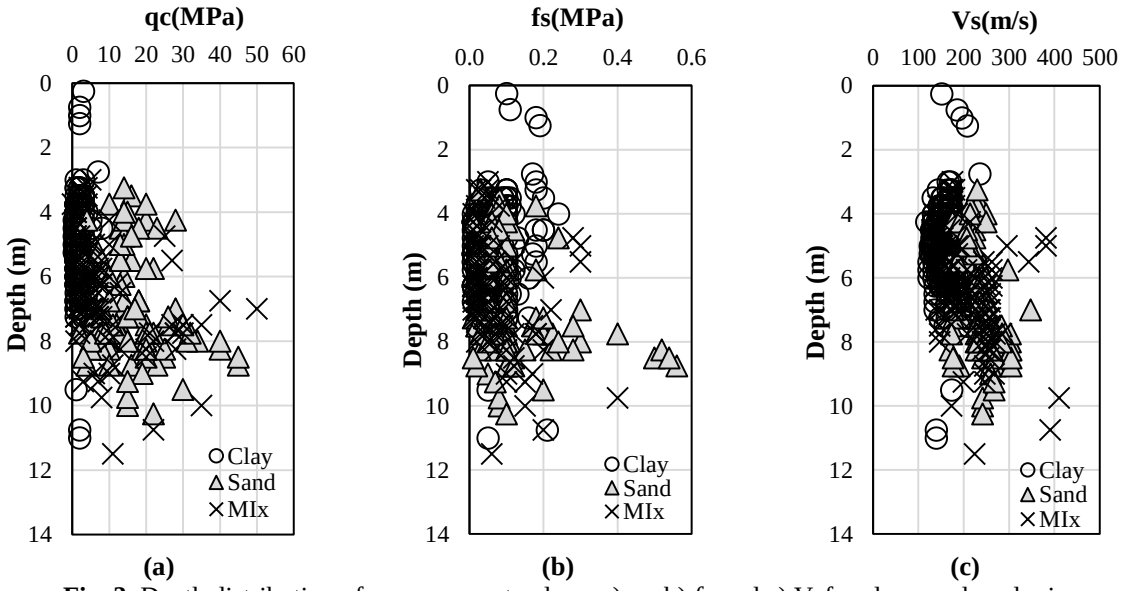

Fig. 3. Depth distribution of measurement values: a) q_c; b) f_s; and c) V_s for clay, sand, and mix

Table 2. A series of CPT and V_s case records in this study

Soil type	q_c (MPa)	f_s (MPa)	V_s
Clay	1.00	0.02	137.40
	2.00	0.10	167.30
Sand	1.00	0.03	185.80
	26.00	0.20	279.40
	16.00	0.10	233.70
	20.00	0.05	250.50
	40.00	0.10	185.80
Mix	1.000	0.010	153.60
	2.000	0.030	172.00

4. Modeling Using Robust Optimization Method

Six correlation models are considered to investigate how parameter uncertainty affects the prediction of V_s. These models are similar to the great majority of those listed in Table 1, in the sense that the V_s is assumed to be independent of any soil parameter, except q_c and f_s. The six equations of the models are as follows:

$$V_S = a_1 + a_2 q_c \quad (25)$$

$$V_S = a_1 + a_2\, ln(\, q_c) \quad (26)$$

$$V_S = a_1 + a_2\, log(\, f_s) \quad (27)$$

$$V_S = a_1 (q_c)^{a_2} \quad (28)$$

$$V_S = a_1 (q_c)^{a_2} {f_s}^{a_2} \quad (29)$$

$$V_S = a_1 + a_2 q_c + a_3 f_s + a_4 {q_c}^2 + a_5 {f_s}^2 + a_6 (q_c f_s) \quad (30)$$

To evaluate the model's performance in this study, several performance indices, including the absolute fraction of variance (R^2) as defined in Eq. (31); the Root Mean Square Error (RMSE) as determined by Eq. (32); the Mean Absolute Percentage Error (MAPE) as calculated using Eq. (33); and the Mean Absolute Deviation (MAD) as given by Eq. (34), were calculated as follows:

$$R^2 = 1 - \left[\frac{\sum_{i=0}^{M} (\, Y(i)_c - Y(i)_o)^2}{\sum_{i=1}^{M} (\, Y(i)_o)^2}\right] \quad (31)$$

$$RMSE = \sqrt{\frac{1}{M}\sum_{1}^{M} (Y(i)_o - \, Y(i)_c)^2} \quad (32)$$

$$MAPE = \frac{\sum_{1}^{M} |Y(i)_o - \, Y(i)_c|}{\sum_{1}^{M} C_{mi}} \times 100 \quad (33)$$

$$MAD = \frac{\sum_{1}^{M} |Y(i)_o - \, Y(i)_c|}{M} \quad (34)$$

where, M: is the number of data, and Yc and Yo: are calculated and observed values, respectively. The optimal model performance will be achieved by lower

RMSE, MAPE, and MAD values. The limitation of R^2 is between 0 to 1 and increasing R^2 leads to higher model accuracy.

5. Results

The linear regression results for the models are presented below. As shown in Table 3, Models 6 and 4 have good accuracy, but based on other statistical parameters, Model 6 is slightly more accurate than Model 4. One of the topics discussed in this study is investigating the effects of uncertainty, and an important question is whether Models 4 and 6 (which have sufficient accuracy) have the same accuracy when the data is uncertain. In the following, the question was answered by examining the uncertainty.

The variation of the coefficient (R^2) is evaluated using the uncertainties of the four soil types. The results are summarized in Figures 4 and 5. Figure 4 shows that as the uncertainty increases, the variability decreases and approaches a stable value. It is important to note here that if the uncertainty is set to zero (for example, Figure 4f of this study), this method reduces to an ordinary least squares multiple regression technique with the same coefficients (Table 2).

Table 3. The regression results for the models

	Soil type	a1	a2	a3	a4	a5	a6	R^2	RMSE	MAPE	MAD
Model 1	Clay	5.59	150.13	-	-	-	-	0.9687	22.70	9.875	17.7
	Sand	4.59	209.28	-	-	-	-	0.8235	37.65	12.67	28.4
	Mixed	3.82	200.05	-	-	-	-	0.8580	34.10	12.01	25.9
	All	5.84	171.05	-	-	-	-	0.8550	34.41	12.07	26.1
Model 2	Clay	153.44	15.38	-	-	-	-	0.9695	22.62	9.86	17.7
	Sand	118.44	63.28	-	-	-	-	0.8208	37.92	12.72	28.6
	Mixed	167.72	44.12	-	-	-	-	0.8804	31.79	11.57	24.2
	All	148.77	50.25	-	-	-	-	0.8656	33.32	11.86	25.3
Model 3	Clay	175.66	11.42	-	-	-	-	0.9676	22.82	9.898	17.8
	Sand	381.57	89.93	-	-	-	-	0.8179	38.23	12.78	28.8
	Mixed	407.92	135.09	-	-	-	-	0.8875	31.06	11.44	23.7
	All	339.56	98.86	-	-	-	-	0.8313	36.85	12.52	27.8
Model 4	Clay	152.80	0.48	-	-	-	-	0.9988	19.61	9.297	15.5
	Sand	237.63	0.84	-	-	-	-	0.9958	19.92	9.355	15.7
	Mixed	175.10	2.52	-	-	-	-	0.9965	19.84	9.34	15.7
	All	171.33	1.71	-	-	-	-	0.9958	19.91	9.354	15.7
Model 5	Clay	151.60	0.09	0.00	-	-	-	0.9701	22.56	9.85	17.6
	Sand	227.67	0.13	0.08	-	-	-	0.8266	37.33	12.61	28.2
	Mixed	266.12	0.13	0.13	-	-	-	0.9151	28.22	10.91	21.7
	All	172.75	0.19	0.04	-	-	-	0.8742	32.43	11.69	24.7
Model 6	Clay	139.59	16.86	-77.19	-2.29	42.38	36.68	0.9988	19.60	9.296	15.5
	Sand	168.71	6.31	423.58	-0.06	-661.30	-0.98	0.9960	19.89	9.35	15.7
	Mixed	126.81	11.41	989.63	-0.32	-1237.26	2.90	0.9971	19.78	9.329	15.7
	All	132.99	12.96	284.00	-0.30	-399.72	7.47	0.9971	19.77	9.328	15.6

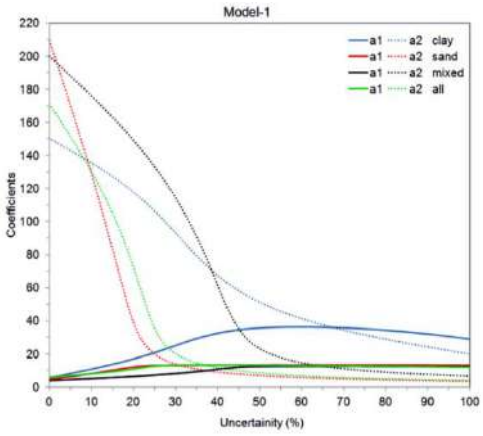

(a)

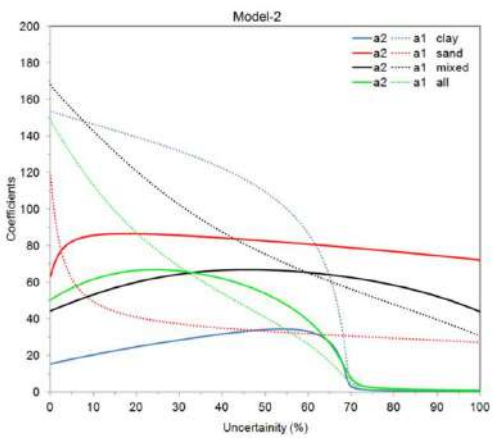

(b)

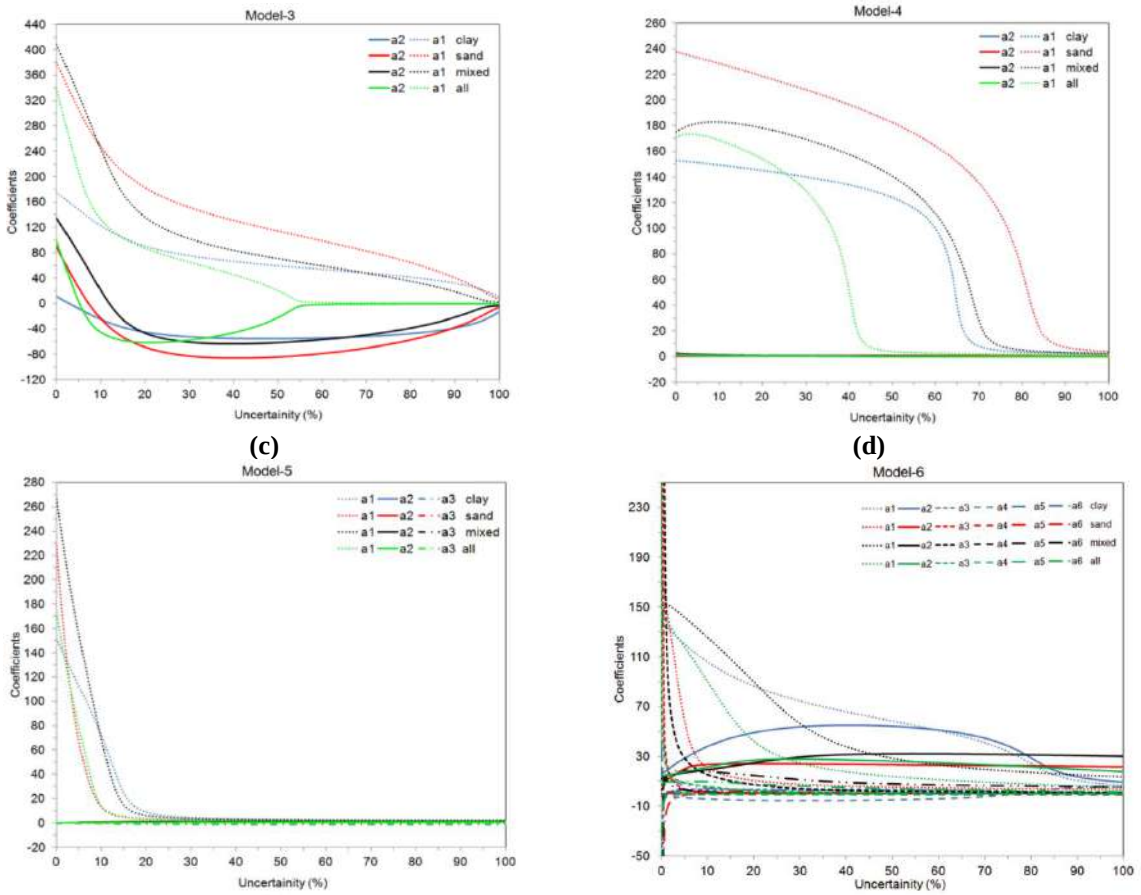

Fig. 4. Variations of coefficients versus uncertainties for different models and different soil types: a) Model-1 (Eq. (25)); b) Model-2 (Eq. (26)); c) Model-3 (Eq. (27)); d) Model-4 (Eq. (28));, e) Model-5 (Eq. (29)); and f) Model-6 (Eq. (30))

Figure 4 constitutes the sensitivity analysis of each coefficient of the variables related to the uncertainty level. In other words, it was proved that these respective variables had greater sensitivity for the coefficients with greater variations. Figure 5 shows the variation of R^2 versus uncertainties for each model of interest. As shown in Figure 5, the best-matched correlation amongst the others was in the form of Eq. (28) (Figure 5d when uncertainty is zero). However, the least error in the estimation of V_s was obtained by the polynomial models. As illustrated in Figure 5, the models mentioned above can make fairly accurate predictions when uncertainties are not taken into account, but they are not as reliable when dealing with high levels of uncertainty. In each sub-set, the proposed method achieved more accurate predictions assuming uncertainty.

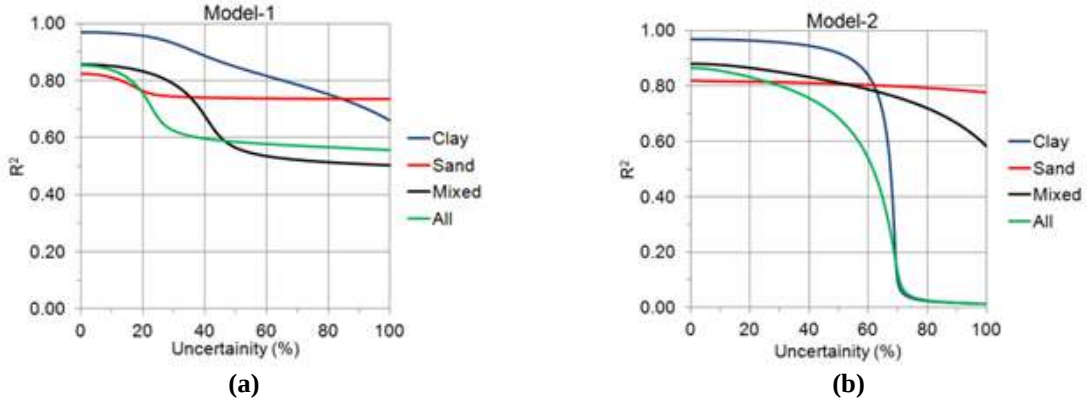

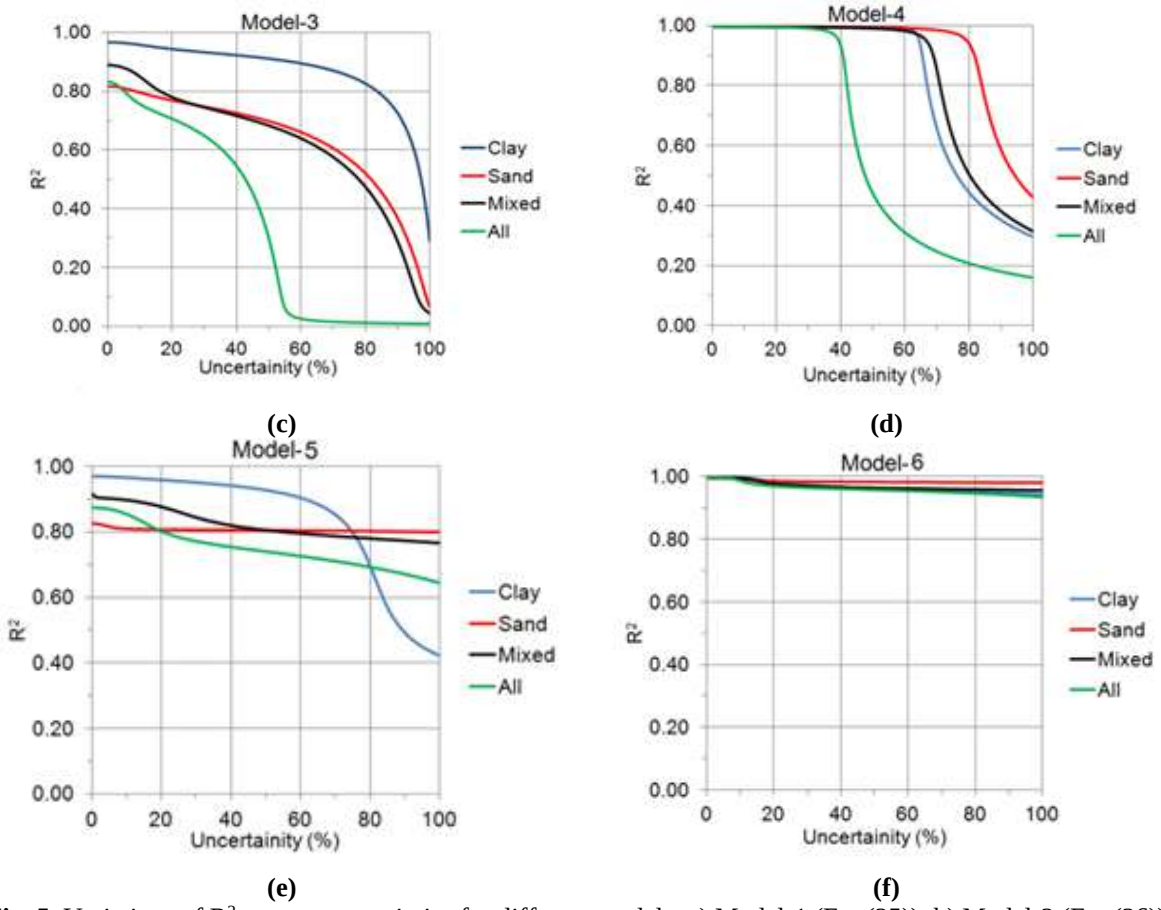

Fig. 5. Variations of R^2 versus uncertainties for different models: a) Model-1 (Eq. (25)); b) Model-2 (Eq. (26)); c) Model-3 (Eq. (27)); d) Model-4 (Eq. (28)); e) Model-5 (Eq. (29)); and f) Model-6 (Eq. (30))

As presented in Eq. (30), the polynomial model provided a better fit to the observed data than the others. It can be easily seen that although the uncertainty level was almost 100 %, the value of R^2 was greater than 0.9. For a more detailed explanation of Figures 4 and 5, it should be borne in mind that by using this method and taking data uncertainty into account, model coefficients are obtained, and the search for a logical relationship between the uncertainty and the predicted value reveals this term. In other words, by knowing the measurement accuracy associated with the data and determining the corresponding uncertainty, the corresponding uncertainty coefficient can be determined and the model output value can be predicted from the corresponding graphs. Of course, it is important to mention that all models are converted into linear and matrix models by changing the power with the logarithm.

6. Conclusions

Shear wave velocity is an essential engineering tool required to define the dynamic properties of soils and, preferably, can be determined indirectly by CPT. However, the inaccuracies in measuring or estimating the influencing parameters have consistently been a significant issue. Therefore, different statistical methods have been introduced to mitigate the impact of these inaccuracies on predicting future events by using the robust optimization model.

Six correlation models were considered to investigate the impact of parameter uncertainty on the prediction of V_s. These models were similar to the great majority of those listed in Table 1 in that the V_s was assumed to be independent of any soil parameters, except for q_c and f_s.

Other geotechnical soil properties can be added to obtain a better correlation, such as

relative density, void ratio, porosity, and unit weight. However, this study aimed to present the simplest correlation. The databases were evaluated by dividing them into four different groups, namely, clay, sand, mixed, and all soils. Six empirical correlation models, which different researchers introduced, were evaluated together with the proposed model.

Among the previously proposed equations, the equations suggested in the form of Eq. (28) gave the highest R^2 value. A robust optimization technique was developed to assess the impact of uncertainty of each model parameter, independently of the analysis results. This is an advance compared to limited stochastic approaches that consider parameter variations individually. A new parameter was introduced to represent the level of uncertainty in the data.

Statistical comparison of the models showed that the accuracy of the model based on Eq. (28) was generally close to the polynomial model at very small uncertainty values. However, when data uncertainty is high (especially for the parameters mentioned above), the new polynomial model performs better. All the results obtained in this study showed that such correlations resulting from local records should not directly be used for V_s.

The polynomial proposed relationships could be used for measuring V_s. It is recommend to reanalyze the presented model using data from other regions. It is proposed to adapt the methods of this work to new open model data.

7. References

Alizadeh, F. and Goldfarb, D. (2003). "Second-order cone programming", *Mathematical Programming*, 95(1), 3-51, http://doi.org/10.1007/s10107-002-0339-5.

Anagnostopoulos, A., Koukis, G., Sabatakakis, N. and Tsiambaos, G. (2003). "Empirical correlations of soil parameters based on cone penetration tests for Greek soils", *Geotechnical and Geological Engineering*, 21, 377-387, http://doi.org/10.1023/B:GEGE.0000006064.47819.1a.

Barrow, B.L. and Stokoe, K.E.I.I. (1983). "Field investigation of liquefaction sites in northern California", Geotechnical Engineering Thesis, GT 83-1, Civil Engineering Department, University of Texas at Austin, 212 p.

Bayat, M., Saadat, M. and Hojati, A. (2023). "Optimization of dynamic compaction procedure for sandy soils", *Civil Engineering Infrastructures Journal*, http://doi.org/10.22059/CEIJ.2023.351287.1889.

Ben-Tal, A., El Ghaoui, L. and Nemirovski, A. (2009). *Robust optimization*, Princeton University Press, 28, http://doi.org/10.1515/9781400831050.

Chala, A. and Ray, R. (2023). "Machine learning techniques for soil characterization using cone penetration test data", *Applied Sciences Journal*, 13(14), 8286, http://doi.org/10.3390/app13148286.

Comina, C., Foti, S., Passeri, F. Socco, L.V. (2022). "Time-weighted average shear wave velocity profiles from surface wave tests through a wavelength-depth transformation", *Soil Dynamics and Earthquake Engineering*, 158, http://doi.org/10.1016/j.soildyn.2022.107262.

Eslami, A., Akbarimehr, D., Aflaki, E. and Hajitaheriha, M.M. (2020). "Geotechnical site characterization of the Lake Urmia super-soft sediments using laboratory and CPTu records", *Marine Georesources and Geotechnology*, 38, http://doi.org/10.1080/1064119X.2019.1672121.

Ghose, R. (2004). "Model-based integration of seismic and CPT data to derive soil parameters", *Proceedings of the 10th European Meeting of Environmental and Engineering Geophysics*, B019, http://doi.org/10.3997/2214-4609-pdb.10.B019.

Gilder, C.E., Pokhrel, R.M., De Luca, F. and Vardanega, P.J. (2021). "Insights from CPTu and seismic cone penetration testing in the Kathmandu valley, Nepal", *Frontiers in Built Environment*, 7, 646009, http://doi.org/10.3389/fbuil.2021.646009.

Golub, G.H. and Van Loan, C.F. (2013). *Matrix computations*, 3rd Edition, Baltimore, MD: Johns Hopkins, http://doi.org/10.56021/9781421407944.

Hegazy Y.A. and Mayne, P.W. (1995). "Statistical correlations between vs and cone penetration data for different soil types", *Proceedings of the International Symposium on Cone Penetration Testing (CPT'95)*, Linkoping, Sweden, 4-5 October 1995, *Swedish Geotechnical Society*, 2, 173-178, https://researchgate.net/publication/283361455_Statistical_correlations_between_Vs_and_CPT_data_fordifferentsoiltypes.

Iyisan, R. and Ansal, A. (1993). "Determination of

dynamic soil properties by borehole seismic methods", *2th National Earthquake Engineering Conference*, Proceedings of the Chamber of Civil Engineer's Turkey (in Turkish).

Jakka, R., Desai, A. and Foti, S. (2022). "Guidelines for minimization of uncertainties and estimation of a reliable shear wave velocity profile using masw testing: A state-of-the-art review", *Advances in Earthquake Geotechnics*, 211-253, http://doi.org/10.1007/978-981-19-3330-112.

Kalantary, F., MolaAbasi, H., Salahi, M. and Veiskarami, M. (2013). "Prediction of liquefaction induced lateral displacements using robust optimization model", *Scientia Iranica*, 20(2), 242-250, https://doi.org/10.1016/j.scient.2012.12.025.

Kruiver, P.P., de Lange, G., Kloosterman, F., Korff, M., van Elk, J. and Doornhof, D. (2021). "Rigorous test of the performance of shear-wave velocity correlations derived from CPT soundings: A case study for Groningen, the Netherlands", *Soil Dynamics and Earthquake Engineering*, 140, 106471, http://doi.org/10.1016/j.soildyn.2020.106471.

Madiai, C., Simoni, G. (2004). "Shear wave velocity-penetration resistance correlation for holocene and pleistocene soils of an area in central italy", *Proceedings ISC-2 on Geotechnical and Geophysical Site Characterization*, Viana da Fonseca and Mayne (eds.), Mill Press, Rotterdam, 1687-1694, https://doi.org/10.1400/107037.

Mayne, P.W. and Rix, G.J. (1995). "Correlations between shear wave velocity and cone tip resistance in natural clays", *Soils and Foundations*, 35(2), 107-110, https://doi.org/10.3208/sandf1972.35.2107.

Mayne, P.W. (2006). "Undisturbed sand strength from seismic cone tests", *Geomechanics and Geoengineering*, London, 1(4), 239-257, https://doi.org/10.1080/17486020601035657.

Mayne, P.W. (2007). *Cone penetration testing, national cooperative highway research programme*, Synthesis 368, Transportation Research Board, USA, 117pp, https://doi.org/10.17226/23143.

McGann, C.R., Bradley, B.A., Taylor, M.L., Wotherspoon, L.M. and Cubrinovski, M. (2015b). "Development of an empirical correlation for predicting shear wave velocity of Christchurch soils from cone penetration test data", *Soil Dynamics and Earthquake Engineering*, 75, 66-75, http://doi.org/10.1016/j.soildyn.2015.03.023.

Meng. F. and Pei, H. (2023). "Quasi-site-specific prediction of shear wave velocity from CPTu", *Soil Dynamics and Earthquake Engineering*, 172, http://doi.org/10.1016/j.soildyn.2023.108005.

Mohammadikish, S., Ashayeri, I. and Biglari, M. et al. (2023). "Soil liquefaction assessment by CPT and vs data and incomplete-fuzzy c-means clustering", *Geotechnical and Geological Engineering*, https://doi.org/10.1007/s10706-023-02669-1.

Mola-Abasi, H., Dikmen, U. and Shooshpasha, I. (2015). "Prediction of shear-wave velocity from CPT data at Eskisehir (Turkey), using a polynomial model", *Near Surface Geophysics*, 13(2), 155-167, http://doi.org/10.3997/1873-0604.2015010.

Paoletti, L., Hegazy, Y., Monaco, S. and Piva, R. (2010). "Prediction of shear wave velocity for offshore sands using CPT data Adriatic Sea", *2nd International Symposium on Cone Penetration Testing*, Huntington Beach, CA, USA, 1-8, https://www.geoengineer.org/storage/publication/18372/publication_file/2611/29Paopos.pdf.

Robertson, P.K. (2009). "Interpretation of cone penetration tests, A unified approach", *Canadian Geotechnical Journal*, 46(11), 1337-1355, http://doi.org/10.1139/T09-065.

Stolte, A. and Cox, B. (2020). "Towards consideration of epistemic uncertainty in shear-wave velocity measurements obtained via seismic cone penetration testing", *Canadian Geotechnical Journal*, 57, http://doi.org/10.1139/cgj-2018-0689.

Sturm, J.F. (1999). "Using Sedumi 1.02. a Matlab toolbox for optimization over symmetric cones", *Optimization Methods and Software*, 11(1-4), 625-653, https://doi.org/10.1080/10556789908805766.

Sturm, J. (2002). "Implementation of interior point methods for mixed semidefinite and second order cone optimization problems", *Optimization Methods and Software*, 17(6), 1105-1154, https://doi.org/10.1080/1055678021000045123.

Sykora, D.W. and Stokoe, K.H. (1983). "Correlations of in situ measurements in sands of shear wave velocity, soil characteristics and site conditions", The University of Texas, Austin, *Geotechnical Engineering Report*, GR83-33.

Tun, M. (2003). "Investigation of the characteristics of Eskisehir soils due to shear wave velocity and determination of their fundamental vibration periods", Master Thesis, Anadolu University Institute of Science and Technology Department of Physics (in Turkish), http://doi.org/10.13140/RG.2.1.4303.8801.

Tun, M., Ayday, C. (2018). "Investigation of correlations between shear wave velocities and cpt data: A case study at Eskisehir in Turkey", *Bulletin of Engineering Geology and the Environment*, 77, 225-236. https://doi.org/10.1007/s10064-016-0987-y.

Wang, J., Hwang, J. and Lu, C. (2022). "Measurement uncertainty of shear wave

velocity: A case study of thirteen alluvium test sites in taipei basin", *Soil Dynamics and Earthquake Engineering*, 155, http://doi.org/10.1016/j.soildyn.2022.107195.

Wang, J.S., Hwang, J.H. and Lu, C.C. (2022). "Empirical formulas for shear wave velocity prediction and their uncertainties: a case study of thirteen alluvium test sites in the Taipei basin", *Bulletin of Engineering Geology and the Environment*, 81, 450, https://doi.org/10.1007/s10064-022-02949-9.

Wang, T., Xiao, S., Zhang, J. and Zuo, B. (2022). "Depth-consistent models for probabilistic liquefaction potential assessment based on shear wave velocity", *Bulletin of Engineering Geology and the Environment*, 81, 255, http://doi.org/10.1007/s10064-022-02754-4.

Yang, H., Liu, Z., Xie, Y. and Li, S. (2023). "A probabilistic liquefaction reliability evaluation system based on catboost-bayesian considering uncertainty using cpt and vs measurements", *Soil Dynamics and Earthquake Engineering*, 173, http://doi.org/10.1016/j.soildyn.2023.108101.

Zhai, S., Du, G. and He, H. (2024). "Bayesian probabilistic characterization of the shear-wave velocity combining the cone penetration test and standard penetration test", *Stochastic Environmental Research and Risk Assessment*, 38(1), 69-84, https://doi.org/10.1007/s00477-023-02566-2.

Zhang, Y., Xie, Y., Zhang, Y., Qiu, J. and Wu, S. (2021). "The adoption of deep neural network to the prediction of soil liquefaction based on shear wave velocity", *Bulletin of Engineering Geology and the Environment*, 80(6), 5053-5060, http://doi.org/10.1007/s10064-021-02250-1

Zhao, Z., Duan, W. and Cai, G. (2021). "A novel pso-kelm based soil liquefaction potential evaluation system using cpt and vs measurements", *Soil Dynamics and Earthquake Engineering*, 150, http://doi.org/10.1016/j.soildyn.2021.106930.

Zhao, Z., Duan, W., Cai, G., Wu, M. and Liu, S. (2022). "CPT-based fully probabilistic seismic liquefaction potential assessment to reduce uncertainty: integrating xgboost algorithm with Bayesian theorem", *Computers and Geotechnics*, 149, http://doi.org/10.1016/j.compgeo.2022.104868.

Zhou, J., Huang, S., Wang, M. and Qiu, Y. (2022). "Performance evaluation of hybrid GA–SVM and GWO–SVM models to predict earthquake-induced liquefaction potential of soil: A multi-dataset investigation", *Engineering with Computers*, 38, 4197-4215, http://doi.org/10.1007/s00366-021-01418-3.

Civil Engineering Infrastructures Journal 2025, 58(1): 173-182
DOI: 10.22059/ceij.2024.364871.1956

RESEARCH PAPER

Prediction of Compressive Strength of Geopolymer Fiber Reinforced Concrete Using Machine Learning

Kumar, P.[1], Sharma, S.[2] and Pratap, B.[3*]

[1] Assistant Professor, Department of Civil Engineering, Mohan Babu University (SVEC), Tirupati, Andhra Pradesh, India.
[2] Ph.D. Candidate, Department of Civil Engineering, National Institute of Technology Jamshedpur, Jharkhand, India.
[3] Assistant Professor, Department of Civil Engineering, Graphic Era (Deemed to be University), Dehradun, Uttarakhand, India.

Received: 11 Sep. 2023; Revised: 2 Jan. 2024; Accepted: 16 Mar. 2024

ABSTRACT: Geopolymers represent a cutting-edge class of inorganic materials that provide a sustainable substitute for conventional cement and concrete. Through meticulous combinations and ratios of elements like Fly Ash (FA), silica fume, Ground Granulated Blast Slag (GGBS), alkaline solutions, aggregates, superplasticizers, and fibers, geopolymer concrete mixes are generated as part of the experimental program. The investigation concentrates on predicting the 28-day compressive strength, a pivotal parameter in assessing concrete performance. The dataset comprises 96 data points, and two advanced techniques, namely Support Vector Regression (SVR) and Artificial Neural Networks (ANN), are harnessed for this research. The ANN demonstrates an R^2 value of 0.992 on the training dataset, indicating its capacity to elucidate around 99.2% of the variability. On the other hand, SVR boasts an R^2 value of 0.995, signifying an ability to account for about 99.5% of the variance. When applied to the testing data, the ANN achieves an R^2 of 0.96, while SVR attains an R^2 of 0.99. This study suggests that SVR exhibits slightly superior performance in elucidating variance within the testing dataset.

Keywords: ANN, Fly Ash, GGBS, Soft Computing.

1. Introduction

Reinforced Concrete (RC) is a global construction material used worldwide, supported by a substantial global cement production, estimated to be approximately 4.6 Gigatons (Gt) in 2015. Despite its widespread use and durability, RC structures can face challenges over time due to various factors, such as environmental exposure, chemical attack, or structural damage caused by external events (Jindal et al., 2023). Interventions are often necessary to maintain the load-carrying capacity and extend the service life of existing RC structures. Over the last few decades, externally bonded composite materials have emerged as an effective solution for rehabilitating and enhancing RC structures.

Among these materials, Fiber-Reinforced Cementitious Matrix (FRCM) composites have gained significant attention as an alternative to traditional Fiber-Reinforced Polymer (FRP)

* Corresponding author E-mail: bheempratapbind009@gmail.com

composites (D'Antino et al., 2014; Tayeh et al., 2021; Wong, 2022). Both FRCMs and FRPs consist of continuous high-strength fibers embedded within a matrix, but they differ in the composition of the matrix material (Wang et al., 2009). Furthermore, FRCMs exhibit excellent compatibility with concrete, which promotes a strong bond between the composite material and the existing structure (Carloni et al., 2015).

Alkali-activated materials are a diverse group of inorganic materials that include a novel category known as geopolymers (Qaidi et al., 2022). These materials not only provide alternatives to traditional cement-based products but also mitigate environmental impacts by reusing industrial byproducts and reducing carbon emissions (Kumar et al., 2023). Polypropylene fibers (Althoey et al., 2023; Tayeh et al., 2022) are commonly utilized to control cracking in concrete, but they may not be ideal for geopolymer composites due to this weak interaction. Steel fibers are a popular choice for reinforcing cementitious composites.

Steel fibers' tensile strength and ultimate elongations can vary significantly, ranging from 310-2850 MPa and 0.5-3.5%, respectively (Al-Majidi et al., 2017; Sukontasukkul et al., 2018; Wang et al., 2018). The corrugated surface enhances the interaction between the steel fibers and the binder, improving the composite material's performance and strength (Wang et al., 2018; Yin et al., 2015). One significant application of recycled synthetic fibers lies in the construction industry, offering an effective solution for disposing of commonly consumed plastics like Polyethylene Terephthalate (PET) and Polypropylene (PP) on a global scale (Siddique et al., 2008). Among the synthetic fibers used in construction PP, Polyvinyl Alcohol (PVA), Polyethylene (PE), and PET are the most prevalent ones (Farooq et al., 2019; Mastali et al., 2018; Ranjbar et al., 2016; Sukontasukkul et al., 2018). PP, derived from the monomeric C_3H_6, is a cost-effective option with inert characteristics in high PH cementitious environments (Farooq et al., 2019). It helps control plastic shrinkage cracking in concrete and allows for easy dispersion (Larena and Pinto 1993). It has drawbacks such as poor thermal resistance, low modulus of elasticity, and difficulty in forming a strong bond with cementitious matrices due to its inherent hydrophobic nature (Banthia and Gupta 2006; Mu et al., 2002; Yin et al., 2015). On the other hand, PET fibers, produced by recycling PET bottles, exhibit mechanical properties comparable to PP and nylon fibers while being more cost-effective and environmentally friendly to produce (Ochi et al., 2007).

Soft Computing (SC) is an effective approach for addressing complex problems, particularly when mathematical models struggle to express relationships among parameters. SC offers a notable advantage in solving nonlinear and linear problems by accommodating intricate relationships that may be challenging to model mathematically (Ghanbari et al., 2017). A key strength of SC lies in its ability to incorporate human-based knowledge, recognition, understanding, and learning into computational processes (Vadel et al., 2019). In recent years, researchers have increasingly harnessed Artificial Intelligence (AI) methods and Machine Learning (ML) techniques as integral components of SC in predicting various properties of concrete. AI and ML, as sub-branches of SC, bring advanced computational capabilities to the forefront (Shariati et al., 2022). However, accurately predicting the compressive strength of Geopolymer Concrete (GPC) poses challenges due to the significant influence of physical and chemical variables.

Fortunately, AI and ML have emerged as promising solutions to enhance accuracy and efficiency in predicting concrete strength (Naghibzadeh et al., 2022). While traditional regression methods lacked accuracy, ML methodologies have significantly improved predictions, the advanced techniques such as Genetic Engineering Programming (GEP), SVR,

ANN, and ensemble approaches (Sahu et al., 2023). SVR constructs hyperplanes that best separate data points based on their features, enabling it to make precise predictions (Li et al., 2022; Shariati et al., 2022). Its ability to handle high-dimensional data and capture nonlinear relationships has made SVR a popular choice in concrete strength estimation.

Inspired by the human brain's functioning, ANN is a deep learning technique capable of learning and generalizing from large datasets (Kaveh and Khavaninzadeh, 2023). As ANN layers process and transform input data, the model comprehensively understands the relationships between variables, leading to highly accurate predictions. Ensemble approaches combine multiple models to improve predictive accuracy by leveraging the strengths of individual algorithms (Huang et al., 2023).

The primary aim of the current research is to create models that can predict experimental data by utilizing two specific techniques: SVR and ANN. The focus of this study is centered around geopolymer concrete, a unique type of concrete made from components such as FA, silica fume, GGBS, as well as Polyvinyl Alcohol Fiber (PVA) and steel fiber. To evaluate the effectiveness of the prediction models (SVR and ANN), the parameter chosen for analysis is the compressive strength of the geopolymer concrete after a curing period of 28 days.

This 28-day compressive strength is a critical indicator of the concrete's performance and durability. By using the SVR and ANN models, the study aims to establish accurate predictions of this compressive strength based on the specific combinations of materials used in the geopolymer concrete.

2. Materials and Data Demonstrations

The experiment involves the development of a novel type of concrete called geopolymer hybrid fiber-reinforced concrete. This concrete is designed to have enhanced strength and durability by combining various materials and fibers. The main components used in this experiment are FA, Silica fume, GGBS, alkaline solutions, fine and coarse aggregates, superplasticizers, and a hybrid combination of steel fiber and PVA fiber. Concrete relies on binding agents to ensure that its components are properly linked together.

In addition to binding materials, concrete also contains fine and coarse aggregates like sand and gravel. The experimental program involves creating different concrete mixes by varying the proportions of these materials. The specific combinations and ratios of FA, Silica fume, GGBS, alkaline solutions, aggregates, superplasticizers, and hybrid fibers are detailed in Table 1 of the experiment. This mix design is a roadmap for producing batches of geopolymer hybrid fiber-reinforced concrete with consistent and controlled properties. ML approaches necessitate a diverse set of input variables (Wang et al., 2018). These input variables and the corresponding outputs are derived from an experimental program.

Table 1. Mix design of the experimental program

Mix designations	P0S1	P0S2	P0S3	P1S4	P1S0	P2S0	P3S0	P4S0
FA	585	585	585	585	585	585	585	585
Silica fume	32.5	32.5	32.5	32.5	32.5	32.5	32.5	32.5
GGBS	32.5	32.5	32.5	32.5	32.5	32.5	32.5	32.5
Na_2SiO_3	156	156	156	156	156	156	156	156
NaOH	104	104	104	104	104	104	104	104
Fine aggregate	850	850	850	850	850	850	850	850
Coarse aggregate	800	800	800	800	800	800	800	800
Super plasticizer	10	10	10	10	10	10	10	10
Polyvinyl alcohol fiber	0	0	0	0	0.10%	0.20%	0.30%	0.40%
Steel fiber	0.10%	0.20%	0.30%	0.40%	0	0	0	0

*P1S0: is Polyvinyl alcohol fiber 0.1% and Steel fiber 0%.

This specific study focuses primarily on predicting the 28-day compressive strength, a critical parameter for evaluating concrete performance. The models employed for this purpose involve a selection of input variables, and their correlation with the 28-day compressive strength is investigated.

The chosen input variables encompass a variety of factors that contribute to the properties of the concrete mixture. These variables include cement, water, sand, coarse aggregate, superplasticizer, silica fume, FA, alkali/binder ratio, steel fiber, and PVA fiber. Each of these variables plays a distinct role in shaping the characteristics of the final concrete product.

The dataset used in this study comprises 96 data points, each representing a specific combination of input variables and the corresponding 28-day compressive strength. These data points serve as the basis for training and testing the ML models. Table 2 presents a comprehensive summary of the statistical analysis conducted on the input variables. The statistics presented in the table include the mean, standard deviation, minimum value, and maximum value for each input variable. These statistics collectively offer a thorough understanding of the variability and central tendencies within the input dataset.

3. Methodology

In this study, ML models were employed to estimate the compressive strength of a material, and these models were implemented using Python code through the Anaconda software platform. Anaconda Navigator is a hub for accessing Python and other programming languages crucial for data science and machine learning applications. It emphasizes activities like package development and maintenance to support these tasks effectively. The study employed three distinct techniques, namely ANN and SVR, to predict the compressive strength of a material. These techniques are widely used in ML for regression tasks, where the goal is to predict a continuous numerical output.

To assess the accuracy of the predictions generated by these models, the R^2 was utilized. The R^2 value is a metric that ranges from 0 to 1, with higher values indicating better alignment between the predicted outcomes and the actual measured values. Furthermore, the study conducted rigorous evaluations to gauge the models' performance. This involved statistical checks and error assessments, including Mean Absolute Error (MAE) and Root Mean Squared Error (RMSE). These metrics offer insights into how well the models' predictions align with the actual data by measuring the average magnitude of errors. A lower MAE and RMSE indicate better predictive accuracy and a smaller deviation between predicted and actual values. The data set is generated from the experimental programs. The process involved organizing a dataset into two subsets: a training set and a test set.

Table 2. Statistical description of input variables

	Total	**Mean**	**SD**	**Min.**	**25%**	**50%**	**75%**	**Max.**
FA	96	552.5	26.67	520	520	552.50	585	585
GGBS	96	48.75	13.34	32.5	32.5	48.75	65	65
Silica fume	96	48.75	13.34	32.50	32.50	48.75	65	65
NaOH	96	110.6	14.61	91	100.50	110.50	120.3	130
Na_2SiO_3	96	165.75	21.92	136.50	151.13	165.75	180.4	195
Coarse aggregate	96	850	0	850	850	850	850	850
Fine aggregate	96	800	0	800	800	800	800	800
alk/b	96	0.425	0.056	0.35	0.3875	0.425	0.46	0.50
Superplasticizer	96	10	0	10	10	10	10	10
Polyvinyl alcohol fiber	96	0.125	0.14	0	0	0.05	0.2	0.40
Steel fiber	96	0.125	0.14	0	0	0.05	0.2	0.40
Compressive strength	96	38.81	8.56	21.56	32.26	38.46	44.25	58.8

In the 70-30 data split, a dataset is partitioned into two subsets: 70% is allocated for training a model, and the remaining 30% is reserved for testing the model's performance. Each example in these sets was broken down into individual instances of input features, also known as independent variables, which were associated with a specific target or dependent variable to be predicted. The input features utilized in this analysis were chosen to represent quantifiable aspects that experiments could measure. These features were carefully defined and structured to provide an advantageous learning environment for the various models being evaluated (Figure 1). This structured setup ensured that the models could learn effectively from the data.

The ANN underwent a process of manual fine-tuning to achieve a reasonable level of accuracy in predicting the target variable. This fine-tuning process involved adjusting the model's internal parameters and architecture to minimize prediction errors and enhance performance. Subsequently, the hyper parameters of the ANN were determined based on the outcomes of this initial manual fine-tuning (Pratap et al., 2023). Hyper parameters are settings external to the model but influence its learning process. SVR aims to find the optimal function that best captures the underlying patterns in the data while maintaining a certain margin of error. The fundamental idea is to identify a hyperplane that effectively fits as many data points as possible within a specific epsilon (ε) tube, where the goal is to minimize the deviation of data points from the predicted values while allowing for a controlled tolerance.

SVR employs a mathematical approach to determine the optimal hyperplane by solving a constrained optimization problem. One of the strengths of SVR is its ability to handle non-linear relationships between variables by utilizing kernel functions. These functions transform the original feature space into a higher-dimensional space, enabling the algorithm to capture complex patterns that might not be apparent in the original data.

4. Results and Discussions

The study evaluates the predictive accuracy of the ANN model by comparing its predicted outcomes to the actual measured compressive strengths. The analysis involves two main aspects: the statistical comparison pattern and the model's performance metrics.

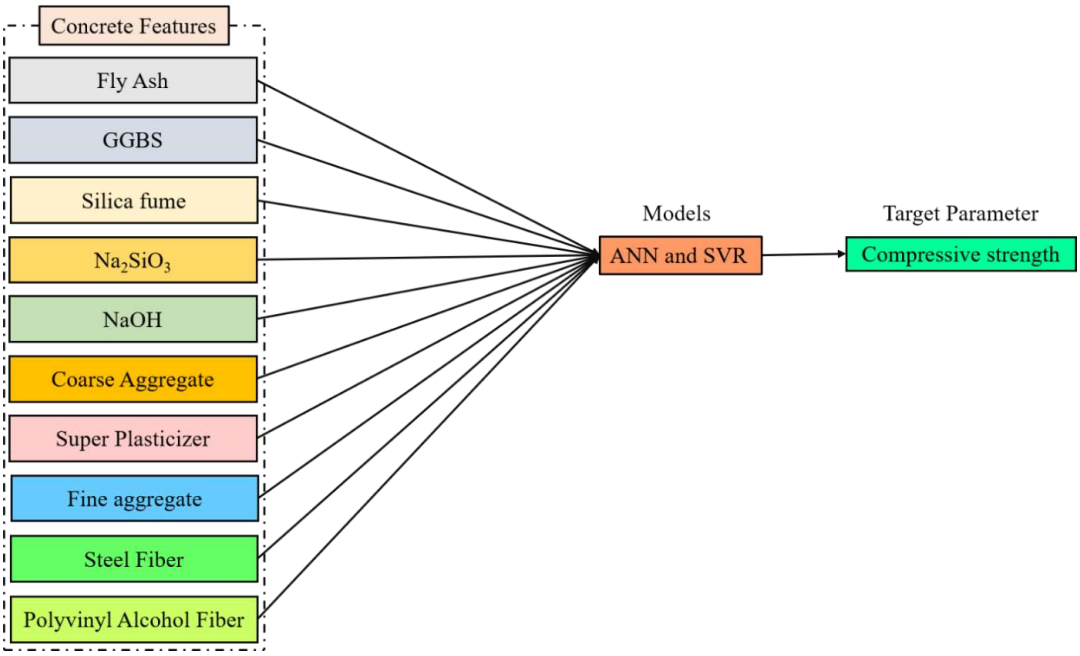

Fig. 1. An input and output roadmap for the ANN and SVR algorithms

In terms of statistical analysis, the study assesses the pattern of outcomes obtained from the actual testing of geopolymer concrete samples and the predictions made by the ANN and SVR models. The R^2 value serves as an indicator of how well the model's predictions match the actual data. In this case, the R^2 value of 0.9924 for training and 0.9672 for testing signifies an excellent performance of the ANN model in accurately calculating the compressive strength outcomes. Figures 2a and 3a visually represent these high R^2 values, highlighting the closeness of the model's predictions to the real data points. On the other hand, Figures 2b and 3b provide a graphical depiction of the distribution of the investigated outcomes compared to the estimated outcomes by the ANN model. These figures allow for a direct comparison, revealing the model's efficacy in capturing the trend of the actual outcomes.

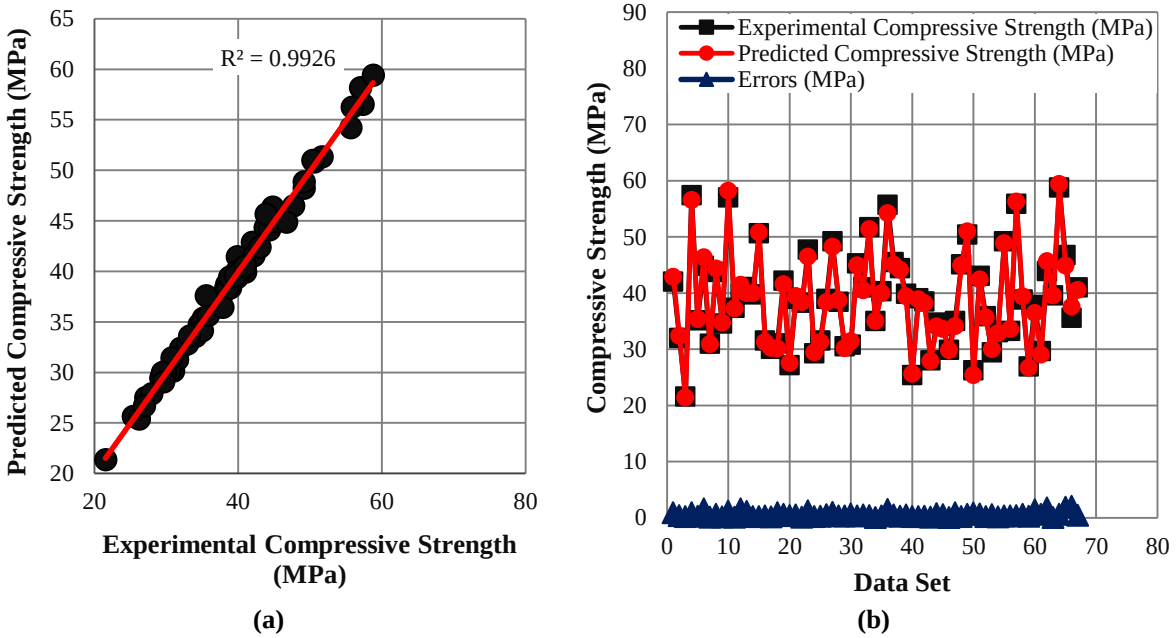

Fig. 2. a) Relation between experimental and predicted values for training model of ANN; and b) Distribution of experimental, predicted and error values for training model of ANN

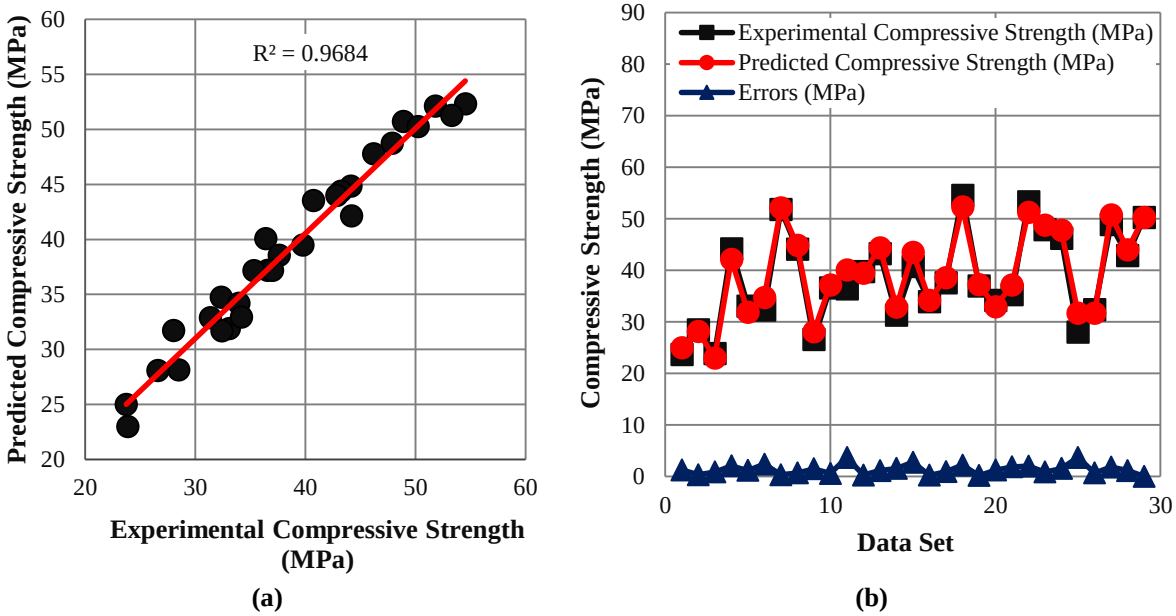

Fig. 3. a) Relation between experimental and predicted values for a testing model of ANN; and b) Distribution of experimental, predicted and error values for a testing model of ANN

The study also addresses the errors associated with the ANN model's predictions. This study analyzes the spread of errors in terms of the largest, lowest, and average error values. For the training phase, the largest error is 2.003 MPa, the lowest error is 0.0314 MPa, and the average error is 0.5646 MPa. Similarly, for the testing phase, the largest error is 3.69 MPa, the lowest error is 0.028 MPa, and the average error is 1.356 MPa. The SVR model demonstrates exceptional performance in accurately predicting compressive strength outcomes, as evidenced by high R^2 values of 0.9985 (Figure 4a) for training and 0.9908 (Figure 5a) for testing. These values highlight the strong alignment between the model's predictions and actual data points. This closeness between predicted and real values is visually represented in Figures 4.

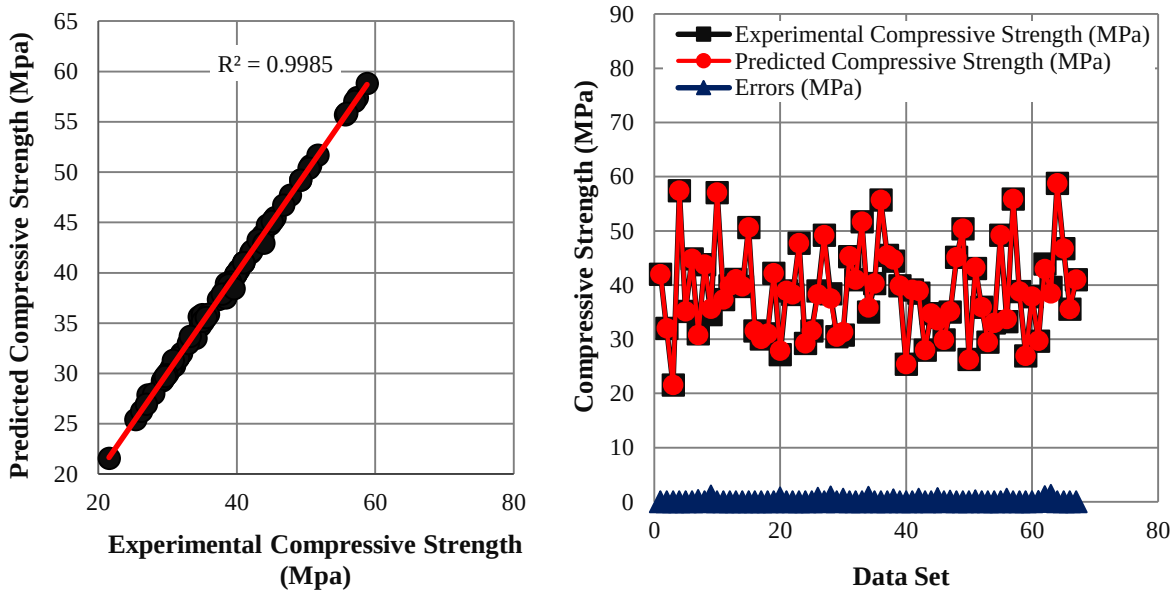

Fig. 4. a) Relation between experimental and predicted values for training model of SVR; and b) Distribution of experimental, predicted and error values for training model of SVR

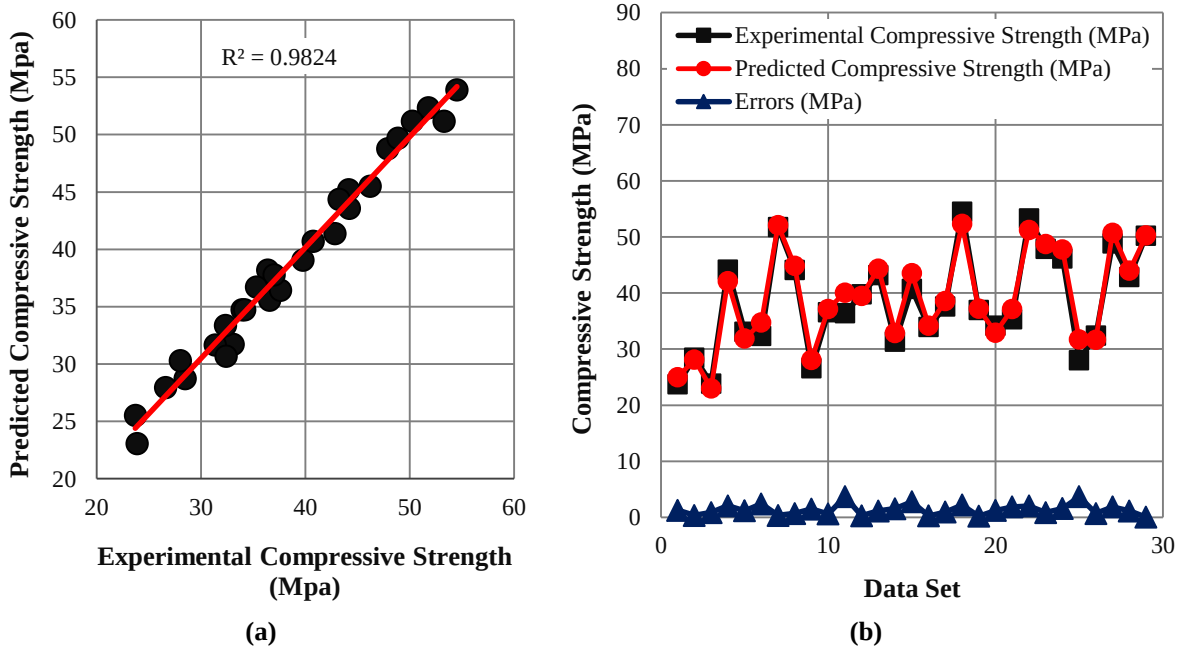

Fig. 5. a) Relation between experimental and predicted values for the testing model of SVR; and b) Distribution of experimental, predicted and error values for a testing model of SVR

Conversely, Figures 4b and 5b visually illustrate how the SVR model's estimated outcomes compare to the investigated outcomes. This direct comparison underscores the model's ability to capture the underlying trends in the actual data (Li et al., 2022). The study also delves into the errors associated with the SVR model's predictions, examining their distribution (Sahu et al., 2023). The analysis of error distribution entails the consideration of the largest, smallest, and average error values.

During the training phase, the most significant error observed is 1.164 MPa, while the smallest error is 0.00053 MPa, and the average error is 0.1389 MPa. Similarly, in the testing phase, the largest error amounts to 2.287 MPa, the smallest error is 0.152 MPa, and the average error is 1.0366 MPa. Table 3 presents the performance metrics of two different machine learning algorithms, ANN and SVR, on a dataset. These metrics are commonly used to evaluate the quality of predictive models. This column simply lists the two machine learning algorithms being compared, which are ANN and SVR. These are different techniques used for regression tasks, where the goal is to predict a continuous numerical output. The ANN has an R^2 of 0.992 on the training set, indicating it explains about 99.2% of the variance, and SVR has an R^2 of 0.995, indicating it explains about 99.5% of the variance. Both values are very high, suggesting strong performance on the training data. ANN has an RMSE of 0.73, while SVR has an RMSE of 0.32. Lower RMSE values indicate better model accuracy, so SVR is performing better on the training data in this regard.

ANN has an MAE of 0.56, and SVR has an MAE of 0.13. Again, lower MAE values indicate better accuracy, and SVR has a lower MAE, suggesting better performance on the training data. ANN has an R^2 of 0.96 on the testing data, while SVR has an R^2 of 0.99, indicating that SVR performs slightly better in terms of explaining variance in the testing data. ANN has an RMSE of 1.65, and SVR has an RMSE of 0.81. Again, lower RMSE values are better, so SVR outperforms ANN on the testing data. ANN has a MAE of 1.35, while SVR has a MAE of 0.53. Like RMSE, lower MAE values indicate better accuracy, and SVR is more accurate on the testing data.

5. Conclusions

This research successfully demonstrated the development of geopolymer concrete through a combination of fibers, FA, and GGBS as precursor materials. Elaborate prediction studies were conducted involving partial replacement of FA with GGBS and silica fume. The conclusions drawn from the results and interpretations can be summarized as follows:

- The performance of the prediction models is assessed using the coefficient of determination (R^2). The ANN achieves an R^2 of 0.992 on the training set, explaining approximately 99.2% of the variance, while the SVR obtains an R^2 of 0.995, explaining about 99.5% of the variance. On the testing data, the ANN's R^2 is 0.96, whereas the SVR's R^2 is 0.99. This indicates that SVR slightly outperforms ANN in terms of explaining variance in the testing data.
- The analysis of error distribution involves assessing the largest, smallest, and average error values. During the training phase, the most significant error observed is 1.164 MPa, while the smallest error is 0.00053 MPa, and the average error is 0.1389 MPa. Similarly, in the testing phase, the largest error amounts to 2.287 MPa, the smallest error is 0.152 MPa, and the average error is 1.0366 MPa.

Table 3. Training and testing results data

Algorithms	Training			Testing		
	R^2	RMSE	MAE	R^2	RMSE	MAE
ANN	0.992	0.73	0.56	0.96	1.65	1.35
SVR	0.995	0.32	0.13	0.99	0.81	0.53

- Overall, both models demonstrate strong performance on the training data, with SVR having a slight advantage in terms of RMSE and MAE. However, when applied to unseen testing data, SVR maintains its superior performance in terms of RMSE, MAE, and R-squared, suggesting that SVR is the more suitable model for this specific dataset. The importance of evaluating a model's performance on both training and testing data is highlighted by the results presented in this table.

6. References

Al-Majidi, M.H., Lampropoulos, A. and Cundy, A.B. (2017). "Steel fibre reinforced geopolymer concrete with improved microstructure and enhanced fibre-matrix interfacial properties", *Construction and Building Materials*, 139, 286-307, https://doi.org/10.1016/j.conbuildmat.2017.02.045.

Althoey, F., Zaid, O., Alsulamy, S., Martínez-García, R., de Prado-Gil, J. and Arbili, M.M. (2023). "Experimental study on the properties of ultra-high-strength geopolymer concrete with polypropylene fibers and nano-silica", *PLoS One*, 18(4), e0282435, https://doi.org/10.1371/journal.pone.0282435.

Banthia, N. and Gupta, R. (2006). "Influence of polypropylene fiber geometry on plastic shrinkage cracking in concrete", *Cement and concrete Research*, 36(7), 1263-1267, https://doi.org/10.1016/j.cemconres.2006.01.010.

Carloni, C., Antino T.D., Sneed, L.H. and Pellegrino, C. (2015). "Role of the matrix layers in the stress-transfer mechanism of frcm composites bonded to a concrete substrate", *Journal of Engineering Mechanics*, 141(6), https://doi.org/10.1061/(ASCE)EM.1943-7889.0000883.

D'Antino, T., Carloni, C., Sneed, L.H. and Pellegrino, C. (2014). "Matrix-fiber bond behavior in pbo frcm composites: a fracture mechanics approach", *Engineering Fracture Mechanics*, 117, 94-111, https://doi.org/10.1016/j.engfracmech.2014.01.011.

Farooq, M., Bhutta, A. and Banthia, N. (2019). "Tensile performance of eco-friendly ductile geopolymer composites incorporating different micro-fibers", *Cement and Concrete Composites*, 103, 183-192, https://doi.org/10.1016/j.cemconcomp.2019.05.004.

Ghanbari, M., Hadian, A.M., Nourbakhsh, A.A. and Mackenzie, K.J.D. (2017). "Modelling and optimization of compressive strength and bulk density of metakaolin-based geopolymer using central composite design: A numerical and experimental study", *Ceramics International*, 43(1), 324-335, Elsevier, https://doi.org/10.1016/j.ceramint.2016.09.159.

Huang, Y., Huo, Z., Ma, G., Zhang, L., Wang, F. and Zhang, J. (2023). "Multi-objective optimization of fly ash-slag based geopolymer considering strength, cost and co2 emission: A new framework based on tree-based ensemble models and nsga-II", *Journal of Building Engineering*, 68, 106070, Elsevier Ltd, https://doi.org/10.1016/j.jobe.2023.106070.

Kaveh, A. and Khavaninzadeh, N. (2023). "Efficient training of two Ann's using four meta-heuristic algorithms for predicting the FRP strength", *Structures*, 52, 256-272, https://doi.org/10.1016/j.istruc.2023.03.178.

Kumar, P., Pratap, B., Sharma, S. and Kumar, I. (2023). "Compressive strength prediction of fly ash and blast furnace slag-based geopolymer concrete using convolutional neural network", *Asian Journal of Civil Engineering*, https://doi.org/10.1007/s42107-023-00861-5.

Jindal, A., RN, G., Kumar, P., Kumar, V. and Rana, D. (2023). "Rehabilitation prospects of concrete pavements with self-compacting concrete containing wollastonite micro fibre", *Civil Engineering Infrastructures Journal*, 56(2), 221-233, https://doi.org/10.22059/ceij.2023.341456.1828.

Larena, A. and Pinto, G. (1993). "The effect of surface roughness and crystallinity on the light scattering of polyethylene tubular blown films", *Polymer Engineering and Science*, 33(12), 742-747, https://doi.org/10.1002/pen.760331204.

Li, Y., J., Shen, Lin, H., Li, H., Lv, J., Feng, S. and Ci, J. (2022). "The data-driven research on bond strength between fly ash-based geopolymer concrete and reinforcing bars", *Construction and Building Materials*, 357, (100), 129384, https://doi.org/10.1016/j.conbuildmat.2022.129384.

Mastali, M., Dalvand, A., Sattarifard, A.R., Abdollahnejad, Z. and Illikainen, M. (2018). "Characterization and optimization of hardened properties of self-consolidating concrete incorporating recycled steel, industrial steel, polypropylene and hybrid fibers", *Composites Part B: Engineering*, 151, 186-200, https://doi.org/10.1016/j.compositesb.2018.06.021.

Mu, B., Meyer, C. and Shimanovich, S. (2002). "Improving the interface bond between fiber mesh and cementitious matrix", *Cement and Concrete Research*, 32(5), 783-787,

https://doi.org/10.1016/S0008-8846(02)00715-9.

Naghibzadeh, H., Saadat, M., Basirat, S. and Iranpour Mobarakeh, M. (2022). "Performance improved multi-objective optimization in applying low-impact development strategies to control urban runoff", *Civil Engineering Infrastructures Journal*, 56(2), 257-276, https://ceij.ut.ac.ir/article88680.html.

Ochi, T., Okubo, S. and Fukui, K. (2007). "Development of recycled pet fiber and its application as concrete-reinforcing fiber", *Cement and Concrete Composites*, 29(6), 448-455, https://doi.org/10.1016/j.cemconcomp.2007.02.002.

Pratap, B., Shubham, K., Mondal, S. and Hanumantha, B. (2023). "Exploring the potential of neural network in assessing mechanical properties of geopolymer concrete incorporating fly ash and phosphogypsum in pavement applications", *Asian Journal of Civil Engineering*, 24, 3575-3589, https://doi.org/10.1007/s42107-023-00735-w.

Qaidi, S.M.A., Sulaiman Atrushi, D., Mohammed, A.S., Unis Ahmed, H., Faraj, R.H., Emad, W., Tayeh, B.A. and Mohammed Najm, H. (2022). "Ultra-high-performance geopolymer concrete: A review", *Construction and Building Materials*, 346, 128495, https://doi.org/10.1016/j.conbuildmat.2022.128495.

Ranjbar, N., Mehrali, M., Behnia, A., Javadi Pordsari, A., Mehrali, M., Alengaram, U.J. and Jumaat, M.Z. (2016). "A comprehensive study of the polypropylene fiber reinforced fly ash based geopolymer", *PLoS One*, (W. Batchelor, ed.), 11(1), e0147546, https://doi.org/10.1371/journal.pone.0147546.

Sahu, A., Kumar, S. and Shrivastav, A.K.L., Pratap B. (2023). "Machine learning approach to study the mechanical properties of recycled aggregate concrete using copper slag at elevated temperature", *Asian Journal of Civil Engineering*, 25, 911-921, https://doi.org/10.1007/s42107-023-00821-z.

Shariati, M., Mafipour, M.S., Ghahremani, B., Azarhomayun, F., Ahmadi, M., Trung, N.T. and Shariati, A. (2022). "A novel hybrid extreme learning machine-grey wolf optimizer (elm-gwo) model to predict compressive strength of concrete with partial replacements for cement", *Engineering with Computers*, 38(1), 757-779, https://doi.org/10.1007/s00366-020-01081-0.

Siddique, R., Khatib, J. and Kaur, I. (2008). "Use of recycled plastic in concrete: A review", *Waste management*, 28(10), 1835-1852, https://doi.org/10.1016/j.wasman.2007.09.011.

Sukontasukkul, P., Pongsopha, P., Chindaprasirt, P. and Songpiriyakij, S. (2018). "Flexural performance and toughness of hybrid steel and polypropylene fibre reinforced geopolymer", *Construction and Building Materials*, 161, 37-44, https://doi.org/10.1016/j.conbuildmat.2017.11.122.

Tayeh, B.A., Akeed, M.H., Qaidi, S. and Bakar, B.H.A. (2022). "Influence of microsilica and polypropylene fibers on the fresh and mechanical properties of ultra-high performance geopolymer concrete (uhp-gpc)", *Case Studies in Construction Materials*, 17, e01367, https://doi.org/10.1016/j.cscm.2022.e01367.

Tayeh, B.A., Zeyad, A.M., Agwa, I.S. and Amin, M. (2021). "Effect of elevated temperatures on mechanical properties of lightweight geopolymer concrete", *Case Studies in Construction Materials*, 15, https://doi.org/10.1016/j.cscm.2021.e00673.

Vadel, M., Khadija, B., Nawal, Z. and Mohamed, S. (2019). "Modelling compressive strength of moroccan fly ash - phosphogypsum geopolymer bricks", *SN Applied Sciences*, 1(12), 1-9, https://doi.org/10.1007/s42452-019-1736-1.

Wang, R., Gao, X., Zhang, J. and Han, G. (2018). "Spatial distribution of steel fibers and air bubbles in uhpc cylinder determined by x-ray ct method", *Construction and Building Materials*, 160, 39-47, https://doi.org/10.1016/j.conbuildmat.2017.11.030.

Wang, X.H., Jacobsen, S., He, J.Y., Zhang, Z.L., Lee, S.F. and Lein, H.L. (2009). "Application of nano indentation testing to study of the interfacial transition zone in steel fiber reinforced mortar", *Cement and Concrete Research*, 39(8), 701-715, https://doi.org/10.1016/j.cemconres.2009.05.002.

Wong, L.S. (2022). "Durability performance of geopolymer concrete: a review", *Polymers*, 14(5), 868, https://doi.org/10.3390/polym14050868.

Yin, J., D'Haese, C. and Nysten, B. (2015). "Surface electrical properties of stainless steel fibres: An afm-based study", *Applied Surface Science*, 330, 65-73, https://doi.org/10.1016/j.apsusc.2014.12.188.

Civil Engineering Infrastructures Journal 2025, 58(1): 183-201
DOI: 10.22059/ceij.2024.368614.1987

RESEARCH PAPER

Behavior of Sheet Pile Wall Adjacent to a Square and Circular Footing

Debnath, A.[1] and Pal, S.K.[2*]

[1] Ph.D. Candidate, Department of Civil Engineering, National Institute of Technology Agartala, Tripura, India.
[2] Professor, Department of Civil Engineering, National Institute of Technology Agartala, Tripura, India.

Received: 25 Nov. 2023; Revised: 16 Mar. 2024; Accepted: 24 Apr. 2024

ABSTRACT: Deep excavations are frequently carried out near structural foundations in densely populated metropolitan areas. Those foundations surrounding the excavation site can impose additional lateral pressure on the retaining wall along with backfill pressure. A three-dimensional finite element analysis has been performed in the present study to determine the effect of square and circular footings of the same plan area on the sheet pile wall behaviour. A parametric study is performed by varying the plan area of footing, embedded depth of sheet pile, magnitude of surcharge loads, position of footing above and below the backfill surface from the top edge of the wall, the depth of the loose soil layer, and dredge line slope angle to find out the wall deflection, bending moment, and backfill ground settlement. The results show that the effect of square and circular footing highly influences the wall and backfill soil. However, the effect of square footing on the wall and backfill soil is more substantial than that of circular footing for the same plan area.

Keywords: Sheet Pile, Finite Element Analysis, Square Footing, Circular Footing, Dredge Line Slope Angle.

1. Introduction

Cantilever Sheet Pile Walls (CSPW) are often recommended for shallow excavation depths (normally less than 5 m) since their stability is primarily dependent on the development of passive resistance below the dredge level (Fall et al., 2019; Singh and Chatterjee, 2020a). The existence of surcharge load in the form of the building foundation, vehicle, and other permanent structures on the backfill soil produces additional stress on the wall, thus triggering higher wall deflection, Bending Moment (BM), and Ground Settlement (GS) (Singh and Chatterjee, 2020b). Several studies have been performed on Sheet Pile Wall (SPW) numerically, experimentally, and analytically for many years. Sowers and Sowers (1967) discussed various cases of failures of anchored bulkhead. They found that anchored SPW failures were governed by excessive lateral Earth Pressures (EPs), lack of attention to deflection, and the influence of construction techniques. In the sand, experiments are carried out to investigate how sloping dredge lines affect the foreslope passive resistance and sheet pile BMs (Schroeder and Roumillac, 1983).

Bose and Som (1998) used the Finite

* Corresponding author E-mail: skpal1963@gmail.com

Element (FE) method to examine the excavation behavior of the diaphragm wall in the Calcutta Metro under the sequential excavation process and strut installation.

Georgiadis and Anagnostopoulos (1998) imolemented an experimental study in the sand with surcharge strip loads. Model test results were compared to BMs calculated using several lateral EP theories and with the results of the FE study by PLAXIS. The computer program FLAC was used to develop a FE model for a braced excavation to estimate the different design parameters that had a significant impact on excavation behavior (Chowdhury et al., 2013). The impacts of the penetration depth were studied to evaluate the diaphragm wall behavior during excavations in sand by the 3D numerical analysis (Bahrami et al., 2018). Ahmadpour et al. (2018) considered a sheet pile supporting excavation system to study the effects of the loose soil layer on deflection and SPWs lateral supporting systems using PLAXIS 2D FE software.

A case study and numerical simulation were conducted on a foundation pit that was supported by U-shaped SPW (Wang et al., 2019). Basha and Elsiragy (2019) conducted a numerical study to examine how SPW driving affects the geotechnical behavior of nearby buildings in the sand. An experimental investigation has been executed to know the SPW behavior nearby to a pre-existing footing (Samadhiya, 2020). Singh and Chatterjee (2020c) investigated the impact of distance between the uniform surcharge and CSPW of varying embedded depths to determine the BM, horizontal EP, deflection, and settlement by FLAC2D. A finite element analysis was performed to investigate the forces in the strut and the estimated earth pressures for braced excavations in anisotropic clay under a plane strain condition (Zhang et al., 2021). Three-dimensional numerical modeling was performed by ABAQUS to evaluate the behavior of a deep excavation supported by a tie-back wall (Tabaroei et al., 2022).

Laboratory tests and numerical analyses were performed by PLAXIS 3D software to determine SPW deformation and bearing capacity of the foundation with vertical loads applied by a model foundation (Ozpolat and Aksoy, 2022). Pradeep et al. (2022) used hybrid ANN with optimization techniques to access the reliability of embedded depth of CSPWs, with cohesive soil below dredge level and cohesion less backfill soil. Li et al. (2022) implemented a numerical analysis of clay soil on the performance of braced excavation, considering the soil's stress-induced anisotropic behavior. A three-dimensional FE study has been performed to identify the effect of strip load as surcharge on the anchored SPW deflection, BM, anchor forces and settlement of the Backfill Ground Surface (BGS) (Debnath and Pal, 2023a). PLAXIS 3D FE software was utilized to analyze the impact of nearby deep excavation on the performance of a loaded individual pile in sandy soil (Hakeem, 2024).

The available literature shows that no attention has been given to the effect of the footing positioned at different depths below the backfill surface on the behavior of sheet pile. No literature exists to analyse the shape effect of footing on the sheet pile behavior. Furthermore, very few articles concentrate on the impact of sloping dredge lines on the behavior of SPW. Hence, a numerical analysis with realistic 3D modelling by ABAQUS FE-based software is performed in this paper to bridge the existing research gap, emphasizing the shape effect of footings (circular and square) positioned at different locations above and below the BGS. A parametric study is also implemented to find the impact of various parameters effecting the deflection, BM, and backfill GS. Then the laboratory experiments are performed to validate the present numerical model.

2. Numerical Modelling

2.1. Soil and Wall Profiles

A three-dimensional FE analysis is used

to model the soil and wall. Dense sand is used for the entire FE analysis and loose sand is employed in layers to replace dense sand from the BGS in order to study the impact of loose soil layers on the SPW behavior. The soil properties are adopted from Singh and Chatterjee (2020 a,c), presented in Table 1. The PZ27 sheet pile is adopted from the USS sheet piling design manual (USS Design Manual, 1984), as selected by Bilgin (2012). The properties of the sheet pile section are presented in Table 2.

The overall wall height is taken as 11.00 m with an excavated depth (H) of 4.50 m and an embedded depth (D) of 6.50 m. The hydrostatic forces balance each other when the water level elevation is equal on either side of the wall (Bilgin, 2012). Hence, in the current study, the elevation of the water table is assumed at 2 m depth on either side of the wall from the wall top edge during the complete analysis. Therefore, the soil is considered to be completely saturated under the water table.

2.2. Finite Element Analysis

ABAQUS FE code is used for the 3D modelling of SPW, footing, and soil. The soil is modelled using the Mohr-Coulomb model with a non-associated flow rule as several researchers have successfully used it to model the cohesion less soils of retaining walls (Hsiung, 2009; Bilgin, 2012; Chowdhury et al., 2013; Bahrami et al., 2018; Ahmadpour et al., 2018; Fall et al., 2019; Guo et al., 2019; Singh and Chatterjee, 2020 a,c; Debnath and Pal, 2023b). The SPW and the footings are modelled as linear elastic materials. The current study chooses the soil-SPW and soil-footing contact to impose the interaction properties. Different options for defining the contact zone are available in ABAQUS, including "node-to-surface" and "surface-to-surface".

The "surface-to-surface" contact is applied due to its accuracy. According to the master-slave concept, the master surface is the harder surface and the master surface is permitted to penetrate into the slave surface (ABAQUS, 2012). The sheet pile and footings are selected as the master surface when considering the interaction between soil-SPW and soil-footing, while the soil mass is treated as the slave surface. During the construction in the field, no walls are constructed perfectly smooth. Hence, to include the roughness effect of the wall, the interface friction angle is adopted as 2/3 times the soil friction angle (Bahrami et al., 2018; Singh and Chatterjee, 2020 a,c).

To obtain a higher degree of accuracy and efficient simulations with less effort sensitivity analysis and mesh refinement is performed. The soil mass, sheet pile and footings are modelled by a 20-nodded hexahedral quadratic brick element with reduced integration (C3D20R). In order to diminish the impact of boundary conditions on the numerical findings, the numerical model boundaries must be kept sufficiently large. Singh and Chatterjee (2020 a,b) adopted numerical model boundaries are used in the present investigation.

Table 1. Description of soil (after Singh and Chatterjee (2020a, 2020c))

Type of soil	Properties			
	Unit weight, γ, (kN/m^3)	Friction angle, φ (degree)	Poisson's ratio, μ	Young's modulus, E, (MPa)
Dense sand	18.40	39	0.30	90
Loose sand	14.00	30	0.38	36

Table 2. Description of SPW (after USS Design Manual (1984) and Bilgin (2012))

Section provided	Cross-sectional area (cm^2/m)	Elastic section modulus (cm^3/m)	Moment of inertia (cm^4/m)
PZ27	168.10	1620	25200

Hence, in the present study, the depth of the numerical model boundary below the base of the sheet pile is assumed to be five times the overall wall height and the length of the model is selected as sixteen times the overall wall height (eight times both behind and in front of the wall) for the cases analysed in this study. Because increasing the overall depth and length of the model boundary beyond these dimensions does not affect the numerical analysis results. The numerical model width is kept five times the width of the square footing (5 × 2.50 = 12.50 m).

According to Singh and Chatterjee (2020 a,b), the selected dimensions are adequate and safe compared to Chowdhury et al. (2013). Figure 1 shows the dimensions, element type, model meshing and model boundaries adopted for the numerical study. The SPW is placed in the middle of the model width. According to the construction sequence, sheet piles are classified as backfilled construction and dredging construction (Tsinker, 1983).

The present study implements the dredging structure during numerical modelling and analysis. The sequences of dredging construction are sheet pile driving, backfilling (if necessary), and dredging of frontfill soil.

The numerical modelling has been made in the following steps: at the initial step to obtain equilibrium condition geostatic stress is imposed in the model, before the sheet pile installation and lateral EP co-efficient at rest (K_0) has been applied and estimated by Jaky's equation (Jaky, 1944), which is (1 - sin ϕ); where ϕ: is the friction angle of soil. Later, the SPW is introduced in the soil continuum and the self-weight is induced into the whole model to reach the model to an equilibrium position again.

After that, the vertical surcharge load of different magnitudes is imposed by a model footing. Finally, the frontfill soil excavation starts sequentially by soil lifting in four steps, the thickness of each lift is 1.125 m, to include the influence of construction techniques throughout the analysis. As the loads are imposed quickly, so, the influence of consolidation and pore pressure changes does not consider during the FE analysis (Deb and Pal, 2019).

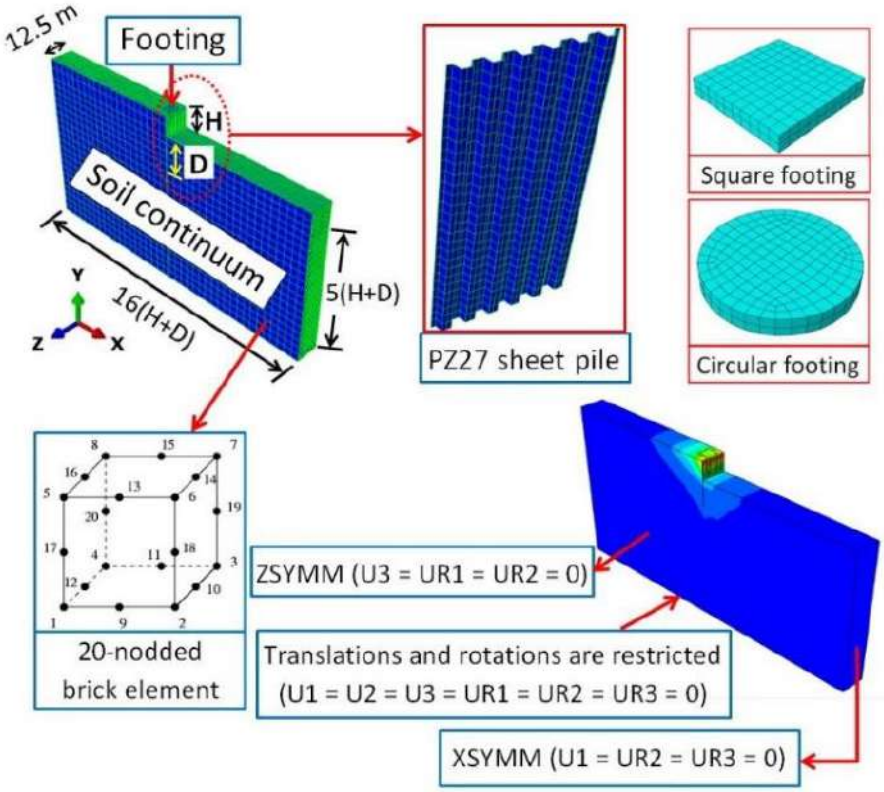

Fig. 1. Dimensions, element type, model meshing and model boundaries adopted for the numerical study

3. Experimental Study

To study the sheet pile, wall behavior, a small-scale laboratory experiment was executed. The model test set-up and experimentation were carried out in three stages: Stage 1 involved soil bed preparation and sheet pile installation, Stage 2 involved the application of vertical load, and in Stage 3 the sequential excavation of frontfill soil was done. The test set-up and the stages of experimentation are illustrated in Figure 2.

The model SPW and footing specifications have been chosen according to the scaling laws (Wood, 2004) as shown in Table 3.

The laboratory model dimensions choosed with a scaling ratio of n (model/prototype) is equal to 30 in order to simulate the small-scale experimental model with the prototype numerical model. The plan area of the model footing was taken as 69.44 cm^2 (6.25 m^2) (The equivalent prototype area is 62500 cm^2).

The experimental set-up consists of a testing tank, where the depth of the tank below the dredge line is selected as five times the height of the SPW above the dredge level (5H) and the backfill length is six times the height of the SPW above the dredge level (6H) in order to retain the developed soil stress inside the tank boundary. Hence, the overall dimensions of the tank are 1.80 m × 0.90 m (length × depth) and the width is kept at 0.75 m.

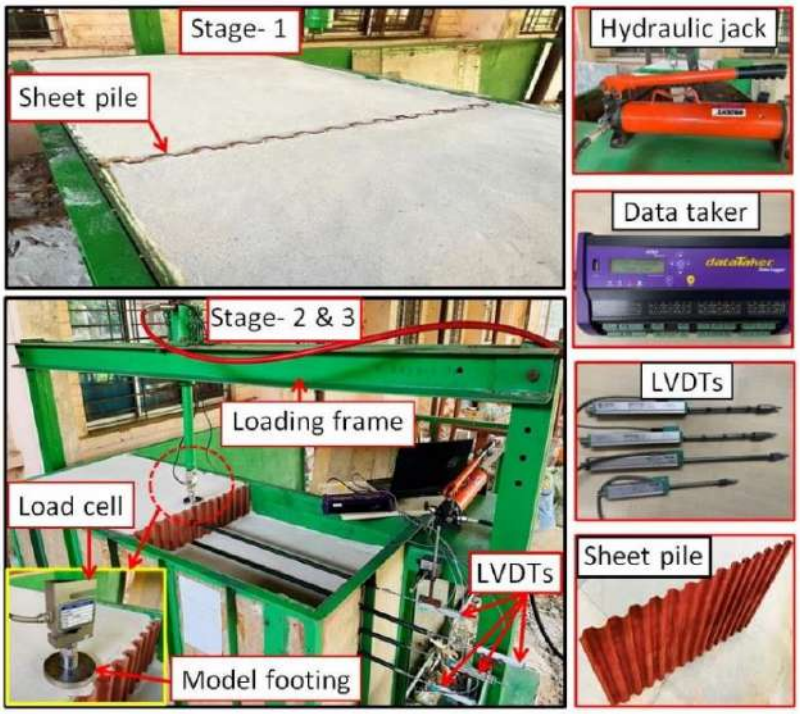

Fig. 2. Experimental test set-up

Table 3. Specifications of the model SPW and footing

Parameters	Symbols	Scaling laws	Numerical model (Prototype)	Experimental model
SPW material	–	1	Steel	Steel
Height of sheet pile above the dredge level (cm)	H	1/n	450	15
Depth of embedment (cm)	D	1/n	650	21.67
Cross-sectional area (cm^2/m)	A_p	$1/n^2$	168.10	0.19
Moment of inertia (cm^4/m)	I	$1/n^4$	25200	31.11×10^{-3}
Young's modulus of the pile (GPa)	E	1	200	200
Plan area of footing (cm^2)	A_F	$1/n^2$	62500	69.44
Thickness of the footing plate (cm)	t	1/n	40	1.33

The test tank is made up of a 10 mm thick translucent Perspex-sheet on the vertical sides and a steel sheet 10 mm thick in the base. Adding a Perspex-sheet on all vertical sides of the testing tank reduces friction between the tank and soil particles. While preparing the dense soil bed, a uniform density is maintained throughout the testing chamber using controlled pouring and tamping procedures.

In this procedure, the amount of sand required for each layer to produce a particular relative density was first weighted, then deposited in the tank and tamped until the required layer height was achieved. To ensure a consistent relative density throughout the sand bed, four cylindrical Aluminium containers were placed at various positions. During the preparation of the sand bed, a tolerance in relative density of 1.50% to 2.10% is accepted.

The soil is poured up to the base of the SPW during the first step of soil bed preparation. The model SPW was then placed in the centre of the test chamber and held in place with detachable temporary supports, ensuring the verticality of the sheet pile throughout the soil bed preparation. After that, the soil was again poured up to the top of the wall and the temporary supports were removed before the beginning of experimentation.

A steel frame was used as a loading frame; a 20-ton capacity hydraulic system was used for applying the vertical load; a 30 kN capacity load cell having an accuracy of 0.01 kN was used to measure the amount of vertical load; Linear Variable Displacement Transducers (LVDTs) with a sensitivity of 0.01 mm were utilized for measuring the lateral wall deflection; a data acquisition system connected with computer to record data directly during the experimentation. The applied load with the hydraulic jack was first transferred to the cylindrical shaft and subsequently to the foundation via the load cell as presented in Figure 2.

The load cell was compressed during loading and records the applied vertical load. During the entire experimentation program, constant surcharge pressure was maintained and lateral deflection of the SPW was recorded after the end of the fourth excavation stage. The experimentation was done in this study only for validation.

4. Validation of the Numerical Model

The developed numerical model was validated with experimental test results to ensure higher accuracy in numerical studies. A similar soil profile and model boundary conditions were maintained while performing experimental analysis to compare the results obtained from the experiment with the numerical results. The experimentation was done by performing tests with square and circular footing with a 100 kPa surcharge load positioned at the wall top edge.

Figures 3a and 3b show the comparison of wall deflection results for square and circular footing respectively, with equal plan area in dense sand. The figures shows that the deflection profile achieved from the numerical model study and the laboratory model test show a similar trend. Figure 3a illustrates that the maximum wall deflection is 63.00 mm for the proposed FE model compared to 54.50 mm found in the experimental study for a square footing. Similarly, Figure 3b illustrates that the maximum wall deflection is 51.00 mm for the proposed FE model for circular footing compared to 43.00 mm found in the experimental study.

The results of the two studies shows a small difference in the deflection results, which could be due to the different approaches to analysis. Hence, the proposed numerical model test results are very close to the experimental results, thus the numerical model and experimental work agreed well.

5. Results and Discussions

A numerical analysis by the FE method was

executed, emphasizing the shape effect of footings positioned at different locations to investigate the behavior of SPW. To determine wall deflections, BMs, and backfill GS, a parametric study was conducted by changing various parameters such as the magnitude of the surcharge load, plan area of footing, wall penetration depth, square and circular footing position along the BGS and depth of the wall, depth of loose soil layer, and dredge line slope inclination.

More explanations regarding each parameter are described in detail in the following subsections. The description of the different parametric data used is described in Table 4. All the analysis has been performed in the dense sand, except the study of the effect of loose layer on SPW and backfill GS.

5.1. Effect of Varying Plan Area of Square and Circular Footing on Maximum Wall Deflection and Bending Moment

The effect of varying plan area of square and circular footing on maximum wall deflection and BM are determined by placing the footing at the wall top edge (X = 0.000 m, Y = 0.000 m) with a 75 kPa surcharge. Figure 4a and 4b illustrates the maximum deflection and BM respectively, for varying plan area of the footing. The maximum deflection and BM increase as the plan area of the square and circular footings increases.

The increment was less up to a footing area of 4.00 m^2; after that, it was found to be significantly increased and reaches its maximum value at a footing area of 12.25 m^2 as shown in Figures 4a and 4b. The reason is that the higher footing area displaces a higher amount of backfill soil below it, producing higher lateral pressure to the wall, leading to a higher deflection and BM. These figures show that the square footing has a substantially greater impact on wall deflection and BM than a circular footing of the same plan area. For example, a plan area of footing 6.25 m^2 produces 1.22 and 1.68 times higher wall deflection and BM respectively, then a circular footing under 75 kPa surcharge load for dense sand. This is because the shape effect of square and circular footing (Shafiqul Islam et al., 2017).

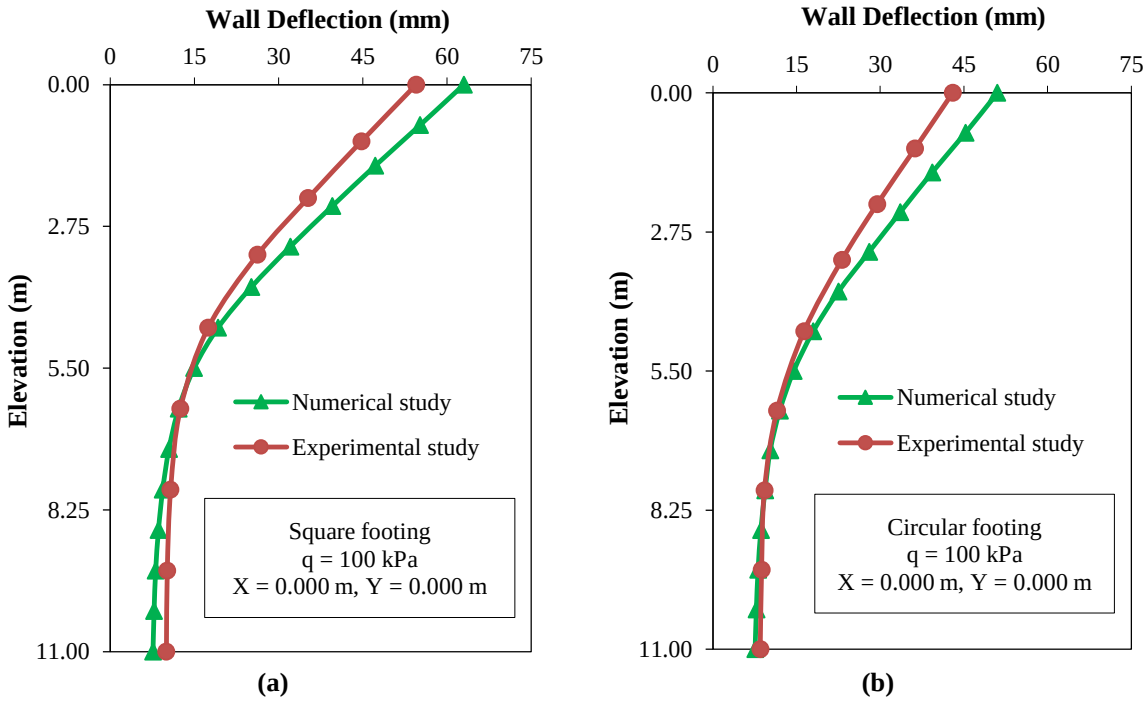

Fig. 3. Wall deflections obtained in the present numerical and experimental studies for: a) Square footing; and b) Circular footing

Table 4. Parameters used for the parametric study

Parameters	Symbol	Values
The magnitude of the surcharge load (kPa)	q	50, 75, 100, 125, and 150
Plan area of square and circular footing (m^2)	A	1.00, 2.25, 4.00, 6.25, 9.00, and 12.25
Embedded depth of wall (m)	D	4.50, 6.50, 8.50 and 10.50
Position of square and circular footing from the wall face along the BGS (m)	X	0.000, 2.250, and 4.500
Position of square and circular footing from the BGS along the depth of wall (m)	Y	0.000, 1.125, 2.250, 3.375, and 4.500
Depth of loose soil layer (m)	L	0.000, 1.125, 2.250, 3.375, 4.500, 5.625, 6.750, and 11.000
Dredge line slope angle (º)	α	0, 10, 20, 25, and 30

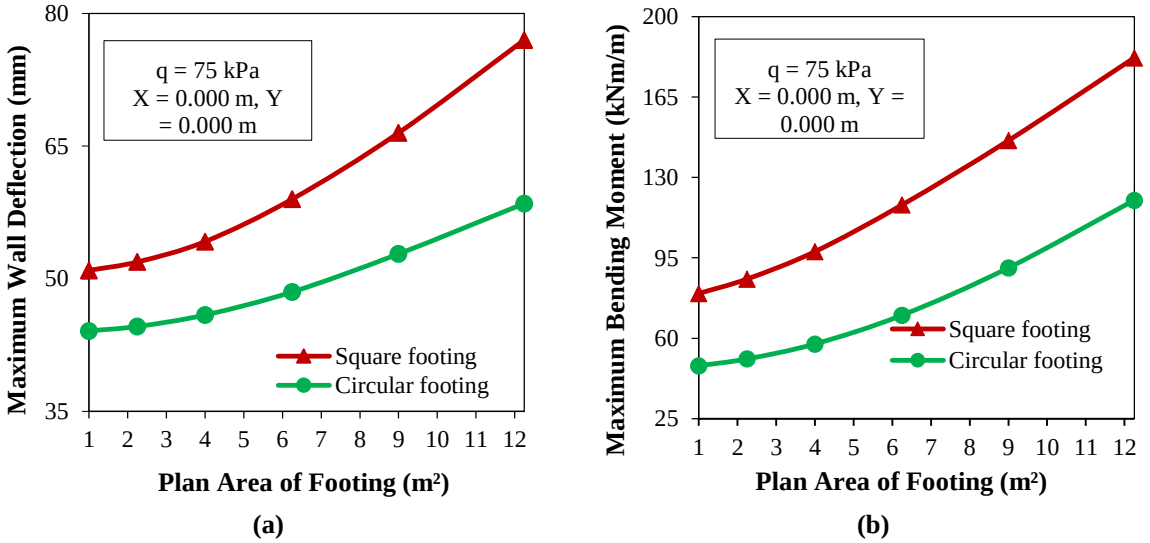

Fig. 4. Effect of varying plan area of square and circular footing for dense sand on maximum: a) wall deflection and b) BM

The horizontal displacement contours of soil for circular footings were developed around the edge of the footing and transmitted to the outward direction of the footing; the extent of the contours was uniform and circular, similar to the footing area. However, due to the corner effect of square footings, the horizontal displacement contours of the square footing were produced first at the corners and then moved to the footing edges. These contours were finally travelled in the outward direction of the footing area. The extent of the contours was found to be maximum at the centre point of the footing edges and minimum at the corner regions of the footing. Because of the higher lateral deformation produced at the middle of the square footing edge due to the corner effect compared to circular footing, hence, the square footing influences the SPW behavior more than circular footing. In the present study, an equal footing area of 6.25 m^2 for both square and circular-shaped footing was adopted for the complete analysis.

5.2. Influence of Embedded Depth on Maximum Wall Deflection and Bending Moment

Various trial embedded depths were chosen to understand the behavior of the wall with square footing positioned at the walls top edge. The present study analyzes 4.50, 6.50, 8.50, and 10.50 m embedded depths. Figures 5a and 5b show the profile of maximum wall deflection and BM respectively, with different surcharge loads.

It has been found that the shallow embedded depth of the wall highly influences the deflection and BM, due to the full mobilization of passive earth resistance (occurs up to plastic zone below the dredge level), which takes place at a larger depth for shallow embedded depth wall below the

dredge level. However, beyond a depth of 6.50 m, the impact of embedded depth on maximum deflection and BM significantly reduces. This reduction occurs because, at greater embedded depths, both wall deflection and BM decrease significantly due to the development of a plastic zone below the dredge level, which leads to a decrease in net EP at the base of the wall. This decrease in the extension of the plastic zone below the dredge level and the net EP at the base of the wall can be attributed to a significant decrease in the horizontal wall movement.

The observed trends are consistent with the findings of Singh and Chatterjee (2020a). For example, a reduction in maximum wall deflection of 0.79, 0.74, and 0.73 times is observed for embedded depths of 6.50, 8.50, and 10.50 m respectively, then 4.50 m embedded depth for 150 kPa surcharge load. Similarly, an increase in maximum BM of 1.41, 1.54, and 1.62 times is observed for embedded depths of 6.50, 8.50, and 10.50 m respectively, then 4.50 m embedded depth for 150 kPa surcharge load. Hence, the present study took an embedded of sheet pile of 6.50 m for the entire analysis.

5.3. Influence of Footing Position on Wall Deflection and BM Behavior

To study the influence of the square and circular footing (an equal plan area of 6.25 m^2) on the SPW behavior; the footing was placed in different horizontal positions along the BGS (X-direction) and vertical positions along the depth of the SPW (Y-direction). The present analysis took different footing positions along the BGS as X = 0.000, 2.250, and 4.500 m from the wall face. Similarly, the different positions along the depth of the SPW were taken as Y = 0.000, 1.125, 2.250, 3.375, and 4.500 m from the BGS.

The plots of maximum wall deflection and BM with surcharge located at different depths from the BGS for varying horizontal positions of footings is shown in Figures 6a-6c and 6d-6f, respectively, for a square footing. Figures 6a-6c and 6d-6f indicate that the maximum deflection and BM occur when the footing is positioned at the wall top edge (i.e., X = 0.000 m, Y = 0.000 m) and decreases gradually as the distance between the wall top edge and the footing increases along both the horizontal and vertical directions.

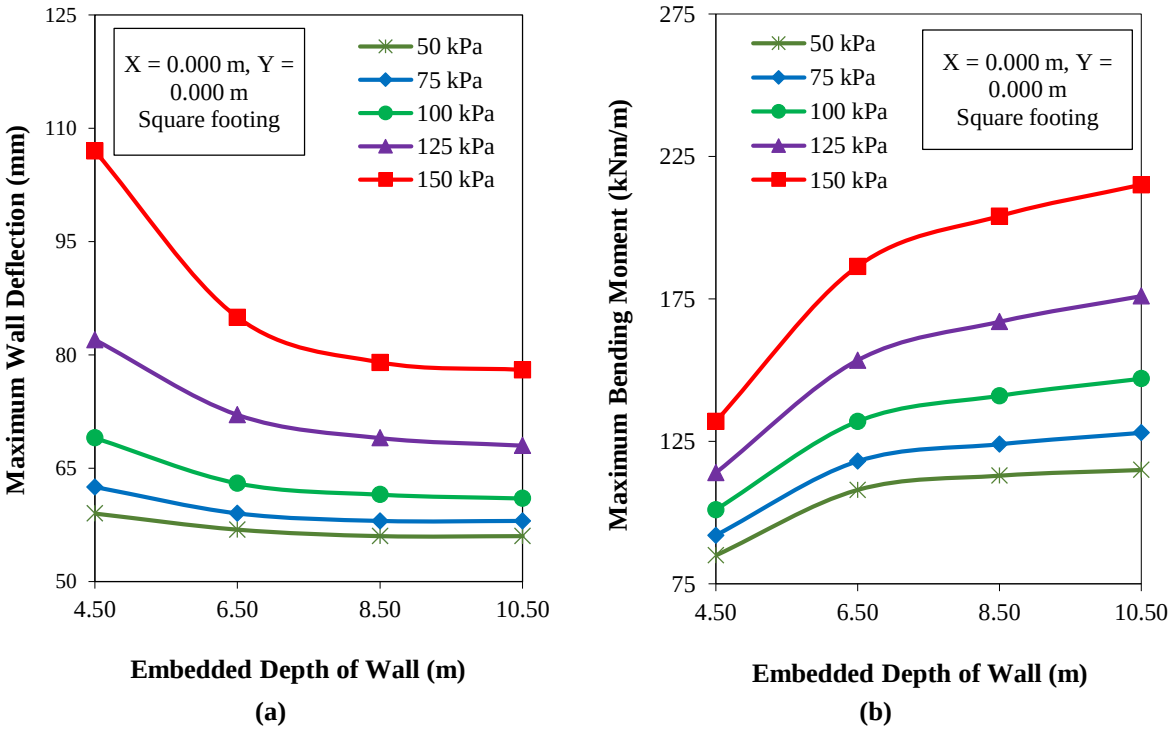

Fig. 5. Effect of varying embedded depths with square footing on maximum: a) Wall deflection; and b) BM

Increasing the footing depth below the BGS reduces the maximum deflection and BM for a specific horizontal position. For example, an increase in depth of the footing below the BGS reduces 0.66, 0.55, 0.50, and 0.47 times the maximum wall deflection for footing positions Y = 1.125, 2.250, 3.375, and 4.500 m respectively, as compared to the position when the footing is positioned at the ground surface (Y = 0.000 m), for a horizontal position of footing X = 0.000 m with 150 kPa surcharge load as shown in Figure 6a. Similarly, an increase in the horizontal distance between the wall and the footing reduces 0.58 and 0.39 times the maximum wall deflection for footing positions X = 2.250 and 4.500 m respectively, as compared to the position when the footing is positioned at the wall top edge (X = 0.000 m), for a vertical position of footing Y = 0.000 m with 150 kPa surcharge load as shown in Figures 6a-6c. Similarly, for a specific vertical footing position, the maximum deflection and BM decrease as the distance of the footing from the wall along the BGS increases. The deflection and BM increase as the surcharge load increases for footings placed in any particular horizontal and vertical positions; the observed trends agree well with Samadhiya (2020) analysis.

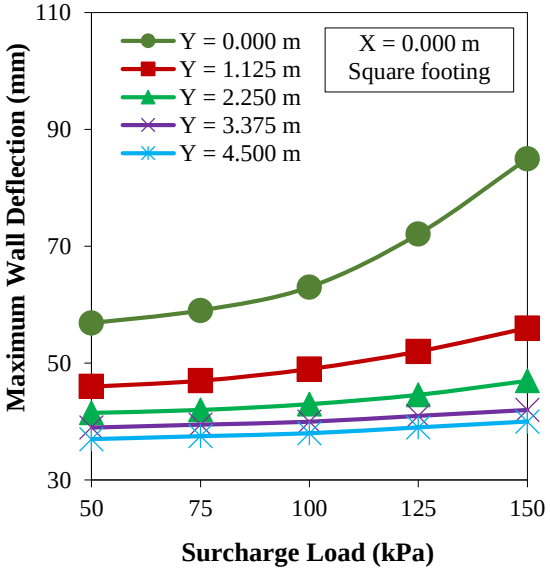

(a)

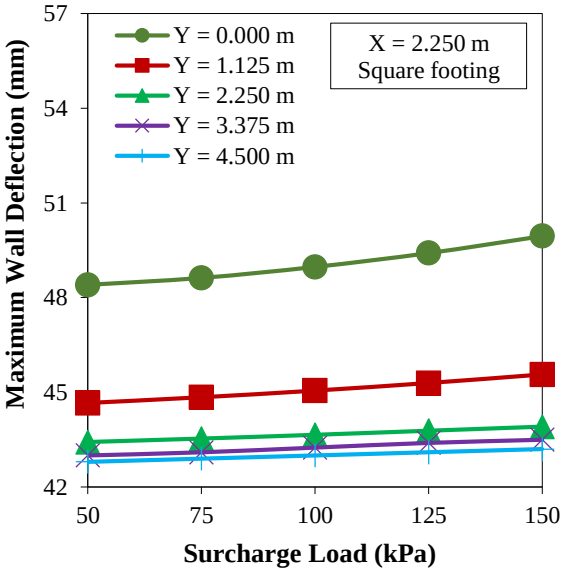

(b)

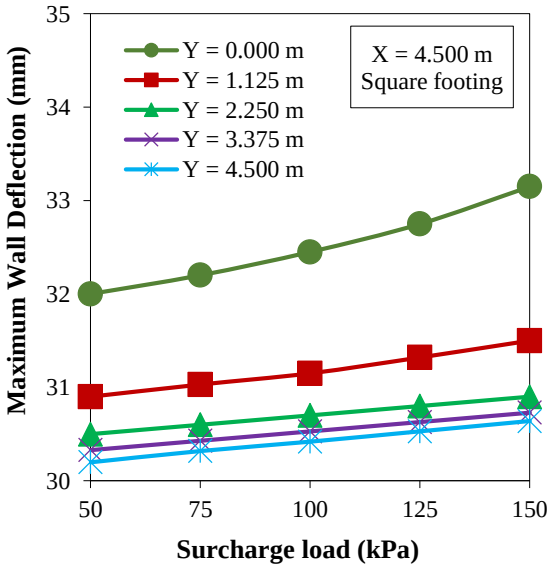

(c)

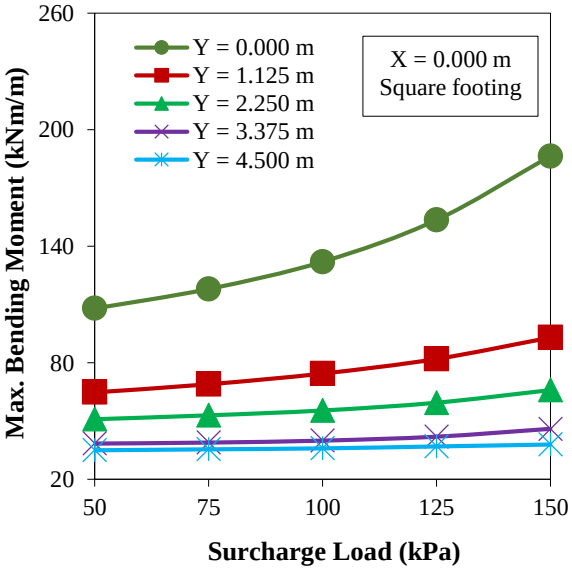

(d)

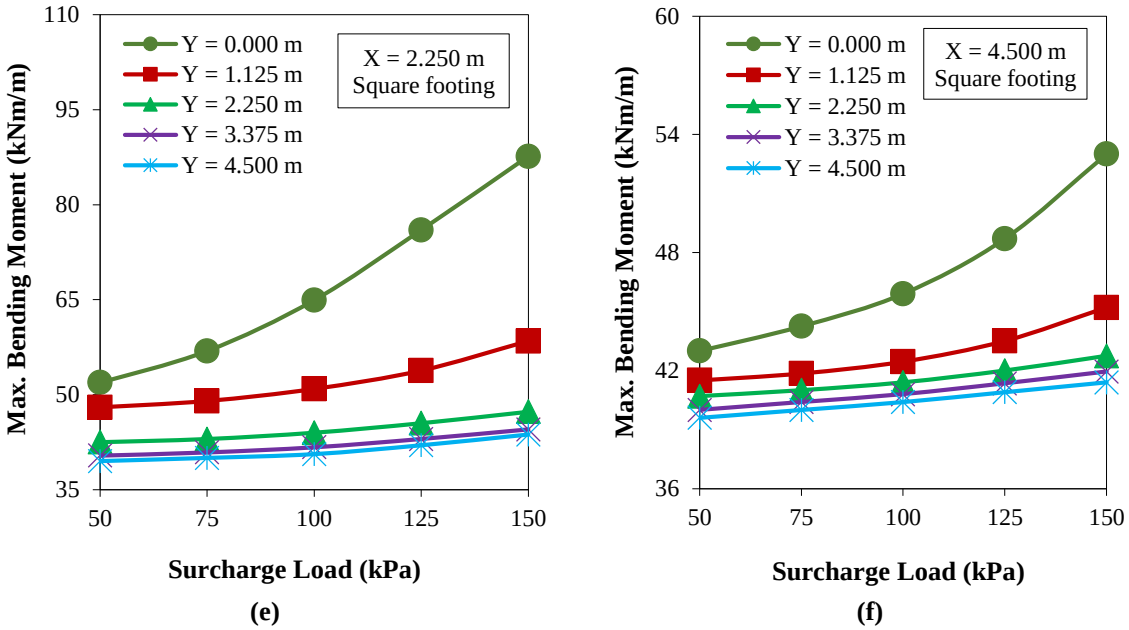

Fig. 6. Plot of maximum: a-c) Wall deflection; and d-f) BM under the surcharge load for a square footing with locations varying vertically and horizontally

Figures 7a-7c and 7d-7f show the plot of maximum deflection and BM with surcharge load respectively, for a circular footing positioned at different horizontal positions along the BGS and vertical positions along the depth of the wall. These figures indicate that increasing the surcharge increases the maximum deflection and BM significantly. Moreover, the maximum deflection and BM reduce substantially as the footing is placed away from the wall top edge.

Figures 8a and 8b show the deflection and BM profiles along the wall depth for various surcharge loads in square footing. Both the deflection and BM profile show an increase in deflection and BM with increased surcharge load. When a circular footing with the same plan area is utilised instead of a square footing, the maximum wall deflection and BM are significantly reduced. Figures 6a, 7a, 6d, and 7d show that a circular footing placed at the wall top edge produces 0.72 and 0.67 times reduced amount of maximum deflection and BM, respectively, than a square footing for a 150 kPa surcharge. The reduction in the deflection and BM is due to the shape effect because, due to the uniformity of the displacement contours under the footing, the displacement of backfill soil below the circular footing is less compared to a square footing of the same plan area. As a result, a smaller amount of lateral deformation of soil is observed for circular footings.

5.4. Influence of Surcharge Load on the Ground Settlement Behavior

Figures 9a and 9b illustrate vertical GS curves along the backfill surface with varying surcharge loads for a square and circular footing respectively, of equal plan area of 6.25 m^2 placed at the wall top edge. These figures indicate that a significantly higher GS is observed when the surcharge load increases for square and circular footing. The square footing, on the other hand, produces a higher GS than the circular footing. For example, a square footing has 1.13, 1.15, 1.18, 1.24, and 1.31 times higher values of maximum GS for 50, 75, 100, 125, and 150 kPa surcharge loads, respectively, than circular footing. Because the displacement contours below the square footing were non-uniform and higher in magnitude than circular footing leading to a higher displacement of backfill soil below the footing.

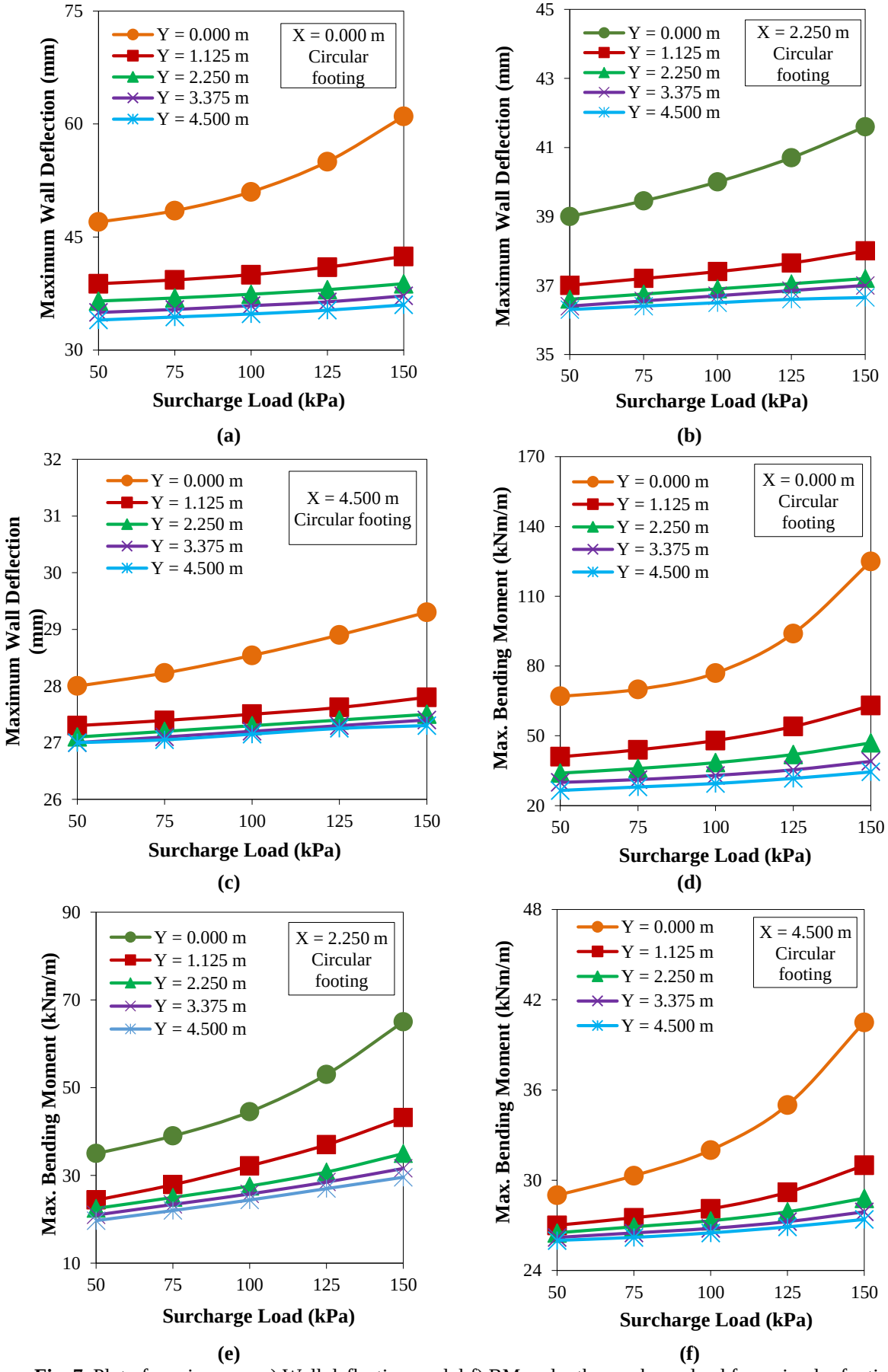

Fig. 7. Plot of maximum: a-c) Wall deflection; and d-f) BM under the surcharge load for a circular footing with locations varying vertically and horizontally

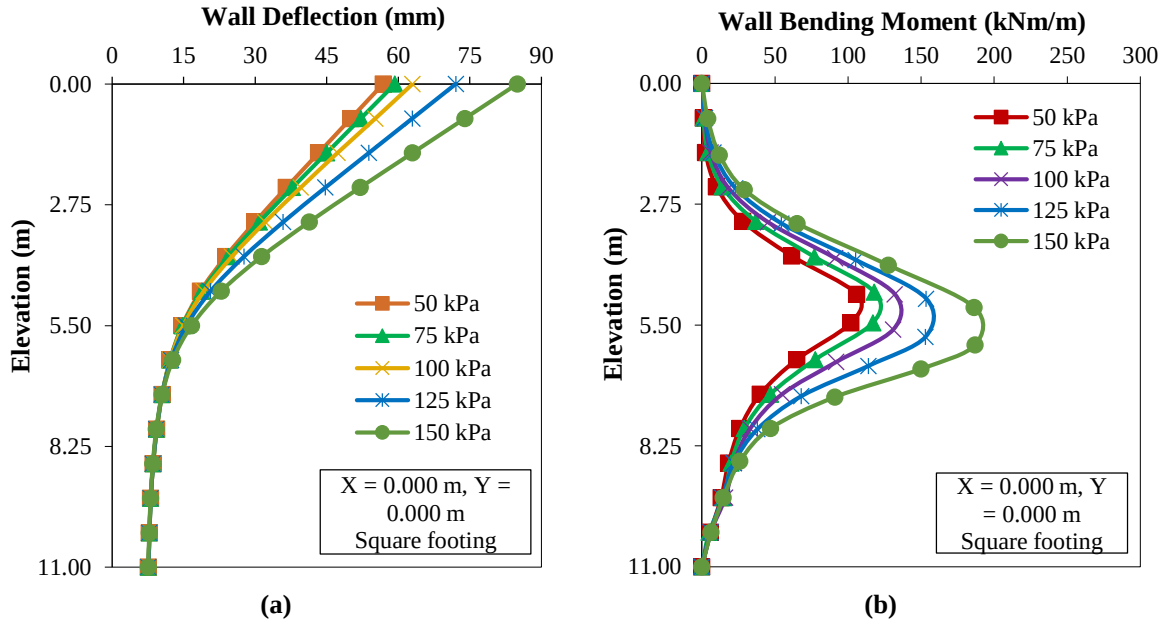

Fig. 8. a) Wall deflection; and b) BM profiles with different surcharge loads for square footing placed at the wall top edge for dense sand

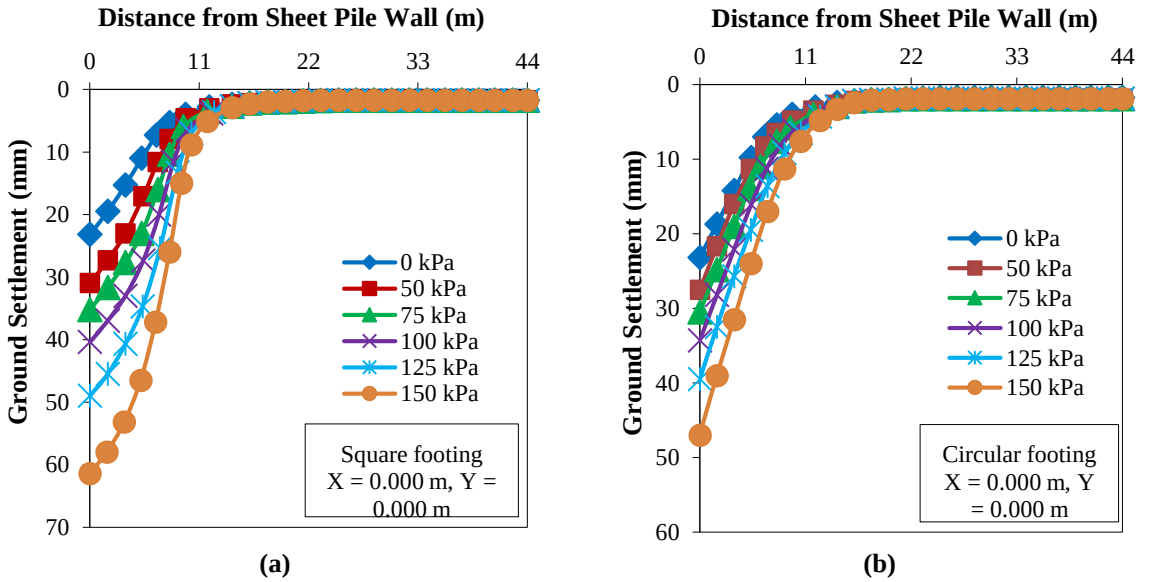

Fig. 9. Variation of vertical GS along the BGS under various surcharge loads placed at the wall top edge (X = 0.000 m, Y = 0.000 m) for: a) Square footing; and b) Circular footing

The settlement profiles for square and circular footing indicate that a significant variation of GS is observed up to a distance of 9 m from the wall for all surcharge loads. After that distance, the variation in GS is negligible and reaches its minimum value. As a result, for all surcharge loads, the settlement influence zone acts at a distance of 2H, as illustrated in Figures 9a and 9b.

The present observation agrees well with the observation of Peck (1969). Hence, reducing the risk of higher GS foundation can be located outside that zone is recommended. The normalized vertical deflection ($\delta_{v\text{-}max}$/H) under a square and circular footing has been obtained in the present study for a 100 kPa surcharge placed at the wall top edge is 0.90 and 0.76%, respectively, where $\delta_{v\text{-}max}$: is the maximum vertical GS of the backfill. Peck (1969) recommended that the normalized vertical displacement should not be more than 1.0% in the case of flexible supports in sands. Therefore, the findings of this study

are consistent with the results recommended by Peck (1969). $\delta_{v\text{-}max}/\delta_{h\text{-}max}$ ratio is obtained as 0.64 and 0.67 for a square and circular footing, respectively, with 100 kPa surcharge load, where $\delta_{h\text{-}max}$: is the maximum lateral wall deflection.

5.5. Influence of the Loose Soil Layer on the Behavior of Wall and Backfill Soils

The influence of a loose soil layer is determined by replacing the dense soil from BGS with loose soil in layers. The depth of the loose layer (L) from the BGS is taken as 0.000, 1.125, 2.250, 3.375, 4.500, 5.625, 6.750, and 11.000 m. In the present study, the effect of a loose layer has been investigated for square and circular footing under a 125 kPa surcharge positioned at the wall top edge. Figures 10 and 11 show that wall deflection, BM, and GS profiles under square and circular footing increase significantly under a 125 kPa surcharge with increasing loose layer depth. The increment is too high when the depth of the loose layer extends below the dredge level.

For example, a square footing produces 1.64 and 3.54 times higher wall deflection for loose layer depths (L) of 4.500 m (at the dredge level) and 11.000 m respectively, in comparison to the absence of a loose layer (L = 0.000 m) for a 125 kPa surcharge, as shown in Figure 10a. Similar incremental trend of results were obtained for BM and GS, as illustrated in Figures 10b and 10c respectively.

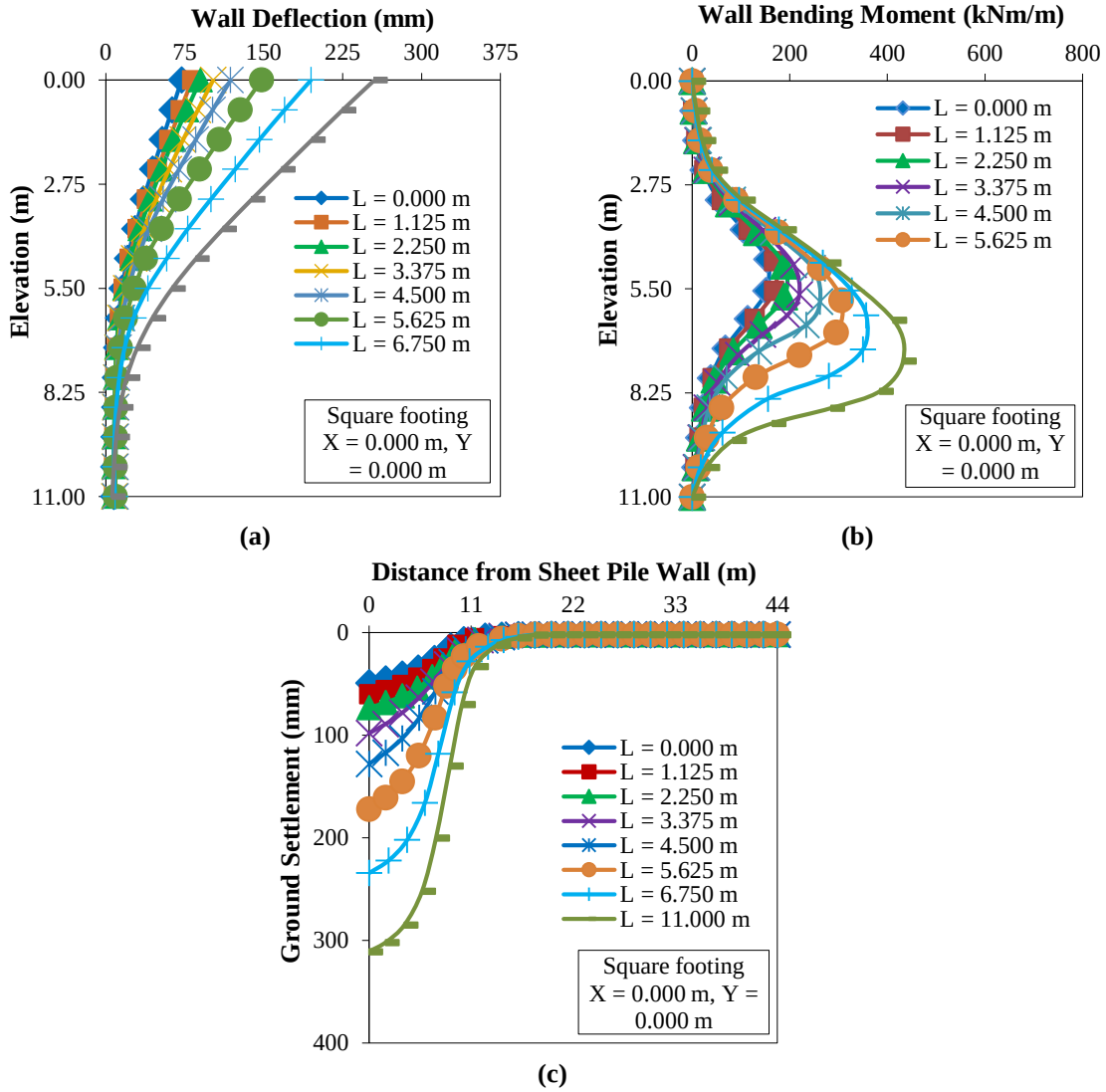

Fig. 10. Plot of: a) Wall deflection; b) BM; and c) GS, for a square footing with 125 kPa surcharge load placed at the wall top edge

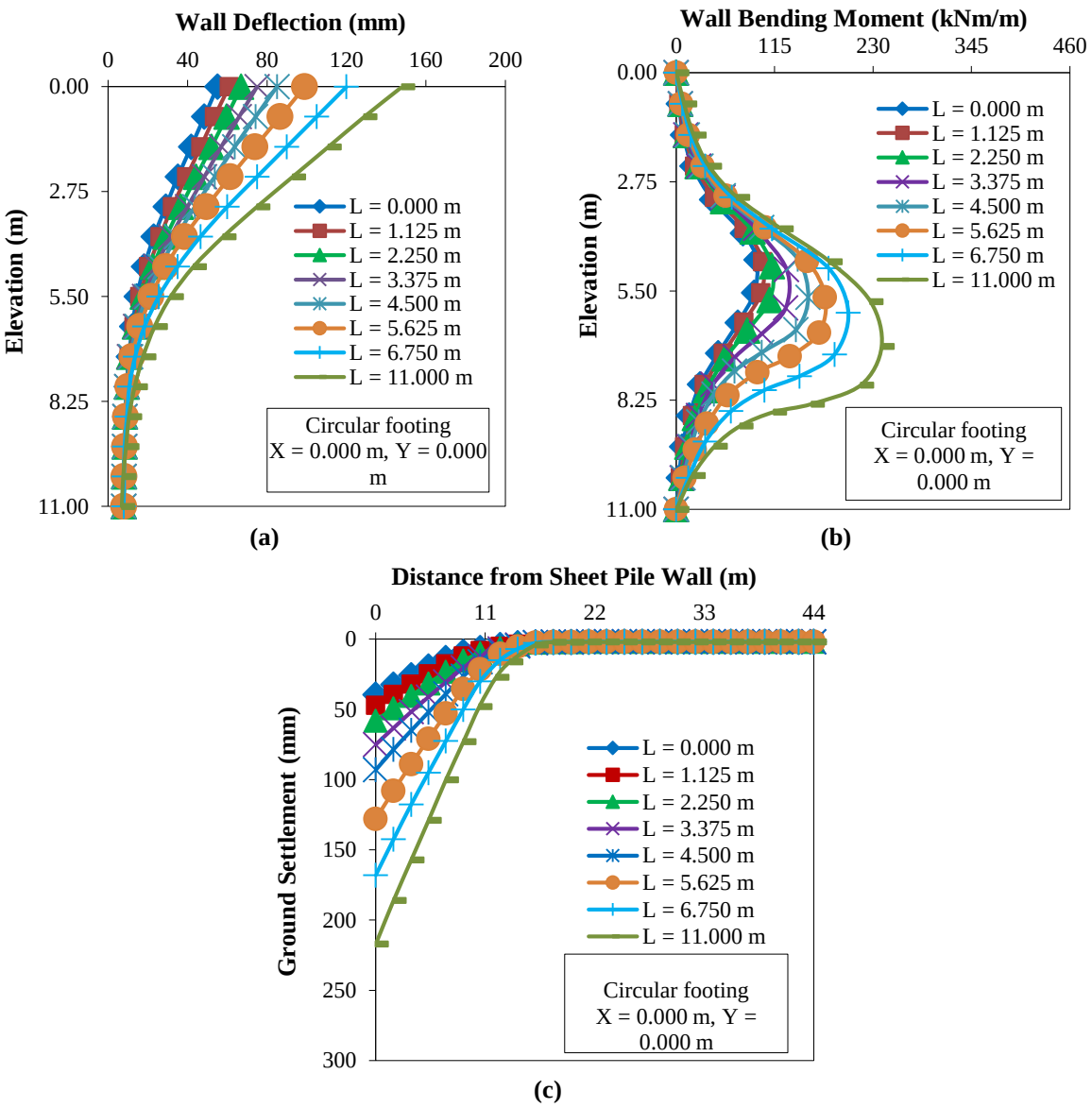

Fig. 11. Plot of: a) Wall deflection: b) BM; and c) GS, for a circular footing with 125 kPa surcharge load placed at the wall top edge

5.6. Influence of Dredge Line Slope Angle on the Sheet Pile and Ground Settlement Behavior

Dredge line inclination angles of 0º, 10º, 20º, 25º, and 30º are used to investigate how sloping dredge levels effect sheet pile and backfill GS behavior. The profiles of the wall deflection, BM, and backfill GS profiles, for a 50 kPa square footing load imposed at the wall top edge with different slope angles are displayed in Figures 12a, 12b, and 12c respectively. The results indicate a significant increase in deflection, BM, and GS with the increase in slope angles. For example, a 50 kPa surcharge load for a 10º, 20º, 25º, and 30º slope angle creates 1.30, 1.97, 3.17, and 4.67 times respectively, higher maximum deflection; 1.25, 1.62, 1.97, and 2.42 times respectively, higher maximum BM; and 1.22, 1.74, 2.30, and 3.06 times respectively, higher maximum GS, than the horizontal dredge level condition.

Furthermore, Figure 12b shows that increasing the slope angle reduces the passive restraint of the wall, resulting in a decrease in the degree of fixity of the wall below the dredge level. As a result, a downward drop in the maximum BM below the dredge level is seen, with more depression recorded at greater slope angles.

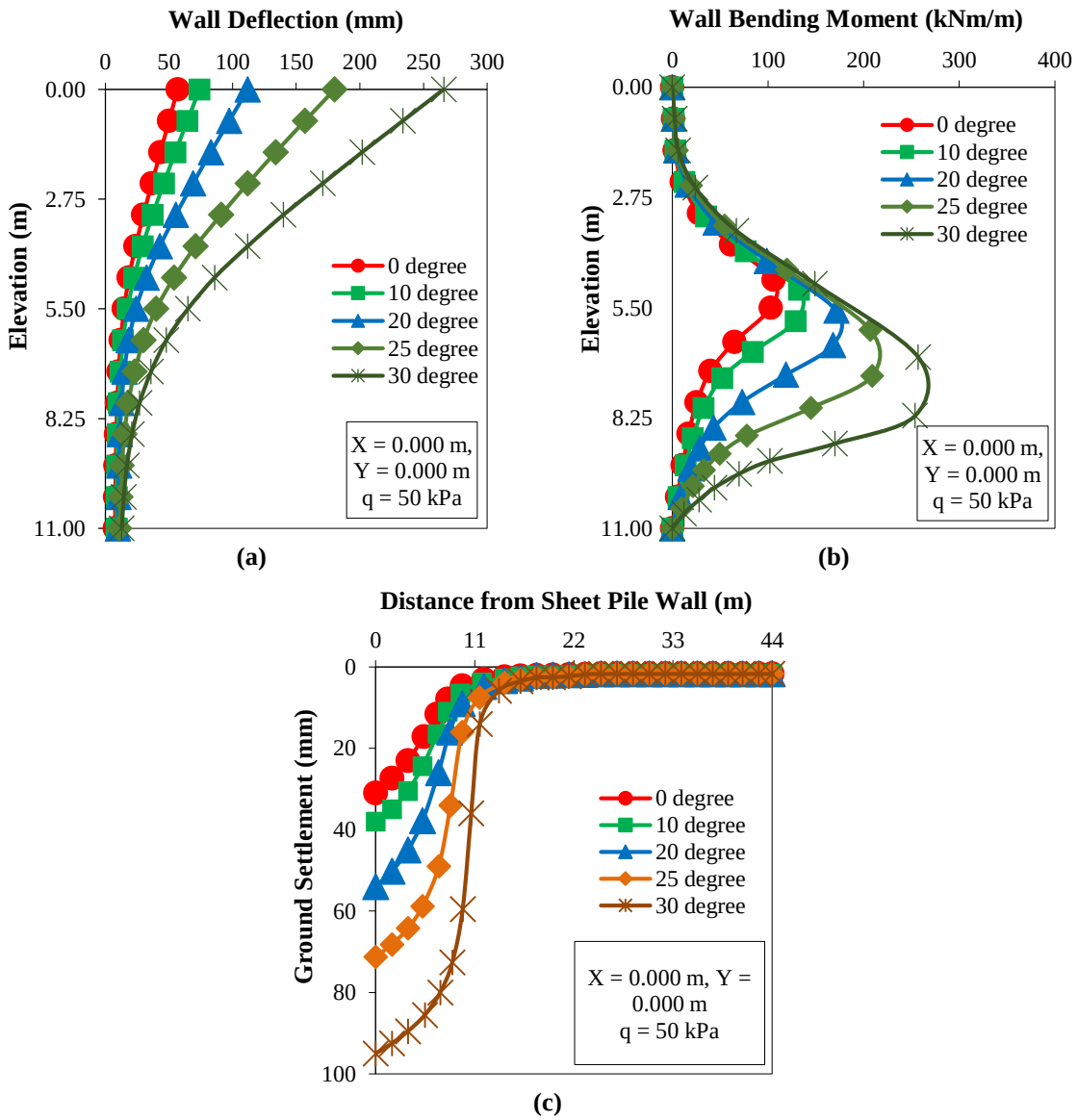

Fig. 12. Plot of: a) Wall deflection; b) BM; and c) GS, for a square footing with 50 kPa surcharge load placed at the wall top edge for various dredge line slope angles

6. Conclusions

In the current study, a numerical analysis with realistic 3D modeling using the FE approach was undertaken to evaluate sheet pile behavior, emphasizing the shape effect of footings. Circular and square footings were placed at different locations above and below the BGS with different surcharge magnitudes to determine the sheet pile behavior. Furthermore, the effects of loose soil layers and the sloping dredge lines on the behavior of SPW were also investigated.

The points to be highlighted from the present FE study are as follows:

- The deflection and BM of the sheet pile increase with the increase in the plan area of the square and circular footing. Because, a higher footing area displaces a higher amount of backfill soil below it, producing higher lateral pressure to the wall, leading to a higher wall deflection and BM.

However, due to the corner effect of square footing, the displacement contours below the square footing are non-uniform and higher in magnitude than circular footing of the same plan area, leading to a higher displacement of backfill soil below the square footing, producing higher lateral pressure to the wall, leading to a higher wall deflection and BM.

- The shallow embedded depth of the wall highly influences the wall deflection and BM, due to the full mobilization of passive earth resistance (occurs up to plastic zone below the dredge level), which takes place at a larger depth for shallow embedded depth wall below the dredge level. But at the higher embedded depths the maximum deflection and BM significantly reduces because of the development of a plastic zone below the dredge level and net EP at the base of the wall decreases. This decrease in the extension of the plastic zone below the dredge level and the net EP at the base of the wall can be attributed to a significant decrease in the horizontal wall movement.
- The wall deflection and BM are maximum when the footing is positioned at the wall top edge. Increasing the distance of the footing along the BGS and along the depth of the wall from the wall top edge significantly reduces the deflection and BM. There is a significant decrease in maximum deflection and BM is witnessed when the circular footing having the same plan area is used instead of square footing due to the shape effect because, due to the uniformity of the deformation contours below the footing, the displacement of backfill soil below the circular footing is less compared to a square footing of the same plan area. As a result, a smaller amount of lateral deformation of soil is observed for circular footings.
- An increase in surcharge loads significantly increases the GS for square and circular footing. The square footing produces greater GS than the circular footing. The settlement profiles for square and circular footing show a significant variation of GS up to a distance of 2H from the wall for all surcharge loads. After that, the variation in GS is negligible and reaches its minimum value. Hence, to reduce the risk of excessive GS, it is recommended that the foundation may be placed beyond the zone of influence.
- Increasing the loose layer depth significantly increases the wall deflection, BM, and GS for square and circular footing under surcharge loads. The increment is too high when the depth of the loose layer extends below the dredge level. The reason behind it, is the decrease in the passive restraint from the frontfill soil due to the inclusion of a loose layer below the dredge level, leading to decreases in the overall stability of the CSPW. Moreover, the influence of a loose soil layer is comparatively less for circular footing.
- With increasing slope angles, there is a significant increase in wall deflection, BM, and backfill GS. Increasing the dredge line slope angle reduces the wall's passive restraint, decreasing its degree of fixity below the dredge level. As a result, there is a downward drop in the point of maximum BM, with higher depression reported at steeper slope angles.

7. Acknowledgment

The authors would like to thank the National Institute of Technology Agartala for providing the laboratory facilities required to complete the research work.

8. References

ABAQUS. (2012). *Abaqus manual (computer software)*, Providence, RI: SIMULIA.

Ahmadpour, B., Sakhi, M.A. and Kamalian, M. (2018). "Study of loose soil layer effects on excavations supported by steel sheet pile walls-a numerical study", *Journal of Engineering Geology*, 12, 31-54, https://doi.org/10.18869/acadpub.jeg.12.5.31.

Bahrami, M., Khodakarami, M.I. and Haddad, A. (2018). "3D numerical investigation of the effect of wall penetration depth on excavations behavior in sand", *Computers and Geotechnics*, 98, 82-92, https://doi.org/10.1016/j.compgeo.2018.02.009.

Basha, A. and Elsiragy, M. (2019). "Effect of sheet pile driving on geotechnical behavior of adjacent building in sand: Numerical study", *Civil Engineering Journal*, 5(8), 1726-1737,

http://doi.org/10.28991/cej-2019-03091366.
Bilgin, Ö. (2012). "Lateral earth pressure coefficients for anchored sheet pile walls", *International Journal of Geomechanics*, 12(5), 584-595, https://doi.org/10.1061/(asce)gm.1943-5622.0000154.
Bose, S.K. and Som, N.N. (1998). "Parametric study of a braced cut by finite element method", *Computers and Geotechnics*, 22(2), 91-107, https://doi.org/10.1016/S0266-352X(97)00033-5.
Chowdhury, S.S., Deb, K. and Sengupta, A. (2013). "Estimation of design parameters for braced excavation: Numerical study", *International Journal of Geomechanics*, 13(3), 234-247, https://doi.org/10.1061/(asce)gm.1943-5622.0000207.
Deb, P. and Pal, S.K. (2019). "Numerical analysis of piled raft foundation under combined vertical and lateral loading", *Ocean Engineering*, 190, 106431, https://doi.org/10.1016/j.oceaneng.2019.106431.
Debnath, A. and Pal, S.K. (2023a). "A numerical analysis on anchored sheet pile wall subjected to surcharge strip loading", *Journal of Engineering Research*, 11(3), 62-74, https://doi.org/10.1016/j.jer.2023.100088.
Debnath, A. and Pal, S.K. (2023b). "Influence of surcharge strip loads on the behavior of cantilever sheet pile walls: A numerical study", *Journal of Engineering Research*, 11(1), 100029, https://doi.org/10.1016/j.jer.2023.100029.
Fall, M., Gao, Z. and Ndiaye, B.C. (2019). "Three-dimensional response of double anchored sheet pile walls subjected to excavation and construction sequence", *Heliyon*, 5(3), https://doi.org/10.1016/j.heliyon.2019.e01348.
Georgiadis, M. and Anagnostopoulos, C. (1998). "Lateral pressure on sheet pile walls due to strip load", *Journal of Geotechnical and Geoenvironmental Engineering*, 124(1), 95-98, https://doi.org/10.1061/(asce)1090-0241(1998)124:1(95).
Guo, P., Gong, X. and Wang, Y. (2019). "Displacement and force analyses of braced structure of deep excavation considering unsymmetrical surcharge effect", *Computers and Geotechnics*, 113, 103102, https://doi.org/10.1016/j.compgeo.2019.103102.
Hakeem, B.M. (2024). "Investigation of a loaded pile responses due to proposed deep excavation in sand soil: Finite element analysis using Plaxis 3d program", *Civil Engineering Infrastructures Journal*, https://doi.org/10.22059/CEIJ.2024.365637.1963.
Hsiung, B.C.B. (2009). "A case study on the behaviour of a deep excavation in sand", *Computers and Geotechnics*, 36(4), 665-675, https://doi.org/10.1016/j.compgeo.2008.10.003
Jaky, J. (1944). "The coefficient of earth pressure at rest", *Journal of the Society of Hungarian Architects and Engineers*, 78(22), 355-358.
Li, Y., Zhang, W. and Zhang, R. (2022). "Numerical investigation on performance of braced excavation considering soil stress-induced anisotropy", *Acta Geotechnica*, 17(2), 563-575, https://doi.org/10.1007/s11440-021-01171-3.
Ozpolat, A. and Aksoy, H.S. (2022). "The effect of distance between sheet pile and foundation on bearing capacity of foundation", *Advances in Civil Engineering*, 2022(1), 7338718, https://doi.org/10.1155/2022/7338718.
Peck, R.B. (1969). "Deep excavations and tunneling in soft ground", *Proceedings of the Seventh ICSMFE*, State of the Art, (pp. 225-290), Mexico,
Pradeep, T., GuhaRay, A., Bardhan, A., Samui, P., Kumar, S. and Armaghani, D.J. (2022). "Reliability and prediction of embedment depth of sheet pile walls using hybrid ANN with optimization techniques", *Arabian Journal for Science and Engineering*, 47(10), 12853-12871, https://doi.org/10.1007/s13369-022-06607-w.
Samadhiya, N.K. (2020). "Evaluation of model sheet pile wall adjacent to a strip footing-an experimental investigation", *International Journal of Geotechnical Engineering*, 14(7), 828-835, https://doi.org/10.1080/19386362.2019.1581459.
Schroeder, W.L. and Roumillac, P. (1983). "Anchored bulkheads with sloping dredge lines", *Journal of Geotechnical Engineering*, 109(6), 845-851, https://doi.org/10.1061/(ASCE)0733-9410(1983)109:6(845).
Shafiqul Islam, M., Rokonuzzaman, M. and Sakai, T. (2017). "Shape effect of square and circular footing under vertical loading: experimental and numerical studies", *International Journal of Geomechanics*, 17(9), 1-9, https://doi.org/10.1061/(ASCE)GM.1943-5622.0000965.
Singh, A.P. and Chatterjee, K. (2020a). "Lateral earth pressure and bending moment on sheet pile walls due to uniform surcharge", *Geomechanics and Engineering*, 23(1), 71-83, https://doi.org/10.12989/gae.2020.23.1.071.
Singh, A.P. and Chatterjee, K. (2020b). "Ground settlement and deflection response of cantilever sheet pile wall subjected to surcharge loading", *Indian Geotechnical Journal*, 50(4), 540-549, https://doi.org/10.1007/s40098-019-00387-1.
Singh, A.P. and Chatterjee, K. (2020c). "Influence of soil type on static response of cantilever sheet pile walls under surcharge loading: A numerical study", *Arabian Journal for Geosciences*, 13, https://doi.org/10.1007/s12517-020-5170-x.

Sowers, G.B. and Sowers, G.F. (1967). "Failures of bulkhead and excavation bracing", *Civil Engineering*, 37(1), 72-77, https://trid.trb.org/View/121910.

Tabaroei, A., Sarfarazi, V., Pouraminian, M. and Mohammadzadeh, D. (2022). "Evaluation of behavior of a deep excavation by three-dimensional numerical modeling", *Periodical Polytechnica Civil Engineering*, 66(3), 967-977, https://doi.org/10.3311/PPci.20353.

Tsinker, G.P. (1983). "Anchored sheet pile bulkheads: Design practice", *Journal of Geotechnical Engineering*, 109(8), 1021-1038, https://doi.org/10.1061/(ASCE)0733-9410(1983)109:8(1021).

USS Design Manual. (1984). "Steel sheet piling United States", Steel Updated and reprinted by US Department of Transportation, FHWA with permission.

Wang, J., Xiang, H. and Yan, J. (2019). "Numerical simulation of steel sheet pile support structures in foundation pit excavation", *International Journal of Geomechanics*, 19(4), 05019002, https://doi.org/10.1061/(ASCE)GM.1943-5622.0001373.

Wood, D.M. (2004). *Geotechnical modelling (Applied Geotechnics; V. 1)*, Boca Raton FL USA, CRC Press Taylor and Francis Group/Books, https://wp.kntu.ac.ir/fz_kalantary/Source/Plasticity/(David%20Muir%20Wood)%20Geotechnical%20modelling.pdf.

Zhang, R., Goh, A.T.C., Li, Y., Hong, L. and Zhang, W. (2021). "Assessment of apparent earth pressure for braced excavations in anisotropic clay", *Acta Geotechnica*, 16, 1615-1626, https://doi.org/10.1007/s11440-020-01129-x.

AIMS AND SCOPE

Since the College of Engineering (Former Faculty of Engineering, FOE) of the University of Tehran has renewed its policy toward scientific publication, the Civil Engineering transaction of the well- built 45 years old Persian journal of *"Nashrieh Daneshkadeh Fanni"* is to be published in English and as separate independent journal with the name of ***Civil Engineering Infrastructures Journal***.

Civil Engineering Infrastructures Journal is an international journal which publishes high quality scientific papers in all areas of engineering and management of civil infrastructures. The civil infrastructures include, but are not limited to: buildings, bridges, dams, transportation systems, geotechnical structures, underground constructions, water distribution systems, offshore platforms, pipelines, ocean structures, airports and power plants.

The scope of this journal encompasses, but is not restricted to the following aspects of engineering and management of infrastructures:

- Mathematical modeling
- Computational and experimental methods
- Environmental Impact assessment
- Passive defense and security issues
- Monitoring and assessment
- Construction and design for durability
- Deterioration modeling and aging
- Failure analysis
- Field testing
- Financial planning
- Inspection and diagnostics
- Life-cycle analysis and prediction

- Maintenance, rehabilitation, repair and replacement strategies
- Non-destructive testing
- Optimization of maintenance and management
- Specifications and codes
- Reliability and risk management
- Supervisory Control and Data Assimilation (SCADA)
- Automation and Robotics in Construction
- Smart civil infrastructure Systems
- Sustainable civil infrastructure systems
- Case studies

Audiences of ***Civil Engineering Infrastructures Journal*** are researchers and practitioners as well as people working in infrastructure design, construction, maintenance and operation. Papers considered for publication must contain a clear and well-defined engineering component and make a significant contribution to the engineering and management of civil infrastructures. All articles submitted to this journal will undergo a rigorous peer review by anonymous independent experts.

Additional information can be obtained from:

Civil Engineering Infrastructures Journal
College of Engineering,
University of Tehran
P.O. Box: 11155- 4563
Tehran, Iran
Tel/ Fax: +98-21-88956097
Web Site: www.ceij.ir
Email: ceij@ut.ac.ir

University of Tehran
College of Engineering

Copyright Transfer Agreement

In order to protect the author(s), from the consequences of unauthorized use, the publisher requests that all author(s) sign the appropriate statement below:
The author(s) undersigned hereby approves submission of this work and all subsequent revisions for publication and transfers, assigns, or otherwise conveys copyright ownership to the Civil Engineering Infrastructures Journal (CEIJ). I (we) acknowledge that i) the submitted material represents original material, ii) does not infringe upon the copyright of any third party, and iii) that no part of the work has been published or under consideration for publication elsewhere unless and until it is rejected by Civil Engineering Infrastructures Journal (CEIJ). I (we) agree to indemnify the publisher against any loss or damages arising out of a breach of this agreement. In the event that my (our) submission is not published, copyright ownership shall revert to the author (s).

Manuscript Title:

Corresponding Author

Author:
Date: Signature;

Author:
Date: Signature:

Author:
Date: Signature:

Author:
Date: Signature:

Please submit the signed agreement with the final manuscript to:
Civil Engineering Infrastructures Journal (CEIJ)
School of Civil Engineering,
College of Engineering, University of Tehran
Enghelab Ave., P.O. Box: 11155-4563, Tehran, Iran.
Tel: 88956097
Fax: 66498981
E-mail: ceij@ut.ac.ir
Website: www.ceij.ir

CIVIL ENGINEERING INFRASTRUCTURES JOURNAL (CEIJ)

is indexed and abstracted in the bibliographical databases including:

Web of Science (ESCI)
http://science.thomsonreuters.com

Scopus
https://www.scopus.com

Islamic World Science Citation Center;
http://www.isc.gov.ir

Directory of Open Access Journals (DOAJ)
https://doaj.org

Google Scholar
https://scholar.google.com

General Impact Factor (GIF)
http://generalimpactfactor.com

Scientific Indexing Services (SIS)
http://www.sindexs.org

International Institute of Organized Research (I2OR)
http://www.i2or.com

Information Matrix for the Analysis of Journals (MAIR)
http://miar.ub.edu

ROAD: the Directory of Open Access scholarly Resources
http://road.issn.org

Scientific World Index
http://www.sciwindex.com

International Innovative Journal Impact Factor (IIJIF)
http://www.iijif.com

Science library index
http://scinli.com

Journal Factor
http://www.journalfactor.org

Open Academic Journals Index (OAJI)
http://oaji.net

Electronic Journals Library (EZB)
https://rzblx1.uni-regensburg.de

Systematic Impact Factor (SIF)
http://www.sifactor.org

COSMOS IMPACT FACTOR
http://www.cosmosimpactfactor.com

Polish Ministry of Science and Higher Education (MSHE)
https://journals.indexcopernicus.com

Magiran
http://www.magiran.com

Scientific Information Database (SID); Iran;
http://www.Sid.ir

Ministry of Science, Research and Technology of Iran has granted the Science and Research (Elmi-Pajouheshi) credit to CEIJ according to the letter No. 3/252445 at 25 Feb. 2012.

College of Engineering

Civil Engineering Infrastructures Journal

Volume 58, Number 1, June 2025

CONTENTS

Civil Engineering Infrastructures Journal (CEIJ)

Volume 58, Number 1, June 2025